Dissertation

Submitted to the

Combined Faculty of Natural Sciences and Mathematics

of the Ruperto Carola University Heidelberg, Germany

for the degree of

Doctor of Natural Sciences

Presented by

Alina Leandra Bendinger, M.Sc.

Born in Osnabrück, Germany

Oral examination: 21.10.2019

Investigation of hypoxia in syngeneic rat prostate tumors after irradiation with photons or carbon ions by multimodal imaging and histology

Referees: PD Dr. rer. nat. Karin Müller-Decker

Prof. Dr. rer. nat. Christian Karger

Publications of this dissertation

Bendinger AL, Debus C, Glowa C, Karger CP, Peter J, Storath M: *Bolus arrival time estimation in dynamic contrast-enhanced magnetic resonance imaging of small animals based on spline models*. **Phys Med Biol**, 2019 Feb 5; **64**(4): 045003.

Bendinger AL, Glowa C, Peter J, Karger CP: *Photoacoustic imaging to assess pixel-based sO_2 distributions in experimental prostate tumors*. **J Biomed Opt,** 2018 Mar; **23**(3): 036009.

Manuscripts in preparation

Bendinger AL, Seyler L, Saager M, Debus C, Peschke P, Komljenovic D, Debus J, Peter J, Floca R, Karger CP, Glowa C: *Impact of single dose photons and carbon ions on perfusion and vascular permeability: A dynamic contrast-enhanced MRI study in the anaplastic rat prostate tumor R3327-AT1*. Submitted.

Bendinger AL, Peschke P, Peter J, Debus J, Karger CP, Glowa C: *High doses of photons and carbon ions induce comparable increase of vascular permeability in R3327-HI prostate tumors: A dynamic contrast enhanced MRI study*. In preparation.

Conference contributions

27th Annual Meeting of the International Society for Magnetic Resonance in Medicine (ISMRM) 2019, Montreal, Canada (Posters, Trainee Stipend):

Bendinger AL, Seyler L, Saager M, Debus C, Peschke P, Komljenovic D, Debus J, Peter J, Floca R, Karger CP, Glowa C: *Response monitoring by DCE-MRI in an experimental prostate tumor after single dose ^{12}C-ion and photon radiotherapy.* In: Proc. Intl. Soc. Mag. Reson. Med. 27: 2337, 2019.

Bendinger AL, Debus C, Glowa C, Karger CP, Peter J, Storath M: *Bolus arrival time estimation for DCE-MRI signals without fast up-slope.* In: Proc. Intl. Soc. Mag. Reson. Med. 27: 2350, 2019.

26th Annual Meeting of the ISMRM 2018, Paris, France (Poster, Trainee Stipend):

Bendinger AL, Karger CP, Debus C, Floca R, Debus J, Peter J, Glowa C: *Longitudinal response monitoring in experimental prostate tumors by DCE-MRI after C-12 ion and photon radiotherapy*. In: Proc. Intl. Soc. Mag. Reson. Med. 26: 1470, 2018.

10th World Molecular Imaging Congress, 2017, Philadelphia, USA (Poster, Travel Award):

Bendinger AL, Glowa C, Peter J, Karger CP: *Photoacoustic imaging to assess pixel-based sO_2 distributions in experimental prostate tumors.*

Table of Contents

List of Figures

List of Tables

Abbreviations

^{12}C-ions	Carbon ions
2CXM	Two compartment exchange model
3D	Three dimensional
AIF	Arterial input function
aqua dest.	Distilled water
a.u.	Arbitrary unit
AUC	Area under the curve
BAT	Bolus arrival time
BOLD	Blood oxygen level dependent
BrdU	5-bromo-2'-deoxyuridine
BrdU$^+$	5-bromo-2'-deoxyuridine-positive
BSA	Bovine serum albumin
CA	Contrast agent
CA IX	Carbonic anhydrase 9
CD31$^+$/SMA$^+$	CD31-positive/ smooth muscle actin-positive
CT	Computed tomography
DAPI	4',6-diamidino-2-phenylindole
DCE-MRI	Dynamic contrast-enhanced magnetic resonance imaging
DNA	Deoxyribonucleic acid
DOF	Degrees of freedom
DSB	Double-strand break
EES	Extracellular, extravascular space
EMD	Earth mover's distance
eq.	Equation
ESR	Electron spin resonance
ETM	Extended Tofts model
FAZA	[^{18}F]fluoroazomycin arabinoside
FMISO	[^{18}F]fluoromisonidazole
GCV	Generalized cross validation
GMM	Gaussian mixture modeling
H&E	Hematoxylin & Eosin

HCl	Hydrochloric acid
Hct	Hematocrit
hdf5	Hierarchical data format 5
HIF-1	Hypoxia-inducible factor-1
HIT	Heidelberg Ion Beam Therapy Center
Hoechst 33342	BisBenzimide H 33342 trihydrochloride
IMRT	Intensity-modulated radiotherapy
i.p.	Intraperitoneal
i.v.	Intravenously
IVC	Individually ventilated cage
LET	Linear energy transfer
MITK	Medical Imaging Interaction Toolkit
MRI	Magnetic resonance imaging
MSE	Mean squared error
O_2	Oxygen
PA	Photoacoustic
PAI	Photoacoustic imaging
PBS	Phosphate-buffered saline
PC	Principle component
PCA	Principle component analysis
PET	Positron emission tomography
PMMA	Polymethylmethacrylate
pO_2	Partial pressure of oxygen
px	Pixel
r_1	Relaxivity
R_1	Longitudinal relaxation rate
R_2	Transversal relaxation rate
R_2^*	Effective transversal relaxation rate
RBE	Relative biological effectiveness
ROI	Region of interest
room temp	Room temperature
ROS	Reactive oxygen species
RT	Radiotherapy
SEM	Standard error of the mean
SMA	Smooth muscle actin

SNR	Signal-to-noise ratio
sO_2	Oxygen saturation
SOBP	Spread-out Bragg-peak
$T1$	Longitudinal relaxation time
$T2$	Transversal relaxation time
$T2^*$	Effective transversal relaxation time
TCC	Tissue concentration curve
TE	Echo time
TIFF	Tagged image file format
TOLD	Tissue oxygen level dependent
TR	Repetition time
TURBO FLASH	Ultrafast fast low angle shot
US	Ultrasound
VDT	Volume doubling time
ZPF	Center for Preclinical Research
$\gamma H2AX^+$	γH2AX-positive

Summary

Tumor hypoxia has been widely recognized as a significant factor that increases treatment resistance and promotes malignant progression. High linear energy transfer (LET) radiotherapy (RT), e.g. with carbon ions (^{12}C-ions), is expected to overcome this resistance factors as its lethality is less dependent on tumor oxygenation as compared to conventional low LET photon irradiation. However, the exact interplay between irradiation response, vascular changes, perfusion, and hypoxia is still not well understood, especially with respect to high LET RT. In the present thesis, the hypoxic status of syngeneic Dunning R3327 rat prostate tumor model sublines was characterized prior to and after irradiation with either low LET photons or high LET ^{12}C-ions by multimodal imaging and histology.

The initial oxygenation status of three subcutaneously transplanted Dunning tumor sublines (H, HI and AT1) was determined by photoacoustic imaging (PAI) which included the development and validation of a new PAI analysis protocol. The new protocol enabled the distinction of the three sublines based on their oxygenation profiles and their response towards external changes in oxygen supply. Subsequently, the effects of curative and sub-curative single dose irradiations with either photons or ^{12}C-ions on the two hypoxic tumor sublines (HI and AT1) were investigated by pharmacokinetic modeling of longitudinal dynamic contrast-enhanced magnetic resonance imaging (DCE-MRI) data. For this, a novel method for estimating the contrast agent's arrival time was developed in cooperation with the group for Image Analysis and Learning of the Interdisciplinary Center for Scientific Computing of Heidelberg University. It enables a delay correction of the contrast agent arrival time which improves fit accuracy and the reliability of the pharmacokinetic modeling results. The moderately differentiated HI-tumor showed increased vascular permeability 7 days after irradiation without any modality or dose dependency, while the anaplastic and chronic hypoxic AT1-tumor revealed an earlier and stronger treatment response after ^{12}C-ion irradiation as compared to the more delayed response after photon irradiation. Again, no dose dependency was detected. Finally, a longitudinal histology study after irradiation of the AT1-tumor with curative doses of either photons or ^{12}C-ions revealed that hypoxia developed slightly faster after ^{12}C-ion than after photon irradiation. Furthermore, this study validated the relative biological effectiveness (RBE) for ^{12}C-ions, which was determined previously for the endpoint local tumor control, on a microscopic level within the first 10 days. Additionally, reasonable time points for a future multimodal imaging study with PAI, sequential positron emission tomography (PET) and DCE-MRI measurements as well as histology were determined.

In conclusion, this thesis proved PAI and the novel analysis protocol to be a feasible method for the characterization of the three Dunning tumor sublines with respect to their oxygenation. The different sensitivities of the HI- and AT1-tumors towards the two irradiation mo-

dalities indicate that the irradiation-induced vascular response depends on the structural-functional status of the tumor vasculature. The dose-independent response of both tumor sublines towards the two irradiation modalities suggests that the initial vascular response only plays a minor role with respect to local tumor control at high single doses.

Zusammenfassung

Hypoxie ist ein wesentlicher Faktor, der zu erhöhter Behandlungsresistenz und progressivem Wachstum von Tumoren führt. Durch Strahlentherapie mit Partikeln wie z. B. Kohlenstoffionen (^{12}C-Ionen), die einen hohen linearen Energietransfer (LET) aufweisen, soll die durch Hypoxie induzierte Strahlenresistenz überwunden werden, da die Letalität von hoch LET-Strahlung, im Gegensatz zu konventioneller niedrig LET Photonenbestrahlung, nicht von der Oxygenierung des Gewebes abhängt. Die genauen Wechselwirkungen zwischen Bestrahlung, insbesondere hoch LET-Strahlung, Blutgefäßen, Perfusion und Hypoxie sind immer noch nicht vollständig verstanden. In der vorliegenden Arbeit wurde der hypoxische Zustand von syngenen Dunning R3327 Ratten Prostatatumorsublinien vor und nach Bestrahlung mit entweder niedrig LET Photonen oder hoch LET ^{12}C-Ionen mit Hilfe von multimodaler Bildgebung und Histologie charakterisiert.

Der initiale Oxygenierungszustand der drei subkutan transplantierten Dunning Tumorsublinien (H, HI und AT1) wurde mit photoakustischer Bildgebung (photoacoustic imaging, PAI) bestimmt. Ein dafür neu entwickeltes und validiertes Analyseprotokoll ermöglichte die Unterscheidung der drei Sublinien aufgrund ihres Oxygenierungsprofils und ihres Verhaltens nach externen Veränderungen der Sauerstoffzufuhr. Des Weiteren wurden die Auswirkungen kurativer und sub-kurativer Einzeldosisbestrahlungen mit Photonen oder ^{12}C-Ionen auf zwei hypoxische Tumorsublinien (HI und AT1) mittels pharmakokinetischer Modellierung von dynamisch kontrastmittelverstärkter Magnetresonanztomographie (DCE-MRI) untersucht. In Kooperation mit der Gruppe für Image Analysis and Learning des Interdisciplinary Center for Scientific Computing der Universität Heidelberg wurde dafür eine neue Methode zur Bestimmung der Ankunftszeit des Kontrastmittels im Gewebe entwickelt. Diese Methode ermöglicht eine Korrektur der Verzögerung zeitlich versetzt ankommender Kontrastmittel-Boli, was wiederum zu einer verbesserten Anpassungsgüte und Belastbarkeit der Ergebnisse der pharmakokinetischen Modellierung führt. Der moderat differenzierte HI-Tumor zeigte sieben Tage nach Bestrahlung eine erhöhte vaskuläre Permeabilität, unabhängig von Strahlenmodalität und -dosis. Der anaplastische und chronisch hypoxische AT1-Tumor wies hingegen einen früheren und stärkeren Behandlungseffekt nach Bestrahlung mit ^{12}C-Ionen im Vergleich zur Bestrahlung mit Photonen auf und zeigte ebenfalls keine Abhängigkeit von der Strahlendosis. Schließlich ergab eine longitudinale Histologiestudie an mit kurativen Photonen- oder ^{12}C-Ionen-Dosen bestrahlten AT1-Tumoren, dass Hypoxie nach ^{12}C-Ionenbestrahlung etwas früher als nach Photonenbestrahlung auftritt. Weiterhin bestätigte diese Studie auf mikroskopischer Ebene die zuvor für den Endpunkt lokale Kontrolle bestimmte relative biologische Wirksamkeit von ^{12}C-Ionen innerhalb der ersten zehn Tage nach Bestrahlung. Abschließend konnten sinnvolle Zeitpunkte für eine multimodale Bildge-

bungsstudie mit PAI, sequentiellen Positronen-Emissions-Tomographie (PET)- und DCE-MRT-Messungen sowie anschließender Histologie bestimmt werden.

In dieser Doktorarbeit wurde gezeigt, dass PAI und das neu entwickelte Analyseprotokoll praktikable Methoden für die Charakterisierung der Oxygenierung in den drei Dunning Tumorsublinien darstellen. Die unterschiedlichen Strahlenempfindlichkeiten der HI- und AT1-Tumore gegenüber beiden Bestrahlungsmodalitäten weist darauf hin, dass die strahleninduzierte vaskuläre Reaktion vom Zustand der Gefäße im Tumor abhängt. Die Dosisunabhängigkeit der Strahlenantwort beider Tumorsublinien gegenüber beiden Bestrahlungsmodalitäten deutet darauf hin, dass initiale vaskuläre Schäden bei hoher Einzeldosisbestrahlung nur eine untergeordnete Rolle für die lokale Tumorkontrolle spielen.

1 Introduction

1.1 Prostate cancer

In 2018, 13.5 % of all male cancer patients were diagnosed with prostate cancer making it the second most frequent cancer with 358 989 deaths worldwide [1]. In Germany, 62 641 new cases of prostate cancer were diagnosed in 2018, making it the fourth most frequently diagnosed cancer [2].

95 % of all prostate tumors are adenocarcinomas i.e. malignant neoplasia of epithelial tissues with glandular origin [3]. With increasing volume, the prostate carcinoma exhibits multiple histological patterns within one tumor. Upon suggestion of the World Health Organization, the Gleason Score was introduced for staging prostate cancer which rates the tumor's glandular structure rather than its cytological characteristics. Gleason patterns range from 1 to 5 where Gleason 1 refers to a highly differentiated adenocarcinoma, Gleason 3 is a moderately differentiated tumor, and Gleason 5 is an anaplastic tumor. The Gleason score is obtained by summing up the most frequent and the second most frequent Gleason pattern found within one tumor. This way, the large morphological heterogeneity of the prostate carcinoma is taken into account [4]. In 2014, an update of the Gleason Score was proposed that also weights the order of the two Gleason patterns (i.e. Gleason $3 + 4 \neq 4 + 3$) [5].

The diagnosis is further manifested by rectal examination of the prostate for size, shape, consistency, boundary, prostate specific antigen level, and, in advanced cases, by skeletal scintigraphy. Depending on the tumor grading, prostate cancer is either treated with surgery (prostatectomy), radiotherapy, hormone therapy (androgen-deprivation therapy) or a combination of these. In rare cases chemotherapy is performed. Low grade prostate tumors and old patients are often subject to watchful waiting meaning that no therapy is started unless the patient's condition impairs [3].

1.2 Radiotherapy with photons and carbon ions

Already at the end of the 19th century, shortly after the discovery of X-rays, the potential of ionizing irradiation for the treatment of cancer patients was recognized and exploited by various scientists [6]. Nowadays, radiotherapy (RT) has become indispensable for the treatment of oncologic patients, either on its own or in combination with other therapies such as chemotherapy and surgery [7].

RT aims at a maximal dose deposition in the tumor to induce lethal DNA damages. During treatment planning, medical physicists optimize the dose that is delivered to the tumor such

that the surrounding normal tissue is maximally spared. Conventional RT uses photon beams which exhibit an exponential decrease in dose with increasing tissue penetration depth (Figure 1 A). To protect the surrounding normal tissue and organs at risk from undesired irradiation exposure, the maximal treatment dose has to be restricted. The introduction of intensity-modulated RT (IMRT), that modulates the fluence of the photon beam during treatment to conform the dose distribution to the shape of the tumor, allows a certain dose-escalation without increasing the dose to the surrounding healthy tissue. IMRT is also applied in the treatment of prostate cancer [8].

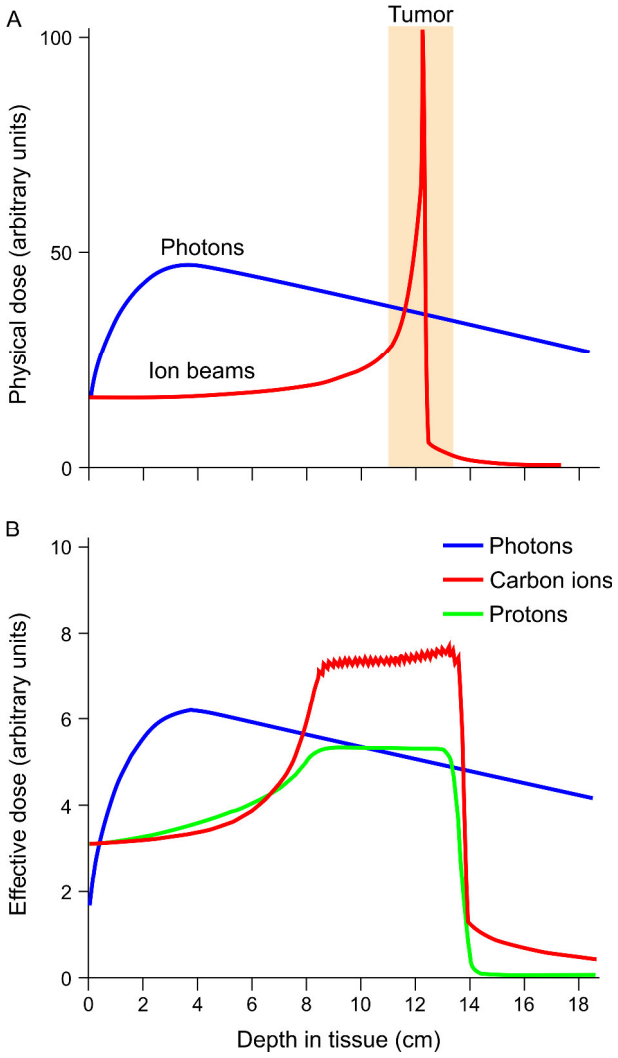

Figure 1 Depth-dose profiles of photons, protons, and ^{12}C-ions. (A) Representative depth-dose profiles for photons (blue), which show an exponential decrease in dose with increasing penetration depth, and for ions (red), which deposit the majority of their dose in the Bragg-peak. (B) Spread-out Bragg-peak (SOBP) for conformal irradiation of large tumors. The SOBP is achieved by superimposing ion beams of different energies. For the same dose in the tumor, the neighboring tissues can be spared better with ions (carbon ions (red) and protons (green)) than with photons. Adapted with permission from Springer Nature: Nature Reviews Clinical Oncology [9]. All rights reserved.

The use of ions instead of photons was introduced to further improve the dose conformity to the tumor. Ions are characterized by an advantageous inverted depth-dose profile as compared to photons: a mono-energetic ion beam emits very low dose in the entrance region and exhibits a maximal dose peak in the energy-dependent Bragg-peak followed by an immediate fall-off in dose (Figure 1 A). By superimposing ion beams of different energies, a so-called spread-out Bragg-peak (SOBP) is formed to cover the entire tumor volume. This allows a precise high-dose tumor irradiation while sparing the surrounding healthy tissue, mainly due to the ions' finite range (Figure 1 B) [10]. The feasibility of proton RT was already demonstrated for prostate cancer patients in 1979 [11]. Proton RT is a form of low linear-energy-transfer (LET) ion RT. The LET indicates the amount of energy per distance which is deposited in the tissue by an ionizing particle and is reported in keV/µm.

The use of heavier ions with higher LETs than protons was already proposed in 1946 [12], and its clinical relevance is currently investigated. Among these heavier ions, carbon ions (^{12}C-ions), which exhibit an even higher dose deposition in the Bragg-peak (Figure 1 B) and a higher LET than protons, are under clinical investigation [13, 14]. Furthermore, heavy ions have a higher relative biological effectiveness (RBE) compared to low LET photons and protons which means that less physical dose is required to achieve the same biological effect [15].

Ionizing radiation holds a therapeutic benefit by damaging the DNA of cancerous cells which eventually leads to cell death. It can induce base loss and modification, crosslinks, single strand breaks, and DNA double strand breaks (DSBs) [16]. The latter are the most complex to repair and, therefore, their occurrence is considered the critical event for lethality [17, 18].

Low LET photons induce DNA damage through indirect effects. They hydrolyze water producing reactive oxygen species (ROS) that induce DNA damage. In the presence of oxygen, this damage is fixated leading to persistent DNA breaks and eventually cell death. However, in the absence of oxygen, DNA radicals are reduced by thiols and the original DNA is restored [19, 20]. Densely ionizing (high LET) radiation acts directly on the phosphodiester bonds inducing more complex and spatially clustered DNA damages which are more difficult to repair and which increase the chance for immediate DNA DSBs [20, 21]. The resulting impaired repair mechanisms are reflected by a faster and higher amount of tumor cell inactivation [10], the impairment of quiescent cells [22], and the overcoming of radioresistance factors such as hypoxia [23], leading to a general reduction of tumor heterogeneity in complex solid tumors [24]. Additional preclinical data suggest that ^{12}C-ions also impact the immune system [25, 26], decrease the tumor metastatic potential [27], and suppress the process of angiogenesis [15, 28].

The reduced lateral scattering and sharp lateral penumbra together with the increased RBE make heavy ions very promising candidates for radiotherapy of deep seated, hypoxic, and radioresistant tumors [29].

The recognized physical and radiobiological advantages of heavier ions compared to photons and protons still require confirmation by clinical trials [29]. Currently, there are 75 clinically operating particle therapy facilities worldwide of which the majority is using protons [30]. In 2017, eleven centers worldwide, situated in Japan, China, Italy, Austria, and Germany, were using ^{12}C-ions [31] and 15 % of the patients treated with ion RT underwent heavy ion irradiation [29]. More heavy ion treatment facilities are in planning, and, along with this rising number, there is an increased need for systematic, large-scale, standardized *in vivo* experiments to obtain parameters related to the effectiveness of ions as a function of physical and biological parameters such as RBE values. The European Particle Therapy Network Work Package 6 is aiming to form a network of research and therapy facilities to standardize radiobiological experiments [32] and to enable the comparison of experimental and treatment results from individual centers.

Clinical trials on the usage of particle therapy for varies cancers (head and neck, lung, central nervous system, breast, intestine, prostate, lymphoma, sarcoma) and for pediatric cancers (central nervous system, head and neck, brain, medulloblastoma, rhabdomyosarcoma) are being performed worldwide [30] with 20 000 patients already having received ^{12}C-ion RT by 2018 [29]. Clinical studies for these malignancies are also running at the Heidelberg Ion Therapy Center (HIT), where particle therapy was successfully included into the clinical routine in 2009 [33]. The feasibility and safety of active raster-scanning ^{12}C-ion RT was demonstrated for patients with skull based chondrosarcomas [34], skull based chordomas [35], and for accelerated hypofractionation on patients with laryngeal malignancies, showing excellent local control rates and only moderate side effects, especially for radioresistant head and neck tumors [36]. The prospective IPI trial, which evaluated hypofractionated irradiation of the prostate with both protons or ^{12}C-ions using active raster-scanning technique, showed comparable toxicities and quality of life parameters for both modalities [37]. A retrospective study comparing treatment results of irradiation with protons and ^{12}C-ions on patients with G1 and G2 skull based chondrosarcomas revealed slightly but non-significantly worse overall survival and local control after 60 months for ^{12}C-ions [38]. However, 3.5 times more patients were treated with ^{12}C-ions than with protons which might have led to a selection bias. ^{12}C-ion RT requires advanced and costly infrastructure making the treatment very expensive. Therefore, Sprave *et al.* have assessed the financial aspects of ^{12}C-ion RT for skull based chordoma evaluating long-term (10 year) outcome data. They concluded that ^{12}C-ion RT is highly cost-effective [39]. Despite the large number of clinical studies, no randomized trials directly comparing ^{12}C-ion RT with modern photon RT were performed so far [40].

Conventional RT schedules provide fractionated irradiation with 5 fractions à 2 Gy over 6 weeks. Lately, enhanced effectiveness and reduced side and long-term effects along with less health care cost and increased convenience for the patients are attributed to hypofractionated treatment schedules, i.e. less fractions with more dose per fraction over a shorter treatment period [41, 42]. However, so far it is still unclear whether hypofractionation will provide a significant therapeutic benefit [42-46]. Single-fraction treatments were proclaimed feasible after performing single-dose escalation studies on patients with inoperable lung tumors using a CyberKnife [47] and on peripheral stage I non-small cell lung cancer patients using doses of up to 50 Gy of ^{12}C-ions [48]. The response of prostate cancer to fractionation is comparable to that of late responding normal tissue suggesting that hypofractionation should be equally effective as conventional fractionation for treating prostate cancer while reducing costs and increasing patient convenience [49]. Brenner *et al.* reported a number of studies that have demonstrated non-inferiority of moderate hypofractionation (typically involving 15 to 25 fractions of 2.5 to 3.5 Gy) compared to conventional fractionation patterns (involving 40 to 45 fractions of approximately 2 Gy each) [49]. The benefits of extreme hypofractionation (typically involving 4 to 7 fractions at doses of 4 to 10 Gy per fraction) are currently investigated [49]. This might lead to a further rethinking of common radiotherapy schedules with 2 Gy per fraction.

1.3 Hypoxia as a resistance factor

Tumor hypoxia belongs to the original hallmarks of cancer [50]. It has already been identified as a key factor promoting radioresistance by Gray *et al.* in 1953 [51] who found that the sensitivity of tumor cells to X-rays was about three times greater when cells were irradiated in a well-oxygenated medium compared to anoxic conditions. This factor is now called the oxygen enhancement ratio (OER) and describes the ratio of the doses required to achieve the same biological effect under hypoxic and normoxic conditions [52].

Changes in physiology and metabolism of tumors lead to an increased growth rate which results in hypoxia as the (immature) vasculature cannot keep up supplying the fast growing tumor volume with oxygen. Two main types of hypoxia have been identified that co-exist with a high spatial heterogeneity in tumors. Chronic hypoxia is the result of diffusion limitation due to enlarged inter-vessel distances and deteriorated diffusion geometries such as U-shaped microvessels and arterious-venous shunts [53]. Acute hypoxia, on the other hand, results from perfusion limitations induced by severe structural and functional abnormalities such as increased vessel permeability, impaired endothelial lining, and microvessel elongations and dilatations, that induce transient perturbations of the microcirculation [54, 55]. Hypoxia-mediated release of pro-angiogenic factors leads to further uncoordinated tumor angiogenesis and expansion of the immature vasculature.

There is no strict and generally applicable hypoxia threshold for all tissue types [56]. Commonly, a partial pressure of oxygen (pO_2) below 10 mmHg is assumed to induce the hypoxia-related genetic and adaptive changes in tumor cells to overcome and survive hypoxic environments [56]. A multitude of genes that regulate e.g. oxygen transport, iron metabolism, angiogenesis, glycolysis, transcription factors, growth factors, cell adhesion, and the extracellular matrix are induced by hypoxia leading to unrestrained angiogenesis and glycolysis, immortalization, genetic instability, apoptosis, tissue invasion, and the formation of metastasis leading to an overall aggressive tumor behavior [57]. The most prominent transcription factor that stabilizes under hypoxic conditions is the hypoxia-inducible factor-1 (HIF-1) that consists of the constitutively expressed HIF-1β subunit and the oxygen regulated HIF-1α subunit [58]. HIF-1 is a key transcription factor that regulates the expression of more than 30 genes involved in energy metabolism, hormone regulation, and vasoreactivity [59] and is increased in many human cancers [60].

Hence, tumor vasculature, hypoxia, and their alterations after treatment are important factors when developing treatment strategies for patients [61]. Concerning RT, it would be of upmost importance to identify hypoxic regions prior to treatment to be able to predict their irradiation response and to consider dose escalation to the hypoxic regions by dose painting [62].

1.4 Imaging of hypoxia

In the clinical routine, imaging is used for diagnostics, treatment planning, and treatment follow-up. As tumor hypoxia is one of the major resistance factors for radiotherapy much effort is put into its visualization. However, as of today, there is no measurement technique available that reliably quantifies the oxygen content three dimensional (3D). In the following, the main approaches for qualitative and quantitative hypoxia imaging are introduced.

Polarographic oxygen electrodes such as the Eppendorf® electrode enable direct measurements of pO_2 in units of mmHg [63]. They measure the current formed at a cathode originating from ionization of oxygen at -0.7 V versus a normal hydrogen electrode [59]. They have been applied in multiple clinical [64-67] and preclinical [68-70] studies where they were considered the gold-standard [59]. However, their usage requires an imaging modality to guide the electrode placing. Furthermore, they are highly invasive, provide only locally restricted information, and repeatable measurements of the same spot are impossible due to the oxygen consumption of the electrode itself [59]. The low signal-to-noise ratio at low oxygen tension represents a further limitation.

Electron spin resonance (ESR) uses reporter molecules to detect species containing unpaired electrons such as molecular oxygen [59]. The spectral line width of those reporter molecules is highly sensitive to oxygen and can be directly associated with oxygen concentration using

calibration curves [59, 63]. O'Hara *et al.* used ESR to determine the timing of hypoxia and re-oxygenation after irradiation in RIF-1 tumors on female mice after single dose and split dose irradiation [71].

Positron emission tomography (PET) visualizes the distribution and accumulation of radiolabeled hypoxia-sensitive tracers. While exhibiting a high specificity, PET suffers from restricted spatial resolution and involves the handling and injection of costly radioactive tracers. A range of hypoxia-sensitive tracers is available for PET imaging [72] of which [^{18}F]fluoromisonidazole (FMISO) [73] is most widely used. It accumulates *in vivo* below a median oxygen level of 10 mmHg. However, its slow pharmacokinetic profile only leads to a moderate signal ratio between hypoxic and normoxic tissue [74], and the resulting PET signal is non-linearly connected to the local oxygen tension [75]. The more hydrophilic [^{18}F]fluoroazomycin arabinoside (FAZA) [76] represents a promising alternative with faster clearance and an improved hypoxia-to-normoxia ratio as compared to other tracers [74, 77].

Magnetic resonance imaging (MRI) offers a variety of possibilities to assess hypoxia non-invasively while obviating exposure to ionizing radiation. Perfluorocarbons, organic compounds where all hydrogen atoms (^{1}H) are replaced by fluorine (^{19}F), are used for quantitative oxygen measurement. The non-toxic and chemically inert contrast agents are injected intravenously or intratumorally up to a few days before the measurement. The ^{19}F longitudinal relaxation rate $R1$ is oxygen sensitive and enhances proportionally to the dissolved oxygen concentration at a given temperature [59, 78, 79]. Due to the ^{1}H comparable MRI sensitivity of ^{19}F and the lack of endogenous ^{19}F in living organisms [80], ^{19}F oximetry potentially provides a high image contrast [80]. However, the ^{19}F concentration needs to be high enough. Also, many fluorinated molecules are insoluble in water. They exhibit long $T1$ relaxation times requiring long repetition times in the acquisition sequences which in turn challenges the clinical practicability of ^{19}F-MRI [80]. Blood oxygen level dependent (BOLD) MRI utilizes the paramagnetic property of de-oxygenated hemoglobin as an endogenous contrast agent that increases the $R2^*$ relaxation rate of the ^{1}H in the blood [63, 81]. The BOLD signal is of qualitative nature rather than providing absolute oxygen concentrations as no absolute relation of BOLD signal to pO_2 could be found [63, 82]. The BOLD signal can be subject to flow and partial volume effects when investigating small vessels [63]. Hallac *et al.* tried to correlate $T1$-based tissue oxygen level dependent (TOLD) MRI signals with pO_2 but found only weak correlations [83].

Dynamic contrast-enhanced (DCE)-MRI involves the administration of a contrast agent (usually gadolinium-based) and measures concentration-time curves in the tissue of interest. By subsequent pharmacokinetic modeling, hemodynamic parameters such as the volume transfer constant, plasma volume fraction, interstitial space, vascular permeability, and flow can be determined [84]. As low-perfused tissue areas are likely to suffer from oxygen depletion, DCE-MRI is considered to be an indirect measure of tissue hypoxia [85].

Optical imaging allows *in vivo* visualization of fluorescence and bioluminescence signals. One drawback of the low-energy optical photons is their high scattering and the corresponding decreased spatial resolution as compared to ionizing photons. As photons in the near infrared spectrum are least affected by scattering in tissue, they are favored for optical imaging. Optical imaging can be performed using target-specific reporters such as ligands, antibodies, and enzyme substrates that are linked to fluorescent dyes (e.g. Cy5, Cy7) [86], quantum dots, nanoparticles, or reporter genes (e.g. green fluorescent protein [87], firefly luciferase [88]). Optical imaging probes can be customized to a high specificity with respect to their target.

Photoacoustic imaging (PAI) is an emerging hybrid imaging modality that comprises the high specificity of optical imaging and the spatial resolution of ultrasound [89]. PAI uses laser light that induces the emission of a pressure wave after being absorbed by a chromophore. This pressure wave is measured as an ultrasound signal and contains the information about the chromophore's location. Because oxygenated and de-oxygenated hemoglobin exhibit different absorption spectra they can be distinguished and the oxygen saturation can be determined by PAI [90]. Its lack of ionizing radiation constitutes a great advantage. However, the imaging depth is limited by the central frequency of the ultrasonic transducer and the penetration depth of the laser light.

On a molecular basis, hypoxia can be assessed by staining for endogenous hypoxia markers such as HIF-1α or the less hypoxia specific carbonic anhydrase 9 (CA IX). Further, exogenous markers such as pimonidazole [91] and EF5 [92], which can be visualized by immunohistochemistry methods on tissue sections, can be used. Effort was also put into the development of fluorescence-coupled *in vivo* detectable tracers that target e.g. HIF-1α [93] and CA IX [86].

1.5 Aim of the thesis

This thesis investigates the temporal development of the treatment response after either photon or ^{12}C-ion irradiation by non-invasive multimodal imaging and histology using sublines of the syngeneic Dunning 3327 rat prostate tumor model.

RT aims at the induction of lethal DNA damage in the tumor. It is known that the effect of conventionally used low LET photons is induced by oxygen-dependent indirect effects, while high LET ^{12}C-ions act directly on the cells' DNA, independent of the oxygenation. Further, *in vitro* as well as *in vivo* studies demonstrated that ^{12}C-ions exhibit an increased relative biological effectiveness (RBE) as compared to photons, especially in highly radioresistant tumors. However, the underlying mechanisms that are responsible for this increased RBE as well as their temporal development are still unclear. Thus, it is of high interest to investigate the interplay between ^{12}C-ions, tumor hypoxia, re-oxygenation, perfusion, and tumor vasculature to reveal the mechanisms that lead to the enhanced biological effectiveness of ^{12}C-ions. This information is of great clinical relevance for the identification of patients that will benefit from such a treatment as well as for the optimization of the respective treatment protocols themselves.

In the first part of this thesis, a new photoacoustic imaging (PAI) protocol is established and used for the initial characterization of three Dunning tumor sublines prior to irradiation based on their intrinsic oxygenation level and their reaction to changes in the external oxygen supply. In the second part, the differential effects of single high doses of either photons or ^{12}C-ions on hypoxia, perfusion, and tumor vasculature are investigated in the acute hypoxic HI-tumor and the chronic hypoxic AT1-tumor by analyzing the data of two longitudinal dynamic-contrast enhanced magnetic resonance imaging (DCE-MRI) studies by pharmacokinetic modeling. To increase the fit accuracy of the pharmacokinetic modeling, a novel correction method is developed. Finally, temporal changes in vascular density, hypoxia, perfusion, proliferation, and DNA double strand breaks upon curative irradiation with either photons or ^{12}C-ions of the highly radioresistant AT1-tumor are histologically investigated.

2 Materials and Methods

2.1 Tumor model

2.1.1 Animal keeping

All experiments were approved by the governmental review committee (Regierungspräsidium Karlsruhe) on animal care. Copenhagen rats were kept in individually ventilated cages (IVC) with a maximal occupancy of four animals per cage in barrier D of the Center for Preclinical Research (ZPF). Light, temperature, and air humidity were controlled automatically in a 12 h rhythm. Food and water was available *ad libitum*.

Copenhagen rats used in the experiments in sections 2.2 and 2.5 were purchased from Charles River Laboratories Inc. (Wilmington, MA, USA). Copenhagen rats used in the experiments of section 2.7 were bred in-house in the ZPF.

2.1.2 The Dunning R3327 prostate tumor model

The original Dunning R3327 tumor arouse spontaneously in the prostate of an aged, Copenhagen rat in 1961 and is thus syngeneic in this rat strain. By further transplantations of the original tumor onto the male F_1 hybrids of male Copenhagen rats and female Fisher rats, *in vitro* passaging, and transplantation onto castrated male Copenhagen rats several tumor sublines emerged. These differ with respect to their volume doubling time (VDT), differentiation, metastatic potential, and hypoxic fraction [94, 95].

In this project, three of the above-mentioned sublines were used [94]. The Dunning R3327 H-tumor is well differentiated, normoxic, and hormone sensitive. It grows slowly with a VDT of 20 days and does not metastasize. The H-tumors' morphology is characterized by abundant acini with secretions. The Dunning R3327 HI-tumor is moderately differentiated and contains mucin-filled prostatic structures. It is acute hypoxic, i.e. its oxygenation status can be influenced externally (e.g. by changing the breathing gas). Furthermore, it is hormone insensitive, has a VDT of 10 days, and exhibits a low metastatic potential. The Dunning R3327 AT1-tumor is anaplastic and does not contain any prostatic structures. It grows rapidly with a VDT of 5 days and is characterized by chronic hypoxia, hormone insensitivity, and low metastatic potential [94].

2.1.3 Tumor induction by transplantation

Tumors were induced by transplantation of fresh tumor fragments. For each experiment, a donor animal was transplanted with a fragment from a cryo-preserved stock of the original tumor. The cryo-preserved tumor fragment was thawed in RPMI-Medium (Biochrom GmbH, Berlin, Germany) and transplanted subcutaneously on the thighs of a male Copenhagen rat. To do so, a small incision was made to the skin and a subcutaneous pocket was formed with scissors. The tumor fragment was placed in the pocket using forceps (Fine Science Tools GmbH, Heidelberg, Germany). The wound was closed by one to two suture clips (MikRon® Autoclip® 9 mm, Clay Adams, Sparks, MD, USA) which were removed after 10 days. When the donor animal's tumors reached diameters of 2 to 3 cm, the animal was euthanized, and the tumor dissected and cut into small pieces of approximately 1 mm^3 each in RPMI medium. These donor tumor fragments were then transplanted subcutaneously onto the experiment rats (male Copenhagen rats, minimum weight 180 g) as described above. This way, all experimental tumors originated from one tumor.

During the transplantation procedure, animals were kept under inhalation anesthesia with a mixture of 2 % Isoflurane (Baxter Deutschland GmbH, Unterschleißheim, Germany) and 2 l/min oxygen (Guttroff GmbH, Wertheim-Reicholzheim, Germany).

Tumor growth was frequently controlled by measuring the largest diameter and the respective orthogonal diameter with calipers.

2.2 Photoacoustic imaging (PAI)

Photoacoustic imaging (PAI) was performed to characterize the oxygenation status of the three Dunning tumor sublines H, HI, and AT1. The text in section 2.2 and the respective subsections was taken from reference [96] and has been originally written by myself.

2.2.1 Basics of PAI

PAI is an emerging non-invasive imaging technique attracting increasing attention for preclinical and clinical applications in various fields [97-99]. Without using ionizing radiation, PAI combines high contrast and specificity of optical imaging with high spatial resolution of ultrasound (US) imaging [89, 98].

PAI is based on the absorption of pulsed laser light by endogenous and exogenous chromophores. This local energy absorption leads to an increase in temperature and a rapid thermoelastic expansion of the heated tissue. The resulting pressure wave then propagates through the tissue and is detected by an US transducer at the surface of the body [89, 100]. Tissue comprises several endogenous chromophores such as hemoglobin and melanin which exhibit characteristic wavelength dependent absorption spectra. This causes contrast in PAI without the need of exogenous contrast agents [89].

PAI can be used to determine *in vivo* oxygen saturations (sO_2) in preclinical and, nowadays, clinical studies [101]. De-oxygenated and oxygenated hemoglobin can be directly distinguished by PAI based on their diverging absorption spectra. sO_2 can be calculated by using laser light of different wavelengths [102]:

$$sO_2 = \frac{[HbO_2]}{[HbO_2] + [Hb]} = \frac{PA_{\lambda_2}\varepsilon_{Hb}^{\lambda_1} - PA_{\lambda_1}\varepsilon_{Hb}^{\lambda_2}}{PA_{\lambda_1}\Delta\varepsilon_{Hb}^{\lambda_2} - PA_{\lambda_2}\Delta\varepsilon_{Hb}^{\lambda_1}} \quad (1)$$

where PA_λ is the photoacoustic (PA) signal at the wavelength λ, $\varepsilon_{Hb}^{\lambda}$ and $\varepsilon_{HbO_2}^{\lambda}$ are the molar extinction coefficients of de-oxygenated and oxygenated blood, respectively, and $\Delta\varepsilon_{Hb} = \varepsilon_{HbO_2} - \varepsilon_{Hb}$ [102].

2.2.2 Experimental set-up for PAI

Prior to PAI, the animals' skin was thoroughly depilated by hair removal creme (Nair™ Hair Remover Lotion, Church & Dwight, Ewing, NJ, USA), and animals were placed on a heatable table that allowed real-time monitoring of body temperature, respiration, and heart rate (Figure 2 A). US gel (Pharma-Depot GmbH, Versmold, Germany) was transferred to 50 mL falcon tubes (Corning®, Fisher Scientific, Pittsburgh, PA, USA) and centrifuged with at least 135 × g for 5 to 10 minutes to eliminate air bubbles before it was generously applied on the entire tumor volume surface (Figure 2 B). Measurements were performed on the commercial systems Vevo 2100 and Vevo 3100 (both Fujifilm VisualSonics Inc., Toronto, Canada) using a tunable Nd:YAG laser (Vevo LAZR, Fujifilm VisualSonics Inc.). The laser emits photons at a 20 Hz pulse rate with a peak energy of approximately 30 mJ and 10 ns length [90]. Imaging was performed with the system-specific linear-array US-transducers exhibiting a center frequency of 21 MHz (transducer LZ250 for Vevo 2100, transducer MX250 for Vevo 3100; both Fujifilm VisualSonics Inc.). For detection of de-oxygenated and oxygenated hemoglobin two excitation wavelengths (750 nm and 850 nm) were used. The PAI system was calibrated before each imaging session.

As experiments on the dependency of PAI results on signal gain and thresholding (section 2.2.4) showed that sO_2-distributions were essentially independent of these settings (section 3.1.2), all measurements were performed with an individually adjusted signal gain and a threshold of 20 %. They were optimized for each measurement using the hemoglobin signal in the "HemoMeaZure" mode of the Vevo imaging software (Fujifilm VisualSonics Inc.) to obtain a homogeneous signal distribution over the entire tumor. All PAI data were acquired in 3D "Oxy-Hemo" mode (Vevo imaging software) with a step size of 0.15 mm and low persistence if not stated differently. Tumor volumes were determined based on simultaneously acquired US B-Mode images in VevoLab software (Fujifilm VisualSonics Inc.).

During PAI, animals were kept under inhalation anesthesia with a mixture of either 2.5 % Isoflurane when measured at the Vevo 2100 or 2.5 % Sevoflurane (Abbott, Wiesbaden, Germany) when measured at the Vevo 3100 and 2 l/min oxygen.

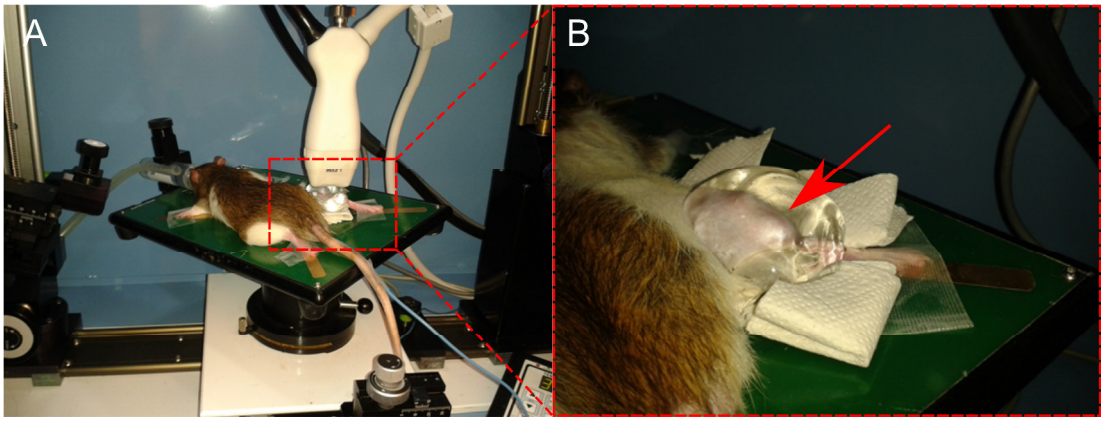

Figure 2 Set-up for photoacoustic imaging (PAI). (A) The anaesthetized rat is fixed on the heatable table. Contact to the golden electrodes allows real-time monitoring of the respiration and heart rates. Temperature is measured with a rectal probe (blue cable). The tumor is covered in ultrasound (US) gel and the transducer is set in the measurement position. (B) Close-up on the depilated tumor (arrow) on the rat's thigh which is covered by air bubble-free US gel.

2.2.3 A new pixel-based oxygen saturation (sO_2) analysis protocol

A new analysis protocol was developed that reflects the inter- and intra-tumor heterogeneity by reporting the pixel-distributions of sO_2 rather than volume-based mean values. The results of the analysis are displayed as frequency distributions. This new analysis protocol is described in detail in the results part (section 3.1.1). The following experiments were analyzed using this protocol.

2.2.4 Dependency of sO_2-distributions on signal gain and threshold

The dependency of the PAI result on signal gain and thresholding was investigated. For this, two animals were transplanted with the HI-tumor as described in section 2.1.3. At the imaging time point, one tumor was small (6 mm × 8.5 mm, HI-1) and the other one was large (14 mm × 15 mm, HI-2). Measurements were performed at the Vevo 2100 with Vevo-LAZR without persistence. The two animals were imaged with three different signal gains (36 dB, 38 dB, 40 dB). Data was analyzed for three different thresholds (0 %, 15 %, 30 %). Both parameters were selected within a range applicable for *in vivo* measurements. Reproducibility of sO_2-distributions was assessed by repeating this procedure after repositioning of animals.

2.2.5 Characterization of the hypoxic status of the H-, HI-, and AT1-tumor

For the characterization of the hypoxic status of the three Dunning sublines two animals per subline were transplanted with H-, HI-, and AT1-tumors on their right thighs as described in section 2.1.3. Tumors were imaged by PA at least three times over a period of up to 41 days. At each imaging time point animals underwent an oxygen challenge experiment during which the animals' breathing gas was altered (Figure 3). Animals were sequentially imaged when breathing 100 % oxygen (O_2), ambient air (i.e. 21 % O_2), and again 100 % O_2. After each alteration of oxygen conditions, a delay of 5 min was added allowing for adaption of the tumor to the new condition. Subsequently, an additional measurement was performed 10 min after clamping the tumor-supplying arteries with a transparent cable retainer which induced acute hypoxic conditions in the tumors while the animals were still breathing 100 % O_2. Immediately thereafter, the cable retainer was removed and the animals were imaged again. For comparison with well-oxygenated normal tissue, these measurements were also performed for the skin of two animals (in the following labelled as reference-1 and reference-2).

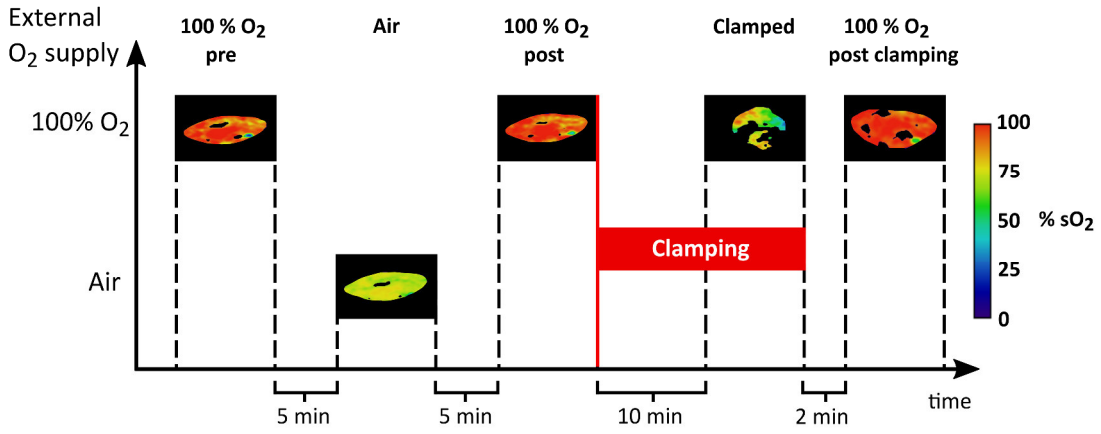

Figure 3 Schematic illustration of the oxygenation conditions during PAI. Color-coded "oxyhemo" images show the same region of interest under different experimental conditions. Figure reproduced from [92] under the CC BY 4.0 license.

2.2.6 Histology and immunohistochemistry

After final imaging of the tumors, animals were injected intravenously (*i.v.*) with pimonidazole as described in section 2.6.2.5. After one hour, Hoechst 33342 dye was injected as a perfusion marker as described in section 2.6.2.6. Tumors were dissected and cryo sections were prepared (section 2.6.1). For evaluation of tumor tissue structures, cryo sections were stained with H&E (section 2.6.2.1). Immunofluorescence double stainings were prepared to assess tumor hypoxia in correlation to the vasculature (staining for pimonidazole and CD31, section 2.6.2.5). All sections were evaluated with an Axio Scan.Z1 microscope (Carl Zeiss Microscopy GmbH, Jena, Germany).

2.3 Tumor irradiation

2.3.1 Photon irradiation

Photon irradiations were performed using a single 6 MV beam of a clinical linear accelerator (Artiste, Siemens, Erlangen, Germany) at DKFZ. For irradiation, rats were individually placed in a custom-built immobilization device [103]. Laser crosshairs were used to position the tumor in the isocenter of the accelerator. The correct position of the tumor in the beam field was verified by a light field. 15 mm polymethylmethacrylate (PMMA) boli were positioned directly in front of and behind the tumor. A field with 15 mm diameter (90 % isodose) was generated by a 12 mm tungsten round collimator covering the entire tumor. The tumor was irradiated with a horizontal beam parallel to the animal's longitudinal body axis with a dose rate of 10 Gy/min. Rats were kept under inhalation anesthesia with a mixture of 2.5 % Sevoflurane and oxygen at 2 l/min using an inhalation mask.

2.3.2 Carbon ion irradiation

^{12}C-ion irradiations were performed at the experimental work place of the Heidelberg Ion Beam Therapy Center (HIT) employing active beam scanning technique [104]. As for photon irradiation, a custom-built immobilization device was used for positioning the rats. The irradiation field was chosen slightly larger for ^{12}C-ion irradiations than for photons because no light field was available to confirm the alignment of the tumor in the beam field.

The tumor was positioned in the center of a homogeneous 20 mm SOBP with a lateral field size of 18×18 mm^2 (90 % isodose). A 39.9 mm PMMA bolus was positioned directly in front of the tumor, and a 15 mm PMMA bolus was positioned directly behind the tumor to ensure that the tumor was positioned in the center of the SOBP [103]. Hence, the first 5 mm and the last 5 mm of the SOBP were located in the proximal and distal boli, respectively. The mean dose-averaged LET in the tumor was 75 keV/µm (range 64 - 96 keV/µm). The tumor was irradiated with a horizontal beam parallel to the animal's longitudinal body axis from the rear direction. Rats were kept under inhalation anesthesia with a mixture of 2.5 % Sevoflurane and oxygen at 2 l/min using an inhalation mask.

2.4 Dynamic contrast-enhanced magnetic resonance imaging (DCE-MRI)

2.4.1 MRI basics

Magnetic resonance imaging (MRI) is a powerful imaging modality in the clinical as well as preclinical setting because of its excellent soft tissue contrast. In contrast to other imaging modalities such as computed tomography (CT) and PET, MRI only involves strong magnetic fields rather than ionizing radiation. The image contrast rises from nuclear relaxation times that differ among morphological structures [105].

In most cases, the MR signal rises from the nucleus of hydrogen atoms (protons) which have a high abundance in the body. Protons possess a nuclear spin which is associated with a magnetic moment. By applying a strong static magnetic field B_0 the spins will precess with a characteristic Lamor frequency and will align either parallel or antiparallel to the respective field in an energetic equilibrium with a small net magnetization parallel to B_0. After applying an oscillating magnetic field B_1 perpendicular to B_0 (also called radio frequency pulse) that rotates the net magnetization into the transversal plane, an alternating current is induced in a close-by receiver-coil, which is the measurable MR signal. The frequency of the B_1-field has to match the Lamor frequency of the spins. When this radio frequency pulse is switched off, the spins leave the transversal plane and start to restore their original equilibrium state. The time required for that is the longitudinal relaxation time $T1$. During this restoration the spins also start to dephase in the transversal plane. The corresponding transversal relaxation time, $T2$, describes the signal decay caused by this dephasing of the spins. Local field inhomogeneities lead to a faster dephasing with the relaxation time $T2^*$. Each nucleus type, e.g. hydrogen, has specific $T1$ and $T2$ times. However, due to small magnetic disturbances in the hydrogen atoms' environment, e.g. by the presence of other molecules in the proximate vicinity, the relaxation behavior of the hydrogen atoms slightly changes.This results in tissue specific $T1$ and $T2$ times that create image contrast. Hence, in a $T1$-weighted image, a tissue structure with a short $T1$-time appears brighter than a tissue structure with a long $T1$-time.

2.4.2 DCE-MRI basics

Dynamic contrast-enhanced MRI (DCE-MRI) involves the administration of a contrast agent (CA) during MR imaging and is often employed to study the perfusion and permeability of tumors in clinical and preclinical studies [84, 106, 107]. Gadolinium-based paramagnetic contrast agents cause a faster $T1$ relaxation and, therefore, an enhanced $T1$ signal; i.e. CA accumulating structures "lighten" up in $T1$-weighted images. Tumors are likely to accumulate a large amount of CA due to their immature and leaky vessels which makes them visible in contrast-enhanced images.

For DCE-MRI, the CA is administered as a bolus and its time course in the tissue of interest is recorded by time-resolved imaging. Pharmacokinetic modeling enables the derivation of hemodynamic parameters from the CA kinetics in the tissue of interest.

2.4.3 Pharmacokinetic modeling basics

Pharmacokinetic modeling aims at the derivation and quantification of physiological parameters from DCE-MRI concentration-time curves. The analysis comprises two major steps: first, changes in MR signal are converted to CA concentrations; second, physiological parameters are derived from concentration-time curves by tracer-kinetic theory [108].

2.4.3.1 MR signal-to-concentration conversion

Models used for pharmacokinetic modeling embrace changes in CA concentration rather than changes in MR signal which requires a transformation of signal intensity curves into concentration curves. In the context of DCE-MRI, $T2^*$-effects are neglected and the relationship between the relaxation rate $R_1(t) = \frac{1}{T_{1(t)}}$ and the CA concentration $C(t)$ can be assumed to be linear in the range of 0 - 5 mM [109] with

$$R_1(t) = R_{1,0} + r_1 \cdot C(t)\,, \tag{2}$$

where r_1 is the relaxivity of the CA and $R_{1,0}$ is the initial relaxation rate of the tissue without CA. Hence, CA concentration can be expressed as

$$C(t) = \frac{1}{r_1}\big(R_1(t) - R_{1,0}\big)\,. \tag{3}$$

The time varying signal intensity $S(t)$ depends on the chosen DCE-MRI sequence and can generally be expressed as

$$S(t) = a \cdot m_z\big(R_1(t)\big)\,, \tag{4}$$

with a being a time-independent constant that combines a number of sequence specific parameters such as a global calibration constant, the equilibrium magnetization, the position dependent coil sensitivity, the flip angle, and $T2^*$-weighting [108]. Due to variations in coil sensitivity, B_1-fields or proton density, these constants may depend on the voxels' position [108]. The longitudinal magnetization m_z is a function of $R_1(t)$ and further MR sequence parameters [108]. Assuming linearity between m_z and $R(t)$ and using equation (3) gives an approximation for the absolute signal enhancement $SE_{\text{abs}}(t)$

$$C(t) = SE_{\text{abs}}(t) = \kappa \cdot \big(S(t) - S(0)\big)\,, \tag{5}$$

where $\kappa = \frac{R_{1,0}}{r_1}$ is a proportionality constant that depends on the flip angle and the coil sensitivity.

2.4.3.2 Tracer kinetics

Indicator dilution theory describes how an indicator, i.e. a detectable substance that is introduced into a physiological system, behaves when added to a system consisting of numerous inlets and outlets [110]. Tracer kinetic modeling is based on the assumption of linear and stationary tissues. Linearity means that the tissue response towards a tracer injection at any given time point is proportional to the injected dose, and stationary means that this response is independent of the time of injection [108, 110].

MR tracers remain extracellular and, therefore, the concentration $C(t)$ always refers to plasma concentration $C_{\mathrm{P}}(t)$. However, only whole blood CA concentration levels $C_{\mathrm{B}}(t)$ can be measured. Hence, the blood CA concentration level $C_{\mathrm{B}}(t)$ must be corrected for the hematocrit Hct to obtain the plasma concentration level $C_{\mathrm{P}}(t)$

$$C_{\mathrm{P}}(t) = \frac{C_{\mathrm{B}}(t)}{1 - \mathrm{Hct}}. \tag{6}$$

Pharmacokinetic modeling uses mathematical models of the tissue architecture which constitute the link between the measured data and the physiological parameters. They are fitted to the measured concentration-time curve of the tissue of interest $C_{\mathrm{T}}(t)$ which can be described by the convolution

$$C_{\mathrm{T}}(t) = I(t) \otimes C_{\mathrm{AIF}}(t)\,. \tag{7}$$

Here, $I(t)$ is the impulse response function that describes the kinetics of the CA in the tissue and $C_{\mathrm{AIF}}(t)$ is the measured arterial input function (AIF) that describes the initial CA inflow [108]. The AIF is ideally recorded directly at the supplying artery of the tissue of interest.

One way to derive the physiological parameters from the concentration-time curves is the model-based deconvolution approach. During the fitting process, the model-parameters are adapted in a way that the convolution of the AIF and the impulse response function $I(t)$ give the best possible fit to the measured concentration-time curve $C_{\mathrm{T}}(t)$. The model parameters correspond to the physiological parameters. There are multiple compartment models available for this approach which differ e.g. in the number of compartments and exchange constants. A compartment is a homogeneous and well-mixed macroscopic physiological volume that does not necessarily coincide with a single spatially-connected volume.

The compartment models considered in this work are the two compartment exchange model (2CXM) [111] and the extended Tofts model (ETM) [112]. The 2CXM assumes two compartments, the plasma compartment and the extracellular, extravascular space (EES) (Figure 4 A). The plasma compartment contains the CA concentration $C_{\mathrm{p}}(t)$, is described by the plasma volume fraction v_{p}, and is perfused with the plasma flow F_{p}. The permeability-surface-area product PS describes the exchange rate through the capillary walls into the EES, which has the volume fraction v_{e} and the CA concentration $C_{\mathrm{e}}(t)$. The total tissue concentra-

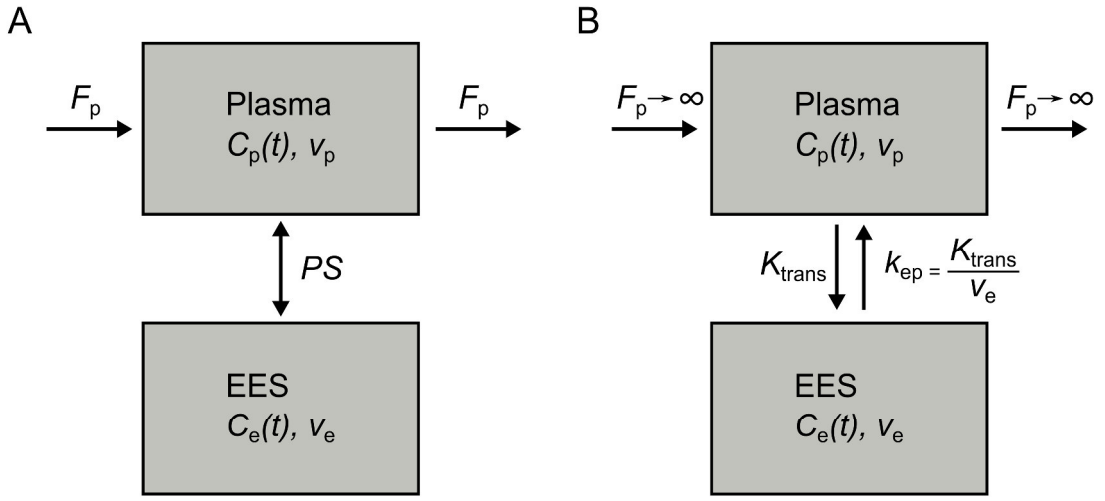

Figure 4 Schema of the two compartment exchange model (2CXM) and the extended Tofts model (ETM). (A) In the 2CXM the exchange rate between the two compartments plasma (i.e. plasma volume fraction v_p with the contrast agent concentration $C_p(t)$), and extracellular, extravascular space (EES, i.e. v_e with the contrast agent concentration $C_e(t)$) is described by the permeability-surface-area product PS. The plasma compartment has a flow F_p. (B) In the ETM the exchange between the two compartments v_p and v_e is described by the volume transfer constant K_{trans} and the efflux rate constant k_{ep}.

tion $C_T(t)$ can be written as [113]

$$C_T(t) = F_p((1-\varepsilon)e^{-tK_1} + \varepsilon \cdot e^{-tK_2}) \otimes C_{AIF}(t), \tag{8}$$

with

$$K_{1,2} = \frac{1}{2}\left(\frac{1}{T_p} + \frac{1}{T_e} \pm \sqrt{\left(\frac{1}{T_p} + \frac{1}{T_e}\right)^2 - 4\frac{1}{T_p}\frac{1}{T_e}}\right) \quad \text{and} \quad \varepsilon = \frac{K_1 - T_B^{-1}}{K_1 - K_2}. \tag{9}$$

Here, T_p and T_e are the plasma and interstitial mean transit times, respectively, and T_B is the mean transit time of an intravascular tracer in blood [113] which are defined by the following relations:

$$T_p = \frac{v_p}{PS + F_p}, \qquad T_e = \frac{v_e}{PS}, \qquad T_B = \frac{v_p}{F_p}. \tag{10}$$

The ETM can be approximated from the 2CXM for the highly perfused regime (i.e. $F_p \to \infty$) or the weakly vascularized regime (i.e. $v_p \to 0$) [114, 115] by substituting the plasma residue function by a delta distribution, yielding the total tissue concentration

$$C_T(t) = \left(v_p \cdot \delta(t) + K_{trans} \cdot e^{-t\frac{K_{trans}}{v_e}}\right) \otimes C_{AIF}(t). \tag{11}$$

In the ETM the volume transfer constant K_{trans} has a mixed flow-permeability weighting (Figure 4 B)

$$K_{\text{trans}} = \frac{F_{\text{p}} \cdot PS}{F_{\text{p}} + PS}, \tag{12}$$

which does not allow for a unique discrimination between permeability and flow [114]. When performing pharmacokinetic modeling, the selection of the model is a crucial step to ensure meaningful results. First, *a priori* knowledge about the physiology of the investigated tissue should be used to limit the number of considered models. Second, goodness of fit and the number of free parameters need to be examined. As a general rule, the best model is the simplest model (i.e. least parameters) that fits the data well [116].

2.4.4 Delay correction by bolus arrival time (BAT) estimation

The text in sections 2.4.4, 2.4.4.1, and 2.4.4.2 was taken from reference [117] and has been originally written by myself.

Accuracy of pharmacokinetic fit results can be impaired due to a delay between the arrival of CA bolus in the artery, from where the AIF is extracted, and the arrival of CA in the tissue of interest [118-120]. Ideally, the AIF is extracted directly form a tumor supplying artery. However, due to limited image resolution and partial volume effects, it is not always possible to choose an artery in the direct vicinity of the tumor. Hence, the AIF is often extracted from a larger artery further upstream or, in the case of small animal imaging, even from the left ventricle. This results in a delayed CA arrival in the tissue of interest compared to the AIF. There are two standard approaches to determine this delay time: the first approach includes the delay as an additional free parameter in the fitting process of the pharmacokinetic model [121, 122]. The second type estimates the bolus arrival times (BATs) separately for the tissue concentration curve (TCC) and for the AIF; that is, the time points where the concentration curves start to rise. The time delay is the difference between the BAT of the TCC and that of the AIF. The advantage of the second type is that it does not require to including the time delay as an additional fit parameter which is likely to decrease fit stability. A study by Kershaw and Buckley showed that the second approach gives more accurate results than the first one [122].

Cheong *et al.* introduced a method for discrete BAT estimation based on fitting a linear or convex quadratic function to the sample points in the neighborhood of the BAT which gives excellent results for TCCs with fast upslopes (i.e. the peak of the signal is close to the BAT) as often observed in patient data [123]. An extension of this method was proposed by Singh *et al.* giving comparable results [124]. However, applying the method of Cheong *et al.* to TCCs that do not exhibit this characteristic upslope, e.g. TCCs of small animals or weakly perfused tissues, may lead to poor results.

A method for continuous BAT estimation of DCE-MRI that do not have a fast upslope – as often observed in small animal data and patient data of tissues without a significant intravascular fraction – was developed. The method is based on approximation of TCCs by splines, which allow to adapt to a large variety of curve shapes after the BAT. This project was realized in cooperation with Dr. Martin Storath of the group for Image Analysis and Learning of the Interdisciplinary Center for Scientific Computing of Heidelberg University.

In the following, the general concept of smoothing splines, which were used for the new BAT estimation method, as well as the generation of the test data sets and the reference method that has been used up to now, are described. Details of the new method itself are presented in the results part (section 3.2).

2.4.4.1 Smoothing splines

Smoothing splines are a classical signal estimation method which have been applied to various biomedical problems [125, 126]. A smoothing spline approximates data by a function that is the optimal tradeoff between smoothness, measured in terms of the integral over its squared k^{th} derivative, and fidelity to the data, as represented by the residual sum of squares.

A smoothing spline of order $k \in \mathbb{N}$ is the solution of the following optimization problem: Find a sufficiently smooth function u on $[t_1, t_N]$ that minimizes the cost function:

$$\sum_{n=1}^{N} (u(t_n) - c_n)^2 + \alpha \int_{t_1}^{t_N} \left(u^{(k)}(\tau)\right)^2 d\tau, \tag{13}$$

where c_n are the measured data points and $u^{(k)}$ denotes the k^{th} derivative of the function u. The parameter $\alpha > 0$ adjusts the relative weight of the data fidelity and smoothness: the larger the value of α, the smoother the resulting spline. To understand the role of the order k, it is instructive to look at the solutions for very large α: For $\alpha \to \infty$, the solution of eq. (13) yields an ordinary polynominal of degree $k-1$ on $[t_1, t_N]$. This is because the smoothness cost (the second term in eq. (13)) is equal to zero exactly for polynominals of maximum degree $k-1$. Thus, for $\alpha \to \infty$, the minimizer of eq. (13) coincides with the least squares approximation by a polynomial of degree $k-1$. Technical details on smoothing splines can be found in [127-130].

2.4.4.2 Data simulation

For validation of the new method for BAT estimation, the proposed method was applied to simulated TCCs and the respective AIFs with known true BAT and to *in vivo* acquired rat data. TCCs were simulated employing the impulse response functions for the ETM (eq. (11)) and the 2CXM (eq. (8)) [111] using the software package "ModelFit" within the "Medical Imaging Interaction Toolkit (MITK)" [131, 132]. Rat TCCs were generated using the model-based AIF proposed by McGrath *et al.* (model B) [133]. Three physiologically realistic TCC

types were simulated for both pharmacokinetic models by varying the input parameters (ETM: K_{trans} = 15 ml/min/100 ml, v_p = 0.05, and v_e = 0.3, 0.6, or 0.1, respectively; 2CXM: F_p = 25 ml/min/100 ml, PS = 10 ml/min/100 ml, v_p = 0.05, and v_e = 0.05, 0.15, or 0.3, respectively).

To show the flexibility of the proposed method, patient data was additionally simulated, using the population-average based AIF proposed by Parker *et al.* [134]. Here, two TCC types were investigated (ETM: K_{trans} = 10 ml/min/100 ml, v_p = 0.1, and v_e = 0.05 or 0.3, respectively; 2CXM: F_p = 25 ml/min/100 ml, PS = 5 ml/min/100 ml, v_p = 0.1, and v_e = 0.15 or 0.05, respectively).

High-resolution TCCs were simulated for an acquisition time of 360 s with a temporal resolution of 0.25 s and BAT at 34.75 s (Figure 5). The true BAT was defined as the last point on the concentration curve's baseline. To evaluate the robustness of the proposed method, simulated TCCs were altered for four temporal resolutions (Δt = 1 s, 2 s, 3 s, 7 s) and three noise levels defined by their signal-to-noise ratio (SNR) (SNR = 50, 25, 10). SNR was defined as the ratio between the maximum of the concentration curve to the standard deviation of the Gaussian noise added to the concentration curve. Different temporal resolutions were realized by respectively down-sampling the original data. 1000 noise realizations per configuration were generated.

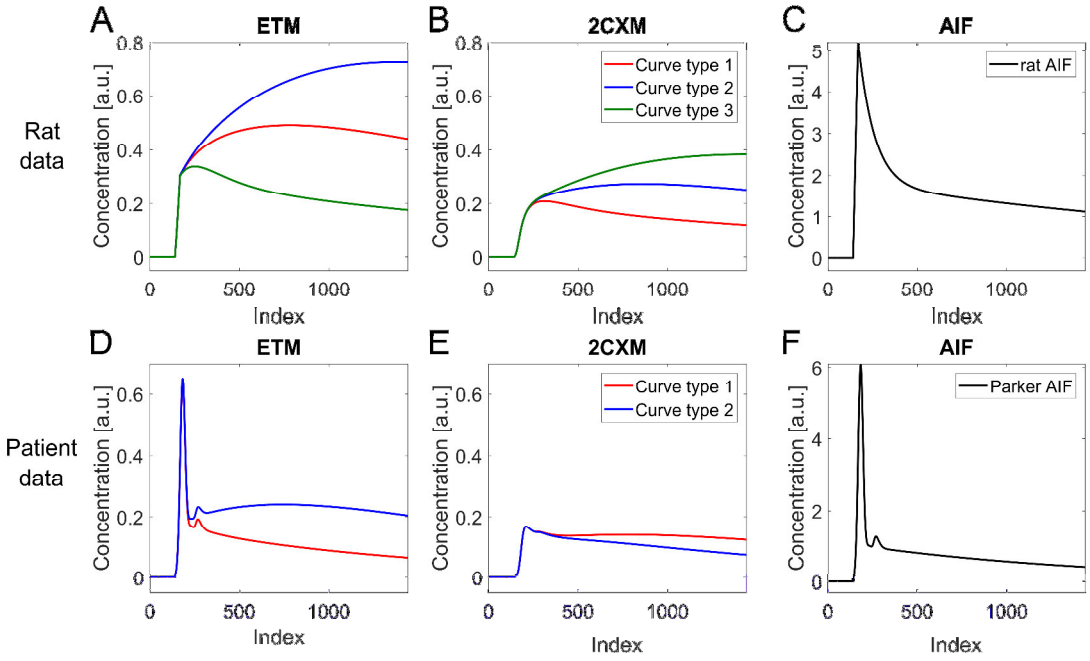

Figure 5 Simulated concentration curves for bolus arrival time (BAT) estimation: (A, B) Rat TCCs simulated with the extended Tofts model (ETM) and the two compartment exchange model (2CXM). (C) Model-based rat AIF as proposed by McGrath *et al.* [133]. (D, E) Patient TCCs simulated with ETM and 2CXM. (F) Population-average based Parker AIF [134].

2.4.4.3 BAT estimation on simulated data

Using the developed estimation method, BATs were estimated for the 1000 generated noise realizations for each configuration (four temporal resolutions with three noise levels each). The results were compared with those of the reference method published by Cheong *et al.* [123].

Cheong's method

To the author's knowledge, Cheong's method [123] is the current gold standard for BAT estimation of DCE-MRI data. The method is based on a parametric approximation model for the concentration curve between the first time frame t_1 and the peak time denoted by t_p. The model functions u are assumed to be constant before the BAT and quadratic polynomial between the BAT and the peak time:

$$u(t_n) = \begin{cases} \beta_0, & \text{if } t_1 \leq t_n \leq t_\mathrm{BAT} \\ \beta_0 + \beta_1 \cdot (t_n - t_\mathrm{BAT}) + \beta_2 \cdot (t_n - t_\mathrm{BAT})^2, & \text{if } t_\mathrm{BAT} < t_n \leq t_\mathrm{p.} \end{cases} \quad (14)$$

Here, $n \in \{1, \dots, p-2\}$ and $\beta_0, \beta_1, \beta_2$ are the model parameters. Additionally, a linear variant is proposed which is obtained by setting β_2 equal to zero. It was found that in average imposing this restriction did not lead to improved estimates, thus the focus was set on the quadratic method. The method proceeds as follows. For each BAT candidate $t_\mathrm{BAT} \in \{t_1, \dots, t_\mathrm{p}\}$, the optimal model parameters are computed by a least squares fit using non-negativity constraints. The candidate that provides the least residual sum of squares is considered as the best estimate for the BAT. It should be noted that with this method the estimated BAT is necessarily one of the discrete sampled time points.

Adapted version of Cheong's method

Additionally, results were compared to an adapted version of Cheong's method which only considers sample points after the CA injection time for BAT estimation (Cheong *et al. adapted*) [117]. Because the experimental set-up of the DCE-MRI experiments in the following studies did not allow for an exact recording of the injection time, a plausible common lower boundary was set at the sample point at 25.37 s as it can be assumed that no CA was injected before 25 s [117].

2.4.5 Experimental set-up for DCE-MRI

In the following, the general DCE-MR imaging protocol is described. The text in section 2.5.1 was taken from reference [135] and has been originally written by myself.

Imaging was performed at a clinical 1.5 T MRI (Symphony, Siemens) using an in-house built small animal coil. $T2$-weighted transversal images (turbo spin echo sequence with repetition time (TR) 3240 ms, echo time (TE) 81 ms, slice thickness 1.5 mm, pixel size

0.35×0.35 mm^2) were recorded and used to position two imaging slices for DCE-MRI (TURBO-FLASH, TR 373 ms, TE 1.67 ms, slice thickness 4.5 mm, pixel size 0.99×0.99 mm^2, matrix size: 144×192). One of the transversal slices was positioned through the heart, the other one was positioned through the largest diameter of the tumors. 20 - 30 s after starting the DCE-MRI sequence, 0.1 mmol/kg Gd-DTPA (Magnevist®, Bayer Healthcare Pharmaceuticals, Berlin, Germany) CA was manually injected into the tail vein. Images were acquired with a temporal resolution of 0.75 s for a total acquisition time of 380 s. In addition, $T1$-weighted reference images of the entire tumors were recorded with a spin-echo sequence (TR 600 ms, TE 14 ms, pixel size 0.31 mm × 0.31 mm, slice thickness 1.5 mm) after (and for the HI-tumors additionally before) the DCE-MRI measurement. $T2$-weigthed images were also used to determine the tumor volumes.

2.4.6 Signal-to-concentration conversion of DCE-MRI data

All handling of experimental DCE-MRI data was performed in MITK. All experimental DCE-MRI data were analyzed voxel-based. Signal intensities were transformed into concentration curves by means of absolute signal enhancement (eq. (5)) with $\kappa = 1$. CA blood concentrations were corrected by the hematocrit level (eq. (6)) using a literature value of 0.45 to obtain CA plasma concentrations [111].

2.4.7 Pharmacokinetic modeling of DCE-MRI data

DCE-MRI concentration-time curves were fitted by the ETM [115], using the tool "ModelFit" [132] within the MITK framework. An image-based AIF was derived from the DCE-MRI heart slice individually for each animal at each imaging session. The AIF was manually chosen as the voxel with the steepest rise, highest signal amplitude, and least noise in the left ventricle of the animals' hearts. Tumor regions of interest (ROIs) were delineated on $T2$-weighted MR-images and transferred to the DCE-MRI images.

Prior to pharmacokinetic analysis, a delay correction was applied to the concentration-time curves. For this, BATs were estimated for both, AIF and the respective tumor concentration-time curves, as described in section 3.2 [117]. AIFs were then shifted according to the delay between the BAT of the AIF and the median of BATs of the concentration-time curves of each tumor voxel fulfilling the plausibility condition $\mathrm{BAT_{AIF}} < \mathrm{BAT_{tumor}}$ per animal.

Start parameters for the fitting procedure were set to K_{trans} = 15 ml/min/100 ml, $v_{\mathrm{e}} = 0.5$, and $v_{\mathrm{p}} = 0.05$. Constraints were applied on v_{e} and v_{p} such that $0 < v_{\mathrm{e}}, v_{\mathrm{p}} < 1$ and $v_{\mathrm{e}} + v_{\mathrm{p}} < 1$ to exclude unphysiological results and to prevent overfitting. Fitting parameters K_{trans}, v_{e}, and v_{p} were determined voxel-wise for each tumor. Results of all voxels were pooled per treatment group and per imaging time point.

2.5 Longitudinal DCE-MRI studies after irradiation

Longitudinal DCE-MRI studies were performed after irradiation to gain initial quantitative information on the impact of high dose ^{12}C-ion irradiation compared to photons on tumor vasculature and perfusion. The acute hypoxic and moderately differentiated HI-tumor and the chronically hypoxic and anaplastic AT1-tumor were chosen for these experiments.

2.5.1 DCE-MRI study of the AT1-tumor

The text in section 2.5.1 was taken from reference [135] and has been originally written by myself.

2.5.1.1 Experimental set-up and treatment groups for the AT1-tumor

AT1-tumors were subcutaneously transplanted on both thighs of 12 male Copenhagen rats as described in section 2.1.3. Animals were included in the experiment when their tumors reached a size of 9 mm × 9 mm (tumor volume 256 ± 120 mm^3). DCE-MRI was performed as described in section 2.4.5 one day prior to and 3, 7, 14, and 21 days after irradiation (Figure 6). Right AT1-tumors were irradiated in four groups as described in sections 2.3.1 and 2.3.2, respectively: Curative single doses of either 37 Gy ^{12}C-ions or 85 Gy photons (isoeffective RBE-weighted doses [24]) were delivered leading to local tumor control. In addition, an iso-absorbed dose of 37 Gy photons and the corresponding isoeffective RBE-weighted dose of 16 Gy ^{12}C-ions (both are sub-curative doses [24]) were selected. The RBE required for the calculation of the isoeffective doses was taken from an earlier conducted dose-response experiment [103]. Left tumors served as non-irradiated controls. Each treatment group consisted of three animals resulting in 12 irradiated and 12 control tumors in total. The longitudinal DCE-MRI measurements and corresponding irradiations, as well as animal keeping and observation were planned and performed by Dr. Christin Glowa.

2.5.1.2 Non-compartment analysis and pharmacokinetic modeling

DCE-MRI data were converted to concentration curves as described in section 2.4.6. Area under the curve (AUC) values were determined over the entire concentration-time curve for each voxel per tumor. AUC values per tumor and time point were normalized to the maximum AUC value of the respective animal's main abdominal artery of the same measurement to eliminate CA administration related effects. In addition, voxel-based pharmacokinetic modeling with the ETM was performed on DCE-MRI data of the AT1-tumor as described in section 2.4.7.

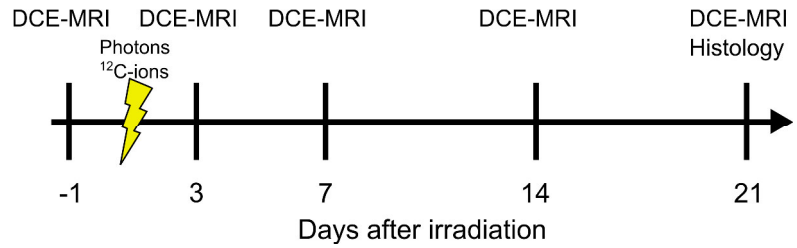

Figure 6 Schematic illustration of the longitudinal DCE-MRI studies. DCE-MRI was performed one day prior to and 3, 7, 14, and 21 days after irradiation. Tumors were irradiated with curative doses of either photons or ^{12}C-ions (yellow flash). After the last imaging time point, tumors were dissected and prepared for histology.

2.5.1.3 Histology and immunohistochemistry 21 days after irradiation

At the last imaging time point, tumors were dissected and cyro-preserved slides were prepared as described in section 2.6.1. Histological and immunhistological stainings were performed to assess tumor morphology (H&E), vasculature and pericyte coverage as a maturity marker (CD31/SMA/DAPI), and proliferation (BrdU/DAPI) (Table 1). Additionally, one animal per dose group was injected with the hypoxia marker pimonidazole consequently stained for pimonidazole/CD31/DAPI (Table 1). Vascular density and vascular maturity, hypoxic fraction, and proliferative activity were quantified by the protocols listed in Table 1.

Table 1 Histology and immunohistochemistry stainings which were performed on the AT1-tumors of the longitudinal DCE-MRI study after irradiation with photons or ^{12}C-ions and references to the respective staining and quantification protocols.

Staining	Staining protocol	Quantification protocol
H&E	2.6.2.1	-
CD31/SMA/DAPI	2.6.2.4 (CD31/SMA)	2.6.4.1 (Vascular density)
CD31/pimonidazole/DAPI	2.6.2.5 (CD31/pimonidazole)	2.6.4.2 (Hypoxic fraction)
BrdU/DAPI	2.6.2.7 (BrdU)	2.6.4.4 (Proliferation)

2.5.2 DCE-MRI study of the HI-tumor

The text in section 2.5.2 was taken from reference [136] and has been originally written by myself.

2.5.2.1 Experimental set-up and treatment groups for the HI-tumor

HI-tumors were subcutaneously transplanted on both thighs of 16 male Copenhagen rats as described in section 2.1.3. Tumors were irradiated when their tumors reached a size of 10 mm × 10 mm (tumor volume 443 ± 378 mm^3). DCE-MRI was performed as described in section 2.4.5 one day prior to and 3, 7, 14, and 21 days after irradiation (Figure 6). Animals were randomly assigned to one of the four single dose treatment groups: 18 Gy ^{12}C-ions

(n = 4) or 37 Gy photons (n = 4) (sub-curative isoeffective doses), the respective isodose 37 Gy ^{12}C-ions (n = 5), or the corresponding isoeffective dose of 75 Gy photons (n = 3) as described in sections 2.3.1 and 2.3.2, respectively. The latter two doses are curative and lead to local tumor control [24]. While the HI-tumors on the right distal thighs were irradiated, the HI-tumors on the left thighs served as controls. The longitudinal DCE-MRI measurements and corresponding irradiations, as well as animal keeping and observation were planned and performed by Dr. Christin Glowa.

2.5.2.2 Pharmacokinetic modeling

DCE-MRI data were converted to concentration curves as described in section 2.4.6. Voxel-based pharmacokinetic modeling with the ETM was performed on DCE-MRI data of the HI-tumor as described in section 2.4.7. As pharmacokinetic modeling revealed a large spread of the resulting model parameters, which can most likely be attributed to the intrinsic biological heterogeneity of this tumor, additional analysis was performed (see section 2.5.2.3).

2.5.2.3 Principle component analysis of DCE-MRI data

Voxel-based concentration-time curves of DCE-MRI data were clustered based on results from a principle component analysis (PCA) as described by Featherstone *et al.* [137]. All analyses were performed in Matlab 2017b (Mathworks, Natick, MA, USA) and used Matlab functions are referenced in italics (e.g. *function.m*).

Concentration-time curves were extracted from all evaluable pixels of all tumor ROIs, aligned at their BAT, and stored in a single matrix for PCA (*pca.m*). The first two principle components (PCs) represent the main shape of the concentration-time curves (Figure 7) and account for 95.1 % (1st PC) and 3.6 % (2nd PC) of the data's variance. The PCA coefficients (loadings) of the first two PCs per concentration-time curve were used to separate the DCE-MRI data into five cluster by Gaussian mixture modeling (GMM) using *fitgmdist.m* with a diagonal and unshared covariance matrix. The number of cluster was chosen based on quali-

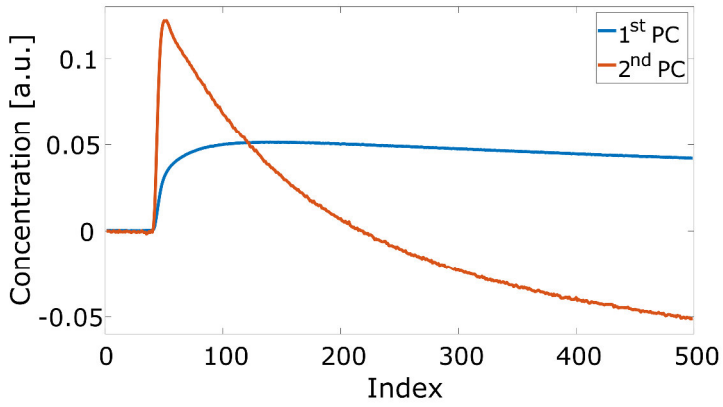

Figure 7 First two principle components (PCs) of the DCE-MRI concentration-time curves of the HI-tumors which account for 95.1 % (1st PC) and 3.6 % (2nd PC) of the data's variance. Figure reproduced from [136].

tative assessment of the concentration levels and shapes of the resulting average concentration-time curves per cluster after GMM. The criteria for finding a reasonable number of cluster were defined as distinguishable levels and curve shapes between mean cluster concentration-time curves. Satisfactory results were found for five cluster. When choosing more or less than five cluster, the clustering of concentration-time curves was dominated by concentration level only rather than curve shape. The fit parameters K_{trans}, v_{e}, and v_{p} of all tumor voxels of all animals of all treatment groups were pooled per cluster. For each tumor and subsequently for each group, the fraction of each cluster type was determined per imaging time point.

2.5.2.4 Histology and immunohistochemistry 21 days after irradiation

Animals were sacrificed after final imaging. Tumors were dissected and prepared as described in section 2.6.1. Cryo-preserved slides were stained with H&E (see section 2.6.2.1) and immunohistological stainings were performed for CD31/SMA/DAPI (see section 2.6.2.4) to assess tumor vasculature and pericyte coverage as a maturity marker, and for Ki67 (see section 2.6.2.8) to assess proliferative activity.

2.6 Histology and immunohistochemistry

2.6.1 Tumor dissection and preparation of cryo sections

At the designated end point, animals were either sacrificed by CO_2 inhalation or by heart puncture and subsequent cardiac relief cut when Hoechst 33342 dye was administered (see section 2.6.2.6). Tumors were dissected and, if large enough, cut along their largest diameter into two parts, frozen in isopentane (Carl Roth GmbH, Karlsruhe, Germany), and stored at -80°C.

For the preparation of cryo sections, tumors were embedded in TissueTek® (Sakura, Alphen aan den Rijn, Netherlands) and attached to a specimen stage which was mounted onto a cryostat (Leica CM3050 S, Leica Biosystems, Wetzlar, Germany). Tumors were trimmed with a slice thickness of 30 - 50 µm until the slice contained a complete cross section. Sequential cryo sections were acquired with a thickness of 7 µm, mounted onto adhesion slides (HistoBond®, Paul Marienfeld GmbH, Lauda-Königshofen, Germany) and fixed in methanol/aceton (1 min methanol, 2 min aceton) at -20°C. Slides were dried and stored at -20°C.

2.6.2 Staining protocols

2.6.2.1 Hematoxylin & Eosin

To assess morphological structures, Hematoxylin & Eosin (H&E) staining was performed. Cryo slides were thawed and dried at room temperature (room temp) for 30 min. They were

washed in aqua dest. for 5 min und subsequently stained in hematoxylin solution acid according to Mayer (Carl Roth GmbH) for 5 min. After a short washing step in aqua dest., the slides were blued in lukewarm running water for 10 min followed by staining in eosin Y-solution (0.5 % in water, Carl Roth GmbH) for 5 min. Slides were washed in aqua dest. again before passing through an ethanol chain for dehydration (2 × 2 min 70 % ethanol, 2 × 2 min 96 % ethanol, 2 × 4 min 100 % ethanol, 2 × 5 min Roticlear® (Carl Roth GmbH)). Slides were mounted in Eukitt® (O. Kindler GmbH, Freiburg, Germany) and covered by cover slips (Menzel-Gläser, Menzel GmbH + Co KG, Braunschweig, Germany). Slides were dried over night.

Hematoxylin stains acidic structures such as the DNA in the cell nuclei blue, while eosin stains alkaline structures such as connective tissue, collagen, cell plasma, muscle, and skin pink. Erythrocytes appear red-orange.

2.6.2.2 Standard immunohistochemistry protocol

The standard protocol for immunohistochemistry is displayed in (Table 2). Negative controls were run with each staining. One negative control was only incubated with the primary antibody to assess its background fluorescence. Another negative control was only incubated with the secondary antibody to assess its antigen binding specificity. The respective missing step was replaced by the vehicle solution (phosphate-buffered saline (PBS, PBS Dulbecco w/o Ca^{2+}, w/o Mg^{2+}, Biochrom GmbH) or bovine serum albumin (BSA, Sigma-Aldrich, Taufkirchen, Germany) in PBS (BSA/PBS)). If sections were not investigated for perfusion, cell nuclei were counterstained by 4′,6-diamidino-2-phenylindole (DAPI, Sysmex Partec GmbH, Münster, Germany).

2.6.2.3 Antigen retrieval

For those immunohistochemistry stainings that required antigen retrieval the following steps were added in between step 1 and step 2 of the standard protocol (Table 2). Plastic cuvettes were filled with sodium citrate buffer and heated to 95°C in a water bath. For the sodium citrate buffer 10 mM sodium citrate (Sigma-Aldrich) were dissolved in 900 ml aqua dest., the pH was adjusted to 6.0 with 1N HCl (Carl Roth GmbH), and the buffer was replenished to 1 l. 0.5 ml Tween 20 (Sigma-Aldrich) was added and stirred until fully dissolved.

After washing for 5 min in PBS, slides were incubated in the 95°C hot sodium citrate buffer for 30 min and subsequently allowed to cool down to 37°C under a fume hood. Afterwards the standard protocol was continued with step 2 (Table 2).

Table 2 Standard protocol for immunohistochemistry. *If tumors contained Hoechst 33342, these steps were performed in the dark.

Nr.	Process	Product	Time	Temperature
1	Drying	Air	≥ 30 min	room temp*
2	Washing	PBS	5 min	room temp*
3	Blocking	Image-iT FX signal enhancer†	30 min	room temp*
4	Washing	PBS	3 × 5 min	room temp*
5	Blocking	DAKO protein block	30 min	room temp*
6	1st primary antibody	In 3 % or 10 % BSA/PBS	over night	4°C*
7	Washing	PBS	3 × 5 min	room temp*
8	2nd primary antibody	In 3 % or 10 % BSA/PBS	2 h	room temp*
9	Washing	PBS	3 × 5 min	room temp*
10	1st secondary antibody	Fluorescence-coupled antibody in PBS or 3 % BSA/PBS	1 h	room temp, dark
11	Washing	PBS	3 × 5 min	room temp, dark
12	2nd secondary antibody	Fluorescence-coupled antibody in PBS or 3 % BSA/PBS	1 h	room temp, dark
13	Washing	PBS	3 × 5 min	room temp, dark
14	Counterstaining	DAPI (100 ng/ml)	5 min	room temp, dark
15	Washing	Aqua dest.	5 min	room temp, dark
16	Mounting	Fluoromount-G®**	few hours	room temp, dark

† Invitrogen, Eugene, OR, USA

** SouthernBiotech, Birmingham, AL, USA

2.6.2.4 Vascular structures and pericyte coverage

Vascular structures were identified by staining for the endothelial surface marker CD31. Pericyte coverage of these structures was appraised as a marker for vessel maturity and was assessed by staining for smooth muscle actin (SMA). A rabbit anti-SMA antibody (Abcam, Cambridge, UK) was used as the first primary antibody in a concentration of 1:800 (step 6 of the standard protocol in Table 2). After overnight incubation, goat anti-CD31 (R&D systems

Inc., Minneapolis, MN, USA) was incubated for 2 h (1:2000) as the second primary antibody (step 8). Binding of the rabbit anti-SMA and goat anti-CD31 antibodies was visualized by incubating with the AlexaFluor 488-coupled secondary antibody donkey anti-rabbit (1:1500, Invitrogen, Eugene, OR, USA) and the AlexaFluor 555-coupled secondary antibody donkey anti-goat (1:2000, Invitrogen), respectively, for 1 h each (steps 10 and 12).

2.6.2.5 Hypoxia in correlation with vascular structures

Pimonidazole hydrochloride (Hypoxyprobe-1 Kit, NPI, Inc., Burlington, MA, USA) is used to detect hypoxia in cells and tissues. It is reductively activated depending on the cells' oxygen-level and forms stable covalent bounds with the thiol-groups of proteins, peptides, and amino acids in hypoxic cells [91]. These pimonidazole-protein adducts can be detected by histological methods.

Pimonidazole was dissolved in saline (B. Braun, Melsungen, Germany) and injected in a weight-dependent manner (60 mg/kg body weight) *i.v.* into the animals' tail vein 2 h prior to sacrification. During *i.v.* injection animals were anesthetized by inhaling 2.5 % Isoflurane mixed with 1.5 l/min oxygen.

Cryo slides were stained according to the standard protocol (Table 2) using a directly FITC-labelled mouse anti-pimonidazole antibody (NPI Inc.) in 3 % BSA/PBS (1:1000) in step 6. The next day, slides were incubated with the second primary antibody goat anti-CD31 in a concentration of 1:2000 (step 8) and its binding was visualized by the AlexaFluor 555-coupled donkey anti-goat secondary antibody (1:2000, step 10). Steps 12 and 13 were omitted.

2.6.2.6 Tumor perfusion

Hoechst 33342 fluorescence dye (bisBenzimide H 33342 trihydrochloride, Sigma-Aldrich) was used as a perfusion marker and administered to the animals prior to sacrification. Therefore, animals were anesthetized by inhaling 2.5 % Isoflurane and 1.5 l/min oxygen. The dermis and subcutis of the animals' abdomen were opened up to the sternum. At this point, the abdominal wall and diaphragm were opened, and the animal's heart was localized. Saline solved Hoechst 33342 dye was administered in a weight dependent manner at 15 mg/kg body weight and was directly injected into the animal's left ventricle followed by a cardiac relief cut. After 30 s, the tumor was dissected from the thigh. Thus, cell nuclei of perfused tissue regions were stained by Hoechst 33342 while non-perfused areas remained unstained. Perfusion was assessed in combination with CD31/SMA staining (section 2.6.2.4) and pimonidazole staining (section 2.6.2.5). If tissue perfusion was examined, step 14 (DAPI staining) of the standard protocol (Table 2) was omitted.

2.6.2.7 Identification of proliferating cells by BrdU incorporation

Proliferative activity was assessed by incorporation of 5-bromo-2'-deoxyuridine (BrdU, Sigma-Aldrich) into the cells' DNA during S-phase [138]. 1 g BrdU powder was dissolved in 24 ml 0.9 % saline and 8 ml EtOH. Animals were lightly anaesthetized by inhaling Isoflurane mixed with oxygen and were injected intraperitoneal (*i.p.*) with the BrdU solution (100 mg/kg body weight) 4 h prior to scarification.

Antigen retrieval was performed as described in section 2.6.2.3. Afterwards, slides were incubated with mouse anti-BrdU (Roche Diagnostics, Mannheim, Germany) as a primary antibody in a concentration of 1:800 for 2 h (step 6 of the standard protocol in Table 2). An AlexaFluor 555-coupled goat anti-mouse antibody (Invitrogen) was used as a secondary antibody in a concentration of 1:2000 (step 10). Steps 8, 9, 12, and 13 were omitted as only one primary antibody was used.

2.6.2.8 Identification of proliferating cells by Ki67

The nuclear protein Ki67 is associated with cell proliferation [139] and was stained by the rabbit anti-Ki67 antibody (1:2000, Abcam) in 3 % BSA/PBS (step 6 of the standard protocol in Table 2). The goat anti-rabbit AlexaFluor-555 antibody (1:2000, Invitrogen) was used as secondary antibody in step 10. Steps 8, 9, 12, and 13 were omitted, as only one primary antibody was used.

2.6.2.9 DNA double-strand breaks

The loss of chromosomal integrity through radiation-induced DNA double-strand breaks (DSBs) was assessed by staining for γH2AX [140], the phosphorylated form of the histone H2AX [140, 141]. First, antigen retrieval was performed on the slides (see section 2.6.2.3). Subsequently, the standard protocol (Table 2) was worked off with a rabbit anti-H2AX antibody (Cell Signaling Technology, Cambridge, UK) in a concentration of 1:1000 in step 6 and the AlexaFluor 555-coupled goat anti-rabbit antibody as the secondary antibody (1:3000) in step 10. Steps 8, 9, 12, and 13 were omitted as only one primary antibody was used.

2.6.3 Fluorescence microscopy and image preparation for analysis

All histological stainings were scanned with the reported exposure times (Table 3) at an Axio Scan.Z1 microscope (Carl Zeiss Microscopy GmbH, Jena, Germany) producing bright field and multi-channel fluorescence whole-mount images of entire tumor sections.

For analysis, the individual microscopy channels were converted to 8 bit images, compressed to 50 % of their original size in the Zen lite 2012 software (Zeiss), and exported as TIFF files. Exported images were manually cleared from artefacts due to reflections of small grains, overlapping tissue, and remaining muscle tissue in the open source software

ImageJ [142]. Tissue areas with no visible cell nuclei were assumed to be necrotic and were cut-out as well. Artefact areas that occurred only in one channel were also removed from the unaffected channels. In the following, these images are referred to as “cleared”.

Table 3 Exposure times for fluorescence microscopy.

Staining	Exposure time
CD31	300 ms
SMA	200 ms
Pimonidazole	300 ms
BrdU	300 ms
γH2AX	400 ms
DAPI	30 – 60 ms
Hoechst 33342	60 ms

2.6.4 Quantitative analyses of histological stainings

2.6.4.1 Vessel density and pericyte coverage

Cleared images were background subtracted using the ImageJ plugin *Subtract background* with a rolling ball radius of 50 - 200 pixels for CD31 images and 20 - 100 pixels for SMA images. Background subtracted images were saved as hdf5-files, and a tumor mask was generated from the DAPI image. The tumor mask was separated into rim and core regions to investigate the spatial distribution of the vessel density. The rim was defined as the outer 1 mm of tumor tissue and was delineated manually in ImageJ. The core was the remaining inner tissue area (Figure 8).

Semi-automatic vessel segmentation was performed on the cleared and background subtracted CD31 images (hdf5-files) in the open source software Ilastik [143] using the plugin *Pixel Classification*. Various features were selected (Color/intensity, edge, texture: 0.3 px, 1.6 px, and 5.0 px) and three labels were delineated in a set of approximately five exemplary images: CD31, blurry background, and background. Marking of only few pixels was sufficient for satisfactory vessel segmentation due to the high contrast of the CD31 images. The segmentation was applied to an entire stack of images. The Same procedure was performed for SMA images. Segmentation results were exported as TIFF images (Figure 8).

An algorithm was written in Matlab R2017b that automatically counts segmented vessels and identifies CD31 and SMA co-expressing vessels ($CD31^+/SMA^+$). The segmentation of the CD31-label (or SMA-label, respectively) was loaded by the Matlab program. A median filter was applied to the CD31 and SMA segmentations to eliminate noise.

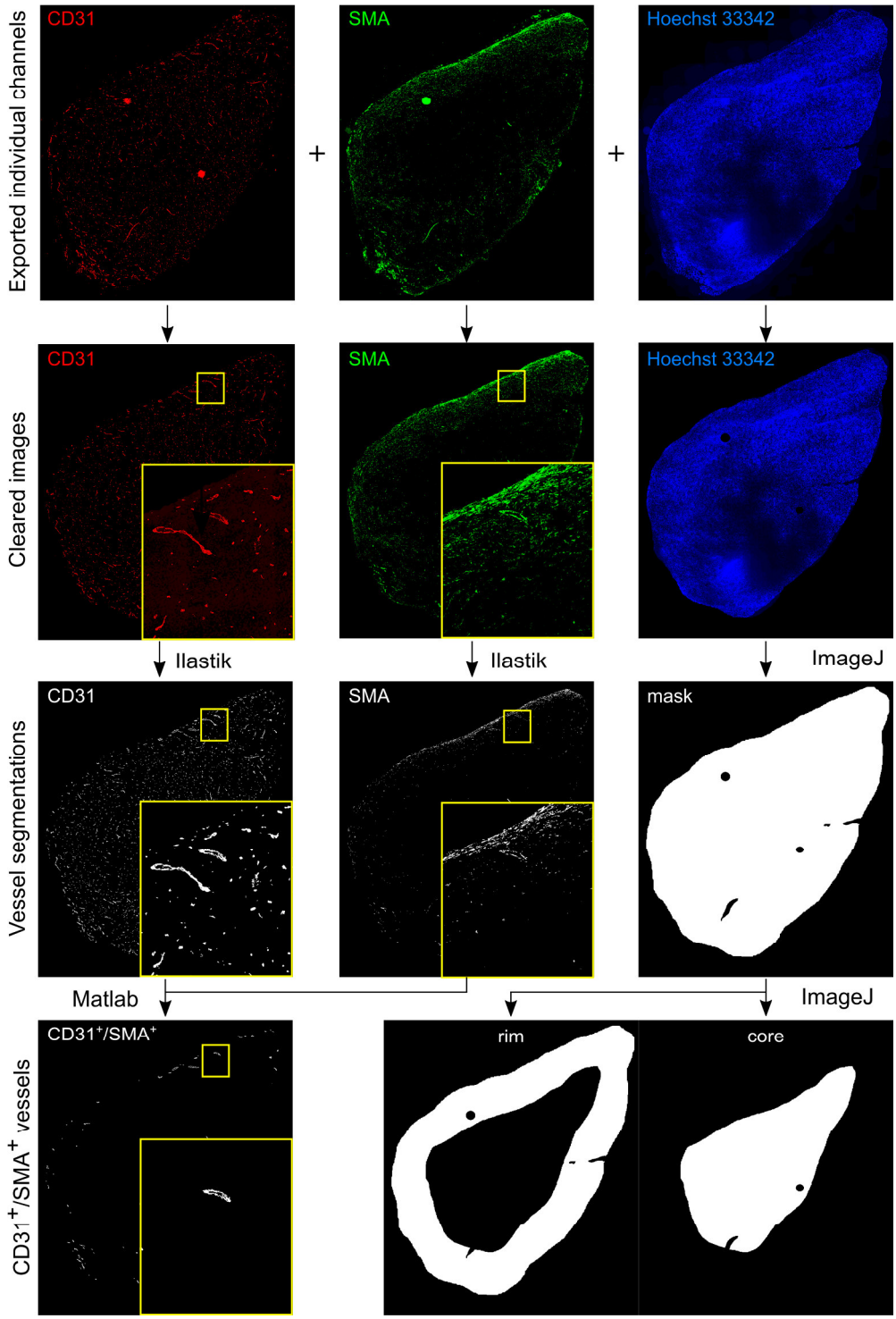

Figure 8 Illustration of the automated vessel counting process from multi-channel fluorescence images. Individual channels were exported and cleared from artefacts. $CD31^+$- (vessels) and SMA^+- (pericyte-covered) structures were semi-automatically segmented from the respective cleared images in Ilastik. The segmentation images were further processed in Matlab to identify and quantify $CD31^+/SMA^+$-structures (i.e. mature vessels). Tumor masks were derived from the cleared Hoechst 33342 or DAPI images. Rim and core masks were generated by manual delineation. Yellow framed images show close-ups of the yellow boxes in the CD31 and SMA whole-mount images.

Objects smaller than 50 pixels (21.125 µm^2, respectively) were eliminated by using the built-in Matlab function *bwareaopen.m*. Subsequently, connected objects were counted by *bwconncomp.m* with a connectivity of 8. Each counted CD31 component was checked for overlap with a SMA segmentation to identify CD31$^+$/SMA$^+$-structures. If an overlap of at least 300 pixels was found, the object was counted as CD31$^+$/SMA$^+$ co-expressing. Objects were also counted on the area of the rim and core masks, and the corresponding vascular densities were acquired by normalizing the number of objects to the area of the respective mask.

2.6.4.2 Hypoxic fraction

Tumor regions were classified as either hypoxic or non-hypoxic based on the pimonidazole-staining intensity of individual areas. An algorithm was written in Matlab R2017b to quantify the pimonidazole-positive area in relation to the overall tumor section. Tumor masks were created from the cleared images of the three channels and read into the Matlab code along with the cleared pimonidazole images.

An intensity threshold for hypoxia was manually set based on visual inspection of the pimonidazole images (8 bit images, i.e. intensity range from 0 to 255): Pixels with intensities above 30 were classified as hypoxic, remaining pixels were classified as non-hypoxic (Figure 9).

The threshold was applied to the cleared pimonidazole images and the resulting pimonidazole-positive image was blurred by Gaussian filtering ($\sigma = 20$), followed by an additional threshold to avoid overestimation of the pimonidazole-positive area due to fading after the blurring. Masks for pimonidazole-positive and pimonidazole-negative parts were generated.

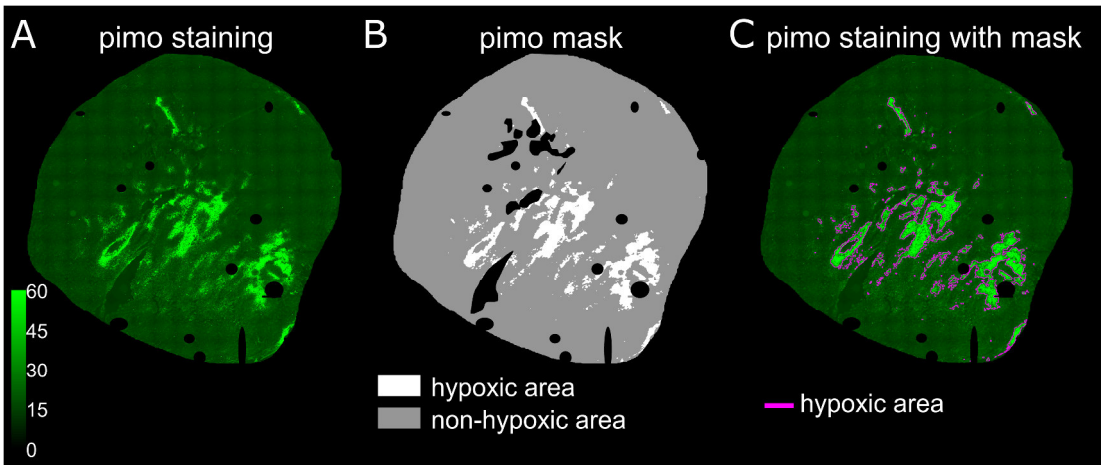

Figure 9 Illustration of the quantification of the hypoxic fraction from pimonidazole fluorescence images. (A) Cleared fluorescence image with pimonidazole staining (pimo, green), i.e. hypoxic areas. (B) Resulting masks for hypoxic (white) and non-hypoxic (gray) areas after thresholding and further processing. (C) Overlay of pimonidazole fluorescence image (green) and boundaries of identified hypoxia regions (magenta).

2.6.4.3 Perfusion classes and respective vessel densities

Tumor regions were classified as highly-perfused, intermediately-perfused, and non-perfused based on the intensity of the cell nuclei staining by Hoechst 33342. A program was written in Matlab R2017b to automatically classify the tumor regions.

Tumor masks were created from the cleared images of the three channels and read into the Matlab program along with the cleared Hoechst 33342 images.

Intensity thresholds for perfusion classes were set manually after visual inspection of the images (8 bit images: i.e. intensity range from 0 to 255). Pixels with intensities higher than 24 were assigned to the high-perfusion class, pixels with intensity lower than 10 were assigned to the non-perfused class. Pixels with intensity between 10 and 24 (including 10 and 24) were classified as intermediately-perfused (Figure 10).

The threshold for highly-perfused areas was applied to the cleared Hoechst 33342 images, the resulting high-perfusion image was blurred by a Gaussian filter ($\sigma = 30$), and an additional threshold was applied to avoid an overestimation of the respective area due to blurring of the edges. A mask was generated for the highly-perfused area.

The procedure was repeated for the non-perfused area: The threshold for non-perfusion was applied to the cleared image, followed by blurring of the resulting image with a Gaussian filter ($\sigma = 30$), and cutting off the blurred edges by an additional threshold. A mask for the non-perfused area was generated. Remaining unclassified pixels were assigned to the intermediately-perfused class.

Furthermore, the vessel density in the three perfusion classes was determined. To this end, the images of the segmented vessels (see section 2.6.4.1) were loaded into Matlab. Using *bwconncomp.m*, the number of vessels (connected components) was counted for each perfusion class mask.

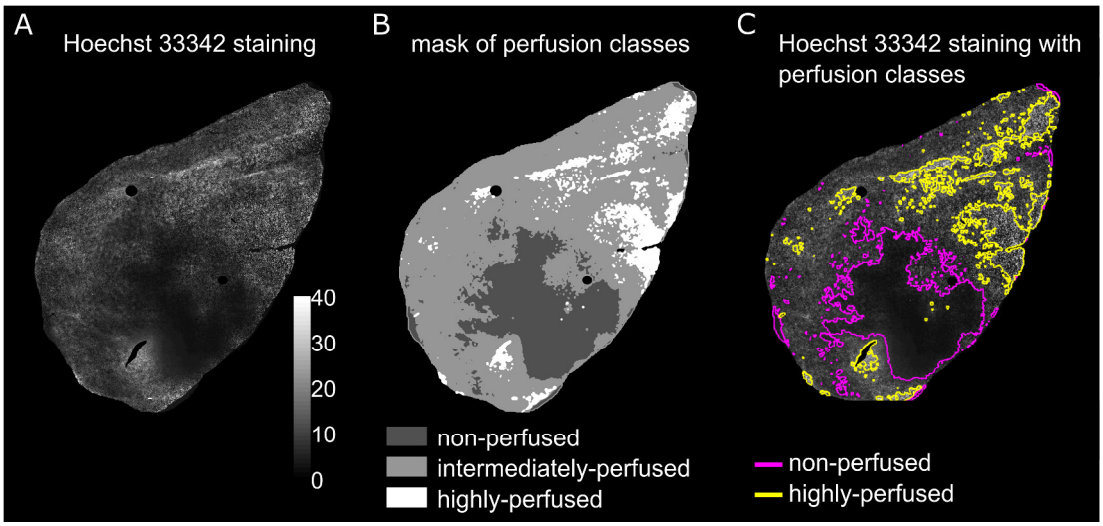

Figure 10 Illustration of the classification and quantification of perfused areas based on Hoechst 33342 fluorescence images. (A) Perfused areas of the tumor were stained by Hoechst 33342 (bright areas). (B) Masks for the three classes non-perfused (dark gray), intermediately-perfused (light gray), and highly-perfused (white) tumor areas were derived from the fluorescence image. (C) Overlay of the Hoechst 33342 fluorescence image and boundaries of the non-perfused (magenta) and highly-perfused (yellow) tissue areas. The remaining area was classified as intermediately-perfused.

2.6.4.4 Proliferation rate based on BrdU incorporation

The total number of cells (DAPI) and the number of cells that had incorporated BrdU were quantified using the open source software CellProfiler™ [144]. A script written by Dr. Jörg Peter was used to access CellProfiler™ on Linux. Furthermore, the script enabled automatic data processing of multiple and very large image files.

Cleared BrdU images were trimmed and normalized using a script by Dr. Jörg Peter. Normalized images were loaded into CellProfiler™ and processed with the parameters listed in Table 4. Those parameters had been optimized on a few randomly chosen exemplary images beforehand. Cell segmentations were saved in the images (Figure 11), and each image was visually checked for the quality of the segmentation. If necessary, respective images were further corrected or the parameters were slightly adapted. The same procedure was repeated for the DAPI images with the respective parameters listed in Table 4. Large images had to be quartered prior to segmentation in CellProfiler™. The proliferation rate was defined as the ratio between the number of BrdU-positive ($BrdU^+$) cells and all cells (DAPI count).

Table 4 Parameters for cell segmentation and counting in CellProfiler™ for $BrdU^+$-cells and $DAPI^+$-cells.

Parameter	BrdU	DAPI
Typical minimum object diameter [px]	10	10
Typical maximum object diameter [px]	50	50
Object declumping method	Shape	Intensity
Object declumping separation	Shape	Intensity
Threshold strategy	Adaptive	Adaptive
Threshold method	Minimum variance	Minimum variance
Adaptive window size [px]	100	100
Threshold smoothing scale	2.0	1.35
Threshold correction factor	0.5	0.5
Lower threshold bound	0.15	0.0
Upper threshold bound	1.0	1.0

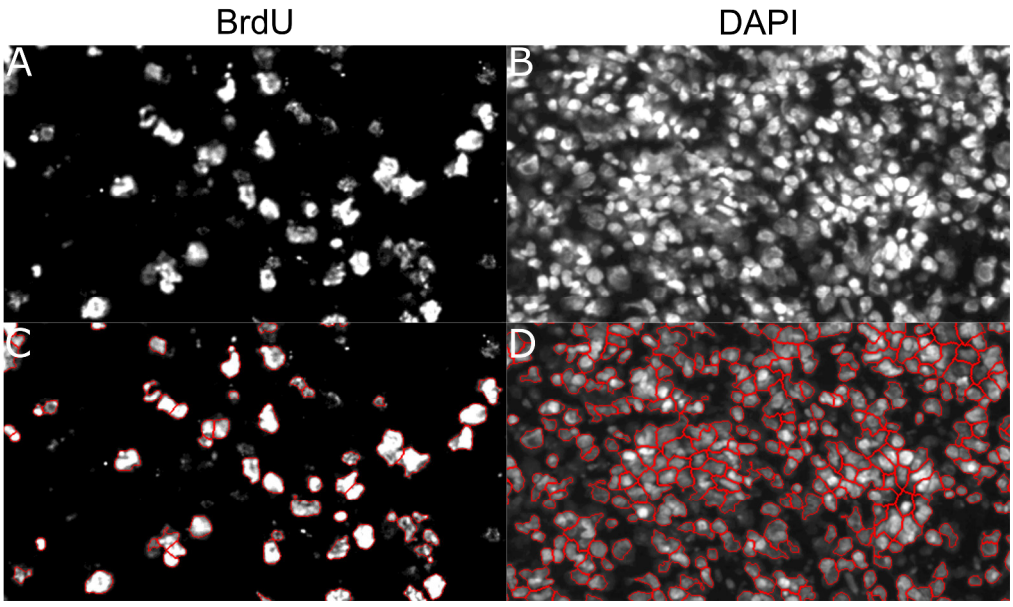

Figure 11 Exemplary cell segmentation results from fluorescence images in CellProfiler™. (A) Fluorescence image of $BrdU^+$-cells and (B) the respective DAPI stained cell nuclei. (C) Segmentation results (red lines) of $BrdU^+$-cells in CellProfiler™. (D) Segmentation results (red lines) of DAPI stained cell nuclei in CellProfiler™. The proliferation rate was defined as the ratio of $BrdU^+$-cells to DAPI stained cells.

2.6.4.5 DNA double-strand break classification

The percentage of cells with DNA DSBs was determined based on the immunohistological staining for the histone γH2AX. Cells that stained positive for γH2AX were classified as high intensity cells and intermediate intensity cells (Figure 12). A script was written in Matlab R2017b to automatically classify and count the cells in the respective classes.

Cleared γH2AX images were slightly smoothed by a Gaussian filter ($\sigma = 1$). Pixels of the 8 bit images (intensity range from 0 to 255) with intensities lower than 7 were classified as background and eliminated leaving behind γH2AX-positive ($\gamma H2AX^+$) objects. Depending on the background signal, some parameters had to be adapted for individual images (numbers in brackets). Objects smaller than 15 (30) pixels were removed using *bwareaopen.m*. ImageJ was called from within Matlab using the implementation "MIJ: Running ImageJ and Fiji within Matlab*"* by D. Sage, which is available at the Matlab File Exchange [145]. The ImageJ plugin *Watershed* was applied to the background subtracted image to separate adherent cells. *bwareaopen.m* was applied again to eliminate objects smaller than 20 (40) pixels, to eliminate small detached cell fragments. Individual cells were counted by *bwconncomp.m.* Finally, counted cells were separated into high and intermediate intensity cells: A threshold was manually set for high intensity cells based on the examination of multiple randomly chosen exemplary images. Counted cells with a mean intensity higher than 13 were classified as high intensity, the remaining cells were classified as intermediate intensity cells (Figure 12).

The total number of cells was counted in the cleared DAPI images in CellProfiler™ (see section 2.6.4.4 and Table 4). The ratio between γH2AX high intensity cells and all cells, and the ratio between γH2AX intermediate intensity cells and all cells were reported.

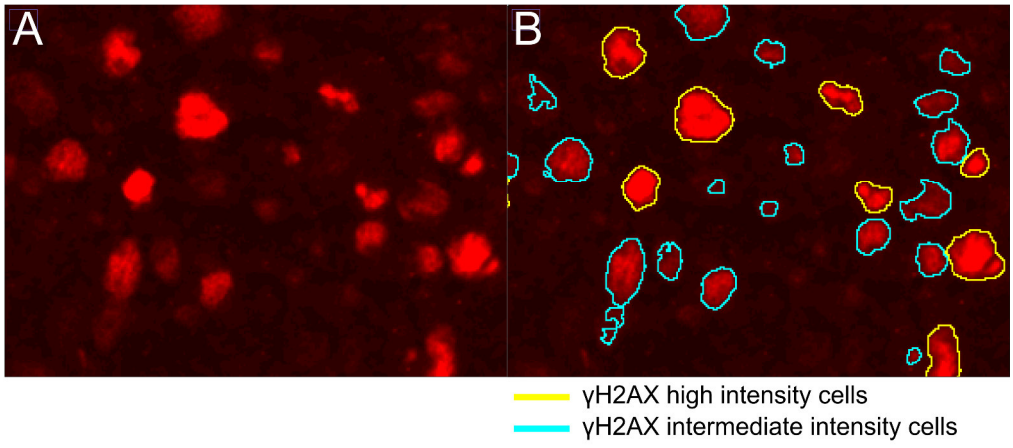

Figure 12 Illustration of the classification of $\gamma H2AX^+$-cells. (A) Fluorescence image of cells that stained positive for γH2AX. (B) Results of automated classification of these $\gamma H2AX^+$-cells into intermediate (cyan) and high intensity cells (yellow).

2.7 Longitudinal histology study of the AT1-tumor after irradiation

The effects of curative single dose irradiations with either photons or ^{12}C-ions on the vasculature, hypoxic fraction, perfusion, DNA DSBs, and cell proliferation of the AT1-tumor were investigated longitudinally by histological methods. The results will be used to choose the optimal time points for future multimodal imaging studies.

AT1-tumors were transplanted subcutaneously on the distal right thighs of adult male Copenhagen rats as described in section 2.1.3. Tumors were either investigated in a longitudinal manner after irradiation or in a volume-dependent manner without irradiation (non-irradiated controls).

For the longitudinal treatment study, tumors were irradiated with curative doses of either 37 Gy ^{12}C-ions or 85 Gy photons when they reached a size of 10 mm × 10 mm. Animals were sacrificed 24 h, 3 days, 7 days, 10 days, 14 days (^{12}C-ion RT only), and 21 days (^{12}C-ion RT only) after irradiation (Figure 13). Each group consisted of five animals.

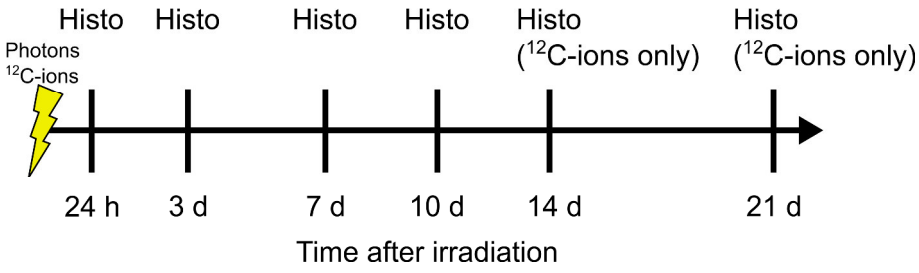

Figure 13 Schematic illustration of the longitudinal histology study of the AT1-tumor. Tumors were irradiated with curative doses of either photons or ^{12}C-ions when they reached a size of 10 mm × 10 mm (yellow flash). They were dissected and prepared for histology (histo) at the pre-defined time points. The 14 and 21 day time points were only performed for ^{12}C-ion treated tumors.

Tumors were dissected as described in section 2.6.1, and the immunohistochemistry stainings that are listed in Table 5 were performed for one cryo slide per staining and tumor, respectively. Due to logistic reasons the experiments were split and the data of the 14 and 21 day groups with respective controls were obtained in a later separate experiment. Unfortunately, the linear accelerator at DKFZ was not available anymore at that time point which is why those time points could only be performed for ^{12}C-ion irradiation and not for photon irradiation.

Table 5 Histology and immunohistochemistry stainings which were performed on the AT1-tumors of the longitudinal histology study after irradiation, and references to the respective staining and quantification protocols. For the CD31/SMA and CD31/pimonidazole staining an additional slide per tumor was prepared and counterstained with DAPI.

Staining	Staining protocol	Quantification protocol
H&E	2.6.2.1	-
CD31/SMA/ Hoechst 33342 (DAPI)	2.6.2.4 (CD31/SMA) 2.6.2.6 (Hoechst 33342)	2.6.4.1 (Vascular density) 2.6.4.3 (Perfusion)
CD31/pimonidazole/ Hoechst 33342 (DAPI)	2.6.2.5 (CD31/pimonidazole) 2.6.2.6 (Hoechst 33342)	2.6.4.2 (Hypoxic fraction)
BrdU/DAPI	2.6.2.7 (BrdU)	2.6.4.4 (Proliferation)
γH2AX/DAPI	2.6.2.9 (γH2AX)	2.6.4.5 (DNA DSBs)

For the volume-dependent study, non-irradiated tumors were dissected at pre-defined sizes of 10 mm × 10 mm (n = 10, mean diameters: 9 - 10.75 mm), 15 mm × 15 mm (n = 10, mean diameters: 14.75 - 16 mm), 20 mm × 20 mm (n = 5, mean diameters: 19 - 21 mm), 25 mm × 25 mm (n = 6, mean diameters: 21 - 24.25 mm), and 30 mm × 30 mm (n = 6, mean diameters: 24 - 29 mm). Tumors were stained for hypoxia (pimonidazole, see section 2.6.2.5 for staining protocol and section 2.6.4.2 for quantitative analysis protocol). Results are reported as mean ± standard error of the mean (SEM).

2.8 Statistical analysis

Longitudinal DCE-MRI study of the AT1-tumor after irradiation

For the longitudinal DCE-MRI study of the AT1-tumor after irradiation (section 2.5.1), the Kruskal-Wallis test and post hoc Bonferroni correction were performed in Matlab R2017b on pooled DCE-MRI voxel results of the control and treatment groups per imaging time point. Due to the large number of voxels per group the significance level was set to 0.1 %. Differences in vessel density and vessel maturity between rim and core per treatment group were tested by the Mann-Whitney U test with a significance level of 5 %. Differences between vascular density and maturity in the rim and core were tested by one-way ANOVA with Bonferroni correction. The significance level was set to 5 %.

Longitudinal histology study of the AT1-tumor after irradiation

The Kruskal-Wallis test and post hoc Bonferroni correction for multiple testing were performed to test for significant differences between all groups in Matlab R2017b. The significance level was set to 5 %.

3 Results

3.1 Photoacoustic imaging (PAI)

PAI was used to characterize the initial oxygenation status of the three Dunning tumor sublines H, HI, and AT1. To exploit the maximum potential of PAI, a new data analysis protocol was developed and validated. This was employed to obtain the sublines' characteristic sO_2-distributions and to investigate their behavior towards external changes in oxygen supply. The text, figures, and tables in section 3.1 and respective subsections were taken from reference [96] and have been originally written and created by myself.

3.1.1 New protocol for the assessment of sO_2-distributions

Commercial PAI systems, such as the software VevoLab available at DKFZ, often only allow the evaluation of mean values of predefined regions of interest (ROI). However, tumors often exhibit highly heterogeneous structures, especially with respect to oxygenation. Therefore, a protocol has been developed to assess pixel-based oxygen saturation (sO_2-) distributions over entire 3D tumor volumes [96]. The following steps were performed on the beam-formed raw PA data acquired at 750 nm and 850 nm and the calculated hemoglobin image which were exported from VevoLab and transformed into image stacks:

I. Data filtering: A 3D Gaussian filter ($\sigma = 2$) was applied to the beam-formed PA raw data of both wavelengths using the image processing software ImageJ [142].

II. Oxygen saturation calculation: Employing eq. (1), sO_2 was calculated pixel-wise from the PA signal at 750 and 850 nm using the molar extinction coefficients of de-oxygenated and oxygenated hemoglobin [146] in Matlab R2016a for each slice of the 3D image stack.

III. Data thresholding: The hemoglobin image was calculated in VevoLab [90] and was then converted into a likelihood-map representing the probability that the signal of one pixel originated from hemoglobin. The likelihood-map was applied to the sO_2 images in Matlab. Only pixels whose probability in the likelihood-map exceeded a predefined threshold were included into further analysis. Pixels whose probability was too low were set to zero.

IV. Region of interest analysis: Tumor ROIs were delineated manually in every 5^{th} image of the 3D stack according to simultaneously acquired B-mode images. Remaining ROIs were generated using the ROI interpolation tool in ImageJ.

V. sO_2-histogram derivation: The sO_2-values of all pixels within the ROIs were condensed into normalized histograms using a bin size of 0.5 %. For comparison of sO_2-distributions, the median as well as the 25^{th} and 75^{th} percentiles (25^{th}/75^{th}) were extracted. Due to the

measurement uncertainty and noise, some of the measured sO_2-distributions showed a negligible amount of histogram entries above 100 % sO_2.

VI. Earth mover's distance calculation: To quantify the similarity of two histograms, the Earth mover's distance (EMD) [147-149], a recognized measure of distance between two probability distributions [150], was calculated. It represents the minimal cost of transferring one distribution into another, when the cost is defined as the sum of the histogram entries times the distance they have to be moved [151]. Recently, it has also been applied in various fields of biological and medical research [152-154]. For the present application in PAI, the EMD can be expressed as follows:

$$EMD = \int_{-\infty}^{\infty} |F_a(x) - F_b(x)| dx, \tag{15}$$

where $F_a(x)$ and $F_b(x)$ are the cumulative distribution functions of the probability densities a and b, respectively [148]. For identical distributions, the EMD is equal to 0, while the maximum EMD is 1, which is only the case for two single-bin histograms located at 0 % and 100 % sO_2.

3.1.2 Dependency of sO_2-distributions on signal gain and threshold

To investigate the robustness of the resulting sO_2-distributions towards measurement settings, the effect of signal gain and thresholding on the resulting sO_2-distributions were investigated on two HI-tumors. The sO_2-distributions for both tumors for all tested settings are displayed in Figure 14, and the quantitative results (i.e. median and 25^{th}/75^{th} percentiles) are summarized in Table 6.

The tumor HI-1 exhibited a homogeneous PA signal with a clearly detectable skin line. Visual inspection of the normalized sO_2-distributions revealed only minor differences in the shape of the distributions for the different settings (Figure 14, 1^{st} and 2^{nd} row). Regarding the 25^{th}/75^{th} percentile ranges, the distributions became slightly narrower with increasing threshold, however, without affecting the medians (Table 6). Repeating the imaging procedure after repositioning the animal did not reveal any differences in shape, medians, and 25^{th}/75^{th} percentile ranges (Figure 14 and Table 6). Depending on the signal gain during measurement and threshold during analysis the number of pixels included into analysis ranged from 40 % to 100 %.

Tumor HI-2, exhibited a very weak PA signal with a hardly detectable skin line, even at a signal gain of 40 dB. Table 6 reveals that even though medians were not affected, the shape and 25^{th}/75^{th} percentile ranges of the sO_2-distributions changed somewhat depending on threshold and signal gain (Figure 14, 3^{rd} and 4^{th} row): While the histograms at 0 % threshold were identical for all signal gains even after repositioning of the animal (Figure 14 and Table 6), a large variability was observed for higher thresholds, especially in combination with a

low signal gain. Under these conditions only a negligible fraction of pixels with signals near the noise-level could be analyzed (e.g. only 10 % of the pixels for all three signal gains at a threshold of 30 %). To obtain reliable and reproducible results, it is therefore important to adjust the measurement settings, especially the signal gain, individually for each animal and each imaging session. The skin layer had been selected as a reliable reference for those adjustments.

Table 6 Medians and $25^{th}/75^{th}$ percentiles of the PAI sO_2-distributions for the investigated combinations of signal gain and threshold. Values are given for two HI-tumors (small and large volume) and two independent positions of the animal (Repos = second positioning). The asterisk (*) indicates measurements where the percentage of pixels unequal to zero was below 10 % resulting in sO_2-distributions which are not anymore representative for the tumor. Table reproduced from [96] under the CC BY 4.0 license.

		HI-1 (600 mm³)		**HI-2 (740 mm³)**	
Gain	**Threshold**	**sO_2 median**	**sO_2 median Repos**	**sO_2 median**	**sO_2 median Repos**
[dB]	[%]	[25 %, 75 %]	[25 %, 75 %]	[25 %, 75 %]	[25 %, 75 %]
36	0	88 [83, 90]	86 [83, 88]	46 [39, 52]	50 [42, 57]
36	15	89 [85, 91]	86 [83, 88]	44 [32, 59]	49 [36, 65]
36	30	90 [87, 91]	87 [84, 89]	44 [29, 74]*	61 [34, 83]*
38	0	88 [84, 91]	86 [83, 88]	46 [38, 52]	47 [39, 56]
38	15	89 [84, 91]	86 [83, 88]	44 [33, 54]	45 [34, 58]
38	30	89 [86, 91]	87 [85, 89]	43 [29, 70]*	50 [27, 76]*
40	0	86 [82, 88]	87 [84, 90]	47 [39, 53]	47 [38, 55]
40	15	86 [81, 89]	87 [84, 90]	45 [35, 53]	44 [35, 55]
40	30	87 [83, 89]	88 [85, 90]	45 [31, 68]*	45 [28, 71]*

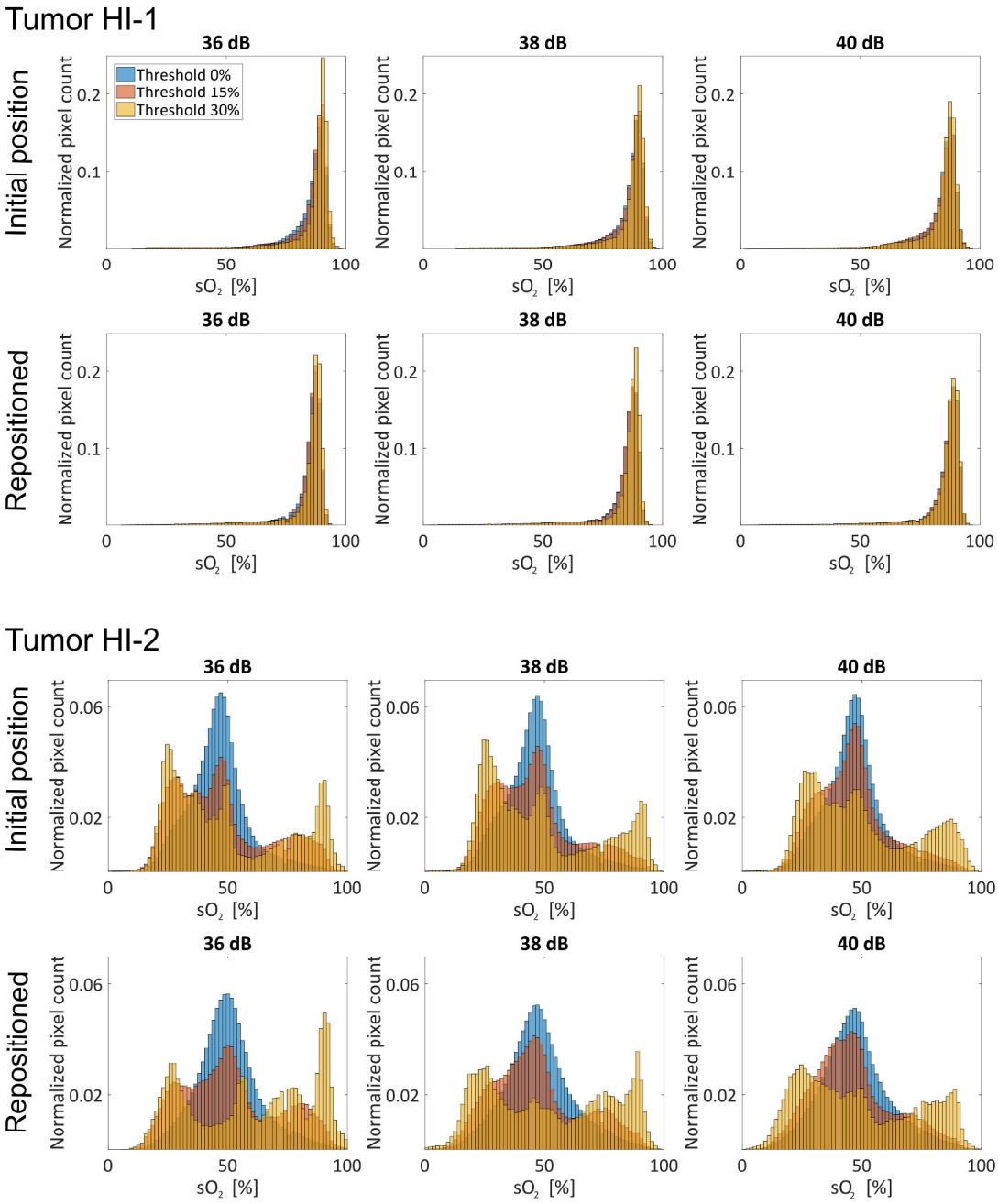

Figure 14 Normalized PAI-derived sO_2-distributions of two HI-tumors for three signal gains and three thresholds at two positions of the animals. Tumor HI-1 exhibited sO_2-distributions that were essentially independent of all measurement settings. The large tumor HI-2 (rows 3 and 4) exhibited identical sO_2-distributions for a 0 % threshold only. With increasing threshold, the variability of the distribution increased due to the very low number of evaluated pixels. Figure reproduced from [96] under the CC BY 4.0 license.

3.1.3 Characterization of the tumor sublines H, HI, and AT1

The oxygenation status of the three Dunning tumor sublines H, HI, and AT1 was characterized by PAI experiments with the new developed data analysis protocol (section 3.1.1).

3.1.3.1 Characteristic sO_2-distributions per tumor subline

Figure 15 displays the pooled sO_2-distributions of two tumors of comparable size per subline while the animals were breathing air. The well oxygenated H-tumor exhibited a narrow and well-defined peak with a median of 73 % (25^{th}/75^{th} percentile range: 69 %/ 76 %). Similarly, the HI-tumor exhibited a median of 71 % with a somewhat wider distribution (25^{th}/75^{th} percentile range: 62 %/ 76 %). By contrast, the distribution of the AT1-tumor was located around a median of 40 % and exhibited a different shape, however, with a comparable 25^{th}/75^{th} percentile range (34 %/ 47 %).

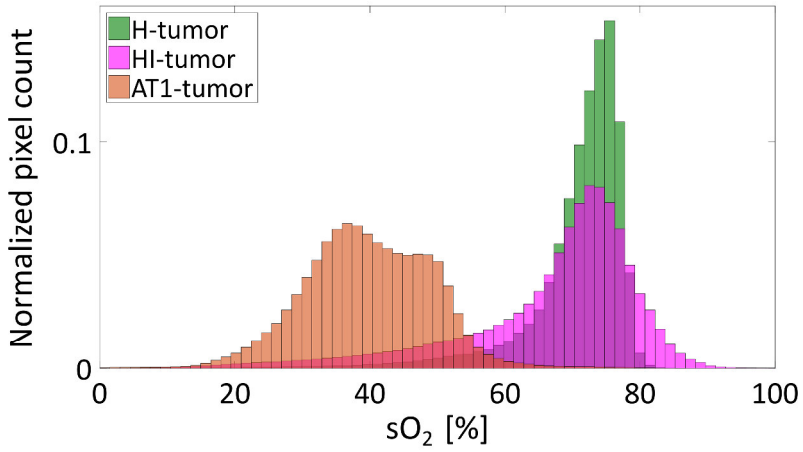

Figure 15 Pooled normalized sO_2-distributions of two tumors per subline while animals were breathing air. The sublines show clearly distinguishable sO_2-distributions for the H-, HI-, and AT1-tumor. Figure reproduced from [96] under the CC BY 4.0 license.

3.1.3.2 Temporal development of sO_2-distributions per tumor subline

PAI was repeated several times over a period of up to 41 days and, as an example, sO_2-distributions at different time points are displayed in Figure 16 A - C. Median values and 25^{th}/75^{th} percentiles for all measurement time points are provided in Table 7.

Repeating the measurement, the tumor H-2 (Figure 16 A) essentially maintained the shape of the distribution; however, the distributions shifted slightly towards lower sO_2-values with time. During the observation period, the volume of this tumor did not change (Figure 16 D). For tumor H-1, the width of the sO_2-distribution increased slightly and the median values shifted slightly towards higher sO_2-values (Table 7).

Tumor HI-3 exhibited a more heterogeneous sO_2-distribution with a peak at high sO_2-values at day 1, which then became broader with an increasing fraction of pixels at low sO_2-values (< 40 % sO_2, Figure 16 B). While the peak of the tumor did not shift significantly, the fraction of low sO_2 pixels changed considerably with time. Figure 16 E illustrates the sO_2-distributions of the same tumor when the animal was breathing 100 % O_2. This tumor exhibited an increased heterogeneity as compared to the air-breathing condition. Distinct regions of different sO_2 levels can be identified in the respective color maps (Figure 16 F). The strong reduction of pixels with low sO_2-values at day 41 spatially correlates with the occurrence of the central region without PA signal.

Although the volumes of the AT1-tumors increased up to sevenfold in 12 days (Figure 16 D), their sO_2-distributions experienced only minor changes in sO_2 medians and 25th/75th percentile ranges (Figure 16 C, Table 7).

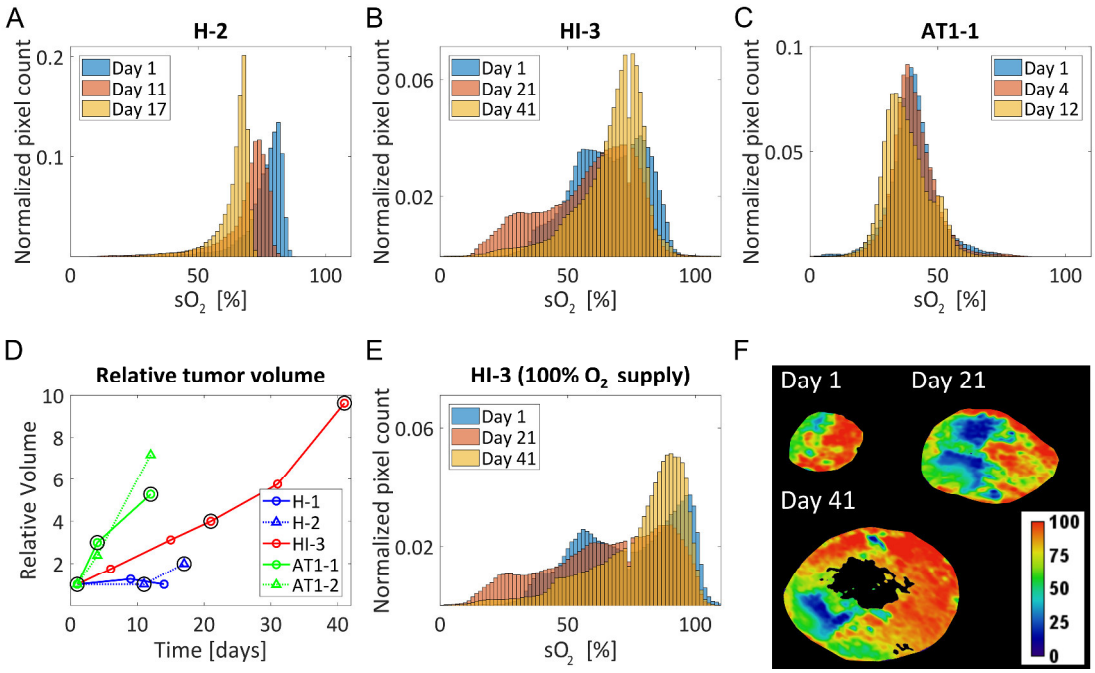

Figure 16 Temporal development of sO_2-distributions for one tumor per subline: (A) H-2, (B) HI-3, and (C) AT1-1 tumor, imaged when the animals were breathing air. Results at other time points and for additional tumors are given in Table 7. (D) Development of tumor volume with time. As tumor HI-4 was only imaged once, it is not listed in D. Black circles indicate imaging time points that are depicted in A - C. (E) sO_2-distributions and (F) representative sO_2 color maps of tumor HI-3 when the animal was breathing 100 % O_2. Figure reproduced from [96] under the CC BY 4.0 license.

Table 7 Summary of oxygen challenge and clamping experiments for the H-, HI-, and AT1-tumor and the skin. Results are displayed as median and 25^{th}/75^{th} percentiles for each tumor and skin for each oxygenation condition. Table reproduced from [96] under the CC BY 4.0 license.

Animal	Day	Size [mm^3]	100 % O_2 pre	Air	100 % O_2 post	100 % O_2 clamped	100 % O_2 post clamping
H							
H-1	Day 1	40		68 [65, 71]			
	Day 9[a]	50	93 [87, 97][b]	73 [70, 76][b]	96 [91, 99]	57 [48, 68][b]	96 [91, 98]
	Day 14	40	84 [75, 92]	76 [69, 81]	85 [75, 93]	36 [29, 42]	97 [92, 100]
H-2	Day 1	20	92 [88, 96]	78 [74, 81]			
	Day 11	20	94 [89, 97][b]	72 [67, 75][b]		50 [42, 58][b]	
	Day 17	40		66 [62, 68]			
HI							
HI-3	Day 1	80	75 [57, 91]	66 [56, 77]		30 [21, 45]	87 [62, 96]
	Day 6	140	92 [73, 97]	82 [64, 82]	91 [76, 96]	25 [18, 41]	96 [76, 96]
	Day 15	250	83 [60, 94]	68 [53, 78]	73 [53, 88]	23 [15, 43]	83 [60, 94]
	Day 21[a]	320	69 [49, 85]	61 [45, 72]	70 [53, 85]	37 [29, 50]	74 [54, 89]
	Day 31	460	85 [71, 93][b]	72 [60, 79][b]	82 [64, 91]	43 [35, 55][b]	73 [54, 89]
	Day 41	770	84 [68, 91]	70 [61, 76]	79 [67, 88]	28 [18, 47]	79 [66, 90]
HI-4[c]	Day 1	580	85 [82, 91]	71 [64, 74]		25 [17, 35]	87 [81, 93]
AT1							
AT1-1	Day 1	110	40 [35, 46]	40 [36, 45]	41 [36, 47]	43 [35, 50]	43 [38, 49]
	Day 4[a]	330	41 [36, 47][b]	40 [36, 45][b]	42 [37, 49]	42 [37, 46][b]	40 [36, 44]
	Day 12	580	37 [31, 44]	37 [32, 43]	38 [32, 45]	40 [30, 48]	42 [36, 49]
AT1-2[d]	Day 1	460	42 [35, 49][b]	40 [32, 48][b]			
	Day 4	1100	45 [38, 51]	46 [39, 52]			
	Day 12	3300	45 [39, 51]	44 [38, 51]			
Skin							
Skin-1	-	-	83 [69, 92][b]	67 [56, 75][b]	77 [63, 86]	16 [12, 22][b]	63 [53, 73]
Skin-2[a]	-	-	82 [67, 91][b]	69 [58, 77][b]	78 [66, 87]	18 [12, 27][b]	84 [73, 90]

[a] Distribution displayed in Figure 17 middle column.

[b] Data included in pooled distributions in Figure 17 left column.

[c] Animal could only be imaged once due to scab formation on the skin.

[d] Location of the tumor did not allow clamping experiment.

3.1.3.3 Sensitivity of tumor sublines to external changes in oxygen supply

Figure 17 displays the changes in sO_2-distributions for the three tumor sublines as well as for the skin when changing the external oxygen supply of the animals. For each of the cases, pooled data of two tumors (left column) and one exemplary full experiment performed in a single tumor (middle column) are shown. All medians and $25^{th}/75^{th}$ percentiles are listed in detail in Table 7.

After switching the external gas supply from 100 % O_2 to air, the PA-signal of the H-tumor immediately shifted to lower sO_2-values while still maintaining its narrow and well-defined peak (Figure 17 A, B and Table 7). When clamping the tumor-supplying arteries, the sO_2-distribution shifted to even lower values, while broadening significantly although the animals were still breathing 100 % O_2. When executing the full oxygen challenge experiment (Figure 17 B), the initial sO_2-distributions were restored after switching back from air to 100 % O_2 ("100 % O_2 post") and after releasing the clamping ("100 % O_2 post clamping"), respectively.

When changing the external oxygen supply from 100 % O_2 to air, the broad sO_2-distributions of the HI-tumors were shifted to lower values (Figure 17 C, D). Clamping of tumors led to further shift and broadening of the peak. Again, when performing the full oxygen challenge experiment (Figure 17 D), the initial sO_2-distributions were essentially restored after switching back from air to 100 % O_2 and after releasing the clamping, respectively.

In contrast to the H- and HI-tumors, essentially no differences were detected for the sO_2-distributions of the AT1-tumors after switching from 100 % O_2 to air and after clamping (Figure 17 E, F).

The skin showed a broad distribution at high sO_2-values when the animals were breathing 100 % O_2 (Figure 17 G, H). When switching to air, the peak of the distribution was shifted to lower sO_2 and clamping lead to a further significant shift and broadening of the distributions. Again, when performing the full oxygen challenge experiment (Figure 17 H), the initial sO_2-distributions were essentially restored after switching back from air to 100 % O_2 and after releasing the clamping, respectively.

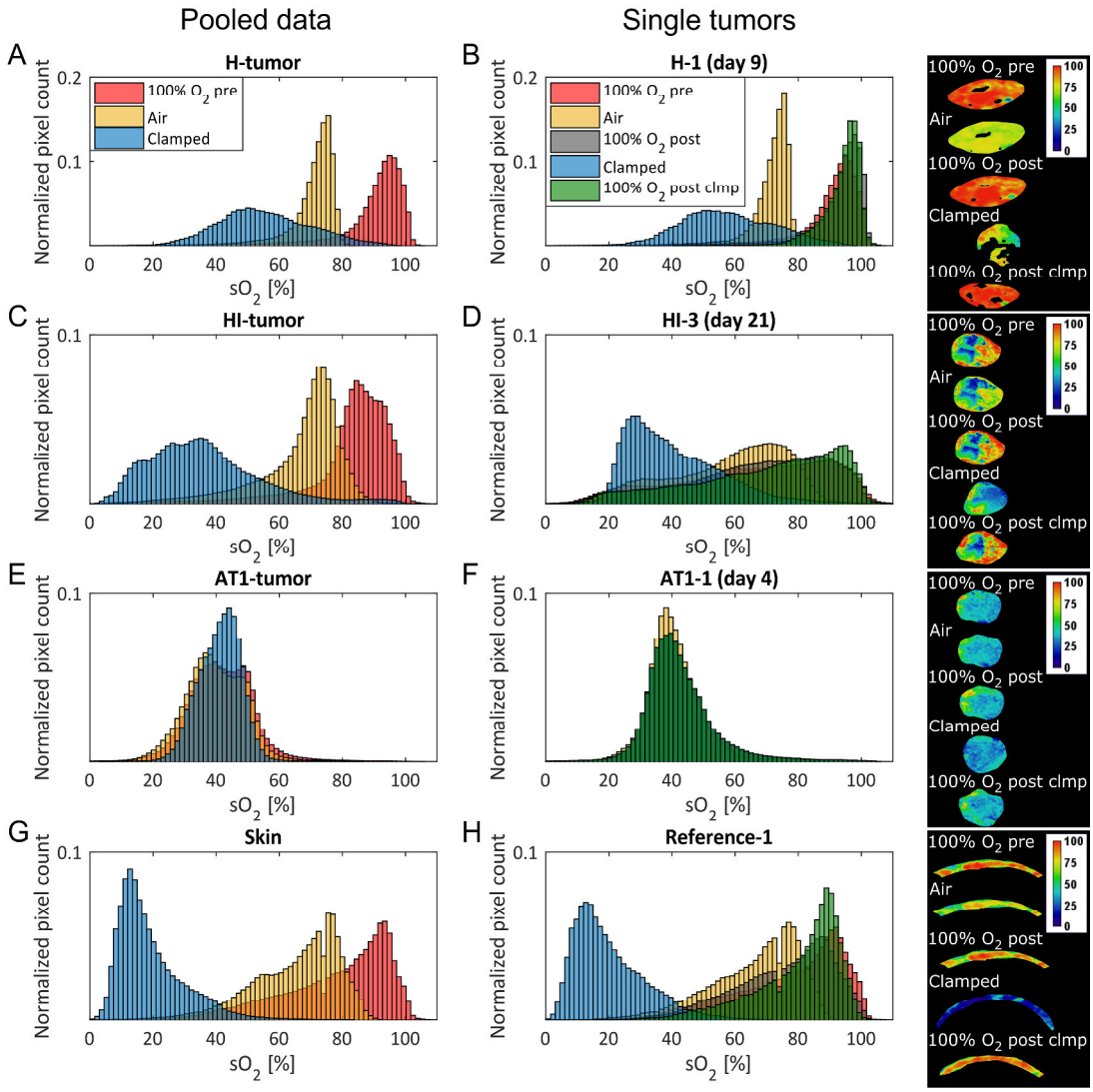

Figure 17 sO_2-distributions of oxygen challenge and clamping experiments for each of the three sublines and the skin (reference tissue). Pooled sO_2-distributions per subline and exemplary distributions of the full experiment for single animals: (A) H (20 and 50 mm^3), (C) HI (460 and 580 mm^3), (E) AT1 (330 and 460 mm^3, for the "clamped"-measurement, the distribution represents only AT1-1), and (G) the skin. Exemplary full oxygen challenge experiments performed for a single tumor per subline and the skin of one animal are shown in the middle column (B, D, F, H). The right column displays representative frames from 3D PAI sO_2 measurements which illustrate the characteristics of the response of the tumors after external changes in O_2 supply. The highly non-uniform response of the HI-tumor exhibiting regions without changes during oxygen challenge (e.g. low sO_2 region in the center of the tumor) and responding regions in the periphery of the tumor (with high initial sO_2) should be noted. Figure reproduced from [96] under the CC BY 4.0 license.

Changes of the sO_2-distributions during the oxygen challenge experiment were quantified by the similarity measure EMD (Figure 18). Using the first measurement, where animals were breathing 100 % O_2, as a reference it can be clearly seen that all other measurements with 100 % O_2 exhibit very low EMD-values (i.e. high similarity), while air breathing and even more clamping exhibited much larger values (decreasingly low similarity). The AT1-tumor

on the other hand showed no response to any external changes and their EMDs remained below 0.05 for all experiments.

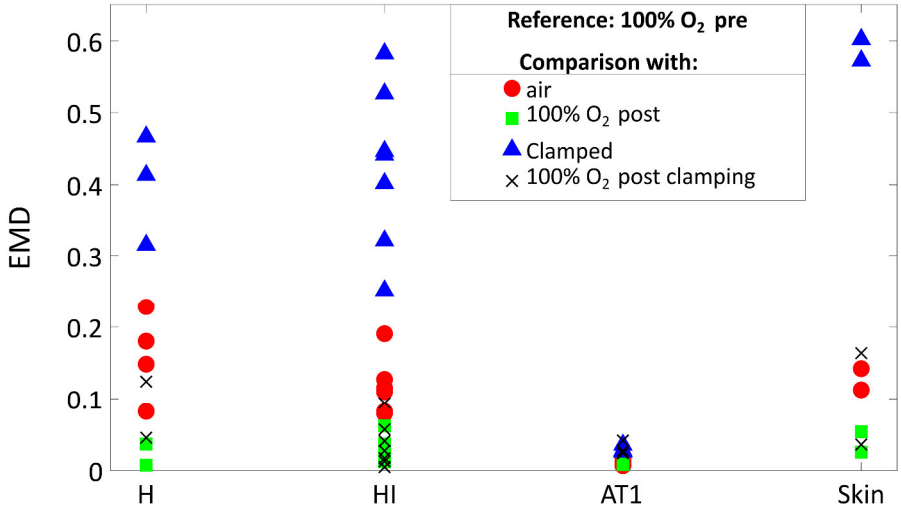

Figure 18 The similarity measure earth mover's distance (EMD) for the oxygen challenge experiment: The EMD was calculated for all sO_2-distributions measured for the three tumor sublines and the skin using the sO_2-distributions of the first measurement with 100 % O_2 ("100 % O_2 pre") as reference. Figure reproduced from [96] under the CC BY 4.0 license.

3.1.4 Histology and immunohistochemistry

After the final imaging tumors were dissected and prepared for immunohistochemistry. Figure 19 displays representative stainings of these tumors. The H-tumor showed to be highly differentiated with glandular structures comparable to normal prostate glands (Figure 19 A) and exhibited mature vessels (Figure 19 D, G). The whole tumor was well perfused, indicated by a uniformly distributed Hoechst 33342 staining. Both H-tumors exhibited only a small, locally confined hypoxic region (Figure 19 D). Apart from those locally confined areas both tumors were negative for pimonidazole.

The moderately differentiated HI-tumor contained mucin secreting glandular structures (Figure 19 B) with immature vessels, though not all of them were perfused (Figure 19 E, H). Hypoxic areas were found to surround vessels at a certain distance (Figure 19 H).

The anaplastic AT1-tumor exhibited only capillaries, but no mature vessels, and showed to be completely undifferentiated without any prostate-specific cells (Figure 19 C). The entire tumor was pervaded by very short and thin capillaries of which only a minority was perfused (mainly at the periphery of the tumor) (Figure 19 F, I). Additionally, prominent hypoxic areas were found (Figure 19 F, I).

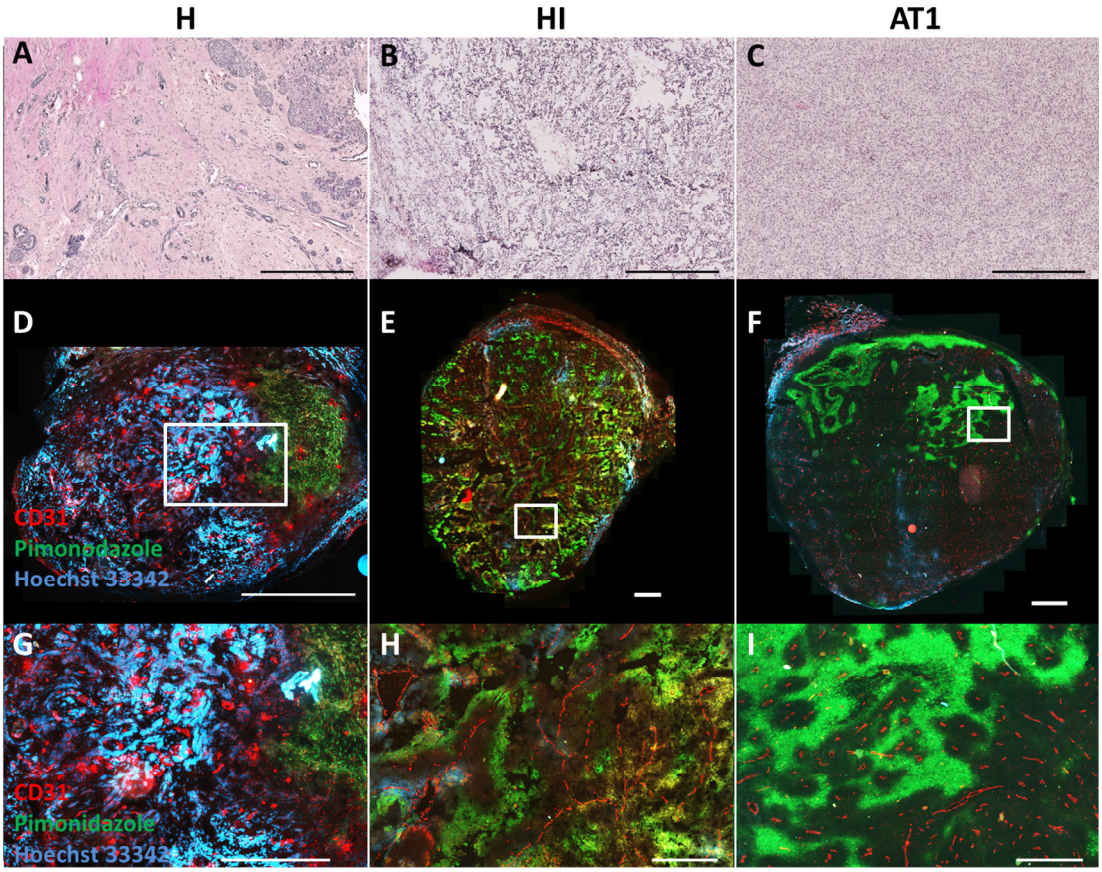

Figure 19 Histological images of the H-, HI-, and AT1-tumors (left, middle, and right column, respectively): (A - C) H&E staining revealed tumor morphology. Scale bars 500 µm. (D - F) Whole-mount fluorescence images of tumors stained for vessels (CD31, red), hypoxia (pimonidazole, green), and perfusion (Hoechst 33342, blue). Scale bars 1000 µm. (G - I) Close-ups of the marked areas in D - F. Scale bars 500 µm. Figure adapted from [96] and used under the CC BY 4.0 license.

3.2 DCE-MRI: a novel method for bolus arrival time (BAT) estimation

A new spline-based method for bolus arrival time (BAT) estimation was developed. It is required for delay correction of DCE-MRI data prior to pharmacokinetic modeling to ensure accuracy of the resulting fit parameters. This project was realized in cooperation with Dr. Martin Storath from the group for Image Analysis and Learning of the Interdisciplinary Center for Scientific Computing of Heidelberg University. The text, figures, and tables in section 3.2 and respective subsections were taken from reference [117].

3.2.1 The new approximation model for BAT estimation

The text in subsection 3.2.1 was taken from reference [117] and has been originally written jointly by Dr. Martin Storath and me. The images of the DCE-MRI measurement are as-

sumed to be acquired at time points t_n $(n = 1, 2, \dots, N)$. After a number of images, the CA is given as a bolus. In the following it is assumed that the MR-signal intensities are already converted into concentrations of the contrast agent (CA). (However, the proposed method is also applicable to the MR data before conversion to concentration.) Thus, the given data c_n are noisy samples of a true tissue concentration curve (TCC) $C(t)$:

$$c_n = C(t_n) + \epsilon_n, \qquad \text{for } n = 1, \dots, N,$$

where the ϵ_n represent error terms. For simplicity, it is focused on the case of uniformly sampled time points, i.e. $t_n = (n-1)\Delta t$, noting that the proposed method could also be extended to the more general case of unevenly sampled time points.

The goal is to estimate the BAT t_{BAT} from the noisy data c_n which is the time point where the true TCC, $C(t)$, starts to rise. It should be noted that t_{BAT} does not necessarily coincide with one of the sample time points t_n. The BAT naturally divides a TCC into two parts: Prior to the bolus arrival, the TCC is constant-valued at zero (unless previous boluses were injected), whereas after the BAT, it rises and adopts different shapes depending on the underlying physiology.

This discussion on the characteristics of a TCC motivates to approximate a TCC by a continuous function that is constant on the interval $[t_1, t_{\mathrm{BAT}}]$, and by a smooth function that is able to adapt to the concentration curve on $[t_{\mathrm{BAT}}, t_N]$. A suitable type of such smooth functions are smoothing splines (see section 2.4.4.1).

Thus, it is proposed to approximate the TCC by a function u^* that is constant until the (unknown) BAT, t_{BAT}, and a smoothing spline afterwards. The function u^* is defined by the minimizing condition

$$u^* = \underset{u}{\operatorname{argmin}} \sum_{n=1}^{N} (u(t_n) - c_n)^2 + \alpha \int_{t_{\mathrm{BAT}}}^{t_N} (u^{(k)}(\tau))^2 d\tau, \qquad (16)$$

$$\text{subject to } u \text{ is constant on } [t_1, t_{\mathrm{BAT}}].$$

A graphical illustration is given in Figure 20. As the approximation function u^* is not required to be smooth at the joint, it typically has a kink at t_{BAT}.

Since u is constant on $[t_1, t_{\mathrm{BAT}}]$, eq. (16) can be reduced to

$$\tilde{u}^* = \underset{\tilde{u}}{\operatorname{argmin}} \sum_{n=1}^{N'} (\tilde{u}(t_{BAT}) - c_n)^2 + \sum_{n=N'+1}^{N} (\tilde{u}(t_n) - c_n)^2 + \alpha \int_{t_{\mathrm{BAT}}}^{t_N} \left(\tilde{u}^{(k)}(\tau)\right)^2 d\tau, \qquad (17)$$

where N' is the index of the last time frame before t_{BAT}; that is, $N' = \max\{n: t_n \leq t_{\mathrm{BAT}}\}$. There is a simple relation between the solutions of the constrained variant in eq. (16) and that of the unconstrained variant in eq. (17):

$$u^*(t) = \tilde{u}^*(t_{\mathrm{BAT}}) \text{ for } t \in [t_1, t_{\mathrm{BAT}}] \quad \text{and} \quad u^*(t) = \tilde{u}^*(t) \text{ for } t \in (t_{\mathrm{BAT}}, t_N]. \tag{18}$$

The principal interest is to estimate the parameter t_{BAT} from the concentration curve. Alongside the estimation of t_{BAT}, the spline parameters α and k have to be determined as well because these are needed for adapting the model to the curve shape after the BAT. All three parameters will be estimated automatically (section 3.2.3).

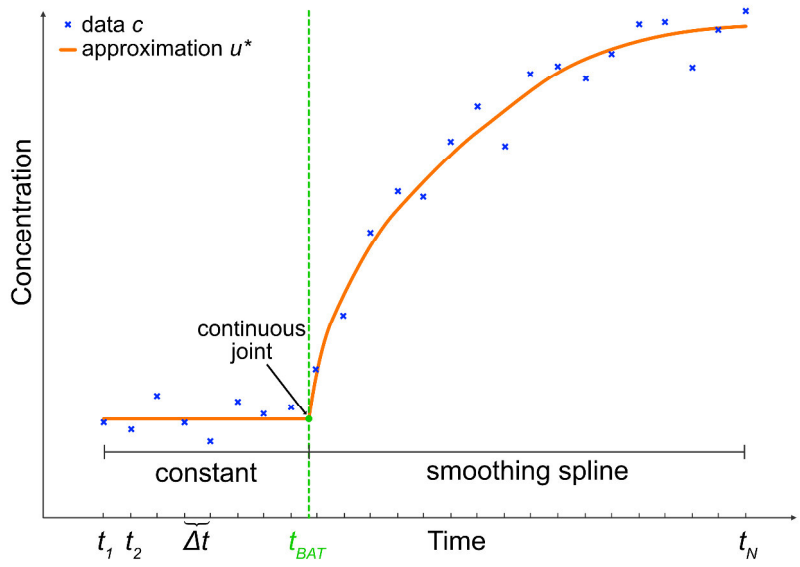

Figure 20 Graphical illustration of the proposed approximation model for bolus arrival time (BAT) estimation (eq. (16)). The given noisy TCC data (blue crosses) are approximated by a continuous piecewise defined function u^*. It is a constant function before the BAT, t_{BAT}, and afterwards a smoothing spline which is able to adapt to the shape of the curve by adjusting its stiffness parameters α and k. An estimate for t_{BAT} is determined automatically along with suitable spline stiffness parameters α and k by generalized cross validation. It should be noted that t_{BAT} does not need to coincide with one of the sample times $t_1, \dots, t_N$.

3.2.2 Discretization and computation of the approximating function

The text in subsection 3.2.2 was taken from reference [117] and has been originally written jointly by Dr. Martin Storath and me. To numerically compute the approximating functions, the optimization problem in eq. (17) is discretized. First, a finite difference approximation of the k^{th} derivative $u^{(k)}$ is employed. A natural choice for the set of discretization nodes q are the BAT and the subsequently sample time points, i.e. $q = (t_{\mathrm{BAT}}, t_{N'+1}, t_{N'+2}, \dots, t_N)$. Let $\tilde{v}$ be the vector that contains the ordinates of $\tilde{u}$ at these discretization nodes; that is, $\tilde{v}_i = \tilde{u}(q_i)$ for $i = 1, \dots, I$ with $I = N - N' + 1$. A first order finite difference approximation of the k^{th} derivative is given by

$$\tilde{u}^{(k)}(q_i) \approx \sum_{j=0}^{k-1} \omega_{ij}^{(k,t_{\mathrm{BAT}})} \tilde{v}_{i+j}, \text{ for } i = 1, \dots, I-k, \tag{19}$$

where the $\omega_{ij}^{(k,t_{\mathrm{BAT}})} \in \mathbb{R}$ are weights which are specified in the following. First, note that the weights depend on t_{BAT} because the first discretization node coincides with t_{BAT}. Determining the weights $\omega_{ij}^{(k,t_{\mathrm{BAT}})}$ is a standard procedure; see e.g. [155]. Further, the integral in eq. (17) is approximated by a Riemannian sum. In summary, the following discretized problem is obtained:

$$\begin{aligned} \tilde{v}^* = \underset{\tilde{v}\in\mathbb{R}^I}{\operatorname{argmin}} & \sum_{n=1}^{N'} (\tilde{v}_1 - c_n)^2 + \sum_{n=N'+1}^{N} (\tilde{v}_{n-N'+1} - c_n)^2 \\ & + \alpha \sum_{i=1}^{I-k} (q_{i+1} - q_i) \left(\sum_{j=0}^{k-1} \omega_{ij}^{(k,t_{\mathrm{BAT}})} \tilde{v}_{i+j} \right)^2 . \end{aligned} \tag{20}$$

Just as $\tilde{v}^*$ is a discrete approximation to the continuous function $\tilde{u}^*$, the expanded vector $v^* = (\tilde{v}_1^*, \dots, \tilde{v}_1^*, \tilde{v}_2^*, \dots, \tilde{v}_I^*)$ (of length N) is a discrete approximation to u^*.

Eq. (20) is a least squares problem in $\tilde{v}$. Reformulated in matrix notation:

$$\tilde{v}^* = \underset{\tilde{v}\in\mathbb{R}^I}{\operatorname{argmin}} \ \|B\tilde{v} - c\|^2 + \alpha \|W\Omega\tilde{v}\|^2 \tag{21}$$

where $\|v\|^2$ denotes the squared Euclidean norm, $\|v\|^2 = \sum_n v_n^2$, and the involved matrices are as follows. W is a diagonal matrix with the entries $W_{ii} = \sqrt{q_{i+1} - q_i}$ for $i = 1, \dots, I-k$. The matrix $B \in \mathbb{R}^{N\times I}$ is defined by

$$B = \begin{bmatrix} \mathbf{1}_{N'-1} e_1^T \\ E_I \end{bmatrix}, \tag{22}$$

where $\mathbf{1}_{N'-1} = (1, \dots, 1)^T$ denotes a vector of $(N'-1)$ ones, $e_1^T = (1, 0, \dots, 0)$ is the first unit vector in $\mathbb{R}^{N'-1}$ and E_I is the identity matrix of size I. Further, Ω implements the discrete approximation to the k^{th} derivative given in eq. (19). It is explicitly given by $\Omega_{i,i+j} = \omega_{ij}^{(k,t_{\mathrm{BAT}})}$ for $i = 1, \dots, I, j = 0, \dots, k-1$, and zero otherwise. For readability, the dependence of the involved matrices on t_{BAT} and k are omitted in the following notation.

A standard computation (differentiation of the functional in eq. (21) with respect to $\tilde{v}$ and setting it equal to zero) reveals that $\tilde{v}^*$ is the solution of the linear system

$$(B^T B + \alpha (W\Omega)^T W\Omega)\tilde{v}^* = B^T c. \tag{23}$$

Solving this equation for $\tilde{v}^*$ and using the relation $v^* = B\tilde{v}^*$ gives the explicit solution

$$v^* = H^{(t_{\mathrm{BAT}},\alpha,k)} c, \tag{24}$$

where $H^{(t_{\mathrm{BAT}},\alpha,k)} \in \mathbb{R}^{N\times X}$ is the influence matrix given by

$$H^{(t_{\mathrm{BAT}},\alpha,k)} = B(B^T B + \alpha(W\Omega)^T W\Omega)^{-1}B^T \,. \tag{25}$$

H depends on t_{BAT}, on α, and on k because the right hand side in eq. (25) does so.

3.2.3 Parameter estimation by generalized cross validation

The text in subsection 3.2.3 was taken from reference [117] and has been originally written jointly by Dr. Martin Storath and me. The principal interest is to determine the BAT by estimating the parameter t_{BAT}. For this, the spline parameters α and k need to be estimated as well, because these affect the adaption of the model to the curve shape after the BAT. A widely used approach for determining such parameters is generalized cross validation (GCV) [125, 156] which has shown to provide good performance for spline-based estimators [157, 158]. The GCV score is a ratio of the mean squared error (MSE), given by $\|v^* - c\|^2/N$, and a quantity based on the degrees of freedom (DOF) of the estimator. As the proposed model leads to a linear estimator, the DOF coincide with the trace of the influence matrix $H^{(t_{\mathrm{BAT}},\alpha,k)}$. Thus, the GCV score has the explicit form

$$\mathrm{GCV}(c; t_{\mathrm{BAT}}, \alpha, k) = \frac{\mathrm{MSE}}{\left(1 - \frac{1}{N}\mathrm{DOF}\right)^2} = \frac{\frac{1}{N}\left\|H^{(t_{\mathrm{BAT}},\alpha,k)}c - c\right\|^2}{\left(1 - \frac{1}{N}\,\mathrm{trace}\, H^{(t_{\mathrm{BAT}},\alpha,k)}\right)^2}. \tag{26}$$

The optimal set of parameters $(t^*_{\mathrm{BAT}}, a^*, k^*)$ in the sense of GCV is the one that provides the minimum GCV score:

$$(t^*_{\mathrm{BAT}}, a^*, k^*) = \underset{t_{\mathrm{BAT}},\alpha,k}{\mathrm{argmin}}\, \mathrm{GCV}(c; t_{\mathrm{BAT}}, \alpha, k)\,, \tag{27}$$

where t_{BAT} is searched in the continuous interval $[t_1, t_{N-k}]$, α in the continuous interval $[0, \infty)$, and k in a set of positive integers $\{k_{\min}, \dots, k_{\max}\}$. For the considered TCCs, $k_{\min} = 3$ and $k_{\max} = 6$ gave satisfactory results. A minimizer t^*_{BAT} is the proposed estimate of BAT. Further technical information can be found in reference [117]. A reference implementation is provided online at https://github.com/mstorath/DCEBE.

3.2.4 Assessment of BAT estimation accuracy on simulated data

The text, tables, and figures in subsection 3.2.4 and respective subsections were taken from reference [117] and have been originally written and created by myself.

3.2.4.1 BAT estimation on simulated rat data

BAT estimation accuracy of the new method was evaluated on data that was simulated with the impulse response functions of the extended Tofts model (ETM) and the two compartment exchange model (2CXM) providing data with known ground truth (section 2.4.4.2). Exem-

plary fits by the proposed method to one TCC type for all temporal resolutions and noise levels are displayed in Figure 21. Results for all TCCs and all configurations are displayed in Figure 22 along with the results from the state-of-the-art method by Cheong *et al.* [123].

Cheong's method provided accurately estimated BATs for AIFs with high temporal resolutions. The accuracy was diminished for AIFs with low temporal resolutions. For curves with a less significant peak in the vicinity of the BAT, such as TCC type 3 for the ETM and TCC type 1 for the 2CXM, the estimated BATs were relatively far off the ground truth and were scattered over a wide range. Cheong's method gave poor results for estimated BATs of the remaining TCCs.

The proposed method gave comparable results for the AIFs at high temporal resolutions and performed better for the AIFs at the lowest temporal resolution. For the TCCs, the proposed method could precisely estimate BATs of all shapes, and the results were robust towards increased noise levels and low temporal resolution of the input data. In most cases, the estimated BATs did not exhibit much variability as indicated by the small range between the 5 % and 95 % percentiles. A slight overestimation of BATs was observed for TCCs simulated with the 2CXM, which exhibited a shallow initial rise in concentration. In almost all configurations the proposed method significantly improved the accuracy of BAT estimation upon the state-of-the-art method for the tested TCCs.

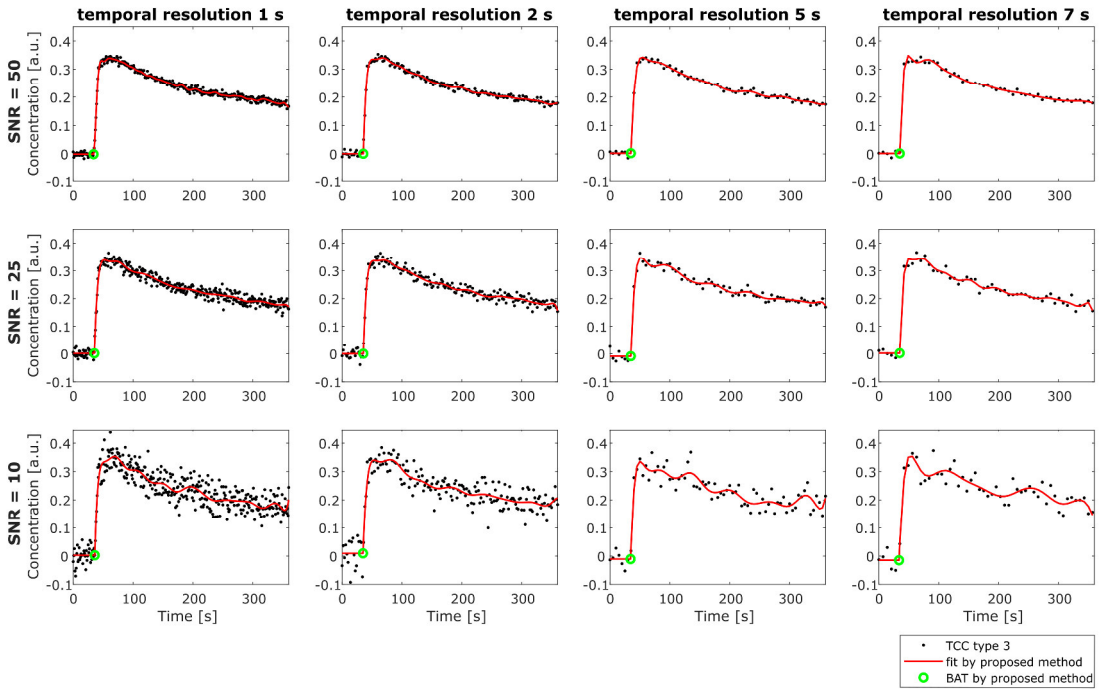

Figure 21 Exemplary results for BAT estimation in rats: type 3 TCCs (black dots) simulated with the extended Tofts model (ETM) are displayed for all temporal resolutions (columns) and signal-to-noise ratios (SNRs, rows) together with the respective fit by the proposed method (red line) and estimated BAT (green circle).

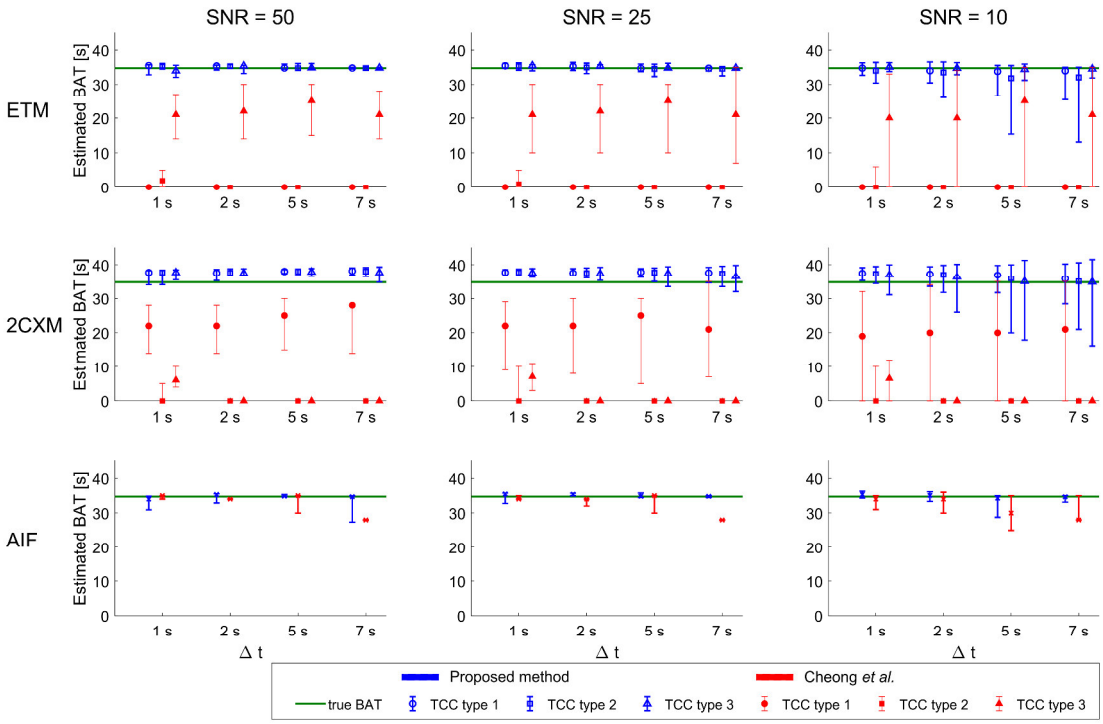

Figure 22 Illustration of the accuracy of BAT estimation for rat data simulated with the ETM and the 2CXM, varied for various signal-to-noise ratios (SNRs) and temporal resolutions (Δ t). Results are presented as medians with 5 % and 95 % percentiles of 1000 repetitions of BAT estimation per TCC type with the proposed method (blue symbols) and Cheong's method (red symbols). The green line indicates the true BAT.

3.2.4.2 BAT estimation on simulated patient data

The BAT estimation accuracy was also tested on simulated patient data and was compared to the BATs estimated by Cheong's method (Figure 23). Cheong's method gave accurately estimated BATs with only small variation for low temporal resolution TCCs. Some major variation in the obtained results could only be observed for data simulated with the 2CXM at the lowest SNR. Cheong's method performed equally well for all simulated patient TCCs.

The proposed method gave results close to the ground truth with a slight overestimation of BATs for low SNR TCCs and data simulated with the 2CXM. Thus, for patient data, the proposed method gave competitive results, yet Cheong's method performed slightly better.

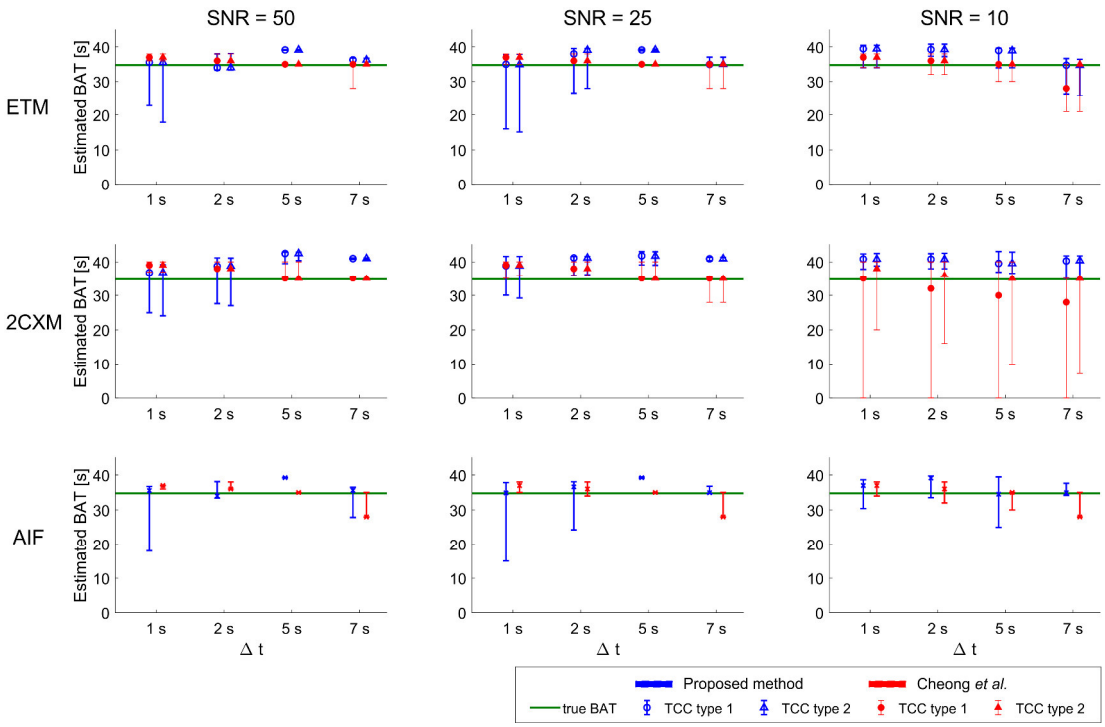

Figure 23 Illustration of the accuracy of BAT estimation for patient data simulated with the ETM and the 2CXM, varied for various signal-to-noise ratios (SNRs) and temporal resolutions (Δ t). Results are presented as medians with 5 % and 95 % percentiles of 1000 repetitions of BAT estimation per TCC type with the proposed method (blue symbols) and Cheong's method (red symbols). The green line indicates the true BAT.

3.2.5 Assessment of BAT estimation accuracy on *in vivo* data

The text, tables, and figures in subsection 3.2.5 were taken from reference [117] and have been originally written and created by myself.

Finally, the proposed method for BAT estimation was validated on *in vivo* DCE-MRI data of five HI-tumor bearing rats from the longitudinal DCE-MRI study (section 2.5.2). The BATs were estimated for each voxel of the ten tumors (Table 8). DCE-MRI curves of animal 2 with estimated BATs for both tumors and the AIF are displayed as exemplary results in Figure 24.

The compared methods estimated virtually identical BATs for the rats' AIFs (Table 8 right column, Figure 24 E, F). However, for the TCCs the BATs estimated by Cheong's method are implausible as almost all of them were estimated to occur even before the lower bound of injection times. The adapted version of Cheong's method which excludes implausible sample points below the lower bound of 25.37 s for BAT estimation (see section 2.4.4.3) resulted in this lower bound in most cases. However, visual inspection reveals that the TCCs did not rise significantly before approximately 35 s. This means that the results of the adapted version remained uninformative in most cases.

The BATs estimated by the proposed methods were very close to each other within one animal and appeared to be at reasonable time points by visual inspection (Table 8, Figure 24 A - D). Despite the noticeable variation in TCC shapes occurring even within one tumor, the proposed method fitted all curves equally well and estimated reasonable BATs. It is noted that the proposed method does not require a lower bound of injection times as *a priori* information.

Table 8 Estimated BATs for five HI-tumor bearing rats of the longitudinal DCE-MRI study (in seconds) by Cheong's original and adapted approach and the proposed method. For the tumor TCCs, the medians and 5 % and 95 % percentiles are reported. The second and the third column indicate the number of evaluated voxels (i.e. TCCs) in the right and in the left tumor, respectively. For Cheong's adapted method a plausible lower boundary of 25.37 s was chosen. Table reproduced from [117].

Animal	M_R	M_L	Method	Right tumor	Left tumor	AIF
1	18	94	Cheong *et al.*	0.00 [0.00, 4.93]	0.00 [0.00, 6.57]	34.33
			Cheong *et al.* (adapt.)	25.37 [25.37, 25.37]	25.37 [25.37, 25.37]	34.33
			Proposed	37.13 [36.24, 37.77]	36.63 [35.64, 37.75]	34.36
2	13	39	Cheong *et al.*	0.00 [0.00, 19.93]	0.00 [0.00, 11.42]	32.09
			Cheong *et al.* (adapt.)	25.37 [25.37,128.77]	25.37 [25.37, 25.37]	32.09
			Proposed	36.17 [35.14, 37.29]	35.54 [34.61, 36.19]	32.04
9	7	31	Cheong *et al.*	0.00 [0.00, 0.00]	0.00 [0.00, 6.68]	32.84
			Cheong *et al.* (adapt.)	25.37 [25.37, 25.37]	25.37 [25.37, 25.37]	32.84
			Proposed	35.47 [34.88, 36.04]	35.41 [34.60, 36.60]	32.82
12	32	26	Cheong *et al.*	0.00 [0.00, 0.00]	0.00 [0.00, 4.63]	33.58
			Cheong *et al.* (adapt.)	25.37 [25.37, 25.37]	25.37 [25.37, 25.37]	33.58
			Proposed	36.90 [35.00, 38.28]	36.81 [35.94, 37.86]	33.81
13	13	7	Cheong *et al.*	0.00 [0.00, 13.92]	0.00 [0.00, 14.18]	30.60
			Cheong *et al.* (adapt.)	25.37 [25.37, 25.37]	25.37 [25.37, 25.37]	30.60
			Proposed	33.32 [33.04, 34.10]	33.47 [33.22, 33.86]	30.50

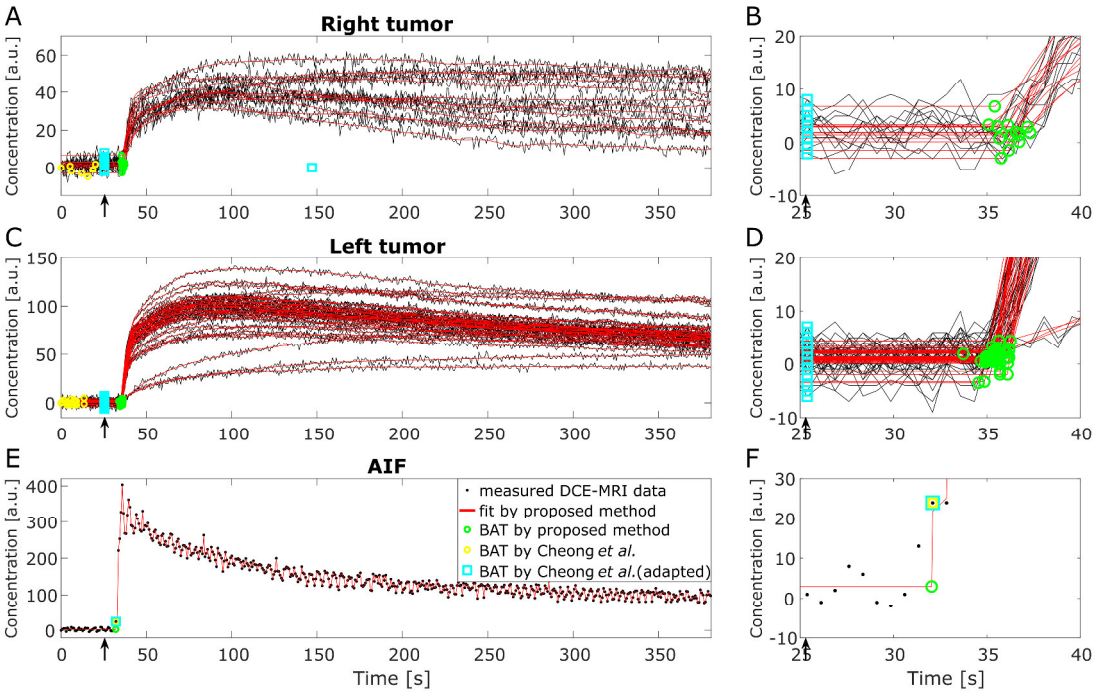

Figure 24 Exemplary pixel-based concentration curves of animal 2 with HI-tumors: (A) right tumor with close-up of the BAT region (B); (C) left tumor with close-up of the BAT region (D); (E) AIF and close-up of the BAT region (F). BATs estimated by the proposed method, by Cheong's original approach, and by Cheong's adapted approach are marked by green and yellow circles and blue squares, respectively. The black arrows indicate the lower boundary used for the injection times (needed for the adapted version of Cheong's method). ©Institute of Physics and Engineering in Medicine. Reproduced with permission from [117]. All rights reserved.

3.3 Longitudinal DCE-MRI study of the AT1-tumor after irradiation

A longitudinal DCE-MRI study was performed to gain initial quantitative information on the impact of high single dose ^{12}C-ion irradiation compared to photon irradiation on vascular damage and perfusion in the anaplastic AT1-tumor (section 2.5.1). The experiments had been planned and conducted by Dr. Christin Glowa while the evaluation of the data has been performed by myself. The text and figures in section 3.3 und respective subsections were taken from reference [135] and have been originally written and created by myself.

3.3.1 Tumor growth after irradiation

Non-irradiated control tumors grew rapidly reaching more than 9 times their initial volume after 21 days (Figure 25). After RT, tumor volumes increased further until day 7 for all treatment groups before their growth stagnated.

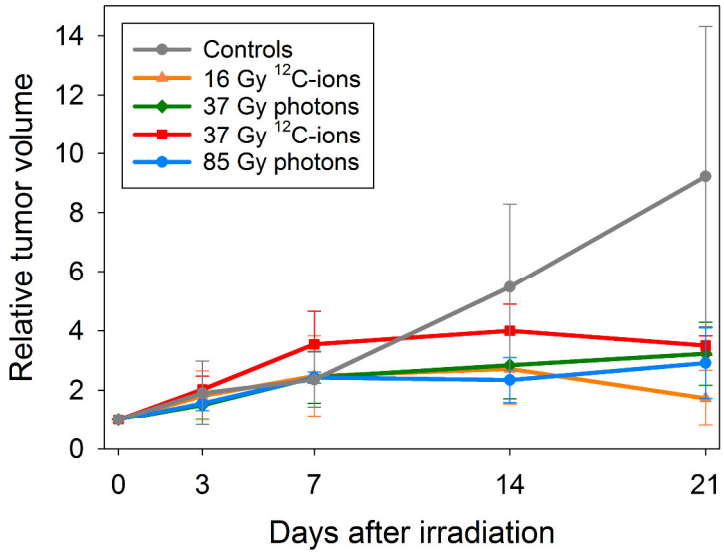

Figure 25 Relative tumor volumes of AT1-tumors up to 21 days after irradiation with either photons or ^{12}C-ions derived from $T2$-weighted images. Tumor volumes were pooled, i.e. n = 3 for treatment groups and n = 12 for control groups per time point. The field of view for $T2$-weighted imaging was kept at constant size over all measurements which resulted in control tumors exceeding the field of view at the last imaging time point. Hence, reported control tumor sizes are underestimated. Data is displayed as mean ± standard deviation. Figure reproduced from [135]. Data was acquired by Dr. Christin Glowa.

3.3.2 Non-compartment analysis and pharmacokinetic modeling

DCE-MRI data was fit with the ETM as described in sections 2.4.6 and 2.4.7. 21 days after RT, control tumors had developed central non-perfused areas like the area of no CA enhancement in the $T1$-weighted images and the deep blue voxels in the tumor parameter maps (Figure 26). At this time point parameter maps of photon treated tumors were rather heterogeneous compared to the ^{12}C-ion treated groups.

Non-irradiated control tumors experienced decrease in all four parameters (normalized AUC, K_{trans}, v_{e}, and v_{p}) over the five imaging time points (Figure 27) and exhibited significantly different parameter distributions than the treated tumors (see Appendix A.1, Table 9, for detailed results of statistical analyses). This decrease was especially apparent in K_{trans} and v_{p}.

Overall, irradiated tumors experienced an increase in normalized AUC over the observation period (Figure 27 A). 3 days after RT the normalized AUC in ^{12}C-ion treated tumors increased significantly as compared to the controls and the photon treated groups whose increase was prolonged to day 7 (37 Gy) or day 21 (85 Gy) after RT. This delay in treatment response was even more distinct in the temporal development of the parameter K_{trans} comprising perfusion and permeability (Figure 27 B). ^{12}C-ions induced strong changes indicated

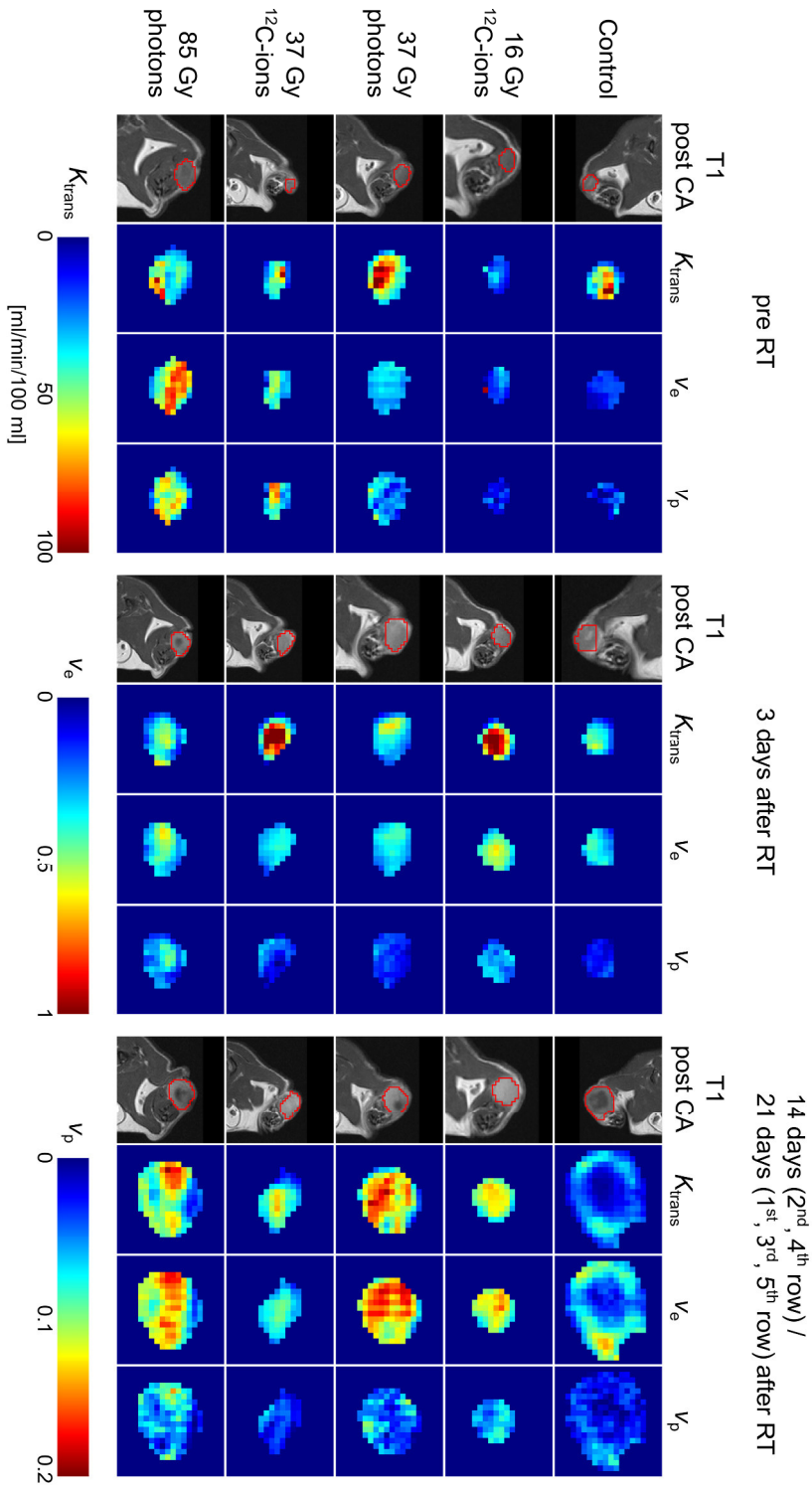

Figure 26 $T1$-weighted MR-images of AT1-tumors after contrast agent injection along with their calculated ETM parameter maps from DCE-MRI measurements for one representative tumor per group at three designated time points. For this illustration, some 21 day results had to be replaced by 14 day results as the corresponding 21 day results suffered from measurement artefacts. K_{trans} = volume transfer constant, v_e = extravascular, extracellular volume fraction, v_p = plasma volume fraction. Figure reproduced from [135]. Measurements were performed by Dr. Christin Glowa.

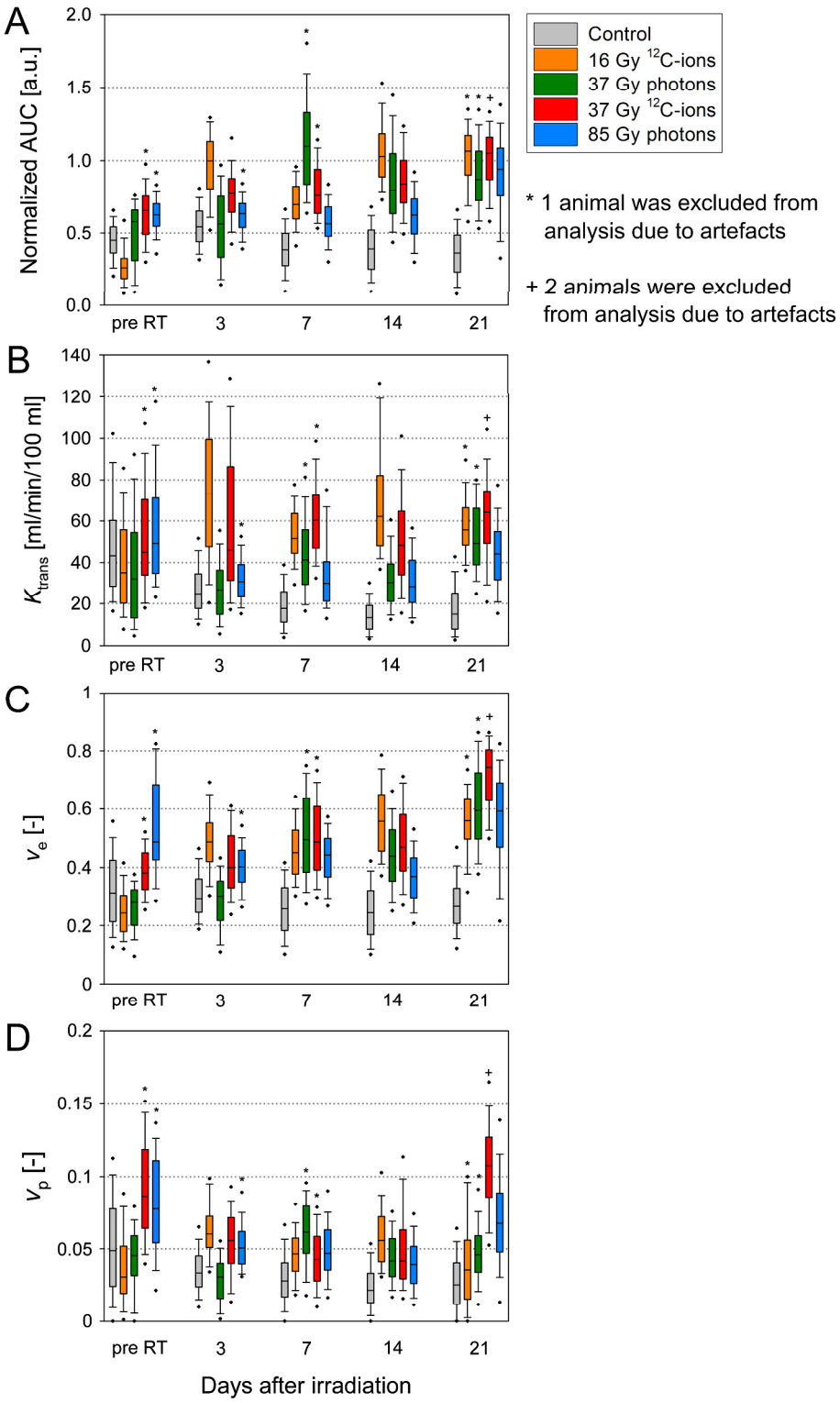

Figure 27 Pooled longitudinal results of voxel-wise non-compartment analysis and pharmacokinetic modeling after irradiation for 3 AT1-tumors per treatment group and 12 controls. Estimated parameters are (A) the normalized area under the curve (AUC), (B) the volume transfer constant K_{trans}, (C) the extravascular, extracellular volume fraction v_e, and (D) the plasma volume fraction v_p. Box plots (25/75 % percentiles) are displayed with medians (line), 10/90 % percentiles (whiskers), and 5/95 % percentiles (dots). Figure adapted from [135].

by significantly increased K_{trans} values already 3 days after RT. The large variations in parameters at this time point, i.e. the wide boxes, reflect the intra-tumor variability (Figure 26) and the fact that one out of three animals for both ^{12}C-ion treated groups did not exhibit an increase in K_{trans} values 3 days after RT (see tumors 14 and 20 in Appendix A.2, Figure 53). Photon treated tumors of both dose groups exhibited constant K_{trans} values until 14 days after RT that only increased to levels comparable to those of ^{12}C-ion treated tumors after 21 days when differences between treatment groups became insignificant.

The low dose ^{12}C-ion group showed the earliest increase in v_e at day 3, followed by the two 37 Gy dose groups (7 days after RT), and the latest response by the 85 Gy photon group at day 21 after RT (Figure 27 C). At the last imaging time point, the photon treated tumors exhibited a broader range of v_e values than ^{12}C-ion treated tumors. Except for the two high dose groups, all treatment groups exhibited comparable v_e distributions.

The vascular fraction v_p exhibited plausible values, however, without apparent temporal changes (Figure 27 D). The 37 Gy ^{12}C-ion and the 85 Gy photon treated groups exhibited slightly increased but significantly different values compared to the other groups at the final imaging time point, that were comparable to their pre-treatment values.

Altogether, photon treated tumors exhibited a delay in treatment response in all parameters as compared to ^{12}C-ions. It is noticeable that all treatment groups experienced comparable parameter values for normalized AUC, K_{trans}, and v_e at the end of the observation period regardless of applied dose and RT modality (Figure 27 and Appendix A.1, Table 9).

Temporal development of fit parameters was also analyzed for each animal individually to ensure that groups exhibited a uniform treatment response (Appendix A.2, Figure 53). One tumor (tumor 23) treated with 85 Gy photons differed from the rest of its group in all measurements and was thus excluded from the pooled histological analyses. Histological results for tumor 23 can be found in the Appendix A.3, Figure 54.

3.3.3 Histology 21 days after irradiation

3.3.3.1 AT1-tumor morphology

H&E staining revealed that 21 days after RT, non-irradiated controls exhibited very dense and heterogeneous tissue structures with large fiber-rich and cell-depleted areas infiltrated with lymphocytes, as well as necrotic areas seamed by irregularly shaped cells (Figure 28 A). ^{12}C-ion treated tumors exhibited loosened, homogeneous tissue structures infiltrated by lymphocytes at 21 days after RT. There were no signs of necrosis (Figure 28 B, D). In contrast, photon treated tumors exhibited more heterogeneous tissue structures, consisting of loosened tumor tissue infiltrated by lymphocytes and intermitted by areas with developing necrosis that was surrounded by enlarged and highly irregularly shaped cells (Figure 28 C, E). Enlarged cells were found independent of radiation dose and quality.

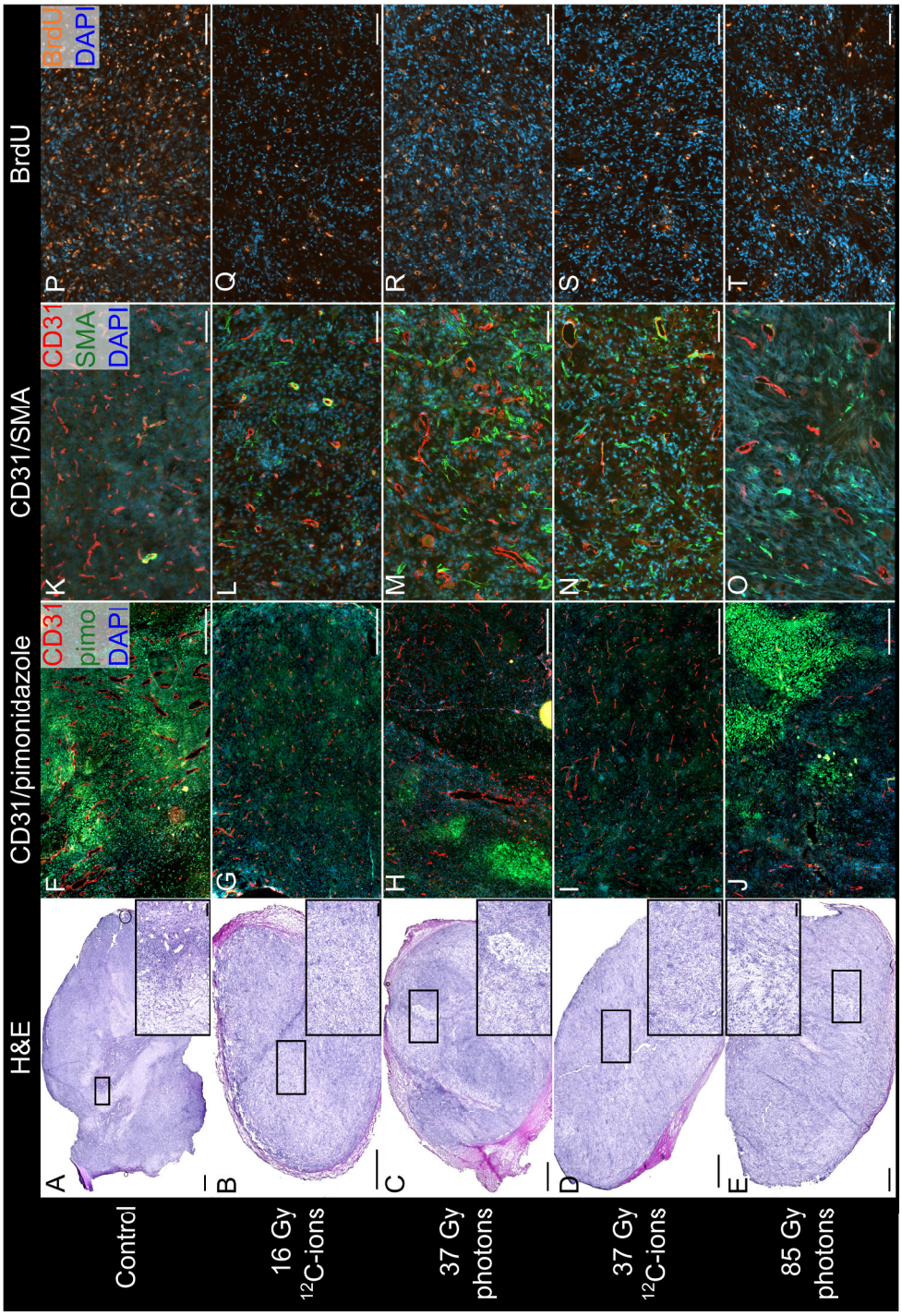

Figure 28 Histological images of AT1-tumors 21 days after irradiation with either photons or ^{12}C-ions and non-irradiated controls. (A - E) Tumor morphology was assessed by H&E staining. Whole-mount images (scale bars 1000 µm) with close-ups (scale bars 200 µm) of the marked areas are displayed. (F - J) Fluorescence images of CD31 (vessels, red), pimonidazole (hypoxia, green), and DAPI (cell nuclei, blue) stained AT1-tumors. Scale bars 500 µm. (K - O) Fluorescence images of CD31, SMA (smooth muscle actin (pericytes), green) and DAPI stained AT1-tumors to assess vessel maturity. Scale bar 200 µm. (P - T) Proliferation was detected via BrdU incorporation (orange) relative to the whole cell count (DAPI). Scale bar 200 µm. Figure reproduced from [135].

3.3.3.2 Vascular density and maturity

Control tumors exhibited the highest microvascular density (Figure 29 A), but the lowest vessel maturity (Figure 29 B). The second highest microvascular density was found in the 37 Gy ^{12}C-ion treated tumors, followed by the 16 Gy ^{12}C-ion group (Figure 29 A). Photon treated tumors exhibited least microvessels. Differences between the control group and all treated groups except the 37 Gy ^{12}C-ion group were significant for vascular density in the rim. Vessel maturity (CD31$^+$/SMA$^+$-structures) was comparably low between the two dose groups and the two modalities (Figure 28 K - O, Figure 29 B). The difference between the rim and core density of CD31$^+$/SMA$^+$-structures was only significant for the control group.

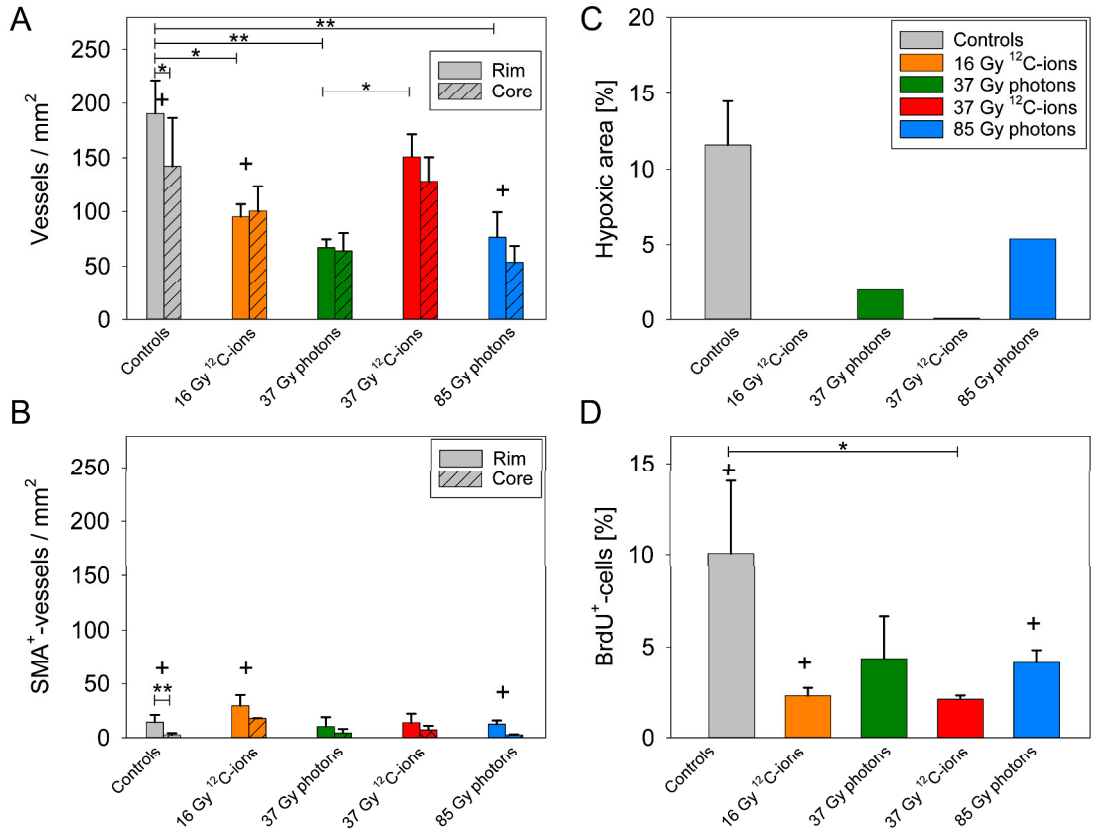

Figure 29 Quantitative results of immunohistochemistry stainings of AT1-tumors 21 days after irradiation with either photons or ^{12}C-ions. (A) Microvascular density calculated as the number of CD31$^+$-vessel structures exceeding an area of 21.125 µm^2 (50 pixels). Tumor sections were separated into a rim (outer 1 mm) and core (remaining inner area) region. (B) Vessel maturity was assessed for tumor rim and core by the number of vessels that co-expressed CD31 and SMA. (C) Percentage of hypoxic area compared to the total tumor area was assessed for one animal per dose group. (D) Proliferative activity was marked by BrdU incorporation in relation to the overall cell count. + One animal had to be excluded from the analysis due to complications during tumor dissection. In the 85 Gy photon group tumor 23 was excluded from analysis. * $p < 0.05$, ** $p < 0.001$. Data is displayed as mean ± standard deviation. Figure adapted from [135].

Staining for endothelial cells and pericytes showed small partially SMA^+-capillaries with a clearly identifiable lumen in the treated tumors (Figure 30 B - E, arrow heads) which were rarely seen in non-irradiated controls at 21 days (Figure 30 A).

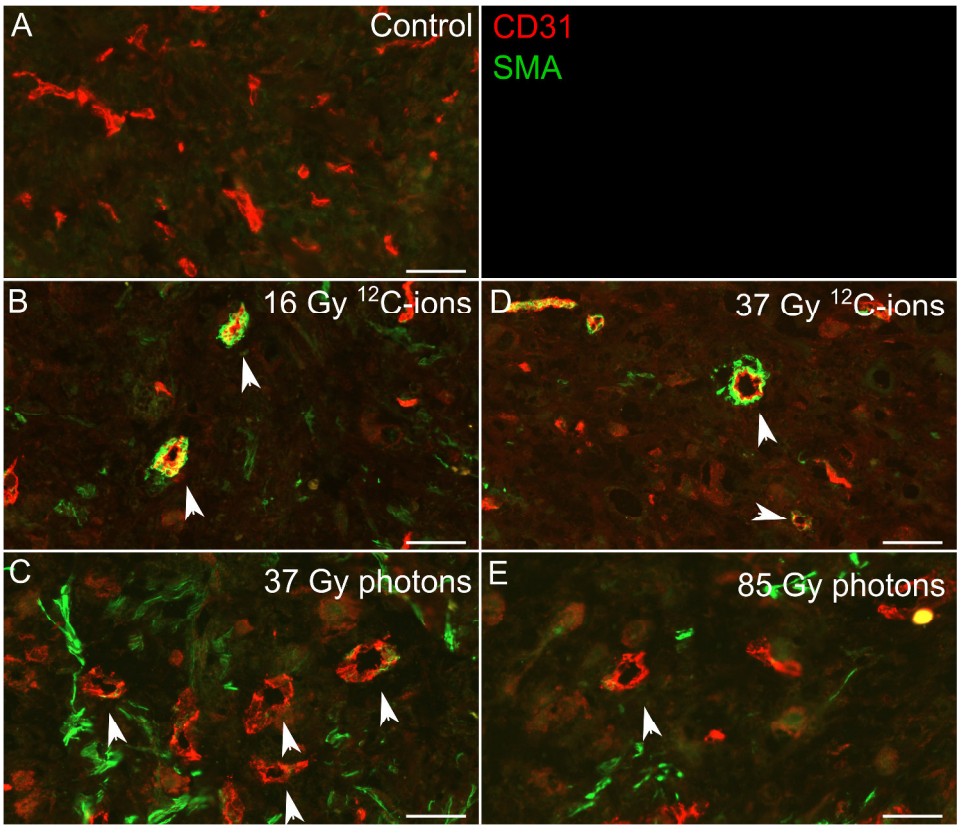

Figure 30 Fluorescence images of AT1-tumors stained for CD31 and SMA. (A) Control tumors exhibited tiny capillaries (CD31, red) without pericyte (SMA, green) coverage while (B - E) small, fully or partially SMA^+-capillaries with clearly identifiable lumen were found in treated tumors (arrow heads). Scale bars 50 µm. Figure adapted from [135].

In non-irradiated controls, locally concentrated capillaries with relatively large diameters and slim endothelial linings were found primarily in the vicinity of hypoxic areas and tissue areas undergoing necrosis (Figure 31 A). These capillaries exhibited inner diameters of up to 300 µm and deviated from the otherwise tiny AT1 characteristic microvessels (Figure 31 B). Few capillaries with large diameters were also found in photon treated tumors, though with a partially disrupted CD31-lining.

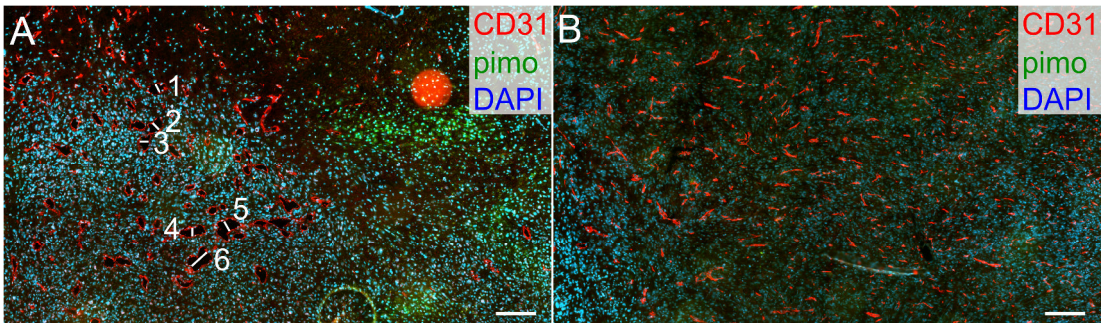

Figure 31 Fluorescence images of AT1-tumors stained for CD31 and pimonidazole. (A) In control tumors, capillaries (CD31, red) with exceptionally large diameters were found in the vicinity of on-setting necrosis (area with few $DAPI^+$-cells (blue) in upper part) and hypoxic areas (pimonidazole (pimo, green) in right part). Some of the diameters were measured: (1) 53 µm, (2) 47 µm, (3) 48 µm, (4) 44 µm, (5) 58 µm, (6) 102 µm. Scale bar: 200 µm. (B) Area of the same tumor with tiny and chaotic capillaries that are characteristic for the AT1-tumor. Scale bar: 200 µm. Figure adapted from [135].

3.3.3.3 Tumor hypoxia

One animal per dose group was injected with pimonidazole as described in section 2.6.2.5. Control tumors exhibited the highest hypoxic fraction (Figure 28 F, Figure 29 C). ^{12}C-ion treated tumors comprised no hypoxic areas (Figure 28 G, I, Figure 29 C) while photon treated tumors exhibited very low hypoxic fractions (< 7 %, Figure 28 H, J, Figure 29 C).

3.3.3.4 Proliferative activity

Non-irradiated control tumors exhibited the highest proliferative activity with approximately 10 % proliferating cells (Figure 28 P, Figure 29 D). The proliferation rate in treated tumors was generally rather low, but slightly higher after photons than after ^{12}C-ions, irrespective of the applied dose (Figure 28 Q - T, Figure 29 D). Significance was only reached between the control group and the 37 Gy ^{12}C-ion group. For ^{12}C-ion treated tumors, $BrdU^+$-cells were distributed homogeneously throughout the tumor sections, while they followed the pattern of on-setting necrosis in photon treated tumors leading to a rather heterogeneous distribution of $BrdU^+$-cells.

3.4 Longitudinal DCE-MRI study of the HI-tumor after irradiation

Longitudinal DCE-MRI experiments were conducted to compare the impact of high dose ^{12}C- ion and photon irradiation on vascular permeability in the moderately differentiated and acute hypoxic HI-tumor (section 2.5.2). The experiments had been planned and conducted by Dr. Christin Glowa while the development of the evaluation strategy as well as the evaluation of the data itself had been performed by myself.

The text and figures in section 3.4 and respective subsections were taken from reference [136] and have been originally written by myself.

3.4.1 Tumor growth after irradiation

During the observation period of three weeks the volume of non-irradiated control tumors increased almost tenfold (Figure 32). The volume of treated tumors increased until 3 days after RT and declined or remained constant thereafter for all treatment groups. It has to be noted that the further increase in the 75 Gy photon group results from a single tumor that continued growing after irradiation although its growth rate was decreased.

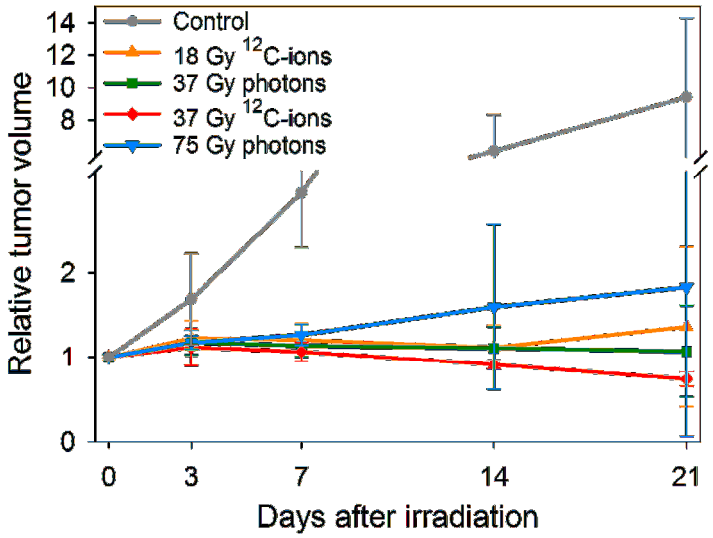

Figure 32 Relative tumor volumes of HI-tumors up to 21 days after irradiation with either photons or ^{12}C-ions derived from *T*2-weighted images. Tumor volumes were pooled per group and time point (n = 3 for 75 Gy photons, n = 4 for 18 Gy ^{12}C-ions and 37 Gy photons, n = 5 for 37 Gy ^{12}C-ions, n = 16 for controls). The field of view for *T*2-weighted imaging was kept at constant size over all measurements which resulted in control tumors exceeding the field of view at the last imaging time point. Hence, reported control tumor sizes are underestimated. Data is displayed as mean ± standard deviation. Figure reproduced from [136]. Data was acquired by Dr. Christin Glowa.

3.4.2 Pharmacokinetic modeling of DCE-MRI data

DCE-MRI data was fit with the ETM as described in sections 2.4.6 and 2.4.7. The pharmacokinetic parameters K_{trans}, v_e, and v_p of the different groups and time points revealed no significant differences (Appendix A.4, Figure 55). This finding reflects neither the observed morphological changes in the images, nor the histological changes at the end of the observation period. Therefore, DCE data was further analyzed by principle component analysis (PCA).

3.4.3 Principle component analysis and Gaussian mixture modeling

Based on the loading matrix of the first two principle components (PCs) of the PCA, the tumors' voxels were separated into five cluster. Each of the five cluster is characterized by an average concentration-time curve (Figure 33 A) and a corresponding characteristic set of ETM parameters (Figure 33 B). Cluster 1 (blue) comprises concentration-time curves with a high initial increase followed by a rapid decrease described by high K_{trans}, high v_e, and high v_p values. The average concentration-time curve of cluster 2 (red) exhibits a lower initial concentration maximum and a slightly shallower decrease as compared to the curve of cluster 1. The curve of cluster 3 (yellow) exhibits a slower CA uptake followed by a plateau at about 150 s. The average concentration-time curves of cluster 4 (purple) and 5 (green) follow the same shape as that of cluster 3 but at lower concentration levels. Except for v_e of cluster 3, all ETM fit parameters decrease steadily from cluster 1 to cluster 5 (Figure 33 B).

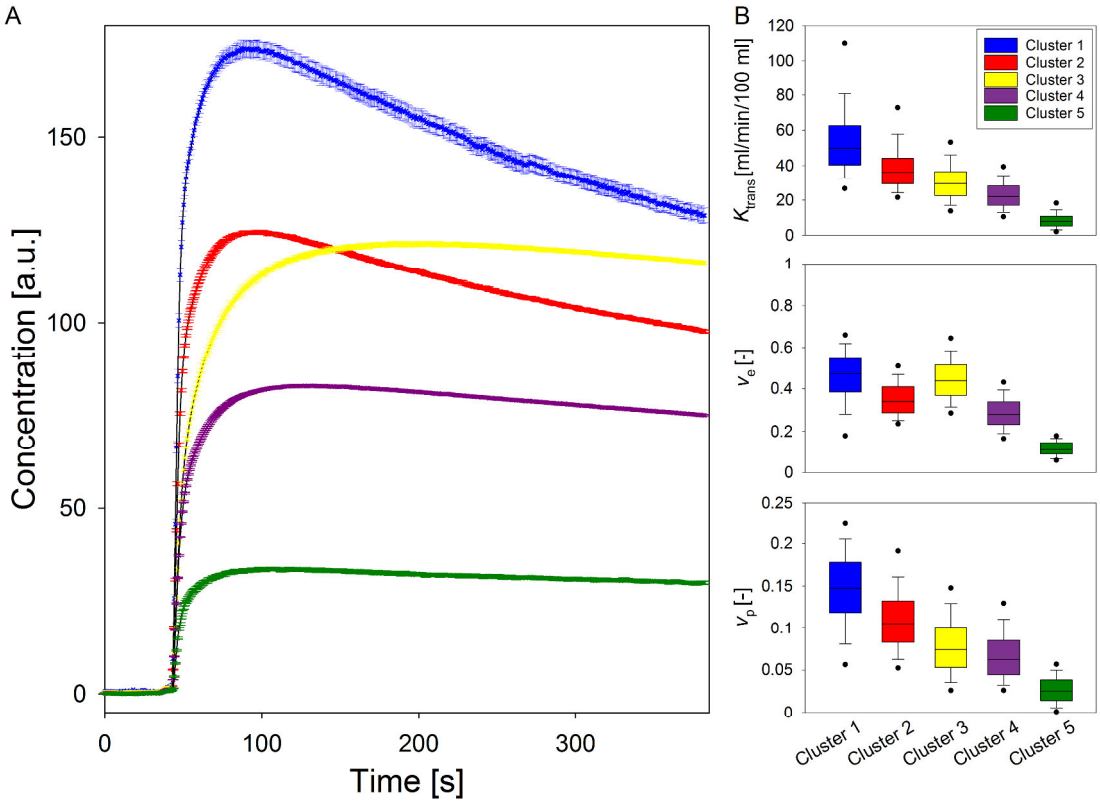

Figure 33 Results for principle component analysis and clustering of DCE-MRI data of HI-tumors. (A) Average concentration-time curves (± SEM) per cluster over all tumor voxels and time points. (B) ETM fit parameters per cluster for all tumor voxels and time points: volume transfer constant K_{trans}, extracellular, extravascular volume fraction v_e, and plasma volume fraction v_p. Figure reproduced from [136].

3.4.4 Treatment response after irradiation

Exemplary $T1$-weighted images after CA administration and their corresponding clustering results are displayed in Figure 34. The longitudinal development of the fraction of each cluster is displayed in Figure 35.

At the initial imaging time point before RT, tumors were characterized mainly by cluster 2 and 4 with minor contributions of the other cluster (the high fraction of cluster 3 for the 75 Gy ^{12}C-ion treated group results from a single animal). Control tumors maintained the initial cluster distributions over 21 days (Figure 35 A).

7 days after RT, the fraction of cluster 3 started increasing and became dominant at 21 days after RT, while the fractions of cluster 1 and 2 decreased to essentially zero for almost all dose groups. As an exception, the increase in cluster 3 was delayed for the 75 Gy photon group and was first observed at the fourth imaging time point 14 days after RT. The tumor in this group, that continued growing with a reduced growth rate until 21 days after RT, showed no further increase in cluster 3 voxels after day 14.

No pronounced differences in the temporal development of this treatment response were found between ^{12}C-ions and photons, and between curative and sub-curative doses of ^{12}C-ions. The lower fraction of cluster 3 for the two photon treated groups was found to originate from a single animal in both groups.

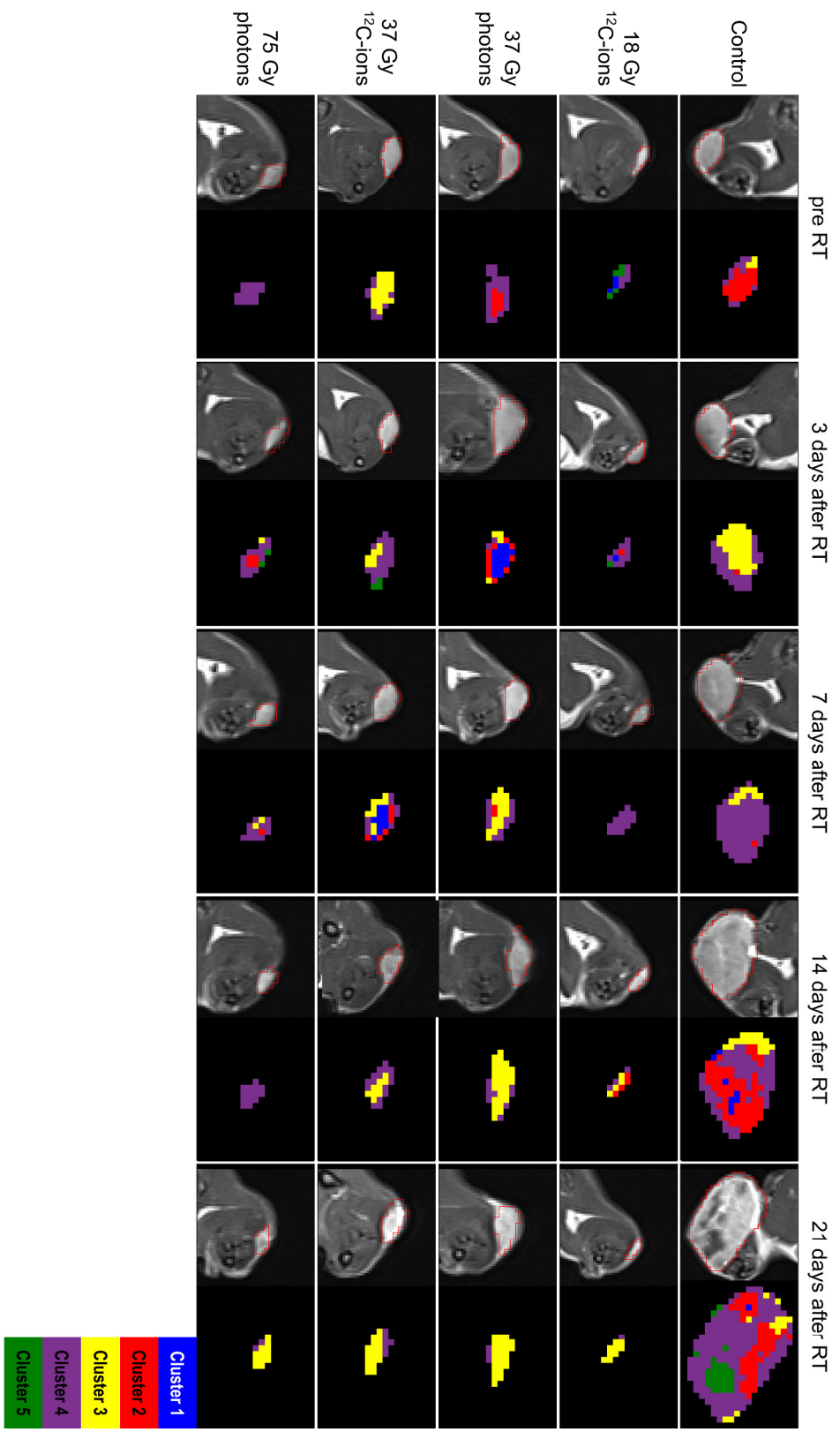

Figure 34 *T*1-weighted images of HI-tumors after CA administration with respective clustering results for one exemplary animal per dose group for each imaging time point. Figure reproduced from [136]. Measurements were performed by Dr. Christin Glowa.

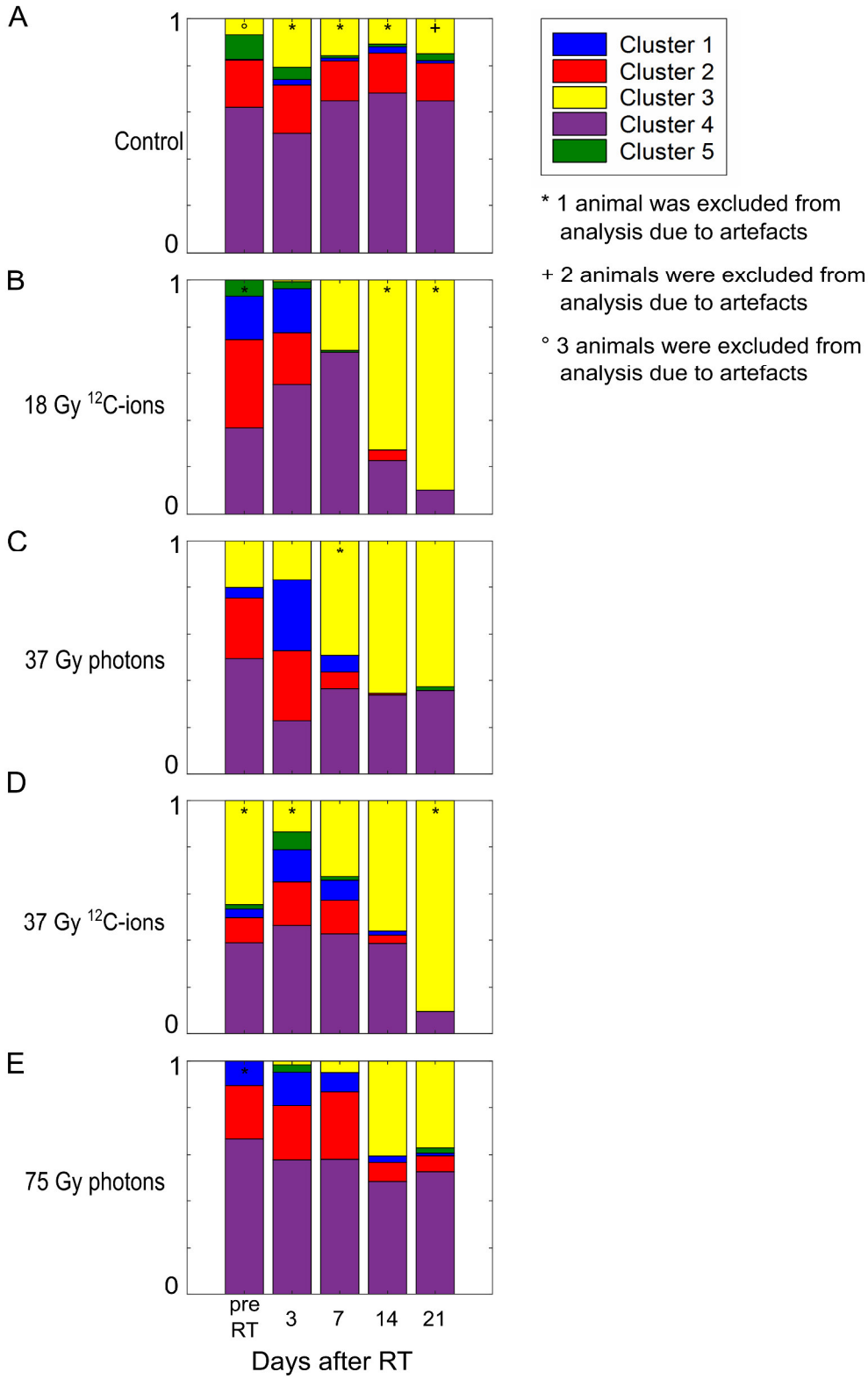

Figure 35 Pooled clustering results for the HI-tumor at different time points after irradiation for (A) non-irradiated controls, and (B) 18 Gy ^{12}C-ions, (C) 37 Gy photons, (D) 37 Gy ^{12}C-ions, and (E) 75 Gy photons treated tumors. Results were pooled for all tumor voxels per treatment group and time point and are displayed with their relative abundance. Figure reproduced from [136].

3.4.5 Histology 21 days after irradiation

H&E staining revealed that non-irradiated controls exhibited typical large mucin filled prostatic structures (Figure 36 A, F). Irradiated tumors exhibited severe structural damages which additionally impeded histological preparation of the tissue. H&E staining revealed that the remaining tumor parts mainly consisted of large vessels embedded in stromal parts containing intact tumor cells, cells with enlarged cell nuclei, and tumor cell fragments (Figure 36 B - E, G - J). For the high dose photon group (75 Gy) only one tumor could be histologically examined at day 21. This tumor showed vessel fragments and enlarged cells. Histological results were comparable among all treatment groups.

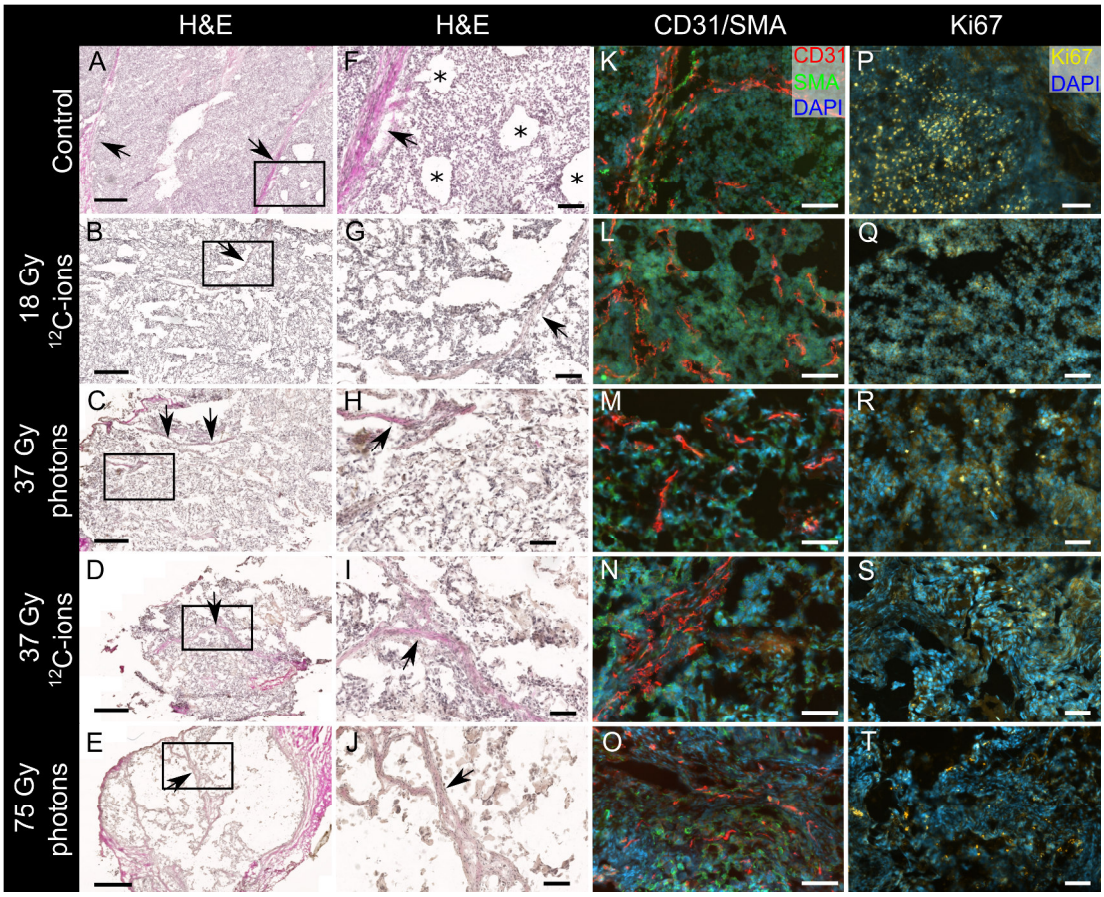

Figure 36 Histological images of HI-tumors 21 days after irradiation with either photons or ^{12}C-ions and non-irradiated controls. (A - E) Tumor morphology was visualized by H&E staining. While mucin-filled structures (asterisks), characteristic for the HI-tumor, were found in non-irradiated controls and to some extent in the low dose treated tumors, the tissue structure has mostly dissolved for the high dose treated tumors. Arrows point at residual vessel structures. Scale bars 500 µm. (F - J) Close-ups on the marked areas in A-E revealing the disrupted tissue structure pervaded by residual vascular structures at 21 days after RT. Scale bars 100 µm. (K - O) Fluorescence images of CD31 (vessels, red) and SMA (smooth muscle actin (pericytes), green) stained HI-tumors reveal the remaining immature vessel fragments that survived RT. Scale bars 100 µm. (P - T) Fluorescence images of Ki67 stained HI-tumors showing isles of proliferating cells in control tumors but only few Ki67^{+}-cells in treated tumors. Scale bars 100 µm. Figure adapted from [136].

Staining for CD31 and SMA showed that non-irradiated controls were pervaded by large, mostly immature, vessels (arrows) (Figure 36 K). Irradiated tumors comprised small, mostly SMA-negative, vessel fragments at 21 days (Figure 36 L - O).

The proliferative activity in irradiated and control tumors was assessed by staining for Ki67. Isles of proliferating cells were found throughout the control tumors (Figure 36 P). 21 days after RT, proliferative active cells were found only very sporadically in irradiated tumors (Figure 36 Q - T).

3.5 Longitudinal histology study of the AT1-tumor after irradiation

A longitudinal histology study was performed on the AT1-tumor after irradiation with curative single doses of either photons or ^{12}C-ions for a better understanding of the longitudinal changes that occur to the tumor tissue and vasculature on a microscopic level. Therefore, AT1-tumors were irradiated when they reached a size of 10 mm × 10 mm and were subsequently dissected at pre-defined time points. Tumor sections were stained for various markers, and microscopic fluorescence images of these were quantitatively analyzed. The AT1-tumor, which is the most radioresistant tumor of the three Dunning sublines used in this work, was chosen as it is chronic hypoxic and exhibits the largest RBE for local tumor control.

3.5.1 Tumor growth after irradiation

In the first week after irradiation with curative isoeffective doses of either photons or ^{12}C-ions, tumors continued growing comparably to non-irradiated controls. After 7 days, their growth decelerated and stagnated so that irradiated tumors reached a maximum of up to 2.7 times their original volume (Figure 37). Tumor shrinkage was finally observed after 18 days in the 21 day ^{12}C-ion treated group.

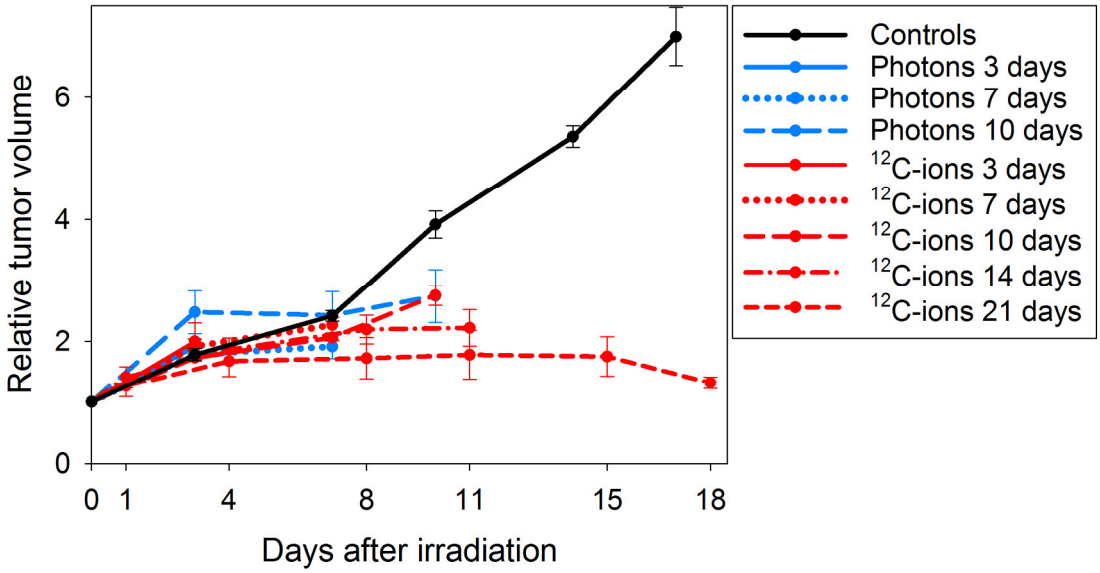

Figure 37 Relative tumor volumes of AT1-tumors after irradiation. AT1-tumors were irradiated with curative doses of either photons (blue) or ^{12}C-ions (red) and dissected after predefined time points. Their volume was calculated from measuring the largest tumor diameter and the corresponding orthogonal diameter. The displayed control group consists of five randomly chosen animals with non-irradiated tumors of the volume-dependent hypoxia study. Data is displayed as mean ± SEM (n = 5).

3.5.2 Tumor morphology

Non-irradiated AT1 control tumors comprised homogeneously distributed and densely packed tumor cells and little stromal parts (Figure 38). With increasing volume, central parts of non- irradiated AT1-tumors became necrotic, leaving only connective tissue behind (data not shown).

Overall, the temporal progression of tumor morphology after irradiation was comparable between isoeffective curative doses of photons and ^{12}C-ions until day 10. An invasion of leukocytes (small round cells whose cytoplasm is almost entirely taken up by the nuclei) was observed as early as 24 h after irradiation with both modalities. Starting at day 3, a decrease in tumor cell density was detected that progressed further until day 7 after irradiation. At this time point, hardly any intact tumor cells were found while the amount of bloated cells was increased. 10 days after irradiation, tumors exhibited a colloidal texture. At this time point, H&E staining revealed areas that mainly consisted of connective tissue with embedded immune cells. Hardly any tumor cells were left. This degraded tissue structure was sustained until 14 and 21 days after ^{12}C-ion irradiation.

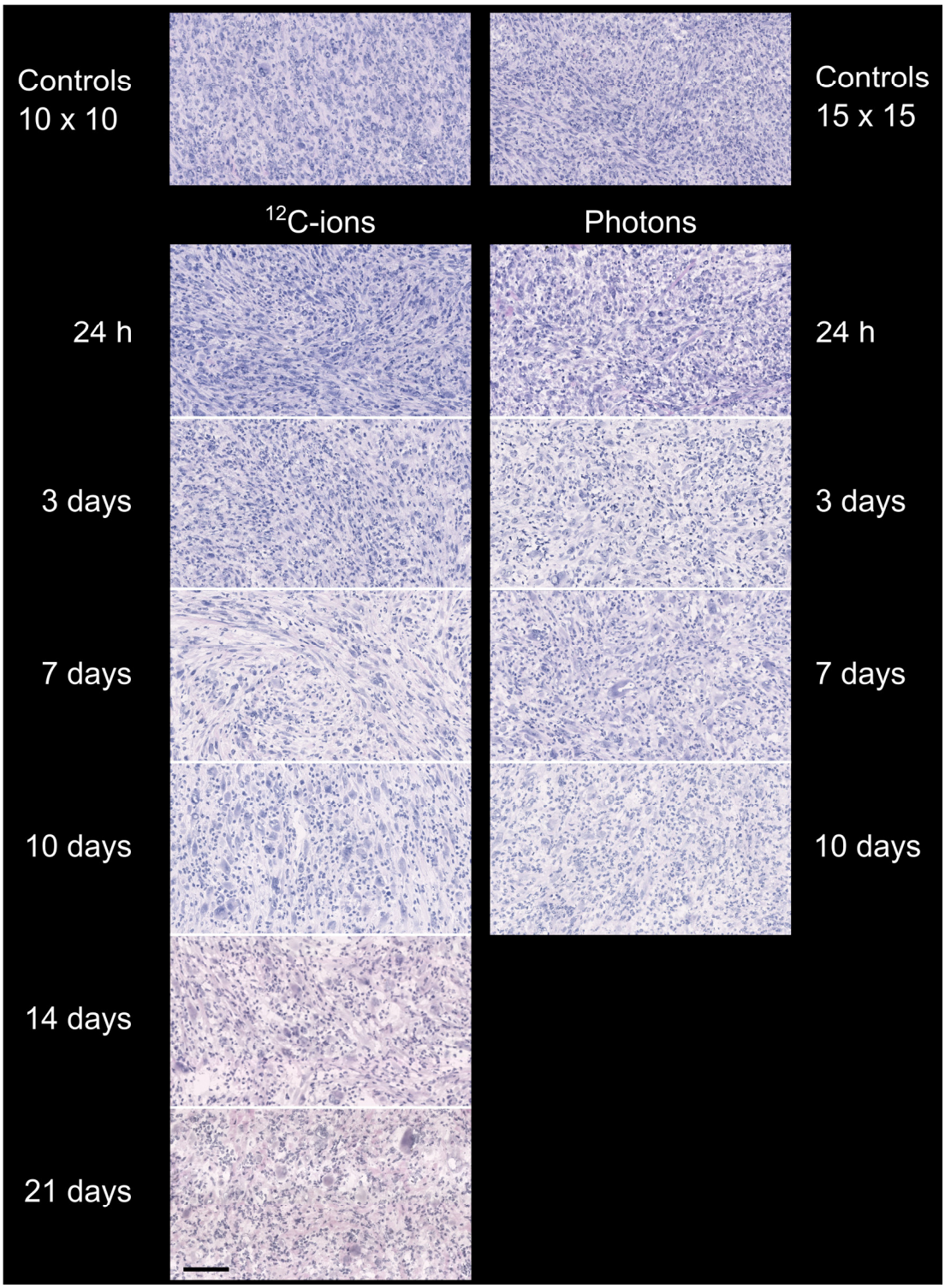

Figure 38 Structural changes in AT1-tumors at several time points after irradiation with either photons or ^{12}C-ions assessed by Hematoxylin/Eosin (H&E) staining. For comparison the morphology of two non-irradiated controls is displayed (10 mm × 10 mm and 15 mm × 15 mm, respectively). Scale bar 100 µm.

3.5.3 Tumor hypoxia

3.5.3.1 Volume dependent tumor hypoxia in non-irradiated controls

Figure 39 exemplarily illustrates the hypoxic microregions that developed in a certain distance to the perfused capillaries of the AT1-tumor.

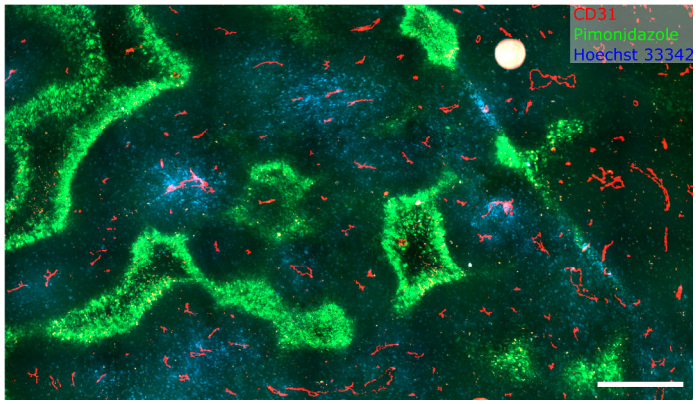

Figure 39 Exemplary fluorescence image of hypoxic microregions in the AT1-tumor. Shown are the AT1-characteristic capillaries (CD31, red) which were partially perfused (Hoechst 33342, blue) and hypoxic microregions (pimonidazole, green), which had developed in undersupplied areas at a certain distance to the perfused capillaries. Scale bar 500 µm.

AT1-tumors became hypoxic when they reached a certain size (Figure 40). Exemplary images of the spatial distribution of the hypoxic regions are displayed in Figure 41.

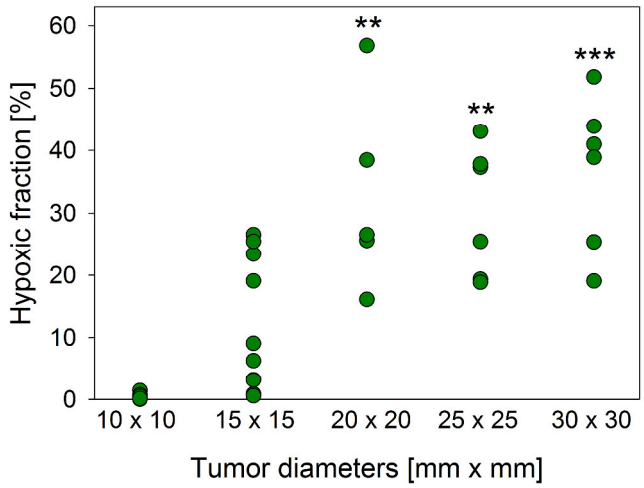

Figure 40 Quantification of the hypoxic fraction in AT1-tumors of different volumes. AT1-tumors were assigned into groups based on their size at dissection which was determined by measuring the largest and the respective orthogonal tumor diameter. Hypoxia was assessed by pimonidazole. The pimonidazole-positive area was set in relation to the overall tumor area for one whole-mount image per animal (necrotic regions were excluded). Statistically significant differences were only found in comparison with the 10 mm × 10 mm control group. ** $p < 0.01$, *** $p < 0.001$ with regard to the 10 mm × 10 mm group (10 × 10, 15 × 15: n = 10; 20 × 20, 25 × 25, 30 × 30: n = 5).

While tumors in the 10 mm × 10 mm control group accumulated no pimonidazole, the slightly larger tumors (15 mm × 15 mm control group) exhibited varying hypoxic fractions ranging from 0 % to 23 %. Tumors with a size of 20 mm × 20 mm and larger exhibited significantly higher hypoxic fractions than the 10 mm × 10 mm group. Their hypoxic fractions ranged from 16 % to 57 %.

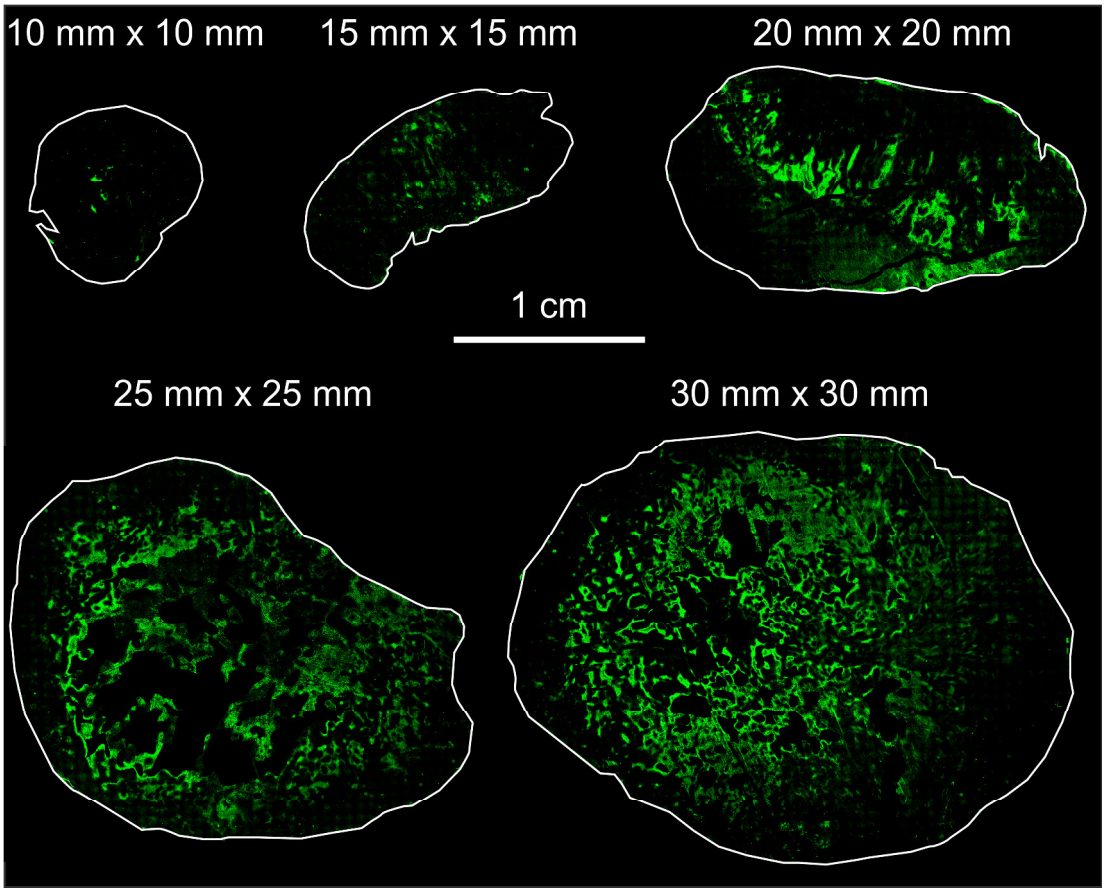

Figure 41 Fluorescence images of the hypoxic fraction in AT1-tumors of different volumes. Tumors were assigned to groups based on their size at dissection which was assessed by measuring the largest diameter and the respective orthogonal tumor diameter (numbers above tumor sections). Hypoxia was detected by pimonidazole (green) and one representative tumor per group is displayed. Necrotic parts were cropped from the images.

3.5.3.2 Tumor hypoxia after irradiation

Quantitative results of the hypoxia development after irradiation with curative doses of either photons or ^{12}C-ions are displayed in Figure 42 and exemplary images are displayed in Figure 43.

At irradiation size of 10 mm × 10 mm, tumors were pimonidazole negative (control group data taken from section 3.5.3.1). 24 h after photon irradiation, hypoxia occurred very irregularly in tumors and ranged from 0 % to 16 % hypoxic fraction. The hypoxic fraction remained below 5 % until AT1-tumors exhibited significantly but non-uniformly increased hypoxic fractions 10 days after irradiation (range 0 - 16 %). 24 h after ^{12}C-ion irradiation, AT1-tumors were pimonidazole-negative but became increasingly hypoxic until a significant maximum was reached at day 7 (range 5 - 13 % hypoxic fraction). During the following two weeks, the hypoxic fraction continuously dropped below 5 % at day 21.

The detected maximum hypoxic fraction was comparable between the two irradiation modalities but was reached faster after ^{12}C-ions (after 7 days) than after photons (after 10 days).

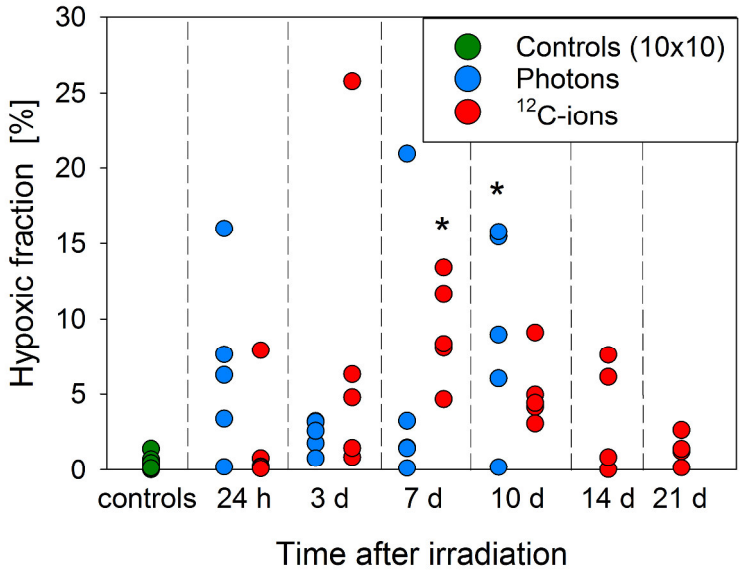

Figure 42 Quantification of the hypoxic fraction in AT1-tumors at several time points after irradiation. Tumors with diameters of 10 mm × 10 mm were irradiated with curative doses of either photons (blue) or ^{12}C-ions (red) and their hypoxic fraction was assessed at several time points from pimonidazole staining. The pimonidazole-positive area was set in relation to the overall tumor area for one whole-mount image per animal (necrotic areas were excluded from analysis). The size-matched control group (green) was taken from Figure 40. Statistically significant differences were only found in comparison with the 10 mm × 10 mm control group, * $p < 0.05$ ($n = 5$; controls: $n = 10$).

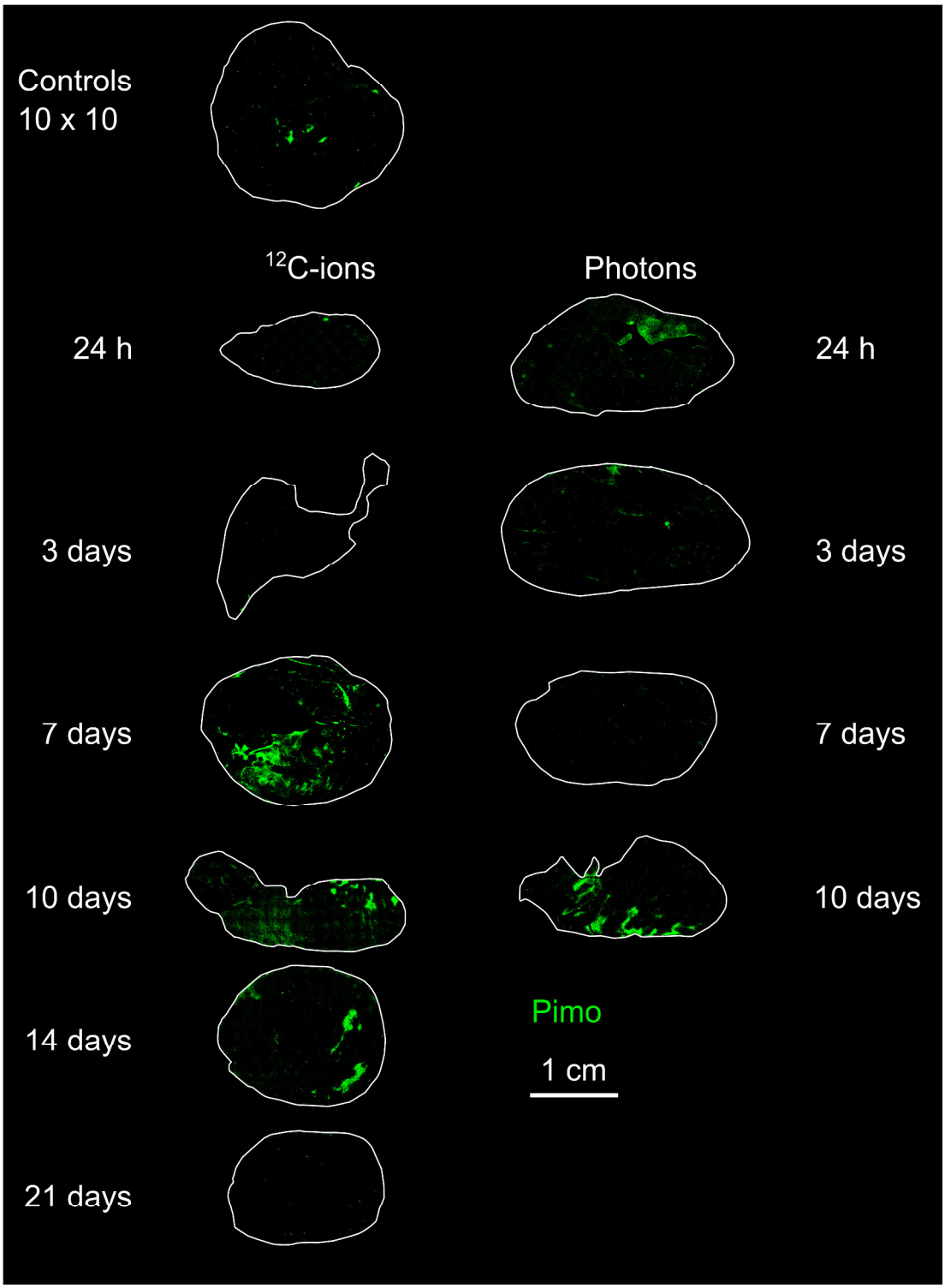

Figure 43 Fluorescence images of the hypoxic fraction in AT1-tumors at several time points after irradiation. Tumors were irradiated with curative doses of either photons or ^{12}C-ions at a size of 10 mm × 10 mm and hypoxia was assessed by pimonidazole (pimo, green) at several time points thereafter. Non-irradiated tumors with a size of 10 mm × 10 mm served as controls. Necrotic parts were cropped from the images.

3.5.4 Vascular density and maturity

No significant differences in vascular density between tumor rim and core were found (data not shown) and therefore, only data of entire tumor sections is shown. The AT1-tumor comprises a high density of tiny and immature capillaries (229 ± 11 vessels/mm^2) without considerable SMA staining (Figure 44, Figure 45). Within the first 24 h after photon and ^{12}C-ion irradiation the vascular density dropped to 73 ± 4 % and 77 ± 6 %, respectively, normalized to the vascular density of the 10 mm × 10 mm control group (Figure 44 A). The vascular density decreased further until day 10 when it became significantly lower than 24 h after irradiation. No significant differences in the longitudinal changes of the vascular density between photon and ^{12}C-ion irradiated tumors were found. The vascular density increased significantly between day 14 and day 21 after ^{12}C-ion irradiation (Figure 44 A).

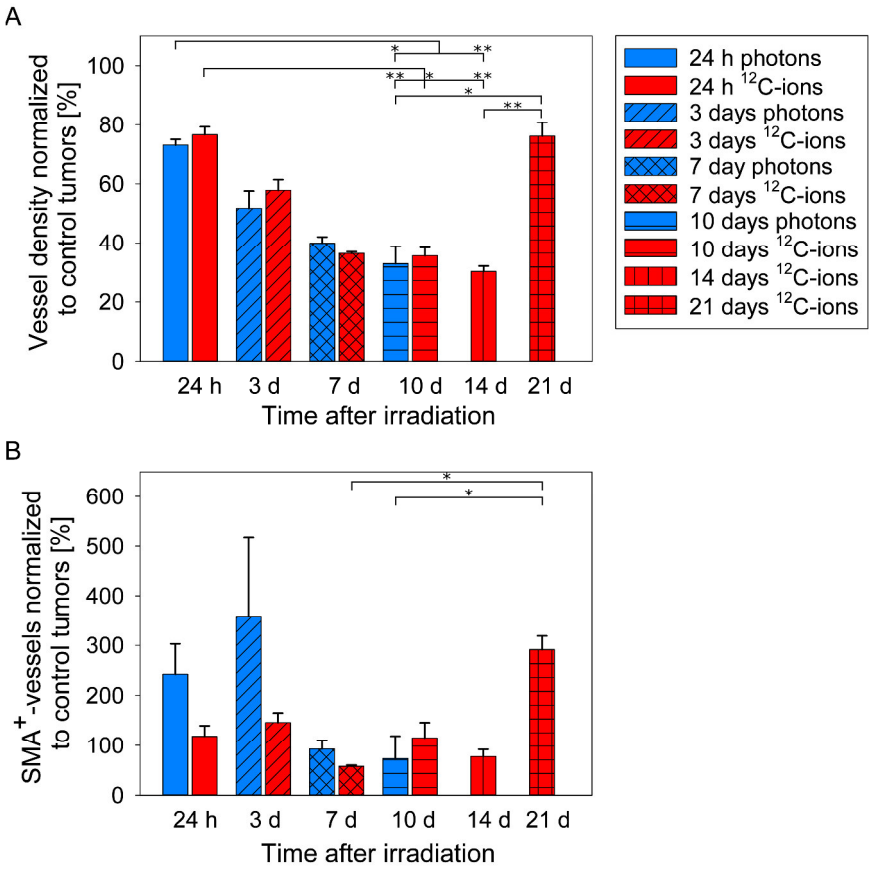

Figure 44 Quantification of the vascular density and maturity in AT1-tumors at several time points after irradiation. Tumors were irradiated with curative doses of either photons or ^{12}C-ions at a size of 10 mm × 10 mm and non-irradiated tumors of the same size were used as controls. (A) CD31$^+$-structures were semi-automatically segmented and objects larger than 21.125 µm^2 (50 pixels) were counted. Vascular density was determined by normalizing the number of vessels to the tumor section area excluding necrotic areas. (B) Smooth muscle actin-positive (SMA$^+$)-structures were semi-automatically segmented and when they overlapped with at least 300 pixels with CD31$^+$-segmented objects those were counted as SMA co-expressing. All results were normalized to the vascular density and the number of SMA-co-expressing vessels, respectively, of the control tumors (10 mm × 10 mm group). Results are displayed as mean ± SEM, * $p < 0.05$, ** $p < 0.01$, *** $p < 0.001$, ($n = 5$).

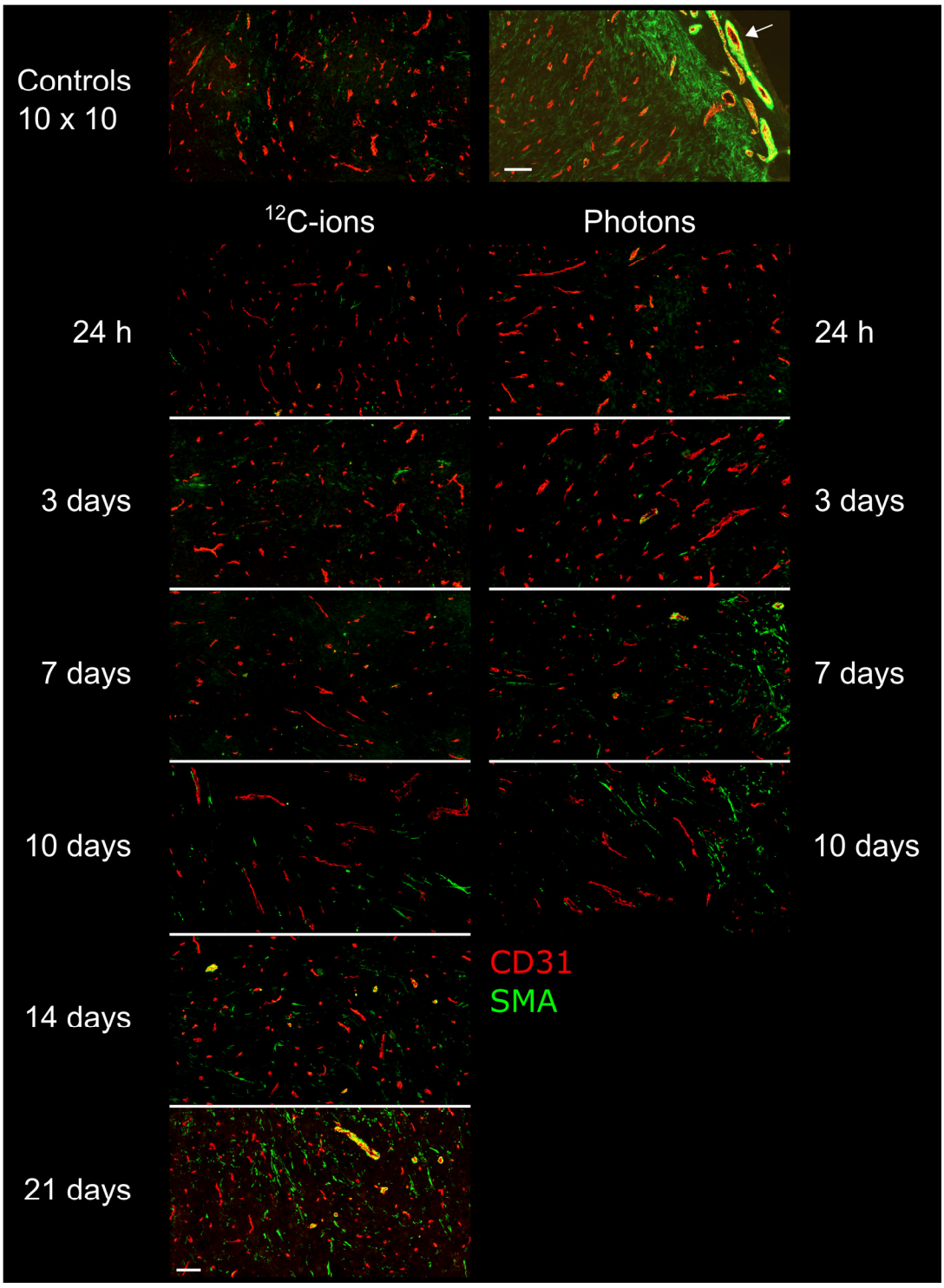

Figure 45 Fluorescence images of CD31 and SMA stained AT1-tumors at several time points after irradiation. Tumors were irradiated with curative doses of either photons or ^{12}C-ions at a size of 10 mm × 10 mm. Non-irradiated tumors of the same size were used as controls. Vessels were stained by the endothelial cell marker CD31 (red), pericytes were associated with vessel maturity and were stained by SMA (smooth muscle actin, green). Direct overlay of CD31 and SMA appears yellow. The upper right image shows a mature, pericyte covered capillary (arrow) in the rim of a control tumor in comparison to the high amount of SMA in the tumor that is not associated with vascular structures. Scale bars: 100 µm.

Overall, irradiated AT1-tumors greatly expressed SMA, however mostly un-associated with $CD31^+$-structures (Figure 45, upper right panel). Control tumors comprised 2.2 ± 1.5 $CD31^+/SMA^+$-vessels per mm^2. Within 24 h after irradiation, the percentage of SMA co-expressing vessels had increased to 242 ± 135 % (5 ± 3 $CD31^+/SMA^+$-vessels/mm^2) and 119 ± 47 % (3 ± 1 $CD31^+/SMA^+$-vessels/mm^2) after photons and ^{12}C-ions, respectively, normalized to the percentage of SMA co-expressing vessels of the 10 mm × 10 mm control group (Figure 44 B). The mean fraction of SMA co-expressing vessels was higher after photons than after ^{12}C-ions within the first week, however with a large error indicating heterogeneous response within this group. At day 10, ^{12}C-ion and photon treated tumors comprised comparable densities of pericyte covered capillaries. The fraction of SMA^+-vessels increased until 21 days after ^{12}C-ions, again showing the small and partially SMA^+-capillaries with clearly identifiable lumen. No significant differences were found between both modalities.

3.5.5 Tumor perfusion

Results of the perfusion classification and quantification are displayed in Figure 46. Exemplary Hoechst 33342 images are displayed in Figure 47.

Control tumors of size 10 mm × 10 mm and 15 mm × 15 mm were mainly intermediately perfused (71 ± 8 % and 65 ± 12 %, respectively) with only 20 ± 11 % and 26 ± 14 % non-perfused areas, respectively, and 10 ± 10 % highly-perfused areas for both sizes (Figure 46 A).

24 h after photon irradiation, the highly-perfused fraction increased at the cost of the non-perfused and intermediately-perfused fraction. At day 3, this perfusion peak had already declined and the initial perfusion proportions were restored (Figure 46 B, G). ^{12}C-ion treated tumors experienced a decline in perfusion 24 h after irradiation (Figure 46 C, H), followed by a hyperperfusion at day 3. Tumor perfusion was recovered by day 7, facing further perfusion impairment 10 and 14 days after irradiation. Tumors became highly-perfused by day 21.

Overall, the highly-perfused areas expressed the highest vessel density in control tumors and after irradiation (Figure 46 D - F). Non-perfused and intermediately-perfused areas comprised lower but comparable vascular densities. The vascular density decreased continuously after irradiation with both modalities and evenly among the three perfusion classes until day 10 (Figure 46 I, J). Intermediately-perfused areas of ^{12}C-ion treated tumors experienced a final increase in vascular density until day 21.

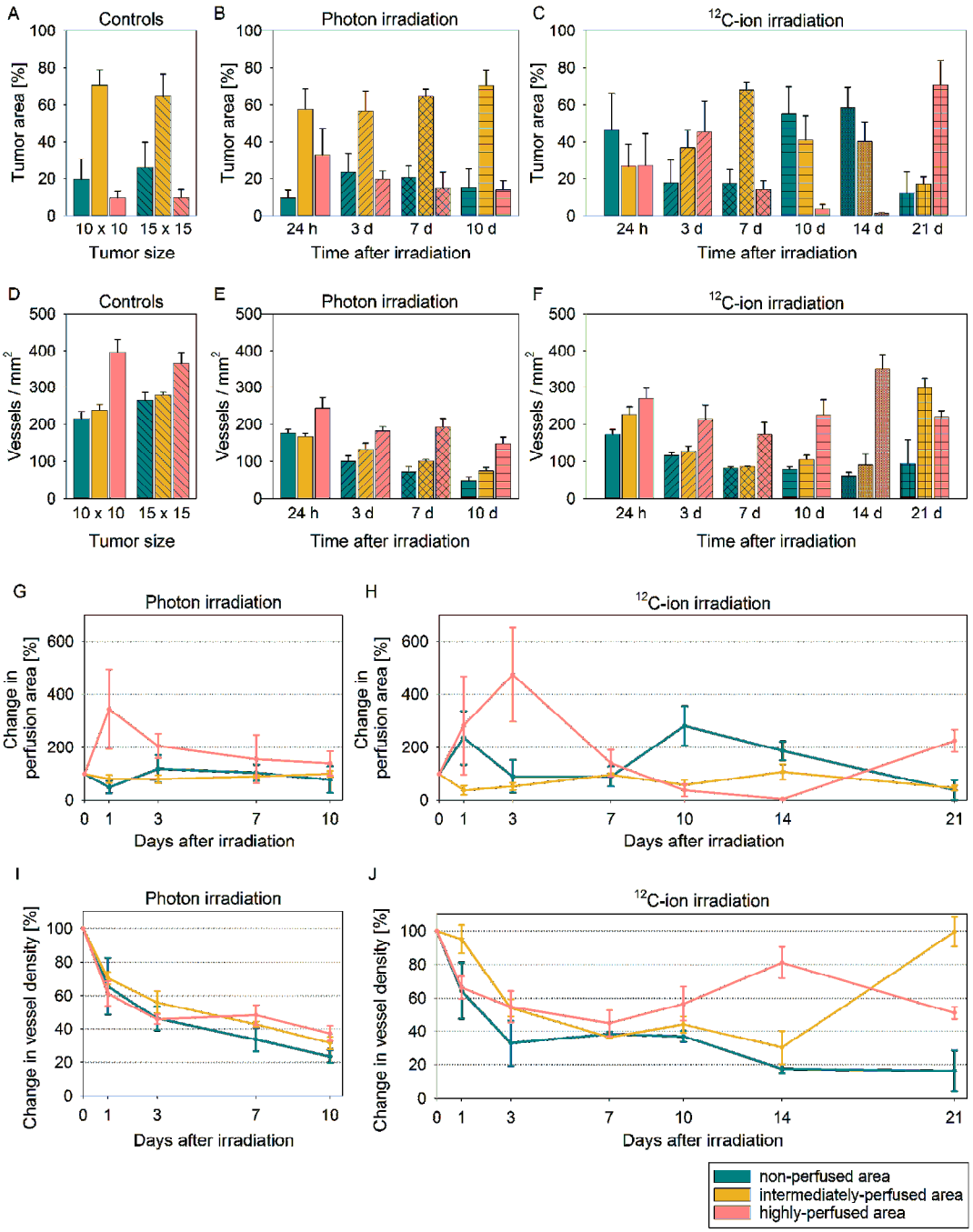

Figure 46 Quantification and classification of the perfusion in AT1-tumors at several time points after irradiation. Tumors at a size of 10 mm × 10 mm were irradiated with curative doses of either photons or ^{12}C-ions. Tumor perfusion was assessed by Hoechst 33342 which stained perfused areas and left non-perfused areas unstained. (A - C) One whole-mount fluorescence image was analyzed per tumor and sub-classified as non-perfused (cyan), intermediately-perfused (yellow), and highly-perfused (dusky pink) based on the intensity of the Hoechst 33342 stain. (D - F) The vessel density per perfusion class was determined by counting the number of CD31^{+}-objects and normalizing them to the respective perfusion area. (G - H) The change in perfusion area relative to the 10 mm × 10 mm control group was determined for each time point. (I - J) The change in vessel density relative to the 10 mm × 10 mm control group was determined for each time point. Results are displayed as mean ± SEM, (n = 5).

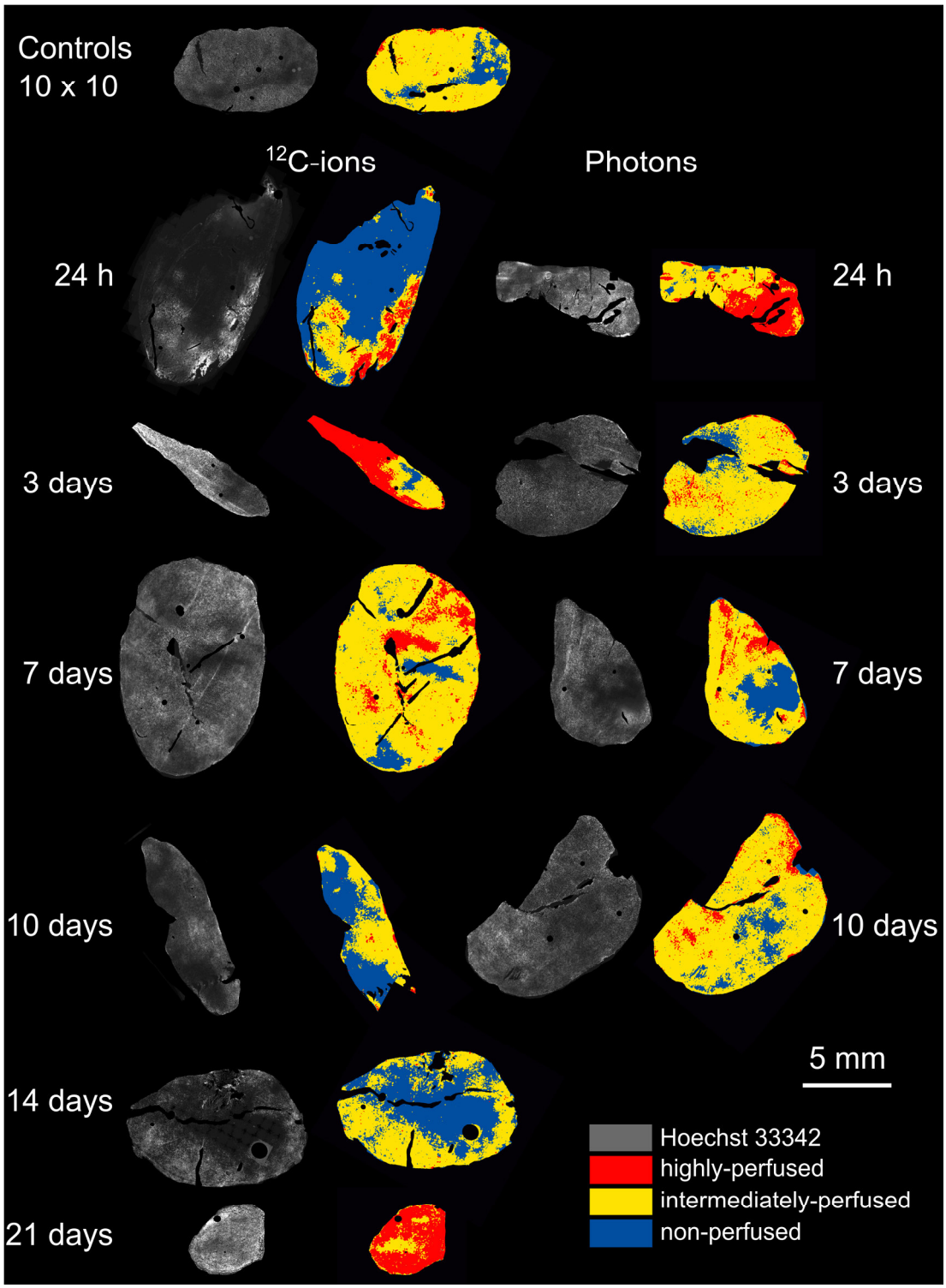

Figure 47 Fluorescence images and perfusion classification of AT1-tumors at several time points after irradiation. Tumors at a size of 10 mm × 10 mm were irradiated with curative doses of either photons or ^{12}C-ions and tumors of the same size served as non-irradiated controls. Perfusion was assessed by Hoechst 33342 which stained perfused areas (bright gray) and left non-perfused areas unstained (dark areas). Tumor regions were classified as non-perfused (blue), intermediately-perfused (yellow), and highly-perfused (red). Necrotic parts were cropped from the images and neglected during perfusion classification and quantification.

3.5.6 Proliferation

Non-irradiated control AT1-tumors exhibited the highest proliferative activity just below 20 % (Figure 48).

Both irradiation modalities induced the same changes on the proliferative activity. 24 h after irradiation, the proliferative activity had dropped to half of its initial value. Proliferative activity resumed its initial value by day 3 and declined from there on. 21 days after ^{12}C-ion irradiation, approximately 4 % of detected cells still proliferated.

BrdU^{+}-cells were distributed homogeneously over entire tumor sections, and no differences in the pattern of proliferating cells could be identified between the two modalities until day 10. The absolute percentage of BrdU^{+}-cells was identical for both modalities within the first 10 days after irradiation. Exemplary fluorescence images of BrdU incorporation are displayed in Figure 49.

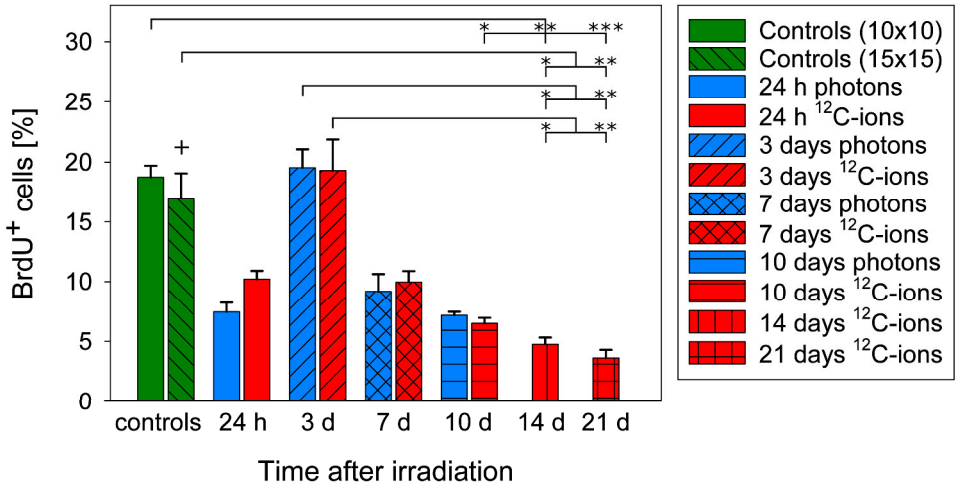

Figure 48 Quantification of the proliferative activity in AT1-tumors at several time points after irradiation. AT1-tumors with a size of 10 mm × 10 mm were irradiated with curative doses of either photons (blue) or ^{12}C-ions (red). Additionally, results of two control groups (10 mm × 10 mm and 15 mm × 15 mm diameters, respectively) are shown (green). Proliferation was assessed by BrdU incorporation. The ratio between cells that stained positive for BrdU and all cells marked by DAPI was determined for one whole-mount fluorescence image per tumor. Results were summarized per group and are displayed as mean ± SEM. + One animal was excluded from analysis due to incomplete BrdU injection. Results for 14 days and 21 days were not significantly different, * $p < 0.05$, ** $p < 0.01$, *** $p < 0.001$, ($n = 5$, controls: $n = 10$).

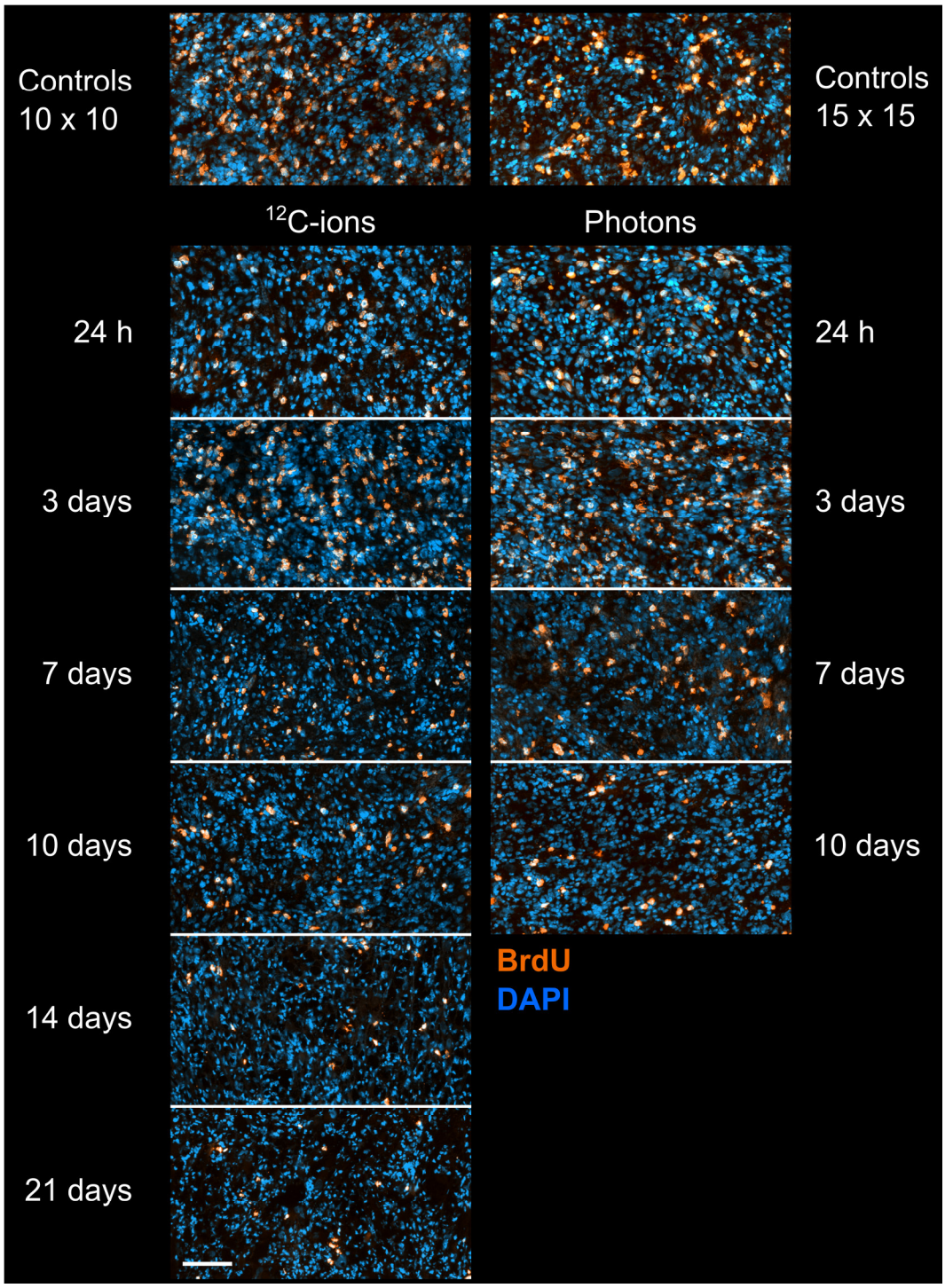

Figure 49 Fluorescence images of BrdU stained AT1-tumors at several time points after irradiation. Tumors were irradiated with curative doses of either photons or ^{12}C-ions at a size of 10 mm × 10 mm. Non-irradiated tumors with a size of 10 mm × 10 mm and 15 mm × 15 mm served as controls. Proliferation was assessed by BrdU incorporation (orange) into the cells' nuclei (DAPI, blue). Scale bar 100 µm.

3.5.7 DNA double-strand breaks

Approximately 15 % of all cells in non-irradiated control tumors were classified as intermediate intensity cells and approximately 0.5 - 1 % were classified as high intensity cells (Figure 50). 24 h after irradiation, the incidence of intermediate γH2AX$^+$-cells doubled for both modalities and returned to initial values until day 3 (Figure 50 A). Thereafter, the incidence of intermediate γH2AX$^+$-cells continuously dropped and stagnated at less than 5 % for ^{12}C-ion treated tumors. The incidence of high intensity γH2AX$^+$-cells peaked 24 h after irradiation (Figure 50 B). At day 3, it dropped below 2 % and remained low until 21 days after irradiation. Exemplary fluorescence images of irradiation-induced DNA DSBs are shown in Figure 51.

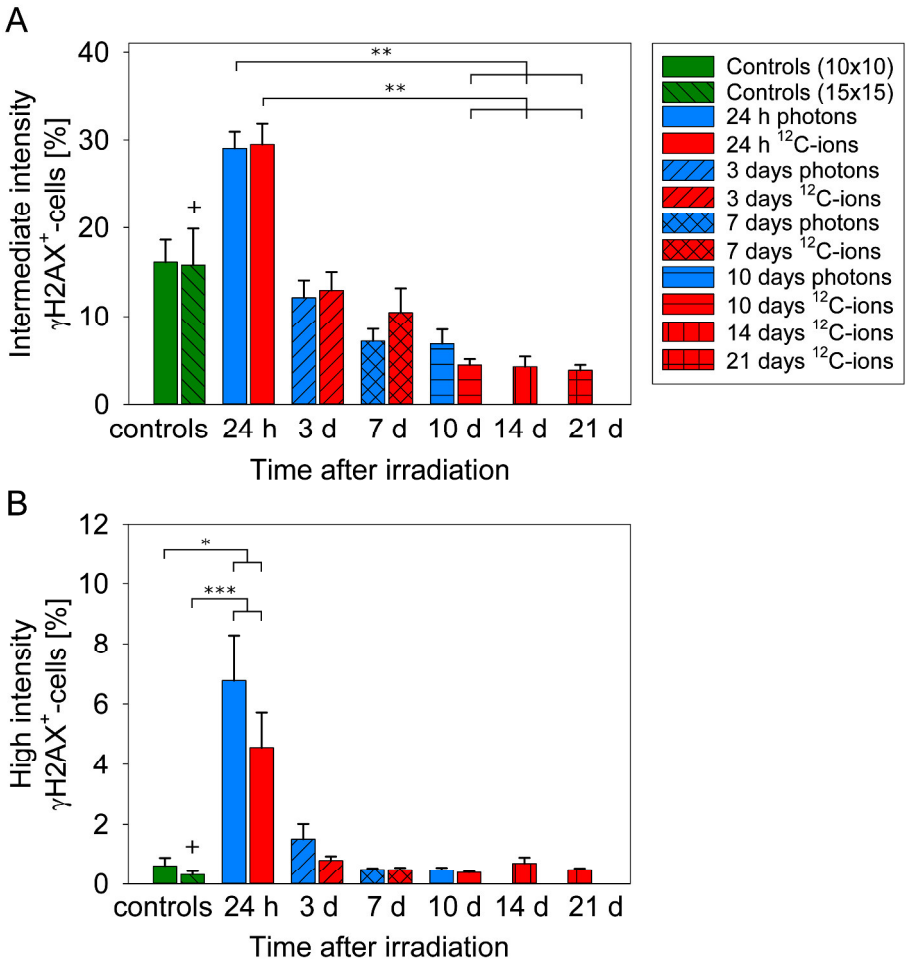

Figure 50 Quantification and classification of DNA double strand breaks in AT1-tumors at several time points after irradiation. AT1-tumors with a size of 10 mm × 10 mm were irradiated with curative doses of either photons (blue) or ^{12}C-ions (red). DNA DSBs were assessed by staining for γH2AX. The γH2AX$^+$-cells were classified as intermediate or high intensity and set in relation to the overall cell count (DAPI cell count) for one whole-mount image per tumor. Additionally, results of two control groups (10 mm × 10 mm and 15 mm × 15 mm diameters, respectively) are shown (green). Results are displayed as mean ± SEM. + Two animals missing due to analysis problems, * $p < 0.05$, ** $p < 0.01$, *** $p < 0.001$ ($n = 5$, controls $n = 10$).

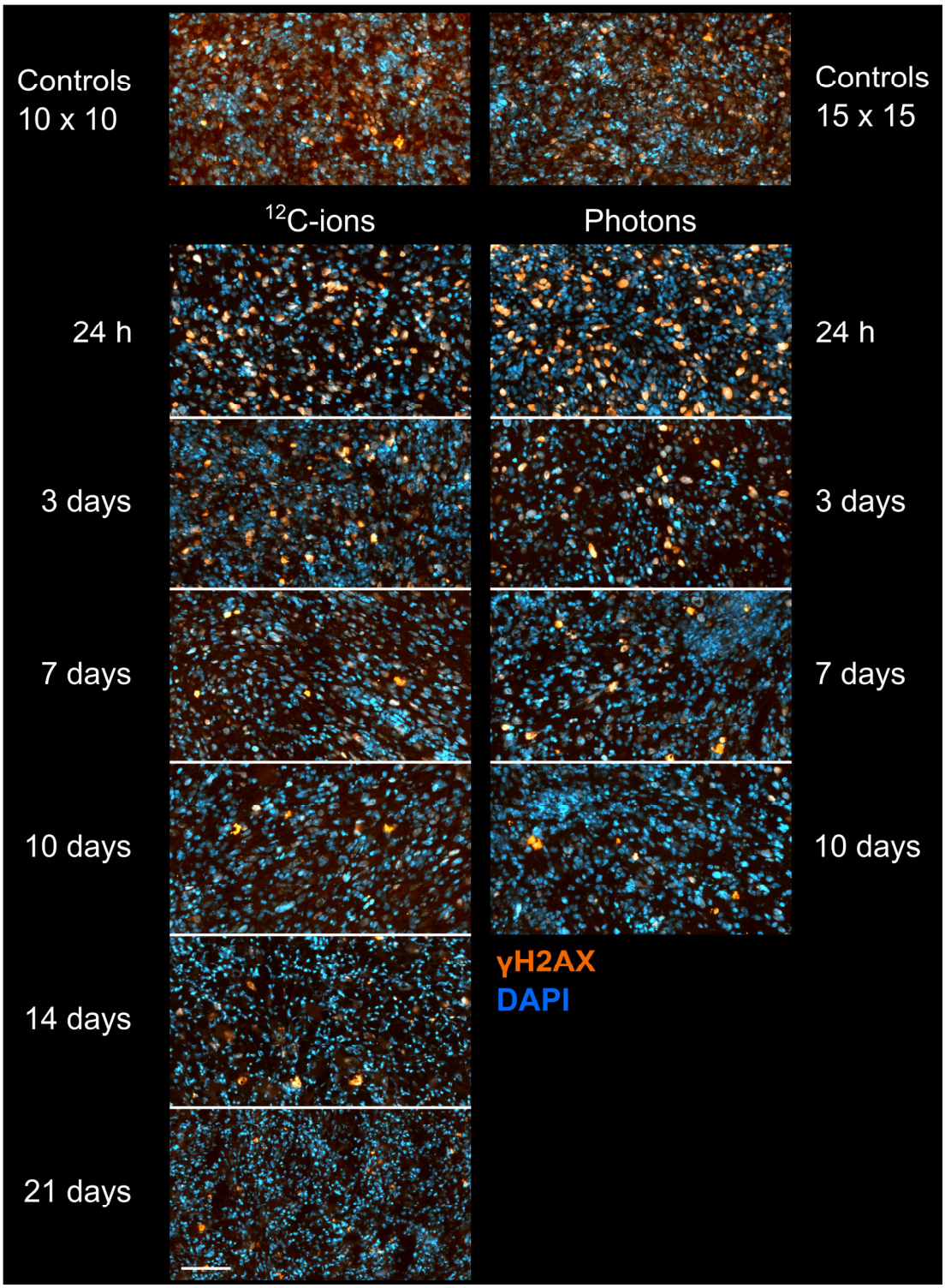

Figure 51 Fluorescence images of γH2AX stained AT1-tumors at several time points after irradiation. Tumors were irradiated with curative doses of either photons or ^{12}C-ions at a size of 10 mm × 10 mm. Non-irradiated tumors with a size of 10 mm × 10 mm and 15 mm × 15 mm served as controls. DNA double-strand breaks were identified by staining for γH2AX (orange) in cell nuclei (DAPI, blue). Scale bar 100 µm.

4 Discussion

Within the scope of this thesis, the hypoxic status of the syngeneic experimental prostate tumors Dunning R3327-H, -HI, and -AT1 was investigated by multiple imaging modalities. First, the tumors' oxygenation profiles were characterized by PAI utilizing a newly developed analysis protocol. Second, the longitudinal perfusion and vascular changes of the acute hypoxic (HI-) and the chronic hypoxic (AT1-) tumor were examined from DCE-MRI data after irradiation with sub-curative and curative single doses of either photons or ^{12}C-ions, including the development of a new method for bolus arrival time (BAT) estimation. Finally, a longitudinal histology study with the AT1-tumor disclosed the alterations in vascular density, hypoxia, perfusion, proliferation, and DNA double strand breaks (DSBs) that occurred after curative irradiation with either photons or ^{12}C-ions on a microscopic level.

In the following, first the methodical aspects of PAI and BAT estimation are discussed, and second the biological investigations are elaborated.

4.1 New analysis protocol for photoacoustic imaging (PAI)

The text in section 4.1 and respective subsections was taken from reference [96] and has been originally written by myself.

PAI is gaining increased interest for preclinical and clinical applications especially in the field of oncology [97-99, 101, 159-162]. It combines the high contrast and specificity of optical imaging with the high spatial resolution of ultrasound (US) imaging avoiding radiation [89, 98]. While many preclinical PAI studies on oxygen saturation provide only ROI-based mean values [163-166], others have developed more advanced imaging and analysis protocols using multispectral PAI [159, 160, 167]. First approaches for pixel- rather than ROI-based analyses were introduced by May *et al.* [168] and Hysi *et al.* [169]. To enable a more detailed display of the tumors' oxygenation status the existing approaches were extended to analyze pixel-based sO_2-distributions of the entire 3D-tumor volumes.

4.1.1 Feasibility of the new analysis protocol

The new protocol enables the characterization of the tumor sublines H, HI, and AT1 based on their sO_2-distributions rather than just mean values. This was used to study the tumor sublines' response after external changes of oxygen supply. Furthermore, it could be investigated whether this response occurs within the entire tumor or only locally and whether this behavior is changing with time indicating morphological or functional changes within the

tumor. This detailed analysis would not have been feasible if only mean values per tumor had been considered.

Tumor HI-3 especially illustrates the potential of the established protocol: During the 41 days of observation, this tumor underwent major morphological changes which were reflected in the changing shapes of the corresponding sO_2-distributions. This makes the developed protocol especially interesting for longitudinal studies (e.g. after treatment), where changes in oxygenation are expected.

The study was conducted using two commercial PAI-systems: the Vevo 2100 and Vevo 3100, both employing the laser Vevo-LAZR. According to the manufacturer, the two systems are largely comparable with respect to system electronics and PA-specific performance (penetration depth, system dynamic range, signal-to-noise ratio, contrast sensitivity). Therefore, the resulting sO_2-distributions should not be affected by the choice of the PAI-system.

4.1.2 Dependency of sO_2-distributions on signal gain and threshold

The dependence of the results on the measurement settings had to be investigated prior to any systematic investigations of the tumor sublines. These investigations confirmed that the resulting sO_2-distributions were largely independent of signal gain, applied threshold, and positioning of the animals. The higher variability of the sO_2-distributions observed for HI-2 can be explained by the overall weak PA signal and the low number of pixels that remained after thresholding which cannot be considered as being representative for the tumor. Hence, the signal gain was adjusted individually per animal and imaging session taking the strong and distinct PA signal of the well oxygenated healthy skin as a reference. This approach is justified by the fact that tumors were always transplanted at the same location according to a fixed protocol while environmental factors such as room temperature, temperature of the animal heating table, and gel temperature were kept constant. Based on these measures, the skin can be considered as reliable and reproducible reference tissue for the selection of individual measurement parameters. Overall, the suitability, sensitivity, and feasibility of the new PAI analysis protocol were demonstrated.

4.2 New method for BAT estimation of DCE-MRI data

Before performing pharmacokinetic modeling of the DCE-MRI data that was acquired for the AT1- and the HI-tumor, the problem of accurate delay correction was addressed. Among other factors, the accuracy of the fit parameters from pharmacokinetic modeling depends critically on the temporal alignment of the arterial input function (AIF) and the tissue concentration curves (TCCs). The bolus arrival in the TCCs is often delayed with respect to its arrival in the AIF due to practical reasons such as the acquisition of the AIF from the left ventricle instead of from a tumor feeding artery. The reason for using the ventricle is that it

provides a larger and easier accessible blood volume and, hence, the AIF is less likely affected by partial volume effects. A new method for bolus arrival time (BAT) estimation which can be used for the alignment of the concentration curves was developed within this thesis.

The following text in this section was taken from reference [117] and has been originally written by myself.

The simulation study showed that the state-of-the art method by Cheong *et al.* [123] works very well for BAT estimation of patient TCCs and AIFs, but that it gives unsatisfactory results for rat TCCs. The main reason for this is that Cheong's method heavily relies on a fast upslope from the BAT to the peak of the concentration curve, which is frequently not the case in small animals such as rats and patient data of tissues lacking a significant intravascular fraction. In contrast, the proposed method estimated BATs that were very close to the ground truth for rat TCCs under all conditions. A central advantage of the proposed method is that it does not require a special curve characteristic after the BAT as the smoothing spline is able to adapt to a large variety of curve shapes.

The arrival of the contrast agent (CA) does typically not coincide with one of the time points of the image acquisition. Cheong's method, however, limits estimation of BATs to those time points which imposes a systematic upper limit to the estimation accuracy. The proposed method estimates BATs on a continuous scale; i.e. the estimated BAT can lie in between the time points of the image acquisition. This improves the accuracy of the results especially for image data with low temporal resolution. Even though the proposed method was developed for small animal data, its feasibility for high temporal resolution and high SNR patient data was demonstrated as the results were competitive with those obtained by the method of Cheong *et al.* [123]. Yet, for lower temporal resolutions and lower SNRs Cheong's method gave more accurate results in patient data. The proposed method was also applied to *in vivo* acquired rat data of the DCE-MRI study with the HI-tumor. As the ground truth is not known for this data only qualitative statements could be made on the results. In these cases, Cheong's approach gave reasonable results for the AIFs which fulfill the criterion of a fast upslope from the BAT to the concentration maximum. For the TCCs, however, the estimated BATs were implausible because they lay before the actual injection time. Adapting Cheong's method to consider only BATs after a plausible lower time point mostly resulted in that lower bound. In either case, the estimates for the BATs were mostly not informative. In contrast, the BATs estimated for the TCCs by the proposed method were found to be very close to each other, for each tumor and each animal, respectively. When evaluating the location of the BATs within the TCCs, they appeared to be set at reasonable positions.

4.3 Characterization of the three sublines H, HI, and AT1 by PAI

PAI and the new protocol were used to characterize the initial oxygenation status of the three tumor sublines H, HI, and AT1. The text in subsection 4.3.1 was taken from reference [96] and has been originally written by myself.

4.3.1 Initial oxygenation, temporal changes, and response to external changes in oxygen supply

The three tumor sublines H, HI, and AT1 are known to differ with respect to several parameters, most importantly their oxygenation status [94, 95, 170]. The highly differentiated and slowly growing H-tumor is most similar to normal prostate tissue. The narrow peaks of the sO_2-distributions at high sO_2-values indicate homogeneously oxygenated tumors, which were confirmed by immunohistochemistry, revealing mature vessels ensuring a sufficient blood supply. The shape of the sO_2-distributions was maintained during the observation period without developing a shoulder at lower sO_2-values as found for the HI-tumor. PAI was sensitive enough to detect the acute changes in oxygenation induced by changing the breathing gas from 100 % O_2 to air as well as by clamping of the tumor-supplying arteries. The response of different animals was highly uniform. A similar finding was described by Zhao *et al.* [171]. The small hypoxic fraction found in immunohistochemistry staining of the H-tumors is also in accordance with previously published work [172] and is negligible in comparison to the other sublines.

The sO_2-distributions of small HI-tumors exhibited narrow sO_2-peaks comparable to those of the H-tumors but showed an additional shoulder in the low sO_2-region. HI-tumors are known to develop hypoxia with time [172], which was also confirmed by the immunohistochemistry staining and by the increasing fraction of low-sO_2 pixels during the long-term observation. The immediate response to external changes in oxygen supply and the presence of responding and non-responding tumor regions has also been described by Zhao *et al.* [173].

The anaplastic AT1-tumor exhibited narrow peaks in the low sO_2-region which remained essentially unchanged with respect to time point and oxygenation conditions (EMD < 0.05 for all comparisons). Immunohistochemistry staining revealed that the immature and hardly perfused capillaries could not sufficiently supply the AT1-tumors, which explains the chronically low sO_2-values [172]. While the results of the oxygen challenge experiment are in accordance with those of Mason *et al.* [68] and Zhao *et al.* [171], other investigators found a very small but statistically significant change in perfusion after changing the external oxygen supply from 100 % O_2 to air [174]. As the results were reproducible over a period of 12 days and since the comparison of different tumor-sublines is based on measurements performed on the same day, any PAI-system related artefacts can be ruled out. The non-responsiveness of the AT1-tumor towards external changes in oxygen supply points at its chronically low oxygenation and its adaption towards this condition (see discussion in section 4.7.2).

4.3.2 Comparison of tumor sublines and normal tissue (skin)

Changing the breathing gas from 100 % O_2 to air showed comparable responses in sO_2-distributions of the H- and HI-tumors as well as the normal tissue (skin) [96]. Similar results were found by Smith *et al.* who investigated the response of several vessel types to different breathing conditions by PAI [175]. Using clamping to restrict perfusion, tumors and normal tissue showed different responses: While the skin showed a strong response towards the perfusion restriction and became acute hypoxic, the H- and HI-tumors' sO_2-distributions were shifted to less extreme sO_2-values after clamping, indicating a reduced oxygen consumption due to an adapted and less oxygen-dependent metabolism compared to the normal tissue skin.

4.4 Longitudinal DCE-MRI study of the AT1-tumor

PAI confirmed the chronic hypoxic status of the AT1-tumor, known to resemble a major resistance factor for conventional photon RT. However, there are indications that this can be overcome by ^{12}C-ion irradiation [24, 176]. Therefore, DCE-MRI and histological techniques were used to gain initial information on treatment-induced functional and morphological alterations after high single doses of ^{12}C-ions or photons in the anaplastic AT1-tumor up to 21 days post-irradiation. While other researcher found changes in perfusion and vascular parameters at early time points after photon RT [71, 177, 178], this study examined a longer time frame of up to 21 days after irradiation. The four-armed study consisted of two isoeffective curative dose groups (37 Gy ^{12}C-ions and 85 Gy photons) and two isoeffective subcurative dose groups (16 Gy ^{12}C and 37 Gy photons). Moreover, the study design allowed also for an iso-absorbed dose comparison at 37 Gy.

The text in subsections 4.4.2 to 4.4.6 was taken from reference [135] and has been originally written by myself.

4.4.1 Selection of pharmacokinetic model

The extended Tofts model (ETM) was selected for pharmacokinetic modeling of the TCCs following the recommendation for data-driven model selection to always choose the simplest model that sufficiently describes the data [114, 116]. However, it needs to be kept in mind that the ambiguity of the parameter K_{trans}, which is composed of the plasma flow F_{p} and the permeability *PS*, marks a limitation of the ETM. Only in the limit where either flow or permeability dominates the CA transport into the tissue, K_{trans} can be directly associated with PS or F_{p}, respectively [114]. In all other situations K_{trans} resembles a mixture of both parameters with unknown contributions. However, the two compartment exchange model [116], which comprises all four parameters F_{p}, PS, v_{e}, and v_{p} independently, was refused as the fits

were found to be instable and provided parameter values in non-physiological ranges. Rejection of this model due to its instability was also reported in other studies [179].

4.4.2 Longitudinal monitoring of treatment response by DCE-MRI

The treatment groups' initial distributions of normalized AUC, v_e, and v_p already varied significantly before irradiation. Hence, the longitudinal development of the fit parameter needs to be evaluated with respect to their initial values.

In control tumors, a decrease of all ETM parameters was observed, presumably attributed to a progressive decline of perfusion within the tiny, immature microvessels characterized by reduced blood flow resulting in a decreased transport of CA. Within the tumor core this process is reflected by an increasing number of hypoxic regions and areas of necrosis which were found in histology.

For all irradiated tumors, an initial increase in tumor volume followed by a steady state up to day 21 is the typical behavior after RT and is in accordance with earlier published results [103]. This might result from irradiation-induced edema formation. Belfatto *et al.* reported comparable results on tumor growth within the first three weeks after sub-curative photon irradiation of AT1-tumors for both, air and O_2 breathing animals [180]. Yet, photon and ^{12}C-ion irradiated tumors differed in their histological appearance and ETM parameters. ^{12}C-ion RT resulted in increased normalized AUC, K_{trans}, and v_e values at day 3, while treatment response was prolonged and less pronounced for photon treated tumors with a tendency to even higher protraction with increasing dose. This effect might be related to the more pronounced complex DNA damage after high LET irradiation inducing enhanced cell death [15]. A comparable increase in K_{trans} one week after photon irradiation was also described by Lin *et al.* [181] and was attributed to either an increase in capillary permeability or perfusion. The normalized AUC value, which is a rather descriptive parameter, cannot be directly associated with a defined physiological process; hence, its increase indicates solely a higher amount of CA reaching the tumor.

The initial increase in the parameter v_e after ^{12}C-ion RT can be attributed to an increased vascular permeability immediately following high LET-irradiation while vascular damage was prolonged after photon RT. A recent study showed that increased vascular permeability occurs 14 days after single high dose photon irradiation [182]. Zhou *et al.* found no increase in v_e in the first week after sub-curative irradiation of AT1-tumors [178]. The elevated v_e values that were observed for all four treatment groups at the last imaging time point, independently of beam quality and dose, reflect well the decreased cell density in the tumors at this point (see section 4.4.4).

The findings of this initial DCE-MRI study are also in line with a fractionated ^{12}C-ion study of prostate cancer patients by Bonekamp *et al.* [106], where the highest elevated K_{trans} and v_{e} values were detected 10 days after the first RT fraction and decreased thereafter.

4.4.3 Re-oxygenation after irradiation

The AT1-tumor is a rapidly growing, anaplastic tumor with poorly perfused microvessels [94], which leads to a considerable number of hypoxic regions preferentially in the central core. At day 21, the hypoxic fraction was lower in irradiated tumors than in the corresponding control tumors compared to no hypoxia at all in ^{12}C-ion treated tumors. Even though only limited conclusions can be drawn from the results of one animal per group, the findings are in accordance with the results of other researchers showing clear signs of re-oxygenation in NFSa fibrosarcomas after a single fraction of 16 Gy ^{12}C-ions 1 to 5 days after RT, which was not observed after treatment with photons [183]. On the histological level, this process was characterized by the disappearance of huge-caliber vessels detected in the vicinity of hypoxic and necrotic areas. These vessels were also found by other researchers [184, 185] and are assumed to be the result of a constant hypoxia-induced stimulus by angiogenic factors [186] and increased levels of nitric oxide that maintain the dilator tone [184, 187, 188].

4.4.4 Correlation with histology after 21 days

The non-perfused areas that were visible in $T1$-weighted images and DCE-MRI parameter maps correlated with necrotic areas that were shown by H&E staining. Photons and ^{12}C-ions evoked differential effects with respect to tumor morphology 21 days after RT: Photon irradiation led to heterogeneous tissue structures which were reflected by wider distributions of v_{e}, while ^{12}C-ion treatment resulted in loose and homogeneous tissue structures with narrower v_{e} distributions. This led to the conclusion that the response to photon irradiation is much more influenced by the local tumor environment than the radiation response to ^{12}C-ions, confirming earlier findings [24].

4.4.5 The role of endothelial cells

In the last three decades, the focus of RT has been expanded by the crucial role of endothelial cells in response to RT [189]. However, results on the exact mechanisms are still inconsistent [190-193] and the extent of endothelial cell contribution to the RT response remains a controversial issue [194, 195]. Several studies were published, indicating that the intrinsic radiosensitivity of tumor cells is the major determinant of tumor response to photon irradiation [194-198] and not the stromal part.

In the investigated anaplastic tumor, a higher microvascular density was found 21 days after ^{12}C-ion RT compared to photons. Yet, independent of the radiation quality, there is evidence of small, but mature capillaries with clearly identifiable lumen showing signs of normaliza-

tion of the tumor vasculature, comparable to observations by Lan *et al.* [199]. Radiation may affect tumor vasculature and maturity in two ways: either the fraction of mature vessels is increased as only the mature vessels are able to survive RT at high doses or these vessels are the product of RT-induced angiogenesis and maturation. This issue will be addressed later in the context of the longitudinal histology study (section 4.7.2). In contrast to the presented results, many authors proclaim that photon RT induces angiogenesis and upregulates endothelial cell conserving factors such as the vascular endothelial growth factor and the basic fibroblast growth factor [200-202], while ^{12}C-ion irradiation inhibits angiogenesis and related actions [28, 203, 204]. Still, a direct correlation with the reported results is difficult, because of the lower doses and the shorter observation times after irradiation used in the referenced studies. Tsai *et al.* [185] have found that even though ionizing radiation increased endothelial cell proliferation, resulting angiogenesis was ineffective as vessel density did not increase in the K1735 murine melanoma model. However, their last examined time point was 14 days after 12 Gy photon irradiation and according to the obtained DCE-MRI results, the time between 14 and 21 days after RT might be crucial for low LET treated tumors as most changes in ETM parameters occurred within this period.

4.4.6 Curative vs. sub-curative doses

Within the selected time window of the study, an ETM-based discrimination between curative and sub-curative doses per modality was not possible. Surprisingly, histological parameters at the final observation day did not reveal striking differences either, leading to the conclusion that at least for this tumor model a longer follow-up is needed to discriminate response differences at different dose levels. When comparing the two groups with the same absorbed isodoses (37 Gy photons and 37 Gy ^{12}C-ions), ^{12}C-ions resulted in a faster and stronger effect on K_{trans} and v_{e}, and higher vessel density, and less hypoxia and proliferation at day 21 as expected for the biologically more effective ^{12}C-ions.

4.4.7 Statistical analysis

The results of the statistical analysis should be regarded with caution as statistically significant results do not necessarily imply biological relevance, and vice versa, especially for this pilot-study-like experiment. Due to the large number of voxels, the significance level was lowered to 0.1 % for the ETM fit parameters. Furthermore, significance tests could not be performed for longitudinal differences as no statistical test is available for dependent data with varying number of data points.

4.5 Longitudinal DCE-MRI study of the HI-tumor

DCE-MRI and histological techniques were also used to gain initial information on treatment-induced functional and morphological alterations after high single doses of ^{12}C-ions and photons in the moderately differentiated HI-tumor up to 21 days post-irradiation. The HI-tumor is better oxygenated than the chronic hypoxic AT1-tumor, comprises larger vessels, and is less radioresistant. This four-armed study consisted of two isoeffective curative dose groups (37 Gy ^{12}C-ions and 75 Gy photons) and two isoeffective sub-curative dose groups (18 Gy ^{12}C and 37 Gy photons). Again, the study design allowed for an iso-absorbed dose comparison at 37 Gy.

The text in section 4.5 and respective subsections was taken from reference [136] and has been originally written by myself.

4.5.1 Principle component analysis for the HI-tumor

Again, the ETM was chosen for pharmacokinetic modeling as it gave satisfying curve-fits and reasonable fit parameters in physiological ranges. However, despite the good fit quality, the obvious treatment-induced changes in tumor volume and histology were not reflected by the fit parameters. Endothelial cell apoptosis has been proposed to occur above threshold doses of 8 to 10 Gy [205-207] which was found in histology but not in the ETM parameters of the HI-tumor. The earlier study on the AT1-tumor (section 3.3.2) had shown that DCE-MRI is in fact suitable to measure the radiation response; see also [135, 208]. The very large inherent heterogeneity of the HI-tumor is suspected to mask potential differences of the fit parameters between the different treatment groups. Therefore, the analysis for the HI-tumor was extended by a principle component analysis (PCA) as demonstrated by Featherstone *et al.* [137]. This allows to classify voxels with similar concentration-time curves, i.e. similar physiology, into the same cluster and to investigate the fractions of each cluster for the different treatment groups and time points.

The five cluster were correlated with possible underlying morphologies on the histological level (Figure 52 A, B). Due to the high initial increase and the subsequent drop of the concentration level, voxels of cluster 1 are presumed to comprise large, intact vessels (Figure 52 C). The related high K_{trans} values therefore correspond to a high perfusion. Voxels of cluster 2 exhibit lower maximum concentration and shallower decrease in concentration as compared to cluster 1. Therefore, they are assumed to comprise large but less-perfused immature tumor vessels which frequently occur in untreated HI-tumors (Figure 52 D). The delayed increase and the plateau found for the curves of cluster 3 together with the associated high v_{e} value indicate an increased vascular permeability relative to cluster 1 and 2. This signal, however, cannot be unambiguously assigned as it could originate either from a few poorly perfused large or a bunch of poorly perfused small vessels (Figure 52 E). Due to the lower concentration level, voxels classified into cluster 4 are associated with a lower density

of small, permeable vessels (Figure 52 F). Voxels classified into cluster 5 accumulate almost no CA and are therefore assumed as barely perfused or potentially necrotic voxels (Figure 52 G). It should be kept in mind that, as a consequence of the low spatial resolution of the DCE-MRI data, the concentration-time curve of one voxel reflects an average value over 4.5 mm^3 tumor tissue.

4.5.2 Treatment response

PCA revealed that the vasculature of non-irradiated tumors mainly consisted of small leaky vessels occurring with low spatial density (cluster 4) intermitted by few large and immature vessels (cluster 2). Additionally, small regions of elevated vessel density (cluster 3) and mucin filled prostatic structures/necrosis (cluster 5) were found. Only very few voxels were assigned to the first cluster reflecting the overall immaturity of the vasculature. Irrespective of their size, non-irradiated control tumors maintained their vascular characteristics over time.

Irradiated tumors revealed vascular changes 7 days after RT (except for the slightly later responding 75 Gy photon group) when large vessels became more permeable. This is indicated by the decrease in the frequencies of cluster 1 and 2 voxels and the on-setting increase of the cluster 3 fraction. Considering the histological results at day 21, it can be concluded that the dominance of the third cluster originates from the remaining large vessels. At the same time, the further increase in the cluster 3 fraction is the combined result of tumor cell death, the subsequent shrinkage of the tumor (i.e. increase of the density of the remaining vessels), and further vessel degradation. No revascularization was observed in histology and DCE-MRI data. For the 75 Gy photon group, the increase in vascular permeability was slightly prolonged. However, the relevance of this delay is debatable due to the long interval between the fourth and the last imaging time point. Changes in vascular parameters, permeability, and blood flow depend highly on the investigated system and were observed as early as within the first 48 h [177, 198] up to 14 days [182] after single high dose photon irradiation by other researchers.

As mentioned in section 4.4.5 the contribution of endothelial cells and the vasculature to the irradiation response is still not fully uncovered and is discussed controversially. The findings of the present study on the HI-tumor accredit only a minor contribution of the vascular component towards overall tumor response as early vascular damage cannot explain the higher effectiveness of ^{12}C-ions in terms of local tumor control which was described earlier for this moderately differentiated tumor and the applied high single doses [24].

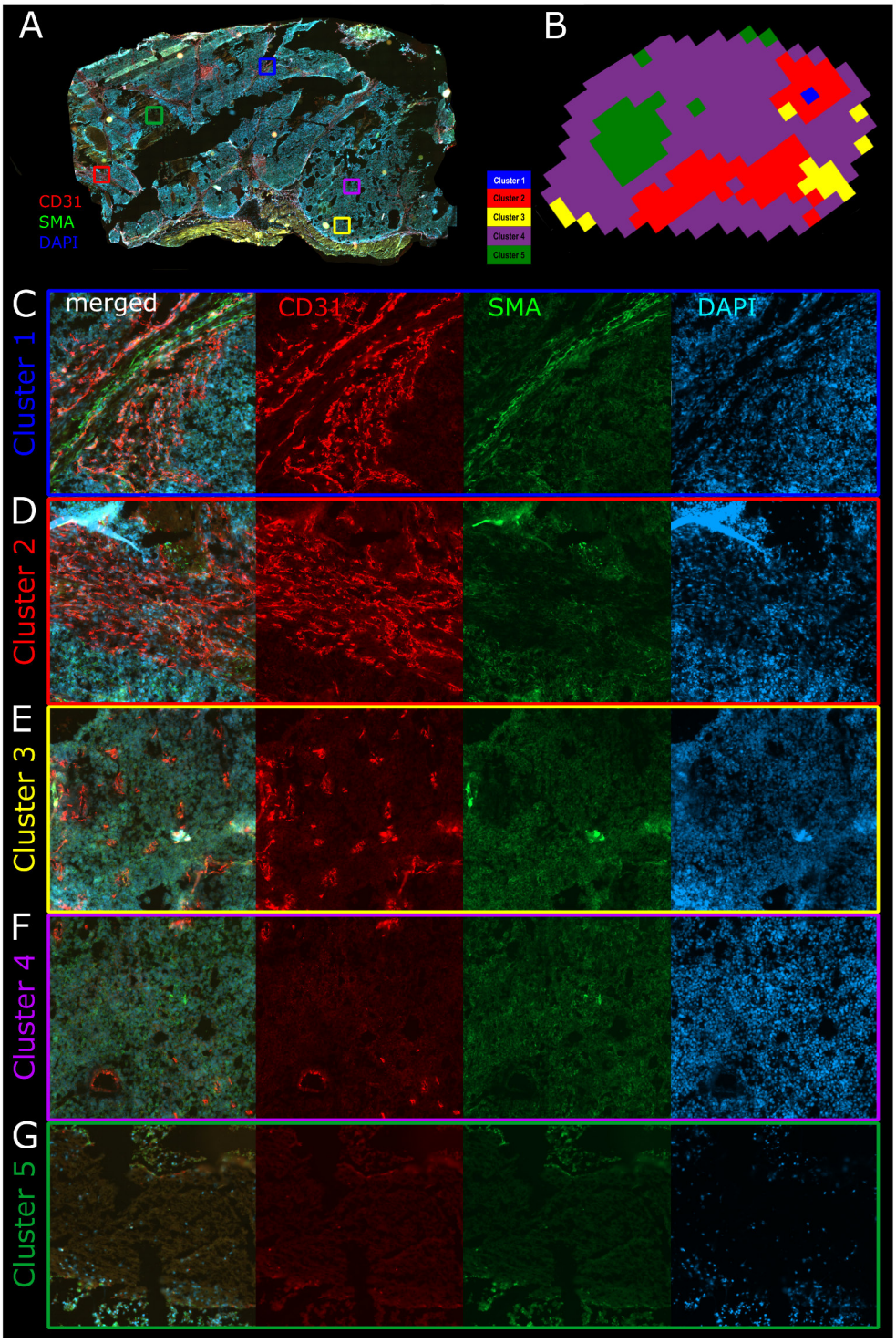

Figure 52 Correlation of the HI-tumor histology with the determined cluster. (A) Whole-mount image of a non-irradiated control tumor stained for vessels (CD31, red), pericytes (smooth muscle actin, SMA, green), and cell nuclei (DAPI, blue). The colored squares mark the positions of the representative close-up cluster images C - G. Their size (edge length of 0.7 mm) coincides with the size of a DCE-MRI voxel (edge length of 1 mm) including a correction factor that accounts for the tissue shrinkage during freezing. (B) Clustering of the same tumor visualized in A. It should be noted that the DCE-MRI slice does not coincide with the histological slide. (C - G) Close-ups of the marked colored squares for cluster 1-5. Figure reproduced from [136].

4.6 Comparison of the AT1- and HI-tumor's treatment response

Even though the ETM was used for both DCE-MRI studies, its parameters should be treated as qualitative rather than quantitative parameters impeding a direct quantitative comparison.

PCA revealed that non-irradiated control HI-tumors maintained their vascular architecture over the three-week observation period despite strongly increasing their volume. In contrast, AT1 control tumors showed a decrease in perfusion especially in the tumor core. This can be attributed to the slower growth rate and the more pronounced vasculature of the HI-tumor which enables the supply of large tumor volumes. Further differences between the tumor sublines were observed for treatment response.

The content of the following section was taken from reference [136] and has been originally written by myself.

The anaplastic AT1-tumor, exhibiting the highest RBE [24], showed a modality dependent treatment response as vascular perfusion/permeability increased already 3 days after ^{12}C-ion irradiation. Furthermore, ^{12}C-ions led to a slightly increased vascular density, lower amount of proliferating cells, and less hypoxia as compared to photons 21 days after RT [135]. In comparison, the moderately differentiated HI-tumor showed a simultaneous permeability increase 7 days after irradiation with both modalities revealing no modality dependency that could be resolved within the performed DCE-MRI study or visualized by immunohistochemistry after 21 days.

The different observed modality-dependencies and treatment response onsets of the two tumor sublines might be explained by differences in their vascular structures. The early responding and modality-sensitive AT1-tumor exhibits mainly small, immature capillaries while the HI-tumor comprises larger vessels of varying sizes. The high LET ^{12}C-ions are more effective on the immature capillaries of the AT1-tumor compared to photons. However, this does not seem to be the case for the larger vessels of the HI-tumor where the increase in vascular permeability was observed at the same time point after ^{12}C-ions and photons indicating elevated radiation tolerance of larger vessels. This is supported by Solevski *et al.* who showed in a human malignant melanoma xenograft that vessels with larger diameters did not lose their functionality after single doses of 15 Gy photons as opposed to smaller vessels, for which the fraction of functional vessels decreased by up to 35 % at 0.5 to 1.5 weeks after irradiation [186]. Interestingly, the results for both tumor sublines were independent of the applied dose (curative or sub-curative). This underpins the hypothesis that early vascular response cannot be the key mechanism that determines the tumors' fate with regard to local control.

4.7 Longitudinal histology study of the AT1-tumor after irradiation

A longitudinal histology study on the anaplastic and radioresistant AT1-tumor after irradiation with curative doses of either photons or ^{12}C-ions was performed to reveal the irradiation-induced changes in tumor perfusion, hypoxia, vascular density, proliferation, and DNA damage on a microscopic level. The time points were chosen in accordance with the DCE-MRI study including additional time points at 24 h and 10 days, respectively.

4.7.1 General tumor development after irradiation

As observed earlier, the AT1-tumors continued growing like the non-irradiated control tumors for one week after RT independent of the irradiation modality, before their growth stagnated and then declined [103, 135, 180]. Edema formation as a consequence of irradiation-induced increased vessel permeability and subsequent transudation of plasma components into the EES [209] might have led to the maintenance of the volume while tumor cells started disintegrating.

No differences in tumor morphology and immune response after single high dose photon and ^{12}C-ion irradiation could be identified on H&E stainings within the first 10 days. However, slight differences were found at day 21 of the DCE-MRI study suggesting that they manifested at a later stage at this high dose level.

4.7.2 Tumor hypoxia, vascularization, and perfusion

Non-irradiated controls

The volume-dependent study of non-irradiated AT1-control tumors revealed hypoxic microregions beyond a tumor size of 15 mm × 15 mm illustrating the tumor's diffusion limited oxygen supply. Increasing hypoxic fractions with increasing AT1-tumor size were also found by Eble *et al.* [210], and large hypoxic fractions in large AT1-tumor were also described by other researchers [68, 83, 172].

Tumors with a size of 10 mm × 10 mm showed no pimonidazole-positive areas which is commonly interpreted as normoxia. On the other hand, there are indications suggesting that the AT1-tumor is not normoxic at this size. The clamping experiments of the PAI study demonstrated an overall reduced oxygen signal (median values of sO_2-distributions ranged from 37 to 46 % sO_2) as well as an unchanged PAI-signal after clamping of the AT1-tumor [96]. These findings are in line with the preliminary results of ongoing experiments, where clamping of AT1-tumors of the same size before and during irradiation with photons results in a maximum OER of 1.05 compared to non-clamped AT1-tumors (unpublished data by Dr. Christin Glowa). Both experiments imply that the AT1-tumor comprises an intrinsically low oxygenation status to such an extent that clamping could not further reduce the oxygen sup-

ply. Nevertheless, the AT1-tumor exhibits a high proliferative rate which might be enabled by the altered enzymatic profile [94] that marks the tumor's adaption to oxygen-depletion.

Generally, pimonidazole has to be considered as a surrogate-marker for hypoxia. Pimonidazole gets reductively activated under hypoxic conditions and subsequently forms adducts with the cells' thiol groups that can be detected by histological methods. In the presence of oxygen, the initially reduced form of pimonidazole gets re-oxidized inhibiting adduct formation [211]. Adduct formation is proclaimed to take place at an pO_2 of 10 mmHg or lower [212, 213] which means that moderate hypoxic regions with an pO_2 slightly above 10 mmHg cannot be identified by pimonidazole [212]. Taking into account the above mentioned experimental findings, this might be the case for the pimonidazole-negative 10 mm × 10 mm AT1-tumors. The ground truth could in principle be detected by electrode measurements; however this method was not available at the DKFZ.

Despite the low fraction of $CD31^+/SMA^+$-capillaries, tumors expressed a SMA-rich texture that might mark myofibroblasts, which are a sign of reactivated stroma associated with tumorigenesis and progression in human prostate cancer [214, 215]. The high fraction of intermediately-perfused tumor areas is the result of vascular immaturity and the absence of large vessels. Overall, the perfused area (combining the intermediately- and highly-perfused regimes) corresponds to that of large AT1-tumors as determined by Mena-Romano *et al.* [172]. Intermediately- and non-perfused tumor areas comprised comparable vessel densities suggesting that a large fraction of capillaries in both classes are non-functional. The vessel density was significantly larger than that reported by Zhao *et al.* (45 ± 13 vessels/mm^2) who counted vessels in selected light microscopy images [171] and Mena-Romano *et al.* (101 ± 131 vessels/mm^2) who manually counted vessels in selected fluorescence images [172]. However, the automatic counting of contrast-rich whole-mount fluorescence images as performed in this study presumably gives superior statistics and thus more reliable results as compared to the previous studies.

Photon irradiation

Photon treated tumors showed pimonidazole staining after 24 h. However, when inspecting the whole-mount images with the three highest hypoxic fractions (16 %, 8 %, and 6 %, respectively), it should be noted that their pimonidazole staining exceeded only slightly the threshold that was set for the analysis and that they were in close vicinity to the still slightly visible original transplantion fragments (identified as continuous avascular areas). This challenges the assumption that the pimonidazole-positive areas are irradiation-induced. No pimonidazole-positive regions were found in the remaining tumor areas. Hence, the hypoxic fractions at 24 h after photon irradiation should be treated with reservation.

Credible pimonidazole staining revealed hypoxia 10 days after photon irradiation when the vascular density was reduced to approximately 40 % of the control's density. The fact that

the preceding steady decrease in vascular density did not go along with any perfusion alterations in the tumors and did not show any dependency on the perfusion class further underpins the assumption that the majority of the $CD31^+$-structures is non-functional and does not contribute to the tumor's supply [55, 186]. A comparably late increase in hypoxia was also found by Bussink *et al.* 11 days after 10 Gy photon irradiation of a human squamous cell carcinoma xenograft [216] and by Goda *et al.* after 20 Gy photon irradiation of MTG-B and RIF-1 tumors [217]. Kallman *et al.* attributed this late occurring hypoxia to eventually manifested stromal injuries and inadequate perfusion through the remaining vasculature [218]. The rapid drop in vascular density within the first 24 h can be attributed to the high irradiation doses [184] and the large number of non-functional vessels [186].

Hyperperfusion after 24 h was also described by Brown *et al.* [177] and conforms to the post-irradiation perfusion changes observed by Bussink *et al.* [216]. It can be assumed that this led to a re-oxygenation shortly after irradiation [217, 219, 220]. The subsequent constant tumor perfusion until 10 days after RT is in accordance with the parameters K_{trans} and normalized AUC of the DCE-MRI study where the hyperperfusion at 24 h was missed. Unchanged perfusion was also found by Tsai *et al.* for the first week after single-fraction and fractionated radiation [185].

^{12}C-ion irradiation

Compared to photons, ^{12}C-ions led to an earlier onset of hypoxia with a maximum at day 7. The temporal decrease in the density of $CD31^+$-structures was identical to that after photon irradiation suggesting that the earlier oxygen depletion originated from functional rather than structural disruptions. Taking the early rise in K_{trans} of the DCE-MRI study at day 3 into account, it can be assumed that ^{12}C-ions increased the capillaries' permeability more than photons did without completely destroying them. In the following this increased permeability might have pandered edema formation which in turn led to compressed capillaries due to the elevated interstitial pressure, eventually leading to reduced blood flow and return to initial values [209]. After its maximum, the hypoxic fraction declines at day 10 and 14 even though the non-perfused tumor fraction is very high. This is due to the intensely reduced number of intact tumor cells that could potentially be hypoxic.

Endothelial turnover in tumors is much faster than in normal tissue [221], so that the increase in vascular density and maturity at day 21 after ^{12}C-ion irradiation could result from neoangiogenesis with coinciding tumor shrinkage rather than survival of SMA^+-vessels. This final increase in vascular density was also reflected in the parameter v_{p} of the DCE-MRI study which also revealed an elevated vascular fraction at that time point.

To further understand the irradiation-induced oxygenation changes, staining for endogenous hypoxia markers such as the transcription factor HIF-1α [222] and the thereby augmented expression of glucose transporters (e.g. Glut-1) [223] and CA IX [224] should be considered.

To better distinguish the temporal changes in vascular perfusion and permeability, the use of differently sized perfusion markers could be considered. Potiron *et al.* used Hoechst 33342 (616 Da) to assess vessel permeability in relation to large dextran molecules (2 MDa), which remained intravascular as a perfusion marker, and medium dextran molecules (10 kDa) to assess interstitial diffusion [225].

Major alterations in hypoxia occurred after one week which would make 7 and 12 days after irradiation suitable candidates for measurement time points of future multimodal imaging studies.

4.7.3 Cellular response

Irradiation-induced DNA DSBs were identified by staining for γH2AX. However, γH2AX foci also form during normal physiological processes such as DNA fragmentation during apoptosis and occur as transitional DSBs during S-phase [226]. Therefore, $\gamma H2AX^+$-cells were divided into intermediate intensity cells and high intensity cells to distinguish intrinsic γH2AX foci already present in non-irradiated AT1 tumors from irradiation-induced γH2AX foci. This analysis approach is supported by the finding that irradiation-induced γH2AX foci are significantly bigger than irradiation-unrelated foci [227, 228]. Although the spatial resolution of the microscopic images was not sufficient to identify individual foci in cell nuclei, the accumulation of many large foci, which is expected after single high dose irradiation, displays as overall bright, i.e. high intensity, nuclei [141]. Nuclei with few small γH2AX foci exhibit low intensities.

The high percentage of initial intermediate intensity $\gamma H2AX^+$-cells underlines the anaplastic and rapid proliferative characteristics of the AT1-tumor [229]. The peak observed after 24 h resembles cells with few irradiation-induced DNA DSBs that were subject to subsequent repair mechanisms. However, it can be assumed that tumor cells accumulated more DNA errors due to mismatching with every cell cycle [230] until undergoing mitotic death [231]. This is mirrored by a steady decrease of $\gamma H2AX^+$-cells below control tumor levels.

The high intensity peak represents cells with a dense incidence of irradiation-induced DNA DSBs. Presumably, this peak was even higher shortly after irradiation as other studies have demonstrated the occurrence of discrete γH2AX foci within minutes after irradiation [141, 226]. The rapid decline of the fraction of high intensity γH2AX cells to 1 % is the joint response to high-single dose-induced instant cell death and partial cellular repair. Averbeck *et al.* observed very efficient rejoining after ^{12}C-ion irradiation and proclaim that misrepair of DNA DSBs plays a major role towards the increased RBE of heavy ions [232]. This is in accordance with the ongoing, but decreasing, proliferative activity of the tumor cells.

BrdU is incorporated into the DNA during S-phase and hence reflects the cells' proliferative activity. The drop in $BrdU^+$-cells within the first 24 h indicates an irradiation-induced cell cycle arrest which is in accordance with the increased $\gamma H2AX^+$-cell fraction at that time

point [233, 234]. Proliferation rates returned to initial values at day 3 which can be considered as the joint result of (i) tumor cells that have died due to severe irradiation-induced DNA damage, (ii) sub-lethally damaged cells that continued proliferation after overcoming cell cycle arrest [235], and (iii) survived tumor cells that were stimulated to proliferate by paracrine signaling of dying cells [236]. As DNA damages manifest to eventually become lethal with every following cell-cycle, the proliferation rate steadily decreases for the later time points. The $BrdU^+$-cells that were found at the late time points were bloated so-called "doomed to die" cells.

A limitation of the analysis protocol is the normalization of the $\gamma H2AX^+$- and $BrdU^+$-cells to the overall DAPI cell count because DAPI non-selectively stains all cell nuclei. This way, not just tumor cells but also the invading immune cells that were identified on H&E stains are included in the overall cell count leading to an underestimation of the fraction of $\gamma H2AX^+$- and $BrdU^+$-cells. With respect to the overall cell count, the identification of AT1-tumor cells would be of upmost interest. In earlier studies, Glowa *et al.* have found that 77.7 % of AT1-tumor cells expressed CK19 [229] which could be used as a tumor cell marker for a rough estimation of remaining tumor cells. Additionally, immune cells could be identified by staining for CD45 [237] to eliminate them from the overall cell count. The immune response could be further assessed by specific staining for macrophages [238] and NK cells (CD16, CD56) [239] which might also give insights into differential effects of photons and ^{12}C-ions on the immune response [25]. Furthermore, the cellular response towards irradiation should be examined in more detail by staining for apoptotic markers such as caspase 3 [240, 241] or by performing a TUNEL assay.

To investigate cell proliferation in hypoxic areas and differentially perfused areas, staining for BrdU in combination with pimonidazole and Hoechst 33342 should be considered for future studies. Furthermore, the proliferation of endothelial cells after irradiation could be assessed by double staining for CD31 and BrdU.

4.8 High LET vs. low LET irradiation

The differential effects of high LET ^{12}C-ions and low LET photons on the anaplastic and chronic hypoxic AT1-tumor and the moderately differentiated HI-tumor were investigated.

The isoeffective doses for ^{12}C-ions and photons of the AT1-tumor were calculated based on the RBE for 100 % local tumor control that was determined by Glowa *et al.* [24]. The identical results for vascular density, proliferation, and DNA DSBs after both, photons and ^{12}C-ions within the first 10 days, confirm this RBE on a histological level. Differences were only observed in the temporal progress of hypoxia and perfusion changes in the DCE-MRI study and on a histological level. Minor histological differences manifested at later time points.

For the HI-tumors, histological data was only available for the time point 21 days after irradiation when tumor degradation was already advanced. No differences between high LET and low LET irradiation were found, neither in the results of the PCA nor on a histological level at day 21.

Photons and ^{12}C-ions act through different mechanisms: while photons damage the DNA mostly through indirect, oxygen-sensitive effects, ^{12}C-ions directly induce clustered DNA DSBs largely independent from the presence of oxygen [21]. In spite of these differences, the differential effects measured by imaging as well as on the histological level were rather subtle for both tumor sublines. This may be explained by the fact that the applied high single doses masked those differences in the response to photon and ^{12}C-ion irradiation. With this respect, even the sub-curative doses that were used in the DCE-MRI studies can be considered as being too high to resolve any differential effects as only dose-independent treatment responses were found. Based on these results, fractionated experiments would be of high interest to further examine the differential effects of photons and ^{12}C-ions on hypoxia.

4.9 Conclusion

In this thesis, novel technical developments as well as biological investigations have been performed. On the technical side, a novel analysis protocol for PAI was developed and has been demonstrated to be feasible for the characterization of the oxygenation status of the three Dunning tumor sublines H, HI, and AT1 under ambient conditions as well as for altered external oxygen supply. Furthermore, a novel method for BAT estimation of DCE-MRI data based on a flexible spline-based approximation model and automatic parameter estimation by generalized cross validation was developed which is able to adapt to various types of TCCs. Its broad applicability was demonstrated.

On the biological side, two longitudinal DCE-MRI studies, which were performed for the AT1- and HI-tumor after irradiation with single curative and sub-curative doses of either photons or ^{12}C-ions, were analyzed to investigate irradiation-induced functional vascular changes. For the anaplastic AT1-tumor, a delayed response after irradiation with photons compared to ^{12}C-ions was found. For the moderately differentiated HI-tumor vascular permeability increased at the same time for both modalities. The different radiation sensitivities of the HI- and AT1-tumor for the two irradiation modalities indicate that the irradiation-induced vascular response depends on the structural-functional status of the tumor vasculature. In addition, the results of both studies were dose-independent, suggesting that the initial vascular response only plays a minor role for local tumor control at high single doses. For the AT1-tumor the RBE for local tumor control was confirmed on a microscopic level within the first 10 days after irradiation. The obtained results suggest that the high single doses mask potential differential mechanistic effects that result from the different microscopic dose deposition patterns of photons and ^{12}C-ions.

5 Outlook

The DCE-MRI studies and the longitudinal histology study provide a first important characterization of the development of hypoxia-related parameters prior to and after irradiation with either photons or ^{12}C-ions. Nevertheless, there were some ambiguous results that require further research. A dedicated longitudinal multimodal imaging- and histology-study after irradiation is expected to contribute significantly towards the understanding of the differential effects of photon and ^{12}C-ion irradiation with regard to tumor hypoxia and perfusion. Such a study is planned for the future taking into account the results of the present thesis for its study design. For each modality and dose level, AT1-tumors will be imaged one day before irradiation and at two time points afterwards. Based on the performed histology study, suitable time points to detect changes in hypoxia were identified to be 7 and 12 days post-irradiation. Each imaging session should consist of PET, DCE-MRI, and PAI measurements. PET measurements will enable the direct visualization of hypoxia with the hypoxia-sensitive tracer [^{18}F]FMISO, PAI will be used to assess overall tumor oxygenation employing the newly developed analysis protocol, and DCE-MRI will give insights into the tumors' perfusion. Further MRI measurements such as diffusion weighted imaging may be added. MRI and PET measurements will be sequentially conducted at the new 9.4 T small animal PET/MRI scanner allowing spatial correlation of the two measurements which was not possible up to now. Furthermore, a higher spatial resolution as compared to the presented studies, which were performed at a clinical 1.5 T MRI scanner, is expected from the higher magnetic field strength. Additionally, after each imaging session a sufficient number of animals will be drawn from the study for histological examinations enabling a direct correlation of the imaging modalities to histology for each time point.

As a further step, it would be of great interest to perform the same multimodal imaging study for the moderately differentiated and acute hypoxic HI-tumor to reveal the influence of the underlying tissue characteristics on the differential irradiation response between low LET photons and high LET ^{12}C-ions.

As the results of the performed studies suggest that the single dose irradiations are so high that differential effects between photons and ^{12}C-ions are masked, fractionated experiments should also be considered for the future.

References

1. Bray F, Ferlay J, Soerjomataram I, Siegel RL, Torre LA, and Jemal A, *Global cancer statistics 2018: GLOBOCAN estimates of incidence and mortality worldwide for 36 cancers in 185 countries.* CA Cancer J Clin, 2018. **68**(6): p. 394-424.
2. Ferlay J, Ervik M, Lam F, Colombet M, Mery L, Piñeros M, Znaor A, Soerjomataram I, and Bray F, *Global Cancer Observatory: Cancer Today*. 2018, Last access: 26.06.2019; Available from: https://gco.iarc.fr/today.
3. Sauer R, *Strahlentherapie und Onkologie*. Vol. 5. 2010, München Elsevier, Urban & Fischer
4. Böcker W, Denk H, and Wiestler OD, *Pathologie*. Vol. 5. 2012, München: Elsevier, Urban & Fischer.
5. Epstein J, Egevad L, Amin MB, Delahunt B, Srigley JR, Humphrey PA, and Committee G, *The 2014 International Society of Urological Pathology (ISUP) Consensus Conference on Gleason Grading of prostatic carcinoma: Definition of Grading Patterns and Proposal for a New Grading System.* Am J Surg Pathol, 2014. **40**(2): p. 244-252.
6. Cosset JM, *The dawn of radiotherapy, between strokes of genius, dramas and controversies.* Cancer Radiother, 2016. **20**(6-7): p. 595-600.
7. Miller KD, Siegel RL, Lin CC, Mariotto AB, Kramer JL, Rowland JH, Stein KD, Alteri R, and Jemal A, *Cancer treatment and survivorship statistics, 2016.* CA Cancer J Clin, 2016. **66**(4): p. 271-289.
8. Bekelman JE, Mitra N, Efstathiou J, Liao K, Sunderland R, Yeboa DN, and Armstrong K, *Outcomes after intensity-modulated versus conformal radiotherapy in older men with nonmetastatic prostate cancer.* Int J Radiat Oncol Biol Phys, 2011. **81**(4): p. e325-334.
9. Durante M and Loeffler JS, *Charged particles in radiation oncology.* Nat Rev Clin Oncol, 2010. **7**(1): p. 37-43.
10. Suzuki M, Kase Y, Yamaguchi H, Kanai T, and Ando K, *Relative biological effectiveness for cell-killing effect on various human cell lines irradiated with heavy-ion medical accelerator in Chiba (HIMAC) carbon-ion beams.* Int J Radiation Oncology Biol Phys, 2000. **48**(1): p. 241-250.
11. Shipley WU, Tepper JE, Prout GR, Verhey LJ, Mendiondo OA, Goitein M, Koehler AM, and Suit HD, *Proton radiation as boost therapy for localized prostatic carcinoma.* JAMA, 1979. **241**(18): p. 1912-1915.
12. Wilson RR, *Radiological use of fast protons.* Radiology, 1946. **47**(5): p. 487-491.
13. Fossati P, Matsufuji N, Kamada T, and Karger CP, *Radiobiological issues in prospective carbon ion therapy trials.* Med Phys, 2018. **45**(11): p. e1096-e1110.
14. Kamada T, Tsujii H, Blakely EA, Debus J, De Neve W, Durante M, Jäkel O, Mayer R, Orecchia R, Pötter R, Vatnitsky S, and Chu WT, *Carbon ion radiotherapy in Japan: an assessment of 20 years of clinical experience.* Lancet Oncol, 2015. **16**(2): p. e93-e100.

15. Allen C, Borak TB, Tsujii H, and Nickoloff JA, *Heavy charged particle radiobiology: using enhanced biological effectiveness and improved beam focusing to advance cancer therapy.* Mutat Res, 2011. **711**(1-2): p. 150-157.

16. Scholz M, *Dose response of biological systems to low- and high-LET radiation*, in *Microdosimetric Response of Physical and Biological Systems to low- and high-LET Radiations: Theory and Applications to Dosimetry*, Y. Horowitz, Editor. 2006, Elsevier Science. p. 1-73.

17. Frankenberg D, Frankenberg-Schwager M, Blöcher D, and Harbich R, *Evidence for DNA double-strand breaks as the critical lesions in yeast cells irradiated with sparsely or densely ionizing radiation under oxic or anoxic conditions.* Radiat Res, 1981. **88**(3): p. 524-532.

18. Iliakis G, *The role of DNA double strand breaks in ionizing radiation-induced killing of eukaryotic cells.* Bioessays, 1991. **13**(12): p. 641-648.

19. Brown JM and Wilson WR, *Exploiting tumour hypoxia in cancer treatment.* Nat Rev Cancer, 2004. **4**(6): p. 437-447.

20. Schlaff CD, Krauze A, Belard A, O'Connell J, and Camphausen KA, *Bringing the heavy: carbon ion therapy in the radiobiological and clinical context.* Radiat Oncol, 2014. **9**(1): p. 88.

21. Hada M and Georgakilas AG, *Formation of clustered DNA damage after high-LET irradiation: a review.* J Radiat Res, 2008. **49**(3): p. 203-210.

22. Masunaga S, Ando K, Uzawa A, Hirayama R, Furusawa Y, Koike S, and Ono K, *The radiosensitivity of total and quiescent cell populations in solid tumors to 290 MeV/u carbon ion beam irradiation in vivo.* Acta Oncol, 2008. **47**(6): p. 1087-1093.

23. Hirayama R, Uzawa A, Takase N, Matsumoto Y, Noguchi M, Koda K, Ozaki M, Yamashita K, Li H, Kase Y, Matsufuji N, Koike S, Masunaga S, Ando K, Okayasu R, and Furusawa Y, *Evaluation of SCCVII tumor cell survival in clamped and non-clamped solid tumors exposed to carbon-ion beams in comparison to X-rays.* Mutat Res, 2013. **756**(1-2): p. 146-151.

24. Glowa C, Karger CP, Brons S, Zhao D, Mason RP, Huber PE, Debus J, and Peschke P, *Carbon ion radiotherapy decreases the impact of tumor heterogeneity on radiation response in experimental prostate tumors.* Cancer Lett, 2016. **378**(2): p. 97-103.

25. Conrad S, Ritter S, Fournier C, and Nixdorff K, *Differential effects of irradiation with carbon ions and x-rays on macrophage function.* J Radiat Res, 2009. **50**(3): p. 223-231.

26. Shimokawa T, Ma L, Ando K, Sato K, and Imai T, *The future of combining carbon-ion radiotherapy with immunotherapy: evidence and progress in mouse models.* Int J Particle Ther, 2016. **3**(1): p. 61-70.

27. Ogata T, Teshima T, Kagawa K, Hishikawa Y, Takahashi Y, Kawaguchi A, Suzumoto Y, Nojima K, Furusawa Y, and Matsuura N, *Particle irradiation suppresses metastatic potential of cancer cells.* Cancer Res, 2005. **65**(1): p. 113-120.

28. Kamlah F, Hanze J, Arenz A, Seay U, Hasan D, Juricko J, Bischoff B, Gottschald OR, Fournier C, Taucher-Scholz G, Scholz M, Seeger W, Engenhart-Cabillic R, and Rose F, *Comparison of the effects of carbon ion and photon irradiation on the*

angiogenic response in human lung adenocarcinoma cells. Int J Radiat Oncol Biol Phys, 2011. **80**(5): p. 1541-1549.

29. Durante M and Debus J, *Heavy Charged Particles: Does Improved Precision and Higher Biological Effectiveness Translate to Better Outcome in Patients?* Semin Radiat Oncol, 2018. **28**(2): p. 160-167.

30. Giap H and Jermann M, *Particle therapy co-operative group website*. 2019, Last access: 26.06.2019; Available from: https://ptcog.ch/index.php/clinical-protocols.

31. Lazar AA, Schulte R, Faddegon B, Blakely EA, and Roach M, *Clinical trials involving carbon-ion radiation therapy and the path forward.* Cancer, 2018. **124**(23): p. 4467-4476.

32. Dosanjh M, Jones B, Pawelke J, Pruschy M, and Sorensen BS, *Overview of research and therapy facilities for radiobiological experimental work in particle therapy. Report from the European Particle Therapy Network radiobiology group.* Radiother Oncol, 2018. **128**(1): p. 14-18.

33. Combs SE, Ellerbrock M, Haberer T, Habermehl D, Hoess A, Jakel O, Jensen A, Klemm S, Munter M, Naumann J, Nikoghosyan A, Oertel S, Parodi K, Rieken S, and Debus J, *Heidelberg Ion Therapy Center (HIT): Initial clinical experience in the first 80 patients.* Acta Oncol, 2010. **49**(7): p. 1132-40.

34. Uhl M, Mattke M, Welzel T, Oelmann J, Habl G, Jensen AD, Ellerbrock M, Haberer T, Herfarth KK, and Debus J, *High control rate in patients with chondrosarcoma of the skull base after carbon ion therapy: first report of long-term results.* Cancer, 2014. **120**(10): p. 1579-85.

35. Uhl M, Mattke M, Welzel T, Roeder F, Oelmann J, Habl G, Jensen A, Ellerbrock M, Jakel O, Haberer T, Herfarth K, and Debus J, *Highly effective treatment of skull base chordoma with carbon ion irradiation using a raster scan technique in 155 patients: first long-term results.* Cancer, 2014. **120**(21): p. 3410-7.

36. Akbaba S, Lang K, Held T, Bulut OC, Mattke M, Uhl M, Jensen A, Plinkert P, Rieken S, Herfarth K, Debus J, and Adeberg S, *Accelerated Hypofractionated Active Raster-Scanned Carbon Ion Radiotherapy (CIRT) for Laryngeal Malignancies: Feasibility and Safety.* Cancers (Basel), 2018. **10**(10).

37. Habl G, Uhl M, Katayama S, Kessel KA, Hatiboglu G, Hadaschik B, Edler L, Tichy D, Ellerbrock M, Haberer T, Wolf MB, Schlemmer HP, Debus J, and Herfarth K, *Acute Toxicity and Quality of Life in Patients With Prostate Cancer Treated With Protons or Carbon Ions in a Prospective Randomized Phase II Study--The IPI Trial.* Int J Radiat Oncol Biol Phys, 2016. **95**(1): p. 435-43.

38. Mattke M, Vogt K, Bougatf N, Welzel T, Oelmann-Avendano J, Hauswald H, Jensen A, Ellerbrock M, Jakel O, Haberer T, Herfarth K, Debus J, and Uhl M, *High control rates of proton- and carbon-ion-beam treatment with intensity-modulated active raster scanning in 101 patients with skull base chondrosarcoma at the Heidelberg Ion Beam Therapy Center.* Cancer, 2018. **124**(9): p. 2036-2044.

39. Sprave T, Verma V, Sterzing F, Bruckner T, Hees K, Land B, Jakel O, Herfarth K, Debus J, and Uhl M, *Cost-Effectiveness of Carbon Ion Radiation Therapy for Skull Base Chordoma Utilizing Long-Term (10-Year) Outcome Data.* Anticancer Res, 2018. **38**(8): p. 4853-4858.

40. Combs SE and Debus J, *Treatment with heavy charged particles: systematic review of clinical data and current clinical (comparative) trials.* Acta Oncol, 2013. **52**(7): p. 1272-1286.

41. Fowler JF, *The radiobiology of prostate cancer including new aspects of fractionated radiotherapy.* Acta Oncol, 2005. **44**(3): p. 265-276.

42. Lee WR, Dignam JJ, Amin MB, Bruner DW, Low D, Swanson GP, Shah AB, D'Souza DP, Michalski JM, Dayes IS, Seaward SA, Hall WA, Nguyen PL, Pisansky TM, Faria SL, Chen Y, Koontz BF, Paulus R, and Sandler HM, *Randomized Phase III Noninferiority Study Comparing Two Radiotherapy Fractionation Schedules in Patients With Low-Risk Prostate Cancer.* J Clin Oncol, 2016. **34**(20): p. 2325-2332.

43. Yeoh EE, Holloway RH, Fraser RJ, Botten RJ, Di Matteo AC, Butters J, Weerasinghe S, and Abeysinghe P, *Hypofractionated versus conventionally fractionated radiation therapy for prostate carcinoma: updated results of a phase III randomized trial.* Int J Radiat Oncol Biol Phys, 2006. **66**(4): p. 1072-1083.

44. Pollack A, Walker G, Horwitz EM, Price R, Feigenberg S, Konski AA, Stoyanova R, Movsas B, Greenberg RE, Uzzo RG, Ma C, and Buyyounouski MK, *Randomized trial of hypofractionated external-beam radiotherapy for prostate cancer.* J Clin Oncol, 2013. **31**(31): p. 3860-3868.

45. Arcangeli G, Saracino B, Gomellini S, Petrongari MG, Arcangeli S, Sentinelli S, Marzi S, Landoni V, Fowler J, and Strigari L, *A prospective phase III randomized trial of hypofractionation versus conventional fractionation in patients with high-risk prostate cancer.* Int J Radiat Oncol Biol Phys, 2010. **78**(1): p. 11-18.

46. Miralbell R, Roberts SA, Zubizarreta E, and Hendry JH, *Dose-fractionation sensitivity of prostate cancer deduced from radiotherapy outcomes of 5,969 patients in seven international institutional datasets: alpha/beta = 1.4 (0.9-2.2) Gy.* Int J Radiat Oncol Biol Phys, 2012. **82**(1): p. e17-24.

47. Le Q-T, Loo BW, Ho A, Christian C, Koong AC, Wakelee H, Kee S, Constantinescu D, Whyte RI, and Donington J, *Results of a phase I dose-escalation study using single-fraction stereotactic radiotherapy for lung tumors.* J Thorac Oncol, 2006. **1**(8): p. 802-809.

48. Yamamoto N, Miyamoto T, Nakajima M, Karube M, Hayashi K, Tsuji H, Tsujii H, Kamada T, and Fujisawa T, *A Dose Escalation Clinical Trial of Single-Fraction Carbon Ion Radiotherapy for Peripheral Stage I Non-Small Cell Lung Cancer.* J Thorac Oncol, 2017. **12**(4): p. 673-680.

49. Brenner DJ and Hall EJ, *Hypofractionation in prostate cancer radiotherapy.* Transl Cancer Res, 2018. **7**(S6): p. S632-S639.

50. Hanahan D and Weinberg RA, *The hallmarks of cancer.* Cell, 2000. **100**(1): p. 57-70.

51. Gray LH, Conger AD, Ebert M, Hornsey S, and Scott OCA, *The concentration of oxygen dissolved in tissues at the time of irradiation as a factor in radiotherapy.* Br J Radiol, 1953. **26**(312): p. 638-648.

52. Hall EJ and Giaccia AJ, *Radiobiology for the Radiobiologist*. 7 ed. 2012, Philadelphia, Pennsylvania, USA: Lippincott Williams & Williams.

53. Multhoff G, Radons J, and Vaupel P, *Critical role of aberrant angiogenesis in the development of tumor hypoxia and associated radioresistance.* Cancers (Basel), 2014. **6**(2): p. 813-828.

54. Vaupel P and Mayer A, *Tumor Hypoxia: Causative Mechanisms, Microregional Heterogeneities, and the Role of Tissue-Based Hypoxia Markers*, in *Oxygen Transport to Tissue XXXVIII - Advanced in Experimental Medicine and Biology*, Q. Luo, et al., Editors. 2016, Springer International Publishing Switzerland: Switzerland. p. 77-86.

55. Vaupel P, *Tumor microenvironmental physiology and its implications for radiation oncology.* Semin Radiat Oncol, 2004. **14**(3): p. 198-206.

56. Höckel M and Vaupel P, *Tumor hypoxia: definitions and current clinical, biologic, and molecular aspects.* J Natl Cancer Inst, 2001. **93**(4): p. 266-276.

57. Harris AL, *Hypoxia--a key regulatory factor in tumour growth.* Nat Rev Cancer, 2002. **2**(1): p. 38-47.

58. Ke Q and Costa M, *Hypoxia-inducible factor-1 (HIF-1).* Mol Pharmacol, 2006. **70**(5): p. 1469-1480.

59. Gallez B, Baudelet C, and Jordan BF, *Assessment of tumor oxygenation by electron paramagnetic resonance: principles and applications.* NMR Biomed, 2004. **17**(5): p. 240-262.

60. Semenza GL, *Defining the role of hypoxia-inducible factor 1 in cancer biology and therapeutics.* Oncogene, 2010. **29**(5): p. 625-634.

61. Stewart GD, Ross JA, McLaren DB, Parker CC, Habib FK, and Riddick AC, *The relevance of a hypoxic tumour microenvironment in prostate cancer.* BJU Int, 2010. **105**(1): p. 8-13.

62. Bentzen SM and Gregoire V, *Molecular imaging-based dose painting: a novel paradigm for radiation therapy prescription.* Semin Radiat Oncol, 2011. **21**(2): p. 101-110.

63. Krohn KA, Link JM, and Mason RP, *Molecular imaging of hypoxia.* J Nucl Med, 2008. **49 Suppl 2**: p. 129S-148S.

64. Menon C and Fraker DL, *Tumor oxygenation status as a prognostic marker.* Cancer Lett, 2005. **221**(2): p. 225-235.

65. Turaka A, Buyyounouski MK, Hanlon AL, Horwitz EM, Greenberg RE, and Movsas B, *Hypoxic prostate/muscle pO2 ratio predicts for outcome in patients with localized prostate cancer: long-term results.* Int J Radiat Oncol Biol Phys, 2012. **82**(3): p. e433-439.

66. Milosevic M, Warde P, Menard C, Chung P, Toi A, Ishkanian A, McLean M, Pintilie M, Sykes J, Gospodarowicz M, Catton C, Hill RP, and Bristow R, *Tumor hypoxia predicts biochemical failure following radiotherapy for clinically localized prostate cancer.* Clin Cancer Res, 2012. **18**(7): p. 2108-2114.

67. Le QT, Chen E, Salim A, Cao H, Kong CS, Whyte R, Donington J, Cannon W, Wakelee H, Tibshirani R, Mitchell JD, Richardson D, O'Byrne KJ, Koong AC, and Giaccia AJ, *An evaluation of tumor oxygenation and gene expression in patients with early stage non-small cell lung cancers.* Clin Cancer Res, 2006. **12**(5): p. 1507-1514.

68. Mason RP, Constantinescu A, Hunjan S, Le D, Hahn EW, Antich PP, Blum C, and Peschke P, *Regional tumor oxygenation and measurement of dynamic changes.* Radiat Res, 1999. **152**(3): p. 239-249.

69. Höckel M, Schlenger K, Aral B, Mitze M, Schäffer U, and Vaupel P, *Association between tumor hypoxia and malignant progression in advanced cancer of the uterine cervix.* Cancer Res, 1996. **56**(19): p. 4509-4515.

70. Bentzen L, Keiding S, Grönroos T, Hansen SB, and Overgaard J, *Assessment of hypoxia in experimental mice tumours by [18F]fluoromisonidazole PET and pO2 electrode measurements. Influence of tumour volume and carbogen breathing.* Acta Oncol, 2002. **41**(3): p. 304-312.

71. O'Hara JA, Goda F, Demidenko E, and Swartz HM, *Effect on regrowth delay in a murine tumor of scheduling split-dose irradiation based on direct pO2 measurement by electron paramagnetic resonance oximetry.* Radiat Res, 1998. **150**(5): p. 549-556.

72. Lapi SE, Voller TF, and Welch MJ, *Positron Emission Tomography Imaging of Hypoxia.* PET Clin, 2009. **4**(1): p. 39-47.

73. Rasey JS, Koh W-J, Grierson JR, Grunbaum Z, and Krohn KA, *Radiolabeled fluoromisonidazole as an imaging agent for tumor hypoxia.* Int J Radiat Oncol Biol Phys, 1989. **17**(5): p. 985-991.

74. Fleming IN, Manavaki R, Blower PJ, West C, Williams KJ, Harris AL, Domarkas J, Lord S, Baldry C, and Gilbert FJ, *Imaging tumour hypoxia with positron emission tomography.* Br J Cancer, 2015. **112**(2): p. 238-250.

75. Grimes DR, Warren DR, and Warren S, *Hypoxia imaging and radiotherapy: bridging the resolution gap.* Br J Radiol, 2017. **90**(1076): p. 20160939.

76. Postema EJ, McEwan AJ, Riauka TA, Kumar P, Richmond DA, Abrams DN, and Wiebe LI, *Initial results of hypoxia imaging using 1-alpha-D: -(5-deoxy-5-[18F]-fluoroarabinofuranosyl)-2-nitroimidazole (18F-FAZA).* Eur J Nucl Med Mol Imaging, 2009. **36**(10): p. 1565-1573.

77. Reischl G, Dorow DS, Cullinane C, Katsifis A, Roselt P, Binns D, and Hicks R, *Imaging of tumor hypoxia with [124I]IAZA in comparison with [18F]FMISO and [18F]FAZA - first small animal PET results.* J Pharm Pharmaceut Sci, 2007. **10**(2): p. 203-211.

78. Shi Y, Oeh J, Eastham-Anderson J, Yee S, Finkle D, Peale FV, Jr., Ross J, Hedehus M, van Bruggen N, Venook R, Ross S, Sampath D, and Carano RA, *Mapping in vivo tumor oxygenation within viable tumor by 19F-MRI and multispectral analysis.* Neoplasia, 2013. **15**(11): p. 1241-1250.

79. Hunjan S, Zhao D, Constantinescu A, Hahn EW, Antich PP, and Mason RP, *Tumor oximetry: Demonstration of an enhanced dynamic mapping procedure using fluorine-19 echo planar magnetic resonance imaging in the Dunning prostate R3327-AT1 rat tumor.* Int J Radiat Oncol Biol Phys, 2001. **49**(4): p. 1097-1108.

80. Ruiz-Cabello J, Barnett BP, Bottomley PA, and Bulte JW, *Fluorine (19F) MRS and MRI in biomedicine.* NMR Biomed, 2011. **24**(2): p. 114-129.

81. Ogawa S, Lee TM, Kay AR, and Tank DW, *Brain magnetic resonance imaging with contrast dependent on blood oxygenation.* Proc Natl Acad Sci U S A, 1990. **87**(23): p. 9868-9872.

82. Baudelet C and Gallez B, *How does blood oxygen level-dependent (BOLD) contrast correlate with oxygen partial pressure (pO2) inside tumors?* Magn Reson Med, 2002. **48**(6): p. 980-986.

83. Hallac RR, Zhou H, Pidikiti R, Song K, Stojadinovic S, Zhao D, Solberg T, Peschke P, and Mason RP, *Correlations of noninvasive BOLD and TOLD MRI with pO2 and relevance to tumor radiation response.* Magn Reson Med, 2014. **71**(5): p. 1863-1873.

84. Sourbron SP and Buckley DL, *Tracer kinetic modelling in MRI: estimating perfusion and capillary permeability.* Phys Med Biol, 2012. **57**(2): p. R1-R33.

85. Colliez F, Gallez B, and Jordan BF, *Assessing Tumor Oxygenation for Predicting Outcome in Radiation Oncology: A Review of Studies Correlating Tumor Hypoxic Status and Outcome in the Preclinical and Clinical Settings.* Front Oncol, 2017. **7**: p. 10.

86. Bao B, Groves K, Zhang J, Handy E, Kennedy P, Cuneo G, Supuran CT, Yared W, Rajopadhye M, and Peterson JD, *In vivo imaging and quantification of carbonic anhydrase IX expression as an endogenous biomarker of tumor hypoxia.* PLoS One, 2012. **7**(11): p. e50860.

87. Takahashi E, Takano T, Monura Y, Okano S, Nakajima O, and Sato M, *In vivo oxygen imaging using green fluorescent protein.* Am J Physiol Cell Physiol, 2006. **291**(4): p. C781-C787.

88. Lehmann S, Stiehl DP, Honer M, Dominietto M, Keist R, Kotevic I, Wollenick K, Ametamey S, Wenger RH, and Rudin M, *Longitudinal and multimodal in vivo imaging of tumor hypoxia and its downstream molecular events.* Proc Natl Acad Sci U S A, 2009. **106**(33): p. 14004-14009.

89. Beard P, *Biomedical photoacoustic imaging.* Interface Focus, 2011. **1**(4): p. 602-631.

90. Needles A, Heinmiller A, Sun J, Theodoropoulos C, Bates D, Hirson D, Yin M, and Foster FS, *Development and initial application of a fully integrated photoacoustic micro-ultrasound system.* IEEE Trans Ultrason Ferroelectr Freq Control, 2013. **60**(5): p. 888-897.

91. Varia MA, Calkins-Adams DP, Rinker LH, Kennedy AS, Novotny DB, Fowler WC, and Raleigh JA, *Pimonidazole: a novel hypoxia marker for complementary study of tumor hypoxia and cell proliferation in cervical carcinoma.* Gynecol Oncol, 1998. **71**(2): p. 270-277.

92. Wilson WR and Hay MP, *Targeting hypoxia in cancer therapy.* Nat Rev Cancer, 2011. **11**(6): p. 393-410.

93. Iglesias P, Fraga M, and Costoya JA, *Defining hypoxic microenvironments by non-invasive functional optical imaging.* Eur J Cancer, 2013. **49**(1): p. 264-271.

94. Isaacs JT, Heston WDW, Weissmann RM, and Coffey DS, *Animal model of the hormone-sensitive and -insensitive prostatic adenocarcinomas, Dunning R-3327-H, R3327-HI, and R3327-AT1.* Cancer Res, 1978. **38**: p. 4353 - 4359.

95. Tennant TR, Kim H, Sokoloff M, and Rinker-Schaeffer CW, *The Dunning model.* Prostate, 2000. **43**(4): p. 295-302.

96. Bendinger AL, Glowa C, Peter J, and Karger CP, *Photoacoustic imaging to assess pixel-based sO2 distributions in experimental prostate tumors.* J Biomed Opt, 2018. **23**(3): p. 036009, https://doi.org/10.1117/1.JBO.23.3.036009.

97. Wilson KE, Bachawal SV, Abou-Elkacem L, Jensen K, Machtaler S, Tian L, and Willmann JK, *Spectroscopic Photoacoustic Molecular Imaging of Breast Cancer using a B7-H3-targeted ICG Contrast Agent.* Theranostics, 2017. **7**(6): p. 1463-1476.

98. Wang LV, *Prospects of photoacoustic tomography.* Med Phys, 2008. **35**(12): p. 5758-5767.

99. Mehrmohammadi M, Yoon SJ, Yeager D, and Emelianov SY, *Photoacoustic Imaging for Cancer Detection and Staging.* Curr Mol Imaging, 2013. **2**(1): p. 89-105.

100. Li C and Wang LV, *Photoacoustic tomography and sensing in biomedicine.* Phys Med Biol, 2009. **54**(19): p. R59-R97.

101. Becker A, Masthoff M, Claussen J, Ford SJ, Roll W, Burg M, Barth PJ, Heindel W, Schäfers M, Eisenblätter M, and Wildgruber M, *Multispectral optoacoustic tomography of the human breast: characterisation of healthy tissue and malignant lesions using a hybrid ultrasound-optoacoustic approach.* Eur Radiol, 2017. **28**(2): p. 602-609.

102. Wang X, Xie X, Ku G, Wang LV, and Stoica G, *Noninvasive imaging of hemoglobin concentration and oxygenation in the rat brain using high-resolution photoacoustic tomography.* J Biomed Opt, 2006. **11**(2): p. 024015.

103. Peschke P, Karger CP, Scholz M, Debus J, and Huber PE, *Relative biological effectiveness of carbon ions for local tumor control of a radioresistant prostate carcinoma in the rat.* Int J Radiat Oncol Biol Phys, 2011. **79**(1): p. 239-246.

104. Haberer T, Becher W, Schardt D, and Kraft G, *Magnetic scanning system for heavy ion therapy.* Nucl Instrum Methods Phys Res A, 1993. **330**: p. 296-305.

105. Haacke ME, Brown RW, Thompson MR, and Venkatesan R, *Magnetic Resonance Imaging - Physical Principles and Sequence Design*. 1 ed. 1999, New York: John Wiley & Sons In.

106. Bonekamp D, Wolf MB, Edler C, Katayama S, Schlemmer HP, Herfarth K, and Rothke M, *Dynamic contrast enhanced MRI monitoring of primary proton and carbon ion irradiation of prostate cancer using a novel hypofractionated raster scan technique.* Radiother Oncol, 2016. **120**(2): p. 313-319.

107. Glowa C, Peschke P, Brons S, Neels OC, Kopka K, Debus J, and Karger CP, *Carbon ion radiotherapy: impact of tumor differentiation on local control in experimental prostate carcinomas.* Radiat Oncol, 2017. **12**(1): p. 174.

108. Sourbron S, *Technical aspects of MR perfusion.* Eur J Radiol, 2010. **76**(3): p. 304-313.

109. Pintaske J, Martirosian P, Graf H, Erb G, Lodemann K-P, Claussen CD, and Schick F, *Relaxivity of Gadopentetate Dimeglumine (Magnevist), Gadobutrol (Gadovist), and Gadobenate Dimeglumine (MultiHance) in human blood plasma at 0.2, 1.5, and 3 Tesla.* Invest Radiol, 2006. **41**(3): p. 213-221.

110. Zierler KL, *Theoretical basis of indicator-dilution methods for measuring flow and volume.* Circ Res, 1962. **10**: p. 393-407.

111. Brix G, Kiessling F, Lucht R, Darai S, Wasser K, Delorme S, and Griebel J, *Microcirculation and microvasculature in breast tumors: pharmacokinetic analysis of dynamic MR image series.* Magn Reson Med, 2004. **52**(2): p. 420-429.

112. Tofts PS, *Modeling tracer kinetics in dynamic Gd-DTPA MR imaging.* J Magn Reson Imaging, 1997. **7**(1): p. 91-101.

113. Sourbron S, Ingrisch M, Siefert A, Reiser M, and Herrmann K, *Quantification of cerebral blood flow, cerebral blood volume, and blood-brain-barrier leakage with DCE-MRI.* Magn Reson Med, 2009. **62**(1): p. 205-217.

114. Sourbron SP and Buckley DL, *On the scope and interpretation of the Tofts models for DCE-MRI.* Magn Reson Med, 2011. **66**(3): p. 735-745.

115. Tofts PS, Brix G, Buckley DL, Evelhoch JL, Henderson E, Knopp MV, Larsson HBW, Lee T-Y, Mayr NA, Parker GJM, Port RE, Taylor J, and Weisskoff RM, *Estimating kinetic parameters from dynamic contrast-enhanced T1-weighted MRI of a diffusable tracer: standardized quantities and symbols.* J Magn Reson Imaging, 1999. **10**(3): p. 223-232.

116. Sourbron SP and Buckley DL, *Classic models for dynamic contrast-enhanced MRI.* NMR Biomed, 2013. **26**(8): p. 1004-1027.

117. Bendinger AL, Debus C, Glowa C, Karger CP, Peter J, and Storath M, *Bolus arrival time estimation in dynamic contrast-enhanced magnetic resonance imaging of small animals based on spline models.* Phys Med Biol, 2019. **64**(4): p. 045003.

118. Koh TS, Bisdas S, Koh DM, and Thng CH, *Fundamentals of tracer kinetics for dynamic contrast-enhanced MRI.* J Magn Reson Imaging, 2011. **34**(6): p. 1262-1276.

119. Mehrtash A, Gupta SN, Shanbhag D, Miller JV, Kapur T, Fennessy FM, Kikinis R, and Fedorov A, *Bolus arrival time and its effect on tissue characterization with dynamic contrast-enhanced magnetic resonance imaging.* J Med Imaging, 2016. **3**(1): p. 014503.

120. Nadav G, Liberman G, Artzi M, Kiryati N, and Bashat DB, *Optimization of two-compartment-exchange-model analysis for dynamic contrast-enhanced mri incorporating bolus arrival time.* J Magn Reson Imaging, 2017. **45**(1): p. 237-249.

121. Meyer E, *Simultaneous correction for tracer arrival delay and dispersion in CBF measurements by the H2 15O autoradiographic method and dynamic PET.* J Nucl Med, 1989. **30**(6): p. 1069-1078.

122. Kershaw LE and Buckley DL, *Precision in measurements of perfusion and microvascular permeability with T1-weighted dynamic contrast-enhanced MRI.* Magn Reson Med, 2006. **56**(5): p. 986-992.

123. Cheong LH, Koh TS, and Hou Z, *An automatic approach for estimating bolus arrival time in dynamic contrast MRI using piecewise continuous regression models.* Phys Med Biol, 2003. **48**(5): p. N83-N88.

124. Singh A, Rathore RK, Haris M, Verma SK, Husain N, and Gupta RK, *Improved bolus arrival time and arterial input function estimation for tracer kinetic analysis in DCE-MRI.* J Magn Reson Imaging, 2009. **29**(1): p. 166-176.

125. Craven P and Wahba G, *Smoothing noisy data with spline functions.* Numer Math, 1978. **31**(4): p. 377-403.

126. Unser M, *Splines: a perfect fit for medical imaging.* Medical Imaging 2002: Image Processing (International Society for Optics and Photonics), 2002.

127. De Boor C, *A practical guide to splines*. 1978, New York: Springer-Verlag

128. Reinsch C, *Smoothing by spline functions.* Numer Math, 1967. **10**(3): p. 177-183.

129. Unser M, *Splines: a Perfect Fit for Signal and Image Processing.* IEEE Signal Process Mag, 1999. **16**: p. 22-38.

130. Wahba G, *Spline models for observational data*. CBMS-NSF Regional Conference Series in Applied Mathematics. 1990, Philadelphia, Pennsylvania, USA: Society for Industrial and Applied Mathematics (SIAM).

131. Nolden M, Zelzer S, Seitel A, Wald D, Müller M, Franz AM, Maleike D, Fangerau M, Baumhauer M, Maier-Hein L, Maier-Hein KH, Meinzer H-P, and Wolf I, *The Medical Imaging Interaction Toolkit: challenges and advances : 10 years of open-source development.* Int J Comput Assist Radiol Surg, 2013. **8**(4): p. 607-620.

132. Debus C, Floca R, Ingrisch M, Kompan I, Maier-Hein K, Abdollahi A, and Nolden M, *MITK-ModelFit: A generic open-source framework for model fits and their exploration in medical imaging - design, implementation and application on the example of DCE-MRI.* BMC Bioinformatics, 2019. **20**(1): p. 31.

133. McGrath DM, Bradley DP, Tessier JL, Lacey T, Taylor CJ, and Parker GJ, *Comparison of model-based arterial input functions for dynamic contrast-enhanced MRI in tumor bearing rats.* Magn Reson Med, 2009. **61**(5): p. 1173-1184.

134. Parker GJ, Roberts C, Macdonald A, Buonaccorsi GA, Cheung S, Buckley DL, Jackson A, Watson Y, Davies K, and Jayson GC, *Experimentally-derived functional form for a population-averaged high-temporal-resolution arterial input function for dynamic contrast-enhanced MRI.* Magn Reson Med, 2006. **56**(5): p. 993-1000.

135. Bendinger AL, Seyler L, Saager M, Debus C, Peschke P, Komljenovic D, Debus J, Peter J, Floca R, Karger CP, and Glow C, *Impact of single dose photons and carbon ions on perfusion and vascular permeability: a dynamic contrast-enhanced MRI study in the anaplastic rat prostate tumor R3327-AT1*. Submitted.

136. Bendinger AL, Peschke P, Peter J, Debus C, Karger CP, and Glowa C, *High doses of photons and carbon ions induce comparable increase of vascular permeability in R3327-HI prostate tumors: a dynamic contrast enhanced MRI study.* In preparation.

137. Featherstone AK, O'Connor JPB, Little RA, Watson Y, Cheung S, Babur M, Williams KJ, Matthews JC, and Parker GJM, *Data-driven mapping of hypoxia-related tumor heterogeneity using DCE-MRI and OE-MRI.* Magn Reson Med, 2018. **79**(4): p. 2236-2245.

138. Gratzner HG, *Monoclonal antibody to 5-bromo- and 5-iododeoxyuridine: A new reagent for detection of DNA replication.* Science, 1982. **218**(4571): p. 474-475.

139. Gerdes J, Lemke H, Baisch H, Wacker HH, Schwab U, and Stein H, *Cell cycle analysis of a cell proliferation-associated human nuclear antigen defined by the monoclonal antibody Ki-67.* J Immunol, 1984. **133**(4): p. 1710-1715.

140. Rogakou EP, Pilch DR, Orr AH, Ivanova VS, and Bonner W, *DNA double-stranded breaks induce histone H2AX phosphorylation on serine 139.* J Biol Chem, 1998. **273**(10): p. 5858-5868.

141. Rogakou EP, Boon C, Redon C, and Bonner WM, *Megabase chromatin domains involved in DNA double-strand breaks in vivo*. J Cell Biol, 1999. **146**(5): p. 905-916.

142. Rasband WS, *ImageJ*, U.S.N.I.o. Health, Editor. 1997-2016: Bethesda, Maryland, USA.

143. Sommer C, Straehle C, Köthe U, and Hamprecht FA. *Ilastik: Interactive learning and segmentation toolkit*. in *8th IEEE International Symposium on Biomedical Imaging (ISBI): From Nano to Macro*. March 30 - April 02, 2011. Chicago, Illinios, USA.

144. Lamprecht MR, Sabatini DM, and Carpenter AE, *CellProfiler: free, versatile software for automated biological image analysis*. BioTechniques, 2007. **42**(1): p. 71-75.

145. Sage D, Prodanov D, Tinevez J-Y, and Schindelin J. *MIJ: Making Interoperability Between ImageJ and Matlab Possible*. in *ImageJ User & Developer Conference*. October 24-26, 2012. Luxemburg.

146. Prahl S, *Optical Absorption of Hemoglobin*. 1999, Last access: 01.08.2019; Available from: http://omlc.ogi.edu/spectra/hemoglobin/index.html.

147. Wasserstein L, *Markov processes on countable product spaces describing large systems of automata.* Problemy peredachi informatsii, 1969. **5**(3): p. 64-73.

148. Vallender SS, *Calculation of the Wasserstein distance between probability distributions on the line.* Theory Probab Appl, 1974. **18**(4): p. 784 - 786.

149. Vershik AM, *Long history of the monge-kantorovich transportation problem.* Math Intell, 2013. **35**(4): p. 1-9.

150. Sommerfeld M and Munk A, *Inference for empirical Wasserstein distances on finite spaces*. J R Statist Soc B, 2018. **80**(1): p. 219-238.

151. Rubner Y, Tomasi C, and Guibas LJ, *The Earth Mover's Distance as a metric for image retrieval.* Int J Comput Vis, 2000. **40**(2): p. 99-121.

152. Oudre L, Jakubowicz J, Bianchi P, and Simon C, *Classification of periodic activities using the Wasserstein distance.* IEEE Trans Biomed Eng, 2012. **59**(6): p. 1610-1619.

153. Munk A and Czado C, *Non-parametric validation of similar distributions and assessment of goodness of fit.* J R Statist Soc B, 1998. **60**(1): p. 223-241.

154. Qiu P, *Inferring phenotypic properties from single-cell characteristics.* PLoS One, 2012. **7**(5): p. e37038.

155. Fornberg B, *A Practical Guide to Pseudospectral Methods (Cambridge Monographs on Applied and Computational Mathematics)*. 1996, Cambridge: Cambridge University Press.

156. Golub G, Heath M, and Wahba G, *Generalized cross-validation as a method for choosing a good ridge parameter.* Technometrics, 1979. **21**(2): p. 215-223.

157. Wahba G, *A comparison of GCV and GML for choosing the smoothing parameter in the generalized spline smoothing problem.* Ann Stat, 1985. **13**(4): p. 1378-1402.

158. Aydin D and Omay RE. *The empirical performances of the selection criteria for nonparametric regression using smoothing spline*. in *5th WSEAS Int. Conf. on Computational Intelligence, Man-Machine Systems and Cybernetics*. November 20 - 22, 2006. Venice, Italy.

159. Langhout GC, Grootendorst DJ, Nieweg OE, Wouters MW, van der Hage JA, Jose J, van Boven H, Steenbergen W, Manohar S, and Ruers TJ, *Detection of melanoma metastases in resected human lymph nodes by noninvasive multispectral photoacoustic imaging.* Int J Biomed Imaging, 2014. **2014**: p. 163652.

160. Luke GP and Emelianov SY, *Label-free Detection of Lymph Node Metastases with US- guided Functional Photoacoustic Imaging.* Radiology, 2015. **277**(2): p. 435-442.

161. Laufer J, Zhang E, Raivich G, and Beard P, *Three-dimensional noninvasive imaging of the vasculature in the mouse brain using a high resolution photoacoustic scanner.* Appl Opt, 2009. **48**(10): p. D299-D306.

162. Wang X, Pang Y, Ku G, Xie X, Stoica G, and Wang LV, *Noninvasive laser-induced photoacoustic tomography for structural and functional in vivo imaging of the brain.* Nat Biotech, 2003. **21**(7): p. 803-806.

163. Rich LJ and Seshadri M, *Photoacoustic monitoring of tumor and normal tissue response to radiation.* Sci Rep, 2016. **6**: p. 21237.

164. Eisenbrey JR, Merton DA, Marshall A, Liu JB, Fox TB, Sridharan A, and Forsberg F, *Comparison of photoacoustically derived hemoglobin and oxygenation measurements with contrast-enhanced ultrasound estimated vascularity and immunohistochemical staining in a breast cancer model.* Ultrason Imaging, 2015. **37**(1): p. 42-52.

165. Mallidi S, Watanabe K, Timerman D, Schoenfeld D, and Hasan T, *Prediction of tumor recurrence and therapy monitoring using ultrasound-guided photoacoustic imaging.* Theranostics, 2015. **5**(3): p. 289-301.

166. Raes F, Sobilo J, Le Mee M, Retif S, Natkunarajah S, Lerondel S, and Le Pape A, *High Resolution Ultrasound and Photoacoustic Imaging of Orthotopic Lung Cancer in Mice: New Perspectives for Onco-Pharmacology.* PLoS One, 2016. **11**(4): p. e0153532.

167. Bayer CL, Luke GP, and Emelianov SY, *Photoacoustic imaging for medical diagnostics.* Acoust Today, 2012. **8**(4): p. 15-23.

168. May JP, Hysi E, Wirtzfeld LA, Undzys E, Li SD, and Kolios MC, *Photoacoustic Imaging of Cancer Treatment Response: Early Detection of Therapeutic Effect from Thermosensitive Liposomes.* PLoS One, 2016. **11**(10): p. e0165345.

169. Hysi E, Wirtzfeld LA, May JP, Undzys E, Li SD, and Kolios MC, *Photoacoustic signal characterization of cancer treatment response: Correlation with changes in tumor oxygenation.* Photoacoustics, 2017. **5**: p. 25-35.

170. Smolev JK, Heston WDW, Scott WW, and Coffey DS, *Characterization of the Dunning R3327H prostatic adenocarcinoma: an appropriate animal model for prostatic cancer.* Cancer Treat Rep, 1977. **61**(2): p. 273-287.

171. Zhao D, Rany S, Constantinescu A, Hahn EW, and Mason RP, *Tumor oxygen dynamics: correlation of in vivo MRI with histological findings.* Neoplasia, 2003. **5**(4): p. 308-318.

172. Mena-Romano P, Cheng C, Glowa G, Peschke P, Pan L, Haberkorn U, Dimitrakopoulou-Strauss A, and Karger CP, *Measurement of hypoxia-related parameters in three sublines of a rat prostate carcinoma using dynamic (18)F-*

FMISO-PET-CT and quantitative histology. Am J Nucl Med Mol Imaging, 2015. **5**(4): p. 348-362.

173. Zhao D, Constantinescu A, Hahn EW, and Mason RP, *Differential oxygen dynamics in two diverse dunning prostate R3327 rat tumor sublines with respect to growth and respiratory challenge.* Int J Radiat Oncol Biol Phys, 2002. **53**(3): p. 744 - 756.

174. Zhang Z, Yuan Q, Zhou H, Zhao D, Li L, Gerberich JL, and Mason RP, *Assessment of tumor response to oxygen challenge using quantitative diffusion MRI in an animal model.* J Magn Reson Imaging, 2015. **42**(5): p. 1450-1457.

175. Smith LM, Varagic J, and Yamaleyeva LM, *Photoacoustic Imaging for the Detection of Hypoxia in the Rat Femoral Artery and Skeletal Muscle Microcirculation.* Shock, 2016. **46**(5): p. 527-530.

176. Glowa C, Peschke P, Brons S, Debus J, and Karger CP, *Intrinsic and extrinsic tumor characteristics are of minor relevance for the efficacy of split-dose carbon ion irradiation in three experimental prostate tumors.* Radiother Oncol, 2019. **133**: p. 120-124.

177. Brown SL, Nagaraja TN, Aryal MP, Panda S, Cabral G, Keenan KA, Elmghirbi R, Mikkelsen T, Hearshen D, Knight RA, Wen N, Kim JH, and Ewing JR, *MRI-Tracked Tumor Vascular Changes in the Hours after Single-Fraction Irradiation.* Radiat Res, 2015. **183**(6): p. 713-721.

178. Zhou H, Zhang Z, Denney R, Williams JS, Gerberich J, Stojadinovic S, Saha D, Shelton JM, and Mason RP, *Tumor physiological changes during hypofractionated stereotactic body radiation therapy assessed using multi-parametric magnetic resonance imaging.* Oncotarget, 2017. **8**(23): p. 37464-37477.

179. Kallehauge JF, Tanderup K, Duan C, Haack S, Pedersen EM, Lindegaard JC, Fokdal LU, Mohamed SM, and Nielsen T, *Tracer kinetic model selection for dynamic contrast-enhanced magnetic resonance imaging of locally advanced cervical cancer.* Acta Oncol, 2014. **53**(8): p. 1064-1072.

180. Belfatto A, White DA, Mason RP, Zhang Z, Stojadinovic S, Baroni G, and Cerveri P, *Tumor radio-sensitivity assessment by means of volume data and magnetic resonance indices measured on prostate tumor bearing rats.* Med Phys, 2016. **43**(3): p. 1275-1284.

181. Lin YC, Wang JJ, Hong JH, Lin YP, Lee CC, Wai YY, Ng SH, Wu YM, and Wang CC, *Noninvasive monitoring of microvascular changes with partial irradiation using dynamic contrast-enhanced and blood oxygen level-dependent magnetic resonance imaging.* Int J Radiat Oncol Biol Phys, 2013. **85**(5): p. 1367-1374.

182. Maeda A, Chen Y, Bu J, Mujcic H, Wouters BG, and DaCosta RS, *In vivo imaging reveals significant tumor vascular dysfunction and increased tumor hypoxia-inducible factor-1alpha expression induced by high single-dose irradiation in a pancreatic tumor model.* Int J Radiat Oncol Biol Phys, 2017. **97**(1): p. 184-194.

183. Fukawa T, Takematsu K, Oka K, Koike S, Ando K, Kobayashi H, and Tanishita K, *Differences in pO2 peaks of a murine fibrosarcoma between carbon-ion and X-ray irradiation.* J Radiat Res, 2004. **45**(2): p. 303-308.

184. Chen FH, Chiang CS, Wang CC, Tsai CS, Jung SM, Lee CC, McBride WH, and Hong JH, *Radiotherapy decreases vascular density and causes hypoxia with macrophage aggregation in TRAMP-C1 prostate tumors.* Clin Cancer Res, 2009. **15**(5): p. 1721-1729.

185. Tsai JH, Makonnen S, Feldman M, Sehgal C, Maity A, and Lee WMF, *Ionizing radiation inhibits tumor neovascularization by inducing ineffective angiogenesis.* Cancer Biol Ther, 2005. **4**(12): p. 1395-1400.

186. Solevski OV, Rofstad EK, and Brustad T, *Vascular changes in a human malignant melanoma xenograft following single-dose irradiation.* Radiat Res, 1984. **98**(1): p. 115-128.

187. Fukumura D, Yuan F, Endo M, and Jain RK, *Role of nitric oxide in tumor microcirculation. Blood flow, vascular permeability, and leukocyte-endothelial interactions.* Am J Pathol, 1997. **150**(2): p. 713-725.

188. Andrade SP, Hart IR, and Piper PJ, *Inhibitors of nitric oxide synthase selectively reduce blood flow in tumor-associated neovasculature.* Br J Pharmacol, 1992. **107**(4): p. 1092-1095.

189. Garcia-Barros M, Paris F, Cordon-Cardo C, Lyden D, Rafii S, Haimovitz-Friedman A, Fuks Z, and Kolesnick R, *Tumor response to radiotherapy regulated by endothelial cell apoptosis.* Science, 2003. **300**(5622): p. 1155-1159.

190. Park HJ, Griffin RJ, Hui S, Levitt SH, and Song CW, *Radiation-induced vascular damage in tumors: implications of vascular damage in ablative hypofractionated radiotherapy (SBRT and SRS).* Radiat Res, 2012. **177**(3): p. 311-327.

191. Kozin SV, Duda DG, Munn LL, and Jain RK, *Neovascularization after irradiation: what is the source of newly formed vessels in recurring tumors?* J Natl Cancer Inst, 2012. **104**(12): p. 899-905.

192. Suit HD and Willers H, *Comment on "Tumor response to radiotherapy regulated by endothelial cell apoptosis" (I).* Science, 2003. **302**(5652): p. 1894; author reply 1894.

193. Brown M, Bristow R, Glazer P, Hill R, McBride W, McKenna G, and Muschel R, *Comment on "Tumor response to radiotherapy regulated by endothelial cell apoptosis" (II).* Science, 2003. **302**(5652): p. 1894; author reply 1894.

194. Moding EJ, Castle KD, Perez BA, Oh P, Min HD, Norris H, Ma Y, Cardona DM, Lee C-L, and Kirsch DG, *Tumor cells, but not endothelial cells, mediate eradication of primary sarcomas by stereotactic body radiation therapy.* Sci Transl Med, 2015. **7**(278): p. 278ra34.

195. Gerweck LE, Vijayappa S, Kurimasa A, Ogawa K, and Chen DJ, *Tumor cell radiosensitivity is a major determinant of tumor response to radiation.* Cancer Res, 2006. **66**(17): p. 8352-8355.

196. Ogawa K, Boucher Y, Kashiwagi S, Fukumura D, Chen D, and Gerweck LE, *Influence of tumor cell and stroma sensitivity on tumor response to radiation.* Cancer Res, 2007. **67**(9): p. 4016-4021.

197. Garcia-Barros M, Thin TH, Maj J, Cordon-Cardo C, Haimovitz-Friedman A, Fuks Z, and Kolesnick R, *Impact of stromal sensitivity on radiation response of tumors implanted in SCID hosts revisited.* Cancer Res, 2010. **70**(20): p. 8179-8186.

198. Horsman MR, Nielsen T, Ostergaard L, and Overgaard J, *Radiation administered as a large single dose or in a fractionated schedule: Role of the tumour vasculature as a target for influencing response.* Acta Oncol, 2006. **45**(7): p. 876-880.

199. Lan J, Wan XL, Deng L, Xue JX, Wang LS, Meng MB, Ling H, Zhang X, Mo XM, and Lu Y, *Ablative hypofractionated radiotherapy normalizes tumor vasculature in lewis lung carcinoma mice model.* Radiat Res, 2013. **179**(4): p. 458-464.

200. Sonveaux P, Brouet A, Havaux X, Grégoire V, Dessy C, Balligand J-L, and Feron O, *Irradiation-induced angiogenesis through the up-regulation of the nitric oxide pathway: implications for tumor radiotherapy.* Cancer Res, 2003. **63**(5): p. 1012-1019.

201. Kozin SV, Kamoun WS, Huang Y, Dawson MR, Jain RK, and Duda DG, *Recruitment of myeloid but not endothelial precursor cells facilitates tumor regrowth after local irradiation.* Cancer Res, 2010. **70**(14): p. 5679-5685.

202. Möller BJ, Cao Y, Li CY, and Dewhirst MW, *Radiation activates HIF-1 to regulate vascular radiosensitivity in tumors: role of reoxygenation, free radicals, and stress granules.* Cancer Cell, 2004. **5**(5): p. 429-441.

203. Liu Y, Liu Y, Sun C, Gan L, Zhang L, Mao A, Du Y, Zhou R, and Zhang H, *Carbon ion radiation inhibits glioma and endothelial cell migration induced by secreted VEGF.* PLoS One, 2014. **9**(6): p. e98448.

204. Grabham P and Sharma P, *The effects of radiation on angiogenesis.* Vasc Cell, 2013. **5**(1): p. 19.

205. Fuks Z and Kolesnick R, *Engaging the vascular component of the tumor response.* Cancer Cell, 2005. **8**(2): p. 89-91.

206. Paris F, Fuks Z, Kang A, Capodieci P, Juan G, Ehleiter D, Haimovitz-Friedman A, Cordon-Cardo C, and Kolesnick R, *Endothelial apoptosis as the primary lesion initiating intestinal radiation damage in mice.* Science, 2001. **293**(5528): p. 293-297.

207. Barker HE, Paget JT, Khan AA, and Harrington KJ, *The tumour microenvironment after radiotherapy: mechanisms of resistance and recurrence.* Nat Rev Cancer, 2015. **15**(7): p. 409-425.

208. Hallac RR, Zhou H, Pidikiti R, Song K, Solberg T, Kodibagkar VD, Peschke P, and Mason RP, *A role for dynamic contrast-enhanced magnetic resonance imaging in predicting tumour radiation response.* Br J Cancer, 2016. **114**(11): p. 1206-1211.

209. Baker DG and Krochak RJ, *The response of the microvascular system to radiation: a review.* Cancer Invest, 2009. **7**(3): p. 287-294.

210. Eble MJ, Lohr F, Wenz F, Krems B, Bachert P, and Peschke P, *Tissue oxygen tension distribution in two sublines of the Dunning prostate R3327*, in *Funktionsanalyse Biol*. 1995, Gustav Fischer Verlag: Stuttgart.

211. Arteel GE, Thurman RG, and Raleigh JA, *Reductive metabolism of the hypoxia marker pimonidazole is regulated by oxygen tension independent of the pyridine nucleotide redox state.* Eur J Biochem, 1998. **253**(3): p. 743-750.

212. Gross MW, Karbach U, Groebe K, Franko AJ, and Müller-Klieser W, *Calibration of misonidazole labeling by simultaneous measurement of oxygen tension and labeling density in multicellular spheroids.* Int J Cancer, 1995. **61**(4): p. 567-573.

213. Raleigh JA, Chou SC, Arteel GE, and Horsman MR, *Comparison among pimonidazole binding, oxygen electrode measurements, and radiation response in C3H mouse tumors.* Radiat Res, 1999. **151**(5): p. 580-589.

214. Barron DA and Rowley DR, *The reactive stroma microenvironment and prostate cancer progression.* Endocr Relat Cancer, 2012. **19**(6): p. R187-R204.

215. Tuxhorn JA, Ayala GE, Smith MJ, Smith VC, Dang TD, and Rowley DR, *Reactive stroma in human prostate cancer: Induction of myofibroblast phenotype and extracellular matrix remodeling.* Clin Cancer Res, 2002. **8**(9): p. 2912-2923.

216. Bussink J, Kaanders JHAM, Rijken PFJW, Raleigh JA, and Van der Kogel AJ, *Changes in blood perfusion and hypoxia after irradiation of a human squamous cell carcinoma xenograft tumor line.* Radiat Res, 2000. **153**(4): p. 398-404.

217. Goda F, O'Hara JA, Rhodes ES, Dunn JF, Bacic G, and Swartz HM, *Changes of oxygen tension in experimental tumors after single dose of X-ray irradiation.* Cancer Res, 1995. **55**(11): p. 2249-2252.

218. Kallmann RF and Dorie MJ, *Tumor oxygenation and reoxygenation during radiation therapy: their importance in predicting tumor response.* Int J Radiat Oncol Biol Phys, 1986. **12**(4): p. 681-685.

219. Fokas E, Hanze J, Kamlah F, Eul BG, Lang N, Keil B, Heverhagen JT, Engenhart-Cabillic R, An H, and Rose F, *Irradiation-dependent effects on tumor perfusion and endogenous and exogenous hypoxia markers in an A549 xenograft model.* Int J Radiat Oncol Biol Phys, 2010. **77**(5): p. 1500-1508.

220. Ljungkvist ASE, Bussink J, Kaanders JHAM, Wiedenmann NE, Vlasman R, and van der Kogel AJ, *Dynamics of hypoxia, proliferation and apoptosis after irradiation in a murine tumor model.* Radiat Res, 2006. **165**(3): p. 326-336.

221. Hobson B and Denekamp J, *Endothelial proliferation in tumours and normal tissues: continous labelling studies.* Br J Cancer, 1984. **49**(4): p. 405-413.

222. Semenza GL, *Regulation of mammalian O2 homeostasis by hypoxia-inducible factor-1.* Annu Rev Cell Dev Biol, 1999. **15**: p. 551-78.

223. Chen C, Pore N, Behrooz A, Ismail-Beigi F, and Maity A, *Regulation of glut1 mRNA by hypoxia-inducible factor-1. Interaction between H-ras and hypoxia.* J Biol Chem, 2001. **276**(12): p. 9519-9525.

224. Wykoff CC, Beasley NJP, Watson PH, Turner KJ, Pastorek J, Sibtain A, Wilson GD, Turley H, Talks KL, Maxwell PH, Pugh CW, Ratcliffe PJ, and Harris AL, *Hypoxia-inducible expression of tumor-associated carbonic anhydrases.* Cancer Res, 2000. **60**(24): p. 7075-7083.

225. Potiron VA, Abderrahmani R, Clement-Colmou K, Marionneau-Lambot S, Oullier T, Paris F, and Supiot S, *Improved functionality of the vasculature during conventionally fractionated radiation therapy of prostate cancer.* PLoS One, 2013. **8**(12): p. e84076.

226. Lopez Perez R, Best G, Nicolay NH, Greubel C, Rossberger S, Reindl J, Dollinger G, Weber KJ, Cremer C, and Huber PE, *Superresolution light microscopy shows nanostructure of carbon ion radiation-induced DNA double-strand break repair foci.* FASEB J, 2016. **30**(8): p. 2767-2776.

227. McManus KJ and Hendzel MJ, *ATM-dependent DNA damage-independent mitotic phosphorylation of H2AX in normally growing mammalian cells.* Mol Biol Cell, 2005. **16**(10): p. 5013-5025.

228. Costes SV, Boissiere A, Ravani S, Romano R, Parvin B, and Barcellos-Hoff MH, *Imaging features that discriminate between foci induced by high- and low-LET radiation in human fibroblasts.* Radiat Res, 2006. **165**(5): p. 505-515.

229. Glowa C, Peschke P, Karger CP, Hahn EW, Huber PE, Debus J, and Ehemann V, *Flow cytometric characterization of tumor subpopulations in three sublines of the Dunning R3327 rat prostate tumor model.* Prostate, 2013. **73**(15): p. 1710-1720.

230. Denekamp J, *Cell kinetics and radiation biology.* Int J Radiat Biol Relat Stud Phys Chem Med, 1986. **49**(2): p. 357-380.

231. Denekamp J and Rojas A, *Cell kinetics and radiation pathology.* Experientia, 1989. **45**(1): p. 33-41.

232. Averbeck NB, Topsch J, Scholz M, Kraft-Weyrather W, Durante M, and Taucher-Scholz G, *Efficient Rejoining of DNA Double-Strand Breaks despite Increased Cell-Killing Effectiveness following Spread-Out Bragg Peak Carbon-Ion Irradiation.* Front Oncol, 2016. **6**: p. 28.

233. Bernhard EJ, Maity A, Muschel RJ, and McKenna WG, *Effects of ionizing radiation on cell cycle progression. A review.* Radiat Environ Biophys, 1995. **34**(2): p. 79-83.

234. Jackson SP and Bartek J, *The DNA-damage response in human biology and disease.* Nature, 2009. **461**(7267): p. 1071-1078.

235. Deckbar D, Jeggo PA, and Lobrich M, *Understanding the limitations of radiation-induced cell cycle checkpoints.* Crit Rev Biochem Mol Biol, 2011. **46**(4): p. 271-283.

236. Huang Q, Li F, Liu X, Li W, Shi W, Liu FF, O'Sullivan B, He Z, Peng Y, Tan AC, Zhou L, Shen J, Han G, Wang XJ, Thorburn J, Thorburn A, Jimeno A, Raben D, Bedford JS, and Li CY, *Caspase 3-mediated stimulation of tumor cell repopulation during cancer radiotherapy.* Nat Med, 2011. **17**(7): p. 860-866.

237. Trowbridge IS, Ostergaard HL, and Johnson P, *CD45: a leukocyte-specific member of the protein tyrosine phosphatase family.* Biochim Biophys Acta, 1991. **1095**(1): p. 46-56.

238. Chavez-Galan L, Olleros ML, Vesin D, and Garcia I, *Much More than M1 and M2 Macrophages, There are also CD169(+) and TCR(+) Macrophages.* Front Immunol, 2015. **6**: p. 263.

239. Poli A, Michel T, Theresine M, Andres E, Hentges F, and Zimmer J, *CD56bright natural killer (NK) cells: an important NK cell subset.* Immunology, 2009. **126**(4): p. 458-465.

240. Porter AG and Jänicke RU, *Emerging roles of caspase-3 in apoptosis.* Cell Death Differ, 1999. **6**(2): p. 99-104.

241. McIlwain DR, Berger T, and Mak TW, *Caspase functions in cell death and disease.* Cold Spring Harb Perspect Biol, 2013. **5**(4): p. a008656-a008656.

Appendix

A.1 Statistical analysis of pharmacokinetic modeling results of the AT1-tumor

Normalized AUC values and ETM parameters of the longitudinal AT1 DCE-MRI study (section 3.3.2) were tested for significance by the Kruskal-Wallis test and post hoc Bonferroni correction per imaging time point. Results are displayed in Table 9.

Table 9 Results from the Kruskal-Wallis test and post hoc Bonferroni correction on normalized AUC, K_{trans}, v_e, and v_p values for each imaging time point after irradiation (RT) with either photons (ph) or ^{12}C-ions (^{12}C). Significant differences between groups are marked by red entries, insignificant differences are marked by blue entries. Significance level was set to $p < 0.001$.

	normalized AUC					K_{trans}					v_e					v_p				
pre RT	Control	16 Gy ^{12}C	37 Gy ph	37 Gy ^{12}C	85 Gy ph	Control	16 Gy ^{12}C	37 Gy ph	37 Gy ^{12}C	85 Gy ph	Control	16 Gy ^{12}C	37 Gy ph	37 Gy ^{12}C	85 Gy ph	Control	16 Gy ^{12}C	37 Gy ph	37 Gy ^{12}C	85 Gy ph
Control																				
16 Gy ^{12}C																				
37 Gy ph																				
37 Gy ^{12}C																				
85 Gy ph																				
3 days post RT																				
Control																				
16 Gy ^{12}C																				
37 Gy ph																				
37 Gy ^{12}C																				
85 Gy ph																				
7 days post RT																				
Control																				
16 Gy ^{12}C																				
37 Gy ph																				
37 Gy ^{12}C																				
85 Gy ph																				
14 days post RT																				
Control																				
16 Gy ^{12}C																				
37 Gy ph																				
37 Gy ^{12}C																				
85 Gy ph																				
21 days post RT																				
Control																				
16 Gy ^{12}C																				
37 Gy ph																				
37 Gy ^{12}C																				
85 Gy ph																				

A.2 Individual ETM parameters for each AT1-tumor of the DCE-MRI study

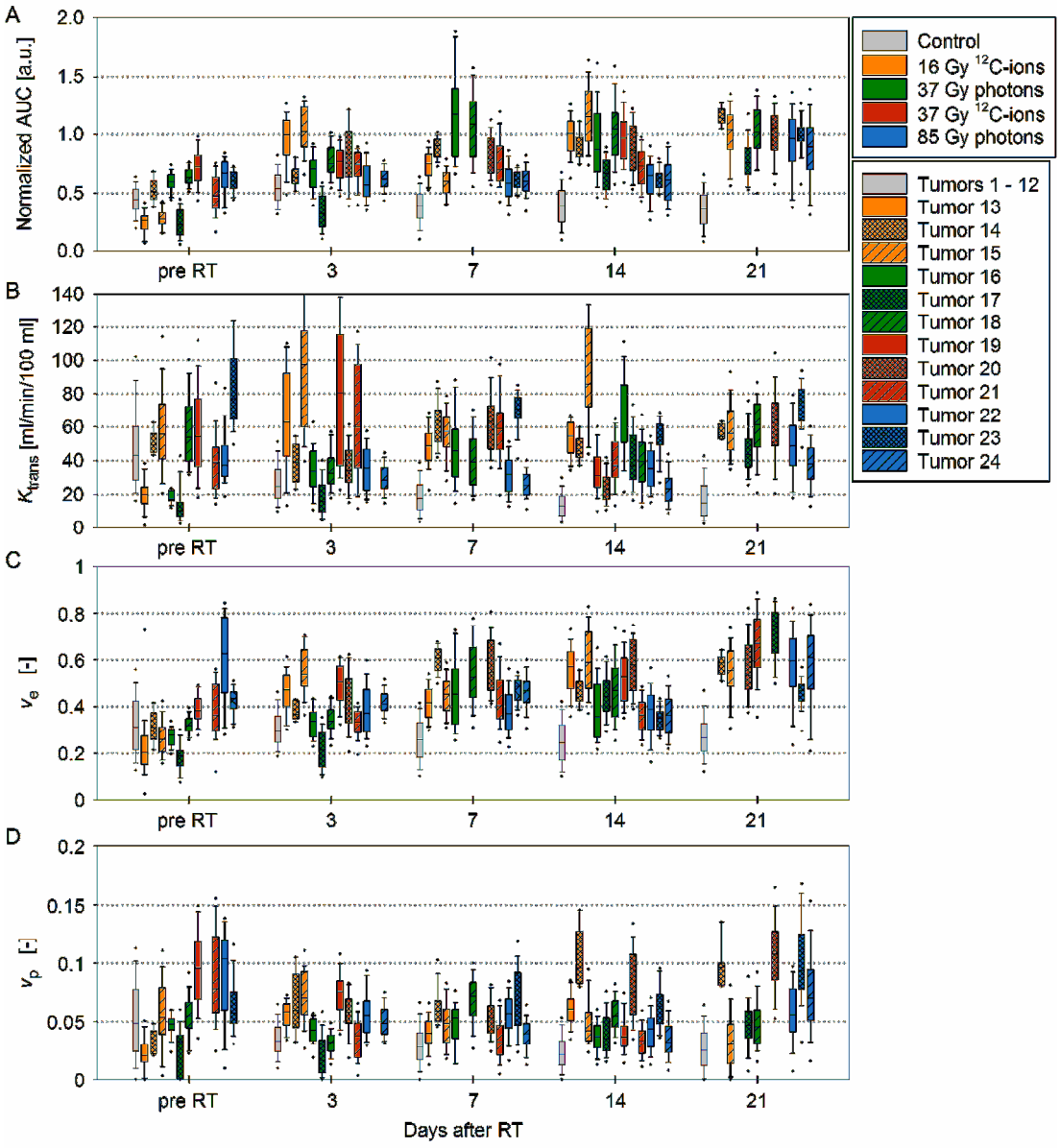

Figure 53 Individual results per animal and imaging time point from non-compartment analysis and ETM parameters. For clarity, the data of the control groups are pooled over all control tumors per time point. Estimated parameters are (A) normalized AUC values, meaning AUC values per animal and time point were normalized to the maximum AUC value of the respective animal's main abdominal artery to eliminate CA administration related effects, (B) the volume transfer constant K_{trans}, (C) the extravascular, extracellular space v_e, and (D) the plasma volume fraction v_p. Boxes mark the 25/75 % percentiles and are displayed with medians (line), 10/90 % percentiles (whiskers), and 5/95 % percentiles (dots).

A.3 Quantitative immunohistochemistry results of the AT1-tumor including tumor 23

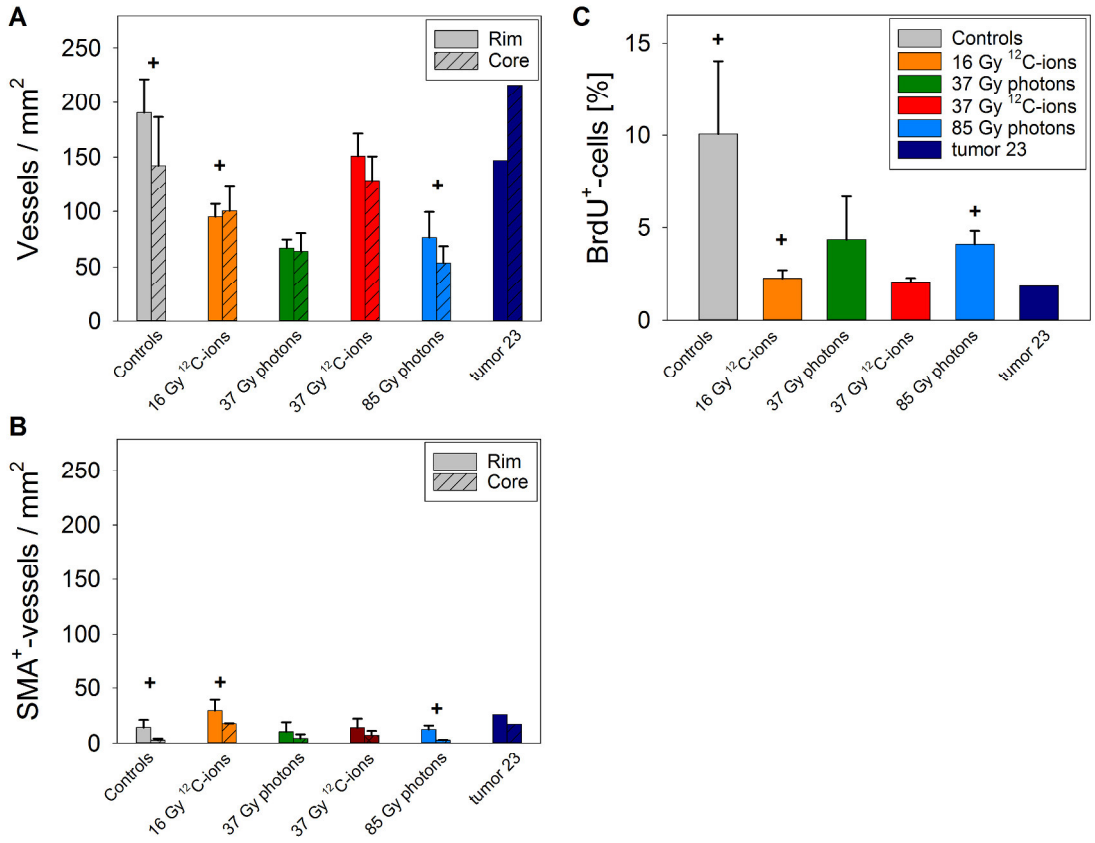

Figure 54 Results of quantitative immunohistochemistry analysis for non-irradiated control tumors and treated tumors 21 days after RT including tumor 23. (A) Microvascular density calculated as the number of $CD31^+$-vessel structures exceeding an area of 21.125 μm^2 (50 pixels). Tumor sections were separated into a rim (outer 1 mm) and core (remaining inner area) region. (B) Vessel maturity was assessed for tumor rim and core by the number of vessels that co-expressed CD31 and SMA ($CD31^+/SMA^+$). (C) Proliferative activity was marked by BrdU incorporation in relation to the overall cell count. $^+$ One animal had to be excluded from the analysis due to complications during tumor dissection.

A.4 Pooled ETM parameters of the HI-tumor

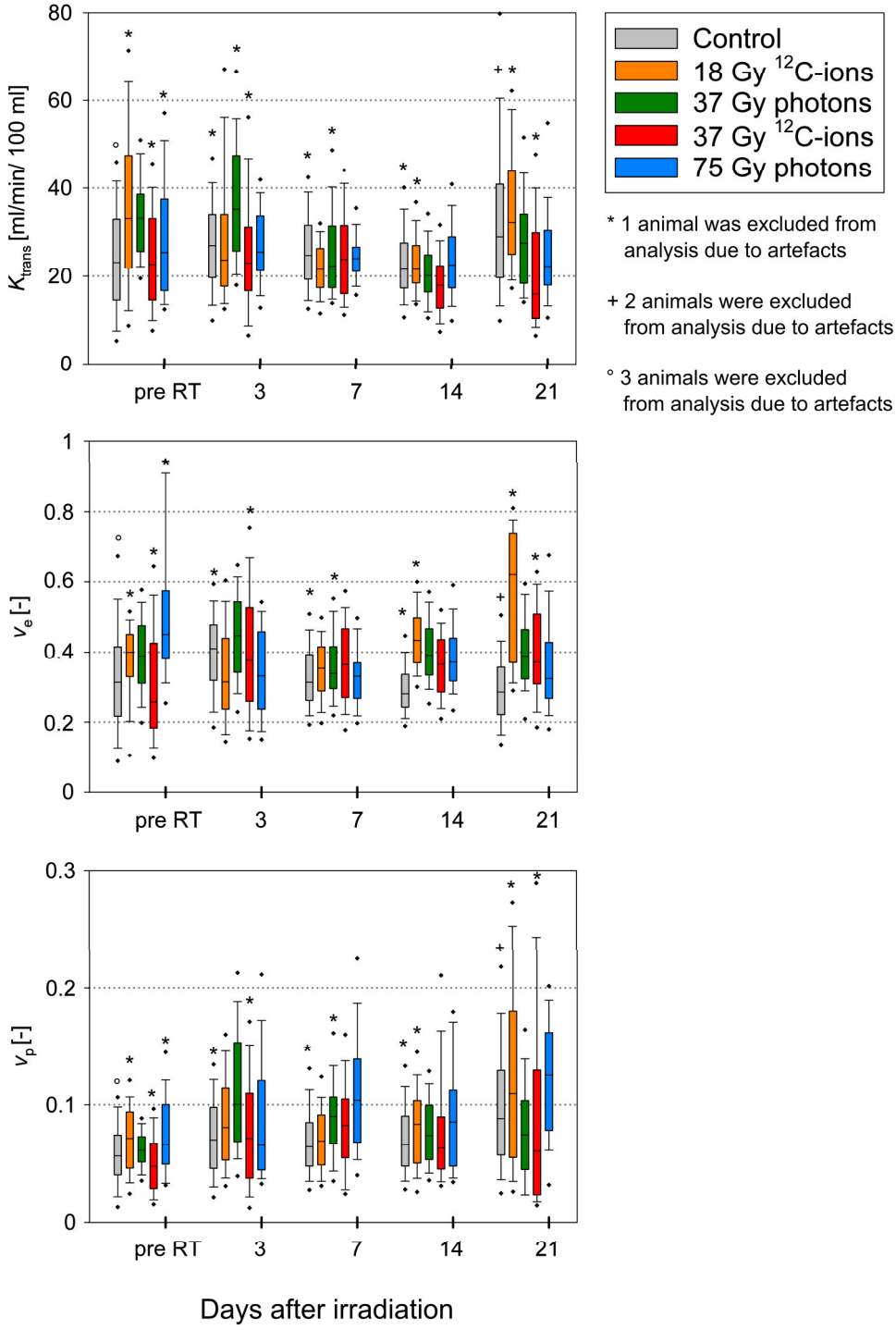

Figure 55 ETM fit parameters of the DCE-MRI study of the HI-tumor pooled per treatment group and imaging time point: the volume transfer constant K_{trans}, the extravascular, extracellular fraction v_e, and the plasma volume fraction v_p. Box plots (25/75 % percentiles) are displayed with medians (line), whiskers representing 10/90 % percentiles, and dots representing the 5/95 % percentiles.

Danksagung

An dieser Stelle möchte ich mich ganz herzlich bei all denjenigen bedanken, die mich auf dem Weg zur Promotion begleitet haben.

Zunächst möchte ich mich bei PD Dr. Karin Müller-Decker für ihre Tätigkeit als Erstgutachterin und bei Prof. Dr. Walter Mier und Prof. Dr. Benedikt Brors für ihre Tätigkeiten als Prüfer bzw. Prüfungskommissionsvorsitzenden bedanken.

Des Weiteren möchte ich mich bei Dr. Jörg Peter bedanken, der mir die Möglichkeit gegeben hat für meine Doktorarbeit ans DKFZ zu kommen und mich in all meinen Vorhaben ermutigt und unterstützt hat. Prof. Dr. Mark Ladd bin ich dankbar für die Ermöglichung der Promotion in seiner Abteilung und der Teilnahme an internationalen Konferenzen und Workshops.

Mein Dank gilt insbesondere Prof. Dr. Christian Karger, an dessen interessanten Projekten ich in den letzten Jahren mitarbeiten durfte, für die Betreuung, die vielen kritischen Fragen, die Integration in seine Gruppe und seine Tätigkeit als Zweitgutachter.

Ein Riesendank geht an Dr. Christin Glowa für ihre großartige Betreuung, ständige Unterstützung, die fruchtbaren Diskussionen, ihre unermüdlichen Anleitungen und ihr detailliertes Korrekturlesen.

Bei Dr. Peter Peschke möchte ich mich für die zahlreichen biologischen Diskussionen und bei Rosemarie Euler-Lange für die tatkräftige Unterstützung im Tierstall und im Labor bedanken. Mein Dank geht auch an Dr. Charlotte Debus für die hilfreichen Diskussionen rund um das Thema DCE-MRT.

Vielen Dank auch an Dr. Dorde Komljenovic und Dr. Ina Kurth und ihre Arbeitsgruppen, deren Labore ich mitbenutzen durfte.

Ich möchte mich weiterhin bei meinen Freunden, nah und fern, für die Unterstützung, die Ablenkungen und die stets offenen Ohren bedanken. Mein herzlicher Dank gebührt auch den Kollegen aus der Abteilung *Medizinische Physik in der Radiologie* (insbesondere Anna, Kerstin, Dominik, Janis und Julian) und der Abteilung *Medizinische Physik in der Strahlentherapie* (insbesondere Alex, Alina, Andrea, Christin, Isabela, Lisa, Philipp, Rosemarie und Stefan) für die positive Arbeitsatmosphäre, die Gespräche und gemeinsame Unternehmungen außerhalb des DKFZs.

Am Ende möchte ich mich noch ganz herzlich bei meinen Eltern bedanken, die mich immer uneingeschränkt in all meinen Vorhaben unterstützt haben. Ohne euch hätte ich es heute nicht bis hierher geschafft. Vielen, vielen Dank für alles! Mein herzlicher Dank geht auch an Martin für die uneingeschränkte Unterstützung, insbesondere in den letzten Monaten.